THIS THESIS MAY BE READ ONLY IN THE LIBRARY

Reader's Declaration

I undertake not to reproduce any portion of, or use any information derived from this thesis without first obtaining the permission, in writing, of the Librarian, Trinity College. If permission is granted, I shall give appropriate acknowledgement for any portion of the thesis used or reproduced.

Date consulted	Name and address in block letters	University or institution	Signature

Nanostructured Composite Materials for Solar Energy Conversion

Lorcan J. Brennan

A thesis submitted to the University of Dublin, Trinity College for the degree of Doctor of Philosophy

School of Chemistry and CRANN

Trinity College Dublin

Dublin 2

Ireland

September 2014

Declaration

This thesis is submitted by the undersigned to the University of Dublin, Trinity College for the examination of Doctorate of Philosophy. It has not been submitted as an exercise for a degree to this or any other university. Except as otherwise stated, the author carried out the work described herein alone. The author agrees that the University Library may lend or copy the thesis upon request. The permission covers only single copies made for study purposes, subject to the Irish Copyright Legislation and Trinity College Library conditions of acknowledgement.

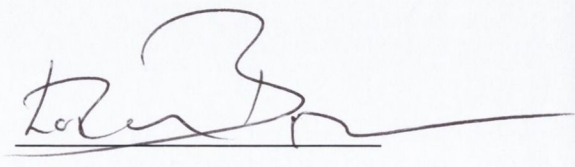

Lorcan J. Brennan

Summary

Sunlight is the largest of all available carbon neutral energy sources. Hence the development of solar energy devices, which can create energy from the sun are of extreme importance to society. In 1991, Gratzel et al. developed a new type of solar energy device, which could effectively convert solar radiation into electrical power. This device is known as the dye sensitized solar cell (DSSC). This development heralded a new era in solar energy research as scientists and engineers developed methods of increasing device efficiency, longevity and routes towards successful scale up of this technology. Largely speaking the DSSC has numerous advantages when compared to conventional Si based devices, which currently dominate the market. DSSCs are relatively easy to produce from cheap abundant materials and they can work effectively in various weather conditions (e.g. under diffuse light and indoors). The full scale development of this technology for commercial use has been limited. This is a result of the devices relative instability over prolonged periods. Devices can be volatile at extreme temperatures and the device contains a liquid component, which inevitably proves difficult to seal within the device for long periods of time. The DSSC also contains some expensive components which somewhat limit the suitability for industrial scale up.

The main aim of this body of work was to develop new materials for DSSCs or solar cells built upon similar architectures. It was envisaged that the development of such materials could open new routes towards the development of a solar energy device which would be free from the problems usually associated with DSSCs. This thesis predominately focused on developing alternatives to the 3 main constituents of the DSSC (the WE, the CE and the electrolyte)

Chapter 1 of the thesis provides an introduction to photovoltaics and provides a literature review on the various photovoltaic technologies, with particular attention paid to the DSSC. This chapter also outlines the main aims of this work.

Chapter 2 describes the details of the experimental procedures carried out during the course of this research. The instrumentation used and the characterisation techniques are also presented in this chapter.

Chapter 3 outlines the work that was carried out in order to optimise the fabrication procedure for DSSC working electrodes from nanoparticulate TiO_2.

Chapter 4 is dedicated to the development of a new type of electrolyte for DSSCs. It describes the development of a composite electrolyte which is free from iodine. The electrolyte was formed from a mixture of an ionic liquid (PMII) and graphene. This work showed that such electrolytes could perform 25 times better than unmodified ILs at very low additive content.

Chapter 5 describes the development of a new method for producing graphene oxide metal nanoparticle composite materials. These materials were deposited as electrodes using electrophoretic deposition. The materials properties were studied using electrochemical techniques and eventually as potential counter electrode materials in DSSCs.

Chapter 6 highlights research carried out into the potential use of plasmonic nanostructures as light harvesters in solar energy devices. This chapter describes new methods which were developed for creating photoactive electrodes, from gold nanoparticles and TiO_2. This chapter also presents results obtained from various experimental techniques and instrumentation that was specifically designed and developed for analysing this system. A full theoretical description of the observed processes is also provided.

Chapter 7 provides a conclusion to this body of work and outlines some of the main highlights and achievements of the research. This chapter also suggests routes that may be explored in the future as a means of understanding and developing these systems further.

Acknowledgements

First and foremost, I would like to express my sincere gratitude to my supervisor, Prof. Yurii Gun'ko, for giving me the opportunity to work under his guidance and supervision. Thank you for all of your help and support and for giving me the freedom to pursue my own interests.

I would like to take this opportunity to thank the School of Chemistry for the use of facilities which made this work possible. Many thanks must also go to the staff of the School of Chemistry, especially Patsy, Mark and Fred who were always available to lend a helping hand. Thanks to the staff of the CMA, especially Mr. Neal Leddy for help and guidance with microscopy and material characterisation.

I wish to express my thanks to Dr. Tania Perova of the School of Electronic Engineering, who gave me the training and freedom to use a range of equipment belonging to her and who was always available for useful discussion.

I would like to thank all the members of the Gun'ko group, past and present. Special thanks must go to Finn, for all of your help with your great microscopy skills, the long hours spent building and calibrating the solar simulator and trying to get to grips with the IPCE setup. I would also like to thank Cormac, Joe McCarthy, Joe Govan, Shane, Amro, Valarie, Sarah, Ritchie, Alex, Raquel, Olan and Iftikhar for all of your help and friendship. Also, this work was greatly helped by the numerous students that have worked with me, Sebastian, Sam, Vanessa, Aurelien, Sarah, Alex and Adeliene.

To all the members of KBB; Sean, Conor, Steve, Si, Gav and Cormac. Thanks for all the musical adventures over the past few years.

To my close group of friends; Liam, Finnian, Chris, Brian and Rob. Thanks for all of the great times we have had together.

I would like to express my warmest thanks to my nearest and dearest. To my family; Mam, Dad, Aine, Muireann and Bibi. You have always encouraged me to achieve my best in life. You have always been there for me and supported me in my education and in everything else that I do. I will always appreciate your love and support. To Ali, my best

friend, thank you for all the help, support and encouragement, especially over the past few months, when I may have been *a little* difficult at times. I'm really looking forward to our holiday together. All of my love x

Abbreviations

DSSC	Dye Sensitised solar cell
PV	Photovoltaic
SQ	Shockley-Queisser
TCO	Transparent Conducting Oxide
WE	Working electrode
CE	Counter electrode
0D	Zero Dimensional
1D	One Dimensional
2D	Two Dimensional
3D	Three Dimensional
SEM	Scanning Electron Microscopy
TEM	Transmission Electron Microscopy
FTO	Fluorine Doped Tin Oxide
ITO	Indium Doped Tin Oxide
XRD	X-ray Diffraction
I-t	Current – Time
eV	Electronvolt
UV-Vis	Ultraviolet- Visible
CVD	Chemical Vapour Deposition
QD	Quantum Dot
HTM	Hole Transporting Material
MEG	Multiple Exciton Generation
IL	Ionic Liquid
AM 1.5	Air Mass 1.5
PMII	1-Methyl-3-Propylimidazolium Iodide

CNT	Carbon Nanotube
MWCNT	Multi Walled Carbon Nanotube
CB	Carbon Black
EETM	Extended Electron Transfer Mechanism
CV	Cyclic Voltammetry
AFM	Atomic Force Microscopy
SCRE	Saturated Calomel Reference Electrode
TGA	Thermogravimetric Analysis
DTGA	Differential Thermogravimetric Analysis
Jsc	Short Circuit Current Density
Isc	Current Density
Voc	Open Circuit Voltage
FF	Fill Factor
η	Efficiency
Rsh	Shunt Resistance
Rs	Series Resistance
I-V	Current – Voltage
J-V	Current Density- Voltage
MPP	Maximum Power Point
GO	Graphene Oxide
rGO	Reduced Graphene Oxide
PtrGO	Platinum – rGO
AurGO	Gold – rGO
FT-IR	Fourier Transform- Infrared
FWHM	Full Width Half Maximum
NP	Nanoparticle

EDX	Energy Dispersive X-ray Spectroscopy
NMP	N-Methyl-Pyrrolidone
EPD	Electrophoretic Deposition
DC	Direct Current
SPR	Surface Plasmon Resonance
SPB	Surface Plasmon Band
PEC	Photo Electrochemical
Hz	Hertz
J_I	Initial Current
J_{SS}	Steady State Current
Eg	Band Gap Energy
IPCE	Incident Photon to Conversion Efficiency
LIA	Lock- in-Amplifier

Table of Contents

Chapter 1: Introduction

Chapter 2: Experimental

Chapter 3 : Graphene – ionic liquid electrolytes for iodine free dye sensitized solar cells

Chapter 4: Metal nanoparticle-graphene oxide composites for solar cell applications

Chapter 5: Generation of enhanced photo-current from plasmonic gold nanoparticles in nanoparticulate TiO_2 films

Chapter 6: Conclusions and future work

List of Publications

List of Figures and Tables

Chapter 1

Chapter 2

Chapter 3

Chapter 4

Figure 5.21 Calculated contributions to $\Delta IPCE(\lambda)$. The graph shows estimated terms $\Delta IPCE_{Au-NP,\,electrons}$, $\Delta IPCE_{Au-NP,\,holes}$, $\Delta IPCE_{TiO_2,\,electrons\ and\ holes}$ and also the calculated full spectrum $\Delta IPCE$.

Figure 5.22 Band diagram of the Au -TiO_2 system and the optical and relaxation processes used in the photocurrent model. Blue and red dots represent photo-generated hot plasmonic electrons and holes, respectively.

Appendix

Figure A.1 Scanning electron microscopy images recorded for single layer deposition of TiO_2 onto FTO glass substrates using the doctor blade method.

Figure A.2 SEM image of a single TiO_2 layer deposited onto FTO glass substrate through the doctor blade method.

Figure A.3 SEM images of multiple layer TiO_2 electrodes fabricated using the doctor blade method. Image a) shows a topographical image of the 2 cm^2 TiO_2 electrode with clear evidence of cracking. Image b) highlights the cracks in the film.

Figure A.4. Side profile SEM image of multiple layer TiO_2 deposition showing the light absorption layer and the scatter layer.

Figure A.5 Profilometry image recorded for a TiO_2 electrode fabricated using the doctor blade method.

Figure A.6 Screen template design for 8 x 1cm^2 photoanodes and photographic image of the screen printing setup

Figure A.7 Outline of sintering profile used for the heat treatment of TiO_2 photoanodes

Figure A.8 Photographic image of 8 1 cm x 1 cm TiO_2 photoanodes on an FTO glass substrate, post sintering.

Figure A.9 Optical absorption of anatase TiO_2 film deposited onto FTO.

Figure A.10 Raman spectra recorded for anatase TiO_2 on a glass substrate.

Figure A.11 X-ray diffraction pattern recorded for degussa P25 anatase TiO_2 powder

Figure A.12 HRTEM images of anatase TiO_2 nanoparticles

Figure A.13 SEM images recorded for TiO_2 photoanodes fabricated using the screen printing method. Images a) and b) shows 20 nm TiO_2 nanoparticles, while images c) and d) show the side profile of the photoanodes, with both the light absorption and light scattering layers.

Chapter 1

Introduction

1.1 Aims and objectives of the project

It is well established that the commercialisation of new types of solar energy conversion devices, which can produce energy efficiently, economically and with long term stability requires the development of new materials and methodologies in order for these demands to be met. The main goal of this thesis is the development of new materials for solar cells which differ from the conventional materials currently employed in these devices. These new materials which have been developed offer new routes for the generation of electric power from light.

The first major aim of this work was the development of a reliable method for producing photoanodes for solar cells devices. The photoanodes were produced from nanoparticulate titanium dioxide. This work is not considered as original or as an advancement of the field; however it served as an essential component of this thesis. The development of this procedure allowed for the reproducible fabrication of TiO_2 photoanodes and these photoanodes were used as the solar cell template for all subsequent chapters of this thesis.

Current trends in the field of solar energy research have focused on the development of solid state devices, which are free from the organic liquid electrolytes that are commonly employed. The past two years has seen major research in this area, in particular with the development of perovskite based materials. Our research also looked at alternative methods for removing the liquid electrolyte layer in DSSCs. We aimed to develop new electrolytes which were based on composites of ionic liquids (ILs) and graphene. The remarkable properties associated with graphene and the recent developments which have led to its mass production means that this material can now be applied to a whole host of applications. We aimed to incorporate this novel composite electrolyte in DSSCs and aimed to use this method to increase the efficiency of the IL based electrolytes. It was also reasoned that these electrolytes would show enhanced stability when compared to the traditional organic based electrolytes as they are free from organic solvents and free iodine.

Another objective of this work was the development of new materials for DSSC counter electrodes (CEs). The platinum ITO CE currently used in DSSCs accounts for 25~35 % of the total device cost and its high cost has limited the mass production of these devices. Hence, the development of new cost effective materials which can effectively carry out the catalytic role of the CE is of great importance. We aimed to develop a method for depositing nanoparticles of both platinum and gold onto 2D graphene oxide substrates and use these materials as materials for DSSC CEs. It was reasoned that this material could serve a useful role for this application as the extremely high surface area of the carbon support would function to provide a large amount of active sites for reduction of redox electrolytes. The presence of heavy metal nanoparticles deposited on the high surface area support should also lead to enhanced catalytic activity for this reduction.

The production of these Pt/Au composites with GO could also show interesting properties. We aimed to study the effect of this metal deposition on the optical conductivity of the insulating GO. Metal nanoparticles are known to show interesting optical properties known as plasmon resonance. A resonance of the metals conduction band electrons can occur when the nanoparticles interact with light of particular frequencies. This process leads to areas of high excited electron density on the surface of the nanoparticles. We aimed to investigate if this effect could be utilised to enhance the conductivity and optical conductivity of these materials, with the aim of producing an opto-electronic material, which may find applications in devices such as optical switches or sensors.

We also aimed to examine the possibility of using the effect of plasmon resonance for the generation of photocurrent. Current photo-sensitizers used are inorganic or organic dyes, which are known to suffer from photo-bleaching and low molar extinction co-efficients when compared to quantum dots, which can also be used for sensitization. Unfortunately, quantum dots are generally made from toxic elements and this is likely to be a limiting factor in their eventual use in these devices. We aimed to employ noble metal nanoparticles, in particular gold and palladium as potential photo-sensitizers in solar cells. This is quite a new concept in the area on solar energy conversion and therefore we aimed to undergo a rigorous experimental and theoretical examination of the processes that occur for these new photo-current generators.

1.2General Introduction

Energy is one of the basic needs of any developed society. Energy is consumed by society in order to facilitate transport, heating, communication, trade, health care and a whole host of day to day activities. Energy exists in many forms such as light, sound, heat, chemical and electrical energy. Energy is generally defined as the ability to do work or the ability to bring about change. Society currently derives the majority of its energy from the combustion of carbon sources such as fossil fuels. Carbon serves as an energy rich fuel for society and much of the world's energy is now harnessed from the exploitation of petroleum, natural gas and coal deposits, found deep below the earth's crust. This energy is deemed to be a non-renewable source of power as global reserves are known to be depleting. Increasing cost of fuel, problems associated with carbon dioxide emission and an ever increasing population has led to the search for alternative methods of energy generation from renewable sources i.e. an energy source which has an infinite supply. The capture and conversion of such an energy source has the capability to greatly reduce global emissions, stabilize energy costs and reduce the exploitation of global resources.

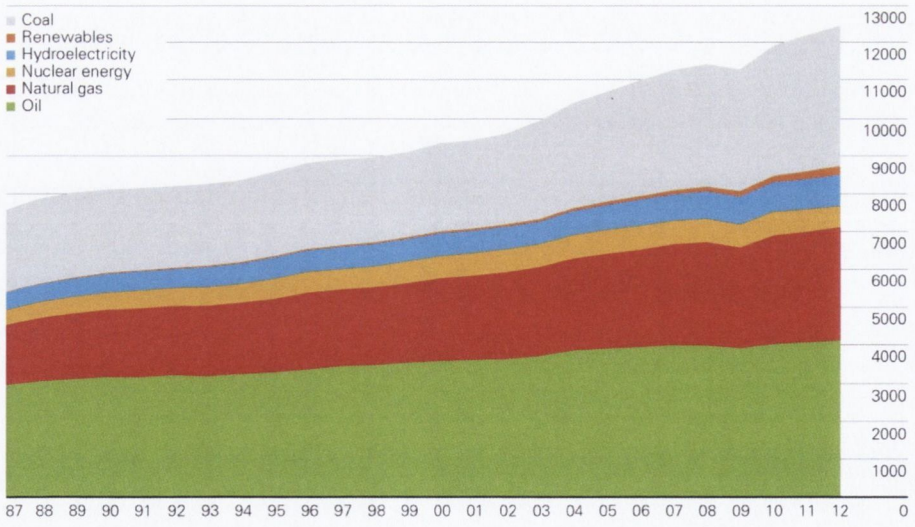

Figure 1.1 World energy consumption as of 2013 (million tonnes oil equivalent)[1]

Several alternatives have been shown to be capable of supplying renewable power. Hydroelectric power, wind power and solar energy are among the renewable energy sources which have been explored in recent decades. Among all of these sources, solar energy has emerged as the most practical and long lasting alternative to a fossil fuel based

energy source. In order to generate power from solar energy it is first necessary to capture the energy and then convert it into another form of energy which can be used to do work. Solar energy can be converted into both heat and electric energy with moderate efficiency. Photovoltaic (PV) cells are used to convert light into electricity and offer a competitive alternative to fossil fuel consumption. Presently, silicon (Si) cells dominate the solar cell market and in total they produce ~ 0.1% of the world's energy.[2] In this introduction chapter we provide an overview of the current trends in solar energy research and outline the aims and objectives of our work.

1.3Solar irradiance

Solar irradiance is defined as the amount of available solar radiation per unit area, measured in watts per square meter (Wm^{-2}). Radiation emitted by the sun is a mixture of electromagnetic waves which includes Infrared radiation (IR), ultraviolet rays (UV), visible light and X-rays. The earth's atmosphere filters the majority of the UV radiation through photo dissociation of ozone from of high energy light. X-ray radiation is absorbed through photo electric absorption through interactions with oxygen and nitrogen atoms in the atmosphere.[3] The majority of the light hitting the earth's surface is composed of visible light (700-400 nm) and IR radiation. The light that reaches the earth has a power of ~1400 Wm^{-2}, this value equates to approximately $3x10^{24}$ J $year^{-1}$, which is about 10^4 times more than the current energy consumption by mankind annually.[4,5] Figure 1.2 below shows the blackbody emission from the sun and how this emission profile is augmented after passing through the atmosphere.

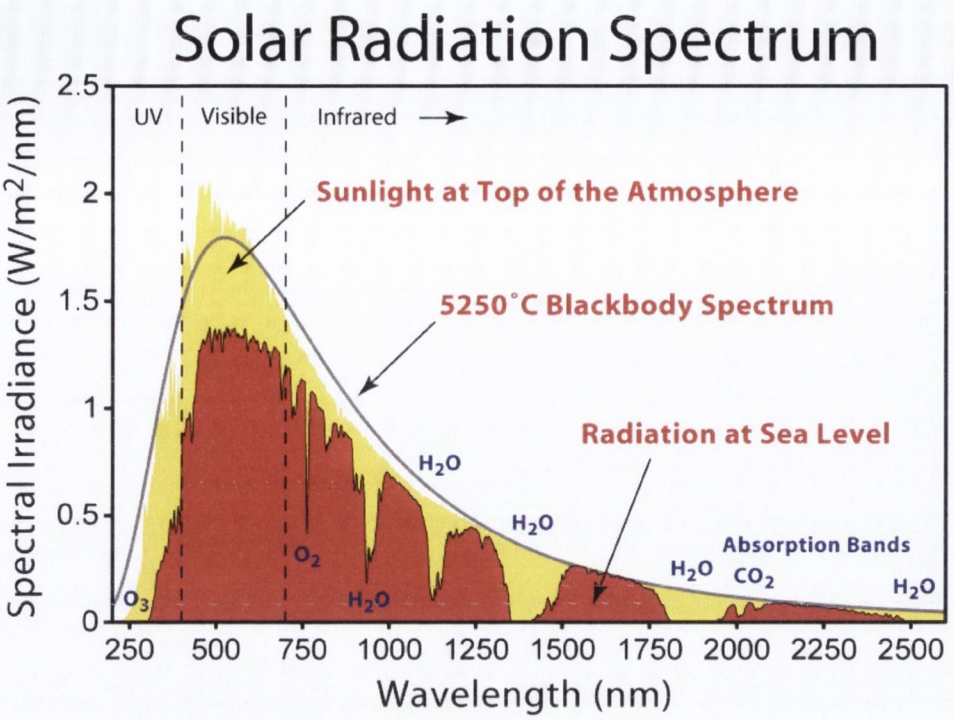

Figure 1.2 The distribution of solar energy hitting the earth's surface [6]

1.4 History of solar energy harvesting and cell types

The photoelectric effect is the processes of electron emission from a metal when illuminated with light. This effect was first observed in 1839 by Becquerel while studying the effect of light on electrolytic cells.[7] The photoelectric effect was developed further by Wiloughby Smith in 1873, while examining the effect of light on the conductive properties of selenium.[8] At the time, classical electromagnetic theory was used to explain the photoelectric effect. It was thought that there was a direct transfer of energy from light to electrons in the metal. If this was to hold true it was reasoned that changes in the amplitude of light incident on a sample would change the rate of electron emission from the metal. However, experimental observations did not agree with this theory and it was found that electron emission only occurred when the light used reached or exceed a threshold frequency. Below this threshold frequency no electron emission would be observed, regardless of the illumination amplitude. This discrepancy was explained by Albert Einstein in 1905 in his paper ''On a Heurestic Viewpoint Concerning the Production and Transformation of Light''.[9] This work described light as a collection of

packets of energy known as photons, which displayed wave particle duality. Using this theory Einstein could account for the experimental observations of the photoelectric effect. The first experimental proof of the photoelectric effect was provided by Robert Milikan in 1916 while measuring the kinetic energy of the photoelectrons emitted from the surface of a clean metal plate when exposed to monochromatic light.[10]

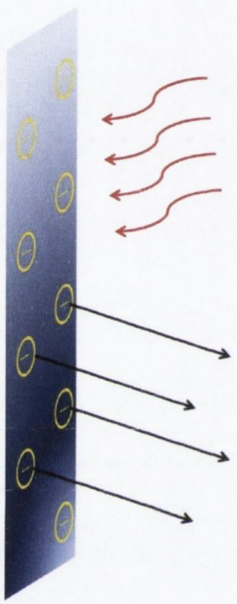

Figure 1.3 Schematic representation of the photoelectric effect. Incident photons (red) emit electrons with kinetic energy (black) proportional to the frequency of the incident light (E=hv)

The first photovoltaic device built using the photovoltaic (PV) effect was fabricated by Charles Fritts in 1885.[11] Here, a thin layer of gold was coated onto selenium and produced an energy conversion efficiency of ~1%. This stood as a fundamental breakthrough in PV understanding as it utilized a junction to create a photo voltage. It was not until 1954 that PV technology was truly developed. The first silicon PV cell was developed at Bell Laboratories in the United States by D. Chaplin. C. Fuller and G. Pearson.[12] Arsenic doped silicon coated in boron was used to create a p-n junction which could separate an electron-hole pair with an energy efficiency of ~6 % when illuminated with solar radiation. Since

this development a large amount of research has focused on the development on methods for increasing the solar to electric efficiency and reaching the thermodynamic maximum efficiency. This is known as the Shockley-Queisser (SQ) limit, which stands at 34 %.[13] This limit was theorized by Shockley and Queisser in 1961, and still stands as an important theory in the field. The limit assumes that for a single p-n junction device with a band-gap of 1.3 eV, the maximum efficiency that can be reached is 34% under an A.M 1.5 solar spectrum. The model has since been developed further to account for hetero-junction devices, which may or may not use solar concentrators. For these devices the SQ limit has been calculated to be 86%.[14]

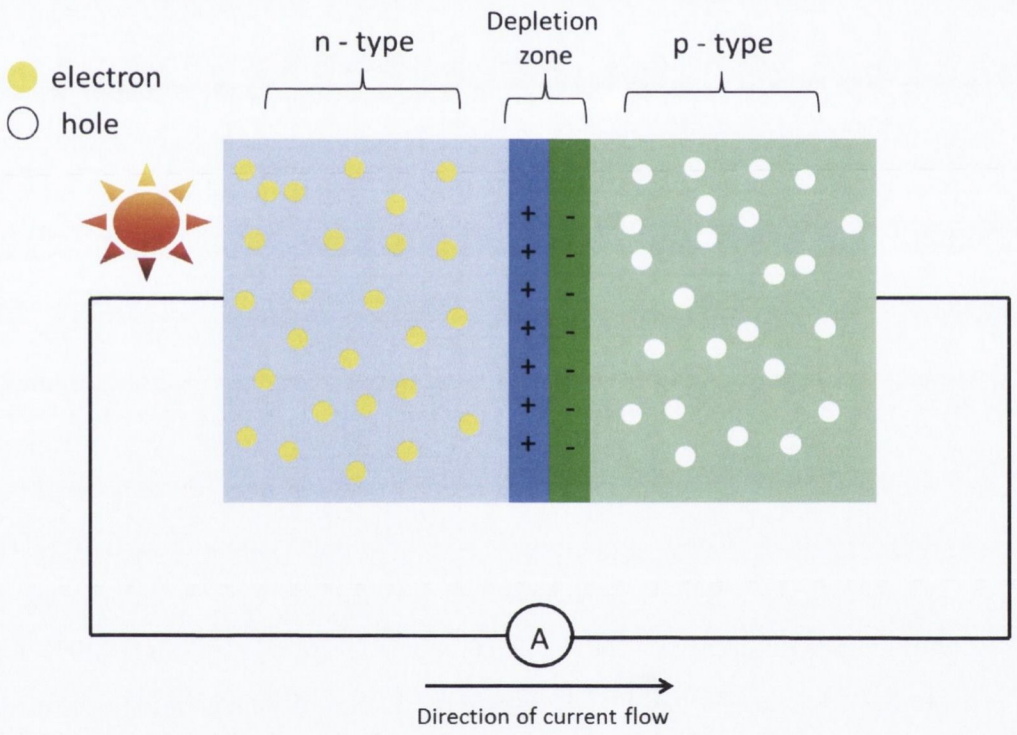

Figure 1.4 Schematic of a p-n junction showing the depletion layer and the creation of photocurrent when illuminated.

The p-n junction is formed in the depletion zone between an n-type material and a p-type material. An n-type material is doped with atoms which have a valency greater than that of the parent crystal atoms. The effect of n-type doping is to increase the negative charge density in the n-doped material. The excess negative charge introduced by doping does not

contribute to the atomic bonding and thus these charges are free to move around the crystal. Since these charges are mobile they can carry an electrical current. On the other hand, a p-type material is doped with atoms which have a valency less than that of the parent crystal atoms, thus increasing the hole density in the p doped region. Common dopants used to dope Si are phosphorous (n-type) and boron (p-type).

When at zero bias, an equilibrium condition is set up in the region of the p-n junction. The establishment of equilibrium sets up a potential deference across the junction. Extra electrons, caused by n-type doping, diffuse into the positively doped p-region. Likewise, holes from the p-region migrate to the negatively dense n-doped region. This movement of electrons and holes causes a buildup of positively charged ions in the n-doped region and negatively charged ions in the p-doped region. This buildup of charge occurs at the junction between the n-p interface and is known as the depletion layer. When light illuminates the n-type side of the junction, an electron can be dislodged and the potential difference across the junction will cause the electron to flow towards the n-electrode, through a load and can be used to do useful work. The electrons then flow into the p-type side through the external circuit where they combine with positively charged holes in the p-doped electrode.

Since the development of the first Si PV devices a large and varied amount of research has focused on the development of new materials and architectures for harnessing solar energy. Currently, Si PV dominates the solar market and accounts for 90% of all commercial solar cells. Two main types of Si PV are available to the consumer, single crystal (c-Si) or poly-crystalline (p-Si). These cells have been termed ''first generation'' devices and enable photo to electric conversion efficiency of ~25% for s-Si and ~20% for poly-Si. The limiting factor impeding the large scale utilization of this technology is cost.[15] Highly pure Si wafers are required for production of high efficiency modules and this represents half the cost in producing first generation devices. When compared to current energy costs for fossil fuel based energy, first generation solar is approximately one order of magnitude more expensive.

The second generation of solar cells was developed with the aim of reducing cost and maintaining efficiency. The second generation of cells are broadly classed as thin film solar cells as they employ an absorber layer of 1-10 μm in thickness. The second generation of cells were formed from a variety of different materials such as amorphous

silicon (a-Si), cadmium indium selenide (CIS), cadmium indium gallium selenide (CIGS) and gallium arsenide (GaAs). The second generation of cells have reported moderate efficiency, generally in the order of ~15% but have not gained significant market share due to technological problems in fabrication and limited stability

The third generation of solar cells radically reduced material and processing cost. Unfortunately, third generation cells have reported moderate efficiency values of ~11%, however recent research has led to the development of new concepts in the design of third generation devices and large efficiency increases have been observed. Third generation devices differ from the previous generation of cells by using different materials and device architectures. Compared to first and second generation cells which are based upon single crystal and hetero-junction semiconducting layers, the third generation has largely focused on sensitisation of semiconductors with large surface area for light absorption and energy conversion. The creation of high surface area semiconducting layers has been possible with advances in nano-technology and materials science. Today most third generation devices incorporate one or more nanostructured materials in devices.

The National Renewable Energy Laboratory (NREL) publishes on the latest developments in solar cell efficiency annually. As can be seen from figure 1.5 below, a large and varied amount of solar energy devices can currently be fabricated. The current solar to electric conversion efficiency record stands at 44.4%, for a multiple junction device (using a photo concentrator). Although this is an extremely high efficiency for a solar cell, these devices will never reach mass manufacture. This is due to the high cost associated with the materials needed for these cells and the fabrication procedures.

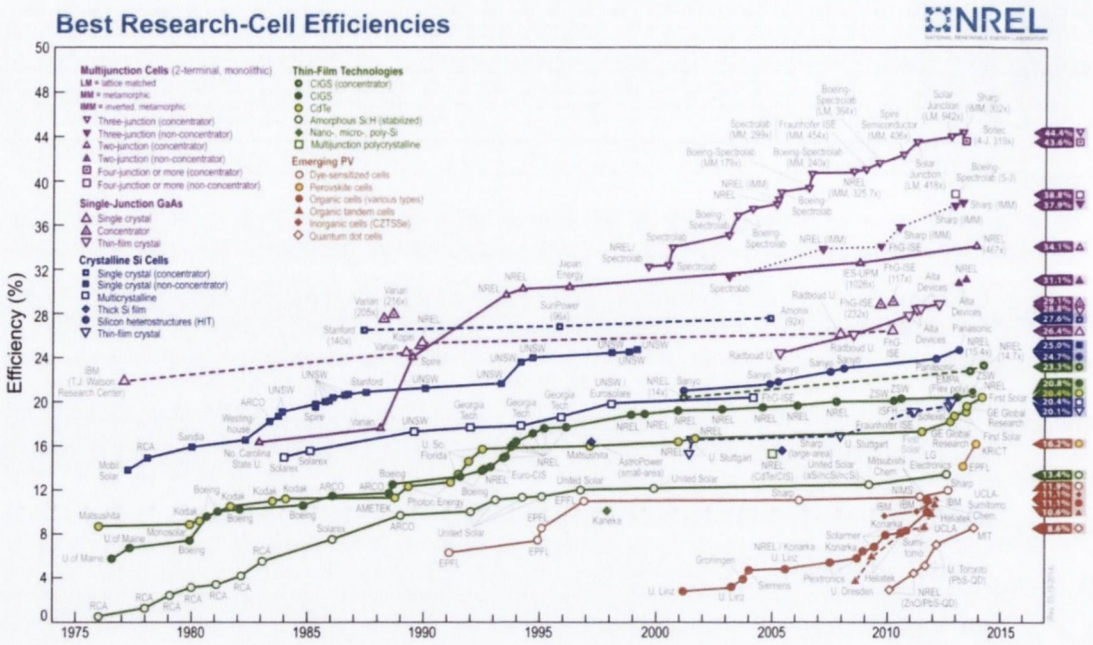

Figure 1.5 Graph representing trends in solar cells efficiencies as of March 2014. This plot is courtesy of the National Renewable Energy Laboratory, Golden, CO.[20]

1.5 The dye sensitized solar cell

Since M. Grätzel and B. O'Regan first reported the 'third generation' solar cell in *École Polytechnique Fédérale de Lausanne (EPFL)* in 1991,[21] dye sensitized solar cells (DSSCs) have been of great interest to many academics and industries.[4,5,22-24] The concept of dye sensitization onto wide band gap semiconductor metal oxides had been around for some time before this breakthrough.[25-30] The major advance in the field came with the use of nanoparticulate TiO_2 instead of monolayer TiO_2 films. The nanocrystalline semiconductor photoanode is a key part of DSSC, which provides the light absorption, charge separation and collection. The most widely used absorbing layer is based on TiO_2 semiconducting oxide, although other wide-band gap semiconductor oxides such as ZnO or SnO_2 have also been employed.[5] Due to the large band gap (3–3.2 eV) of titanium dioxide, it is only able to absorb UV light below 380 nm and so has low conversion efficiencies. This is why, contrary to silicon, a sensitizer is needed to separate the optical absorption and the charge-

generating functions. This sensitizer absorbs light in the visible range, to inject charge carriers into the semiconductor with a wide band gap. The absorption of light by a monolayer of dye is weak, as the area occupied by one molecule is much smaller than the optical cross section required for an effective light capture. A respectable photovoltaic efficiency cannot, therefore, be obtained by using a flat semiconductor surface, but rather by using a porous, nanostructured film with a huge internal surface area. The TiO_2 layer, typically 10-15 μm thick and with a porosity of 50%, has a surface area available for dye chemisorptions over a thousand times that of a flat electrode of the same size.

The use of nanoparticulate TiO_2 as a photoanode greatly increased the active surface of the electrode, enabling increased levels of dye adsorption which resulted in greatly increased photocurrent densities being observed. DSSC technology enables the generation of electrical current by the absorption of a photon by a dye molecule (Figure 1.7 – 1.8). The most common dye molecules are derivatives of cis-Bis(isothiocyanato) bis(2,2'-bipyridyl-4,4'-dicarboxylato ruthenium(II), more commonly termed ''N3'' or ''black dye''. Organic dyes have also proved popular as metal free alternatives. Quantum dot sensitisation of TiO_2 can also produce high levels of photocurrent and has advantageous properties for solar applications due to properties such as a high molar extinction coefficient, resistance to photo bleaching and a tunable absorption spectrum. It has also been suggested that QD sensitization of TiO_2 may allow for multiple excition generation (MEG), a process whereby the absorption of one incident photon can create multiple charge carriers.[31,32]

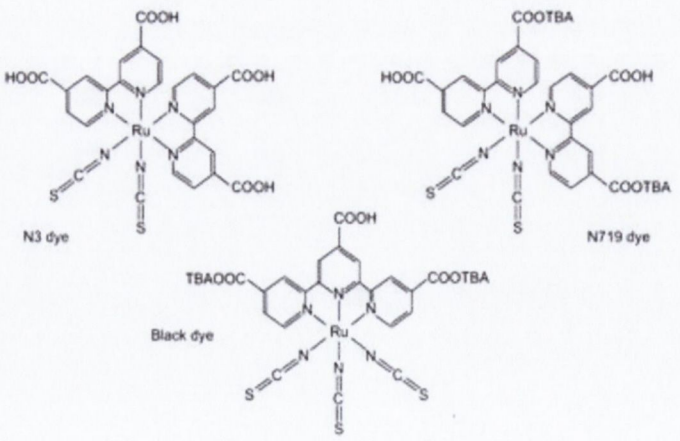

Figure 1.6 The chemical structures of the most common ruthenium sensitizers N3, N719 and black dye.[33]

The absorption of light by the photo sensitizer leads to the excitement and injection of an electron into the conduction band of an n-type semiconductor, such as nanoporous titanium dioxide (TiO_2). The sensitiser is then regenerated by an electrolyte containing a redox couple such as I^-/I_3^-. More recently Co(II/III) redox mediators have proven popular due to their high efficiency and non-caustic nature.[34] The I^-/I_3^- is also known to suffer from a high over potential for dye regeneration[35,36] and competitive light absorption by tri-iodide.[36-38] The oxidized species of this redox couple is reduced at the counter electrode. The counter electrode is normally platinum which acts an electrocatalyst for the reduction of the tri-iodide as it increases the rate of electron transfer from the external circuit back into the electrolyte. The front electrode of a DSSC is composed of a transparent conductive oxide (TCO) on glass. Existing transparent conducting electrodes are mostly based on indium tin oxide (ITO) and fluorine tin oxide (FTO) coated substrates. DSSCs are relatively cheap to produce and they can be printed on flexible substrates, such as plastics. The first reported DSSC recorded an efficiency of 7.1-7.9%[21] in simulated sunlight while the current record efficiency for a liquid junction DSSC is 12.3%, utilizing the Co(II/III) redox mediator with a porphyrin sensitizer.[39]

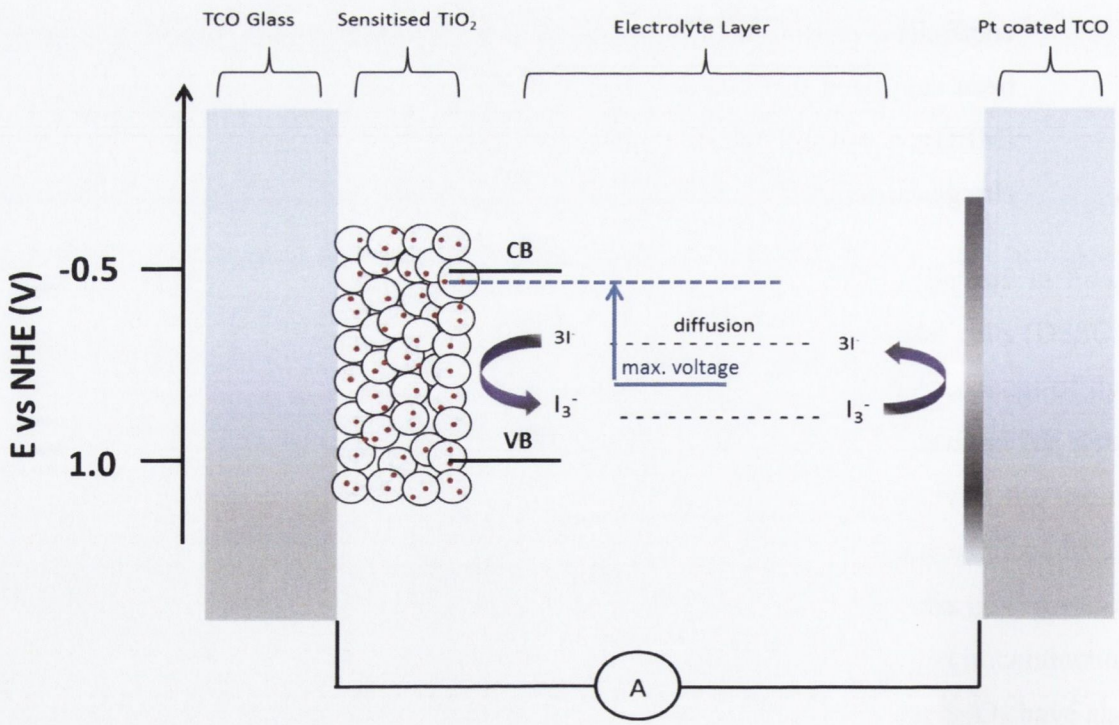

Figure 1.7 Schematic showing the architecture of a DSSC.

The performance of the DSSC is predominantly based upon 4 energy levels between the different components of the device: the sensitizer excited state (approximated as the LUMO) and the sensitizer ground state (HOMO), the Fermi level of the semiconductor, which is usually located below the conduction band and the redox potential of the mediator being used in the electrolyte. The photocurrent that is produced under illumination is determined by the energy difference between HOMO and LUMO levels in the sensitizer, analogous to the bandgap. The energy level between the LUMO and the semiconductor conduction band ($\Delta E1$) is also an important parameter. The LUMO must lie at a potential which is negative with respect to the conduction band in order to be able to inject electrons effectively. The HOMO of the sensitizer must lie at a potential which is positive with respect to the redox potential of the redox mediator, ($\Delta E1$) in order for the oxidised dye to be able to accept electrons efficiently. Both $\Delta E1$ and $\Delta E1$ need to be larger than approximately 200 mV in order to keep the driving force for both of these processes at a high level and ensure efficient electron transfer.

Recombination dynamics in DSSCs play a major part in limiting the conversion efficiency of DSSCs. Recombination in DSSCs is a result of the back transfer of photo-excited electrons, which results in decreased levels of photocurrent. Recombination is DSSCs follows 2 primary pathways. Photo-excited electrons can recombine with oxidized dye molecules on the TiO_2 surface and can also reduce the oxidized form of the redox couple in the electrolyte. In order for the device to work efficiently, the time scales for the electron injection into the semiconductor and removal to the TCO must be significantly faster than the time scales for recombination. It has been calculated that electron injection from the N3 dye to TiO_2 occurs on the order of femtoseconds to picoseconds[40-43] while recombination processes occur in the nanosecond time scale for the oxidized dye.[44] However, for fully assembled devices it is know that the injection rate from dye to TiO_2 is greatly affected by the surrounding medium, most notably the electrolyte. It has been determined that the primary factor which determines the electron injection efficiency is the energy difference between the TiO_2 acceptor states and the dye excited state. This energy gap is strongly influenced by the electrolyte composition and large variations in electron injection efficiency can be observed when the electrolyte composition is changed.[45]

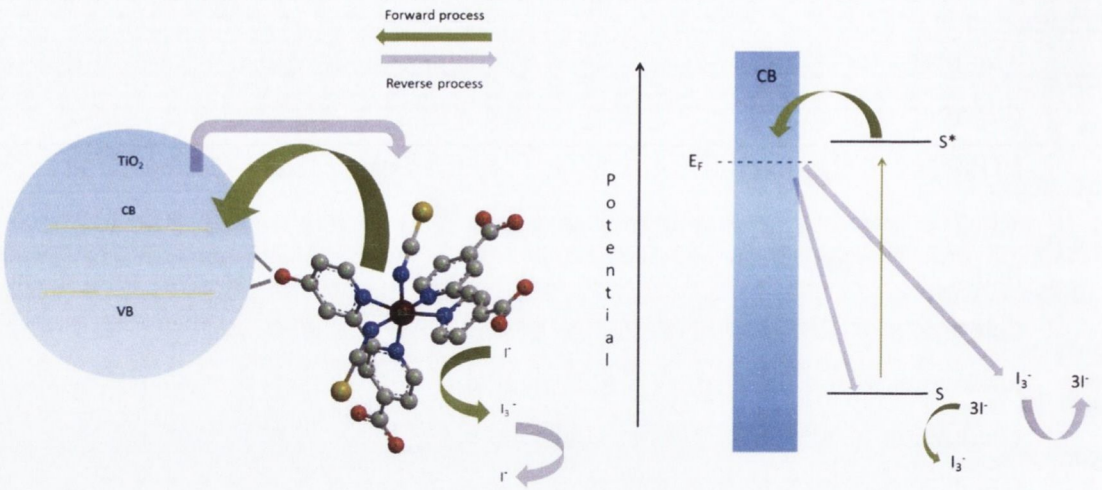

Figure 1.8 Schematic representation of the process occurring at the TiO_2/dye interface.

The recent development of the solid state DSSC (ss-DSSC) was a major advance in the field. Liquid electrolytes have proved to be a major obstacle in the industrial development of stable DSSCs. Evaporation of low boiling point solvents over time and eventual degradation of polymer seals from caustic electrolytes have limited the scalability of these devices. Initial research focused on the solidification of the liquid electrolyte with the addition of solid micro- and nanocomponents [46-50]. More recently all solid state solar cells have been fabricated with a modified architecture compared to the classical DSSC architecture and most importantly with new materials. In these cells a solid state perovskite material is deposited onto a thin TiO_2 layer. The perovskite acts as the light absorption layer and injects photoexcited electrons efficiently into a thin layer of TiO_2. A hole transporting material (HTM) is used to remove photo generated holes from the perovskite and the circuit is completed with a metal back contact. Grätzel's group have reported certified efficiencies of 14.1% while Park has shown efficiencies of 16% and estimates power efficiency will approach 20% in the near future.[51,52]

1.6 Nano-structured TiO_2 and it application in solar energy

Ever since the photo-catalytic water splitting properties of TiO_2 were discovered by Honda and Fujishima in the 1970's,[53] a large and varied amount of work has focused on the developing systems utilising TiO_2 for a range of solar energy systems. TiO_2 can be applied effectively to a number of solar energy systems ranging from solar water splitting for H_2 generation, as a collector material for photo-excited electrons, whereby it effectively separates photo-excited electrons and holes, as a material in hetero-junction PV devices and as a means of degrading organic contaminants through the creation of photo generated free radicals.[54-57] Given its low cost, relative abundance, ease of processing and stability, TiO_2 has proven to be an ideal candidate for a host of applications.

TiO_2 is classed as a wide bandgap n-doped semiconductor, which absorbs strongly in the UV region of the spectrum. The optical bandgap of TiO_2 is ~3.2eV for the anatase phase. The material can crystallize in three different structures; rutile, anatase and brookite. Other phases have been synthesised at high pressures, such as the cotunnite phase,[58] however only the rutile and anatase phase play any major role in applications for TiO_2 and will be solely considered here. The basic building block for both the anstase and the rutile phase consists of a titanium atom coordinated to 6 oxygen atoms in a distorted octahedral configuration. In both structures the apices of the octahedron have slightly longer bond lengths than the equatorial bonds. In the anatase phase the octahedra share each of the four equatorial oxygen atoms with the neighboring octahedra, while in the rutile phase the neighboring octahedra share one corner oxygen atom.[59,60]

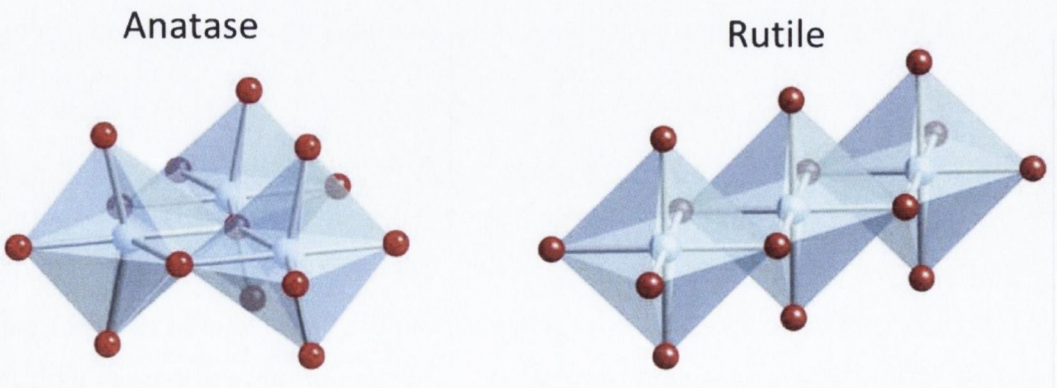

Figure 1.9 Representation of anatase and rutile phase of TiO_2. Modified and reproduced from the literature.[61] (Ti atoms; white, O atoms; red)

Since the first demonstration of the photo-catalytic properties of TiO_2,[53] intensive research has focused on extending the optical absorption properties of the semiconductor as a means of harnessing more of the solar spectrum. Depending on the phase of the material, the maximum absorption of TiO_2 lies between 300-400 nm.[62,63] Considering that the UV region of the solar spectrum has a weak solar flux it has been deemed necessary to expand the absorption of TiO_2 in to the visible region of the spectrum, where the incident flux is greatest. Numerous routes have been proposed and investigated as a means to achieve this.

Ion doping by both metals and non-metals of TiO_2 has been shown to be a successful route for extending the range of TiO_2 absorption. Hoffmann et al. have shown that the presence of transition metal ion dopants in nano sized TiO_2 crystals significantly influences photo reactivity, recombination rates and interfacial electron transfer rates. It was found that Ru^{3+} doping lead to a significant increase in visible light absorption when compared to unmodified TiO_2.[64] The choice of transition metal is important when considering routes extending the spectral range, as certain transition metal ions have been shown to increase spectral range but at the cost of greatly increasing recombination rates.[65,66] The effect of fluorine doping on TiO_2 was investigated by Yu et al. and was again associated with a red shift of the absorption characteristics when compared with the un-doped oxide. Li et al. investigated the effect of boron and nitrogen doping on the optical properties of TiO_2 and found that they could effectively extend the range of TiO_2 absorption past 500 nm, while nitrogen doping by Asahi and co-workers noted similar results and found that the material successfully degraded methylene blue and acetaldehyde when illuminated.[62] Nitrogen and copper doping was also investigated by Fisher and co-workers. They found that doping of TiO_2 led to enhanced visible absorption through the creation of inter-band states and thus shift the absorption into the visible. Photo catalytic studies showed that films made from the doped oxide could effectively degrade methylene blue when illuminated with solar radiation.[54]

The most successful route for extending the optical range of TiO_2 has been dye sensitisation. This mechanism allows for dye molecules to chemisorb onto the surface of the oxide and inject excited state electrons into the conduction band of the semiconductor, provided that the dye excited state lies at a potential more negative with respect to the electrochemical scale than the CB maximum. The most common dyes used in TiO_2 sensitisation are transition metal complexes, porphyrins,[67-70] and semiconducting quantum dots.[71-75] The dye sensitization route has proved extremely successful at extending the

spectral range of TiO_2, most notably with the development of DSSCs. In order for sensitization of the oxide to be successful the sensitizer must contain carboxylic acid functionality in order to bind to the surface of the oxide (for chemisorbed dyes). Many proposed routes for this binding mechanism have been considered,[76-80] and it is now believed that the binding of the dye to the oxide is a combination of bidentate-bridging and H-bonding from 2 neighboring carboxylic acid groups linked on the same bipyridine ligand (for N719 sensitization).[81]

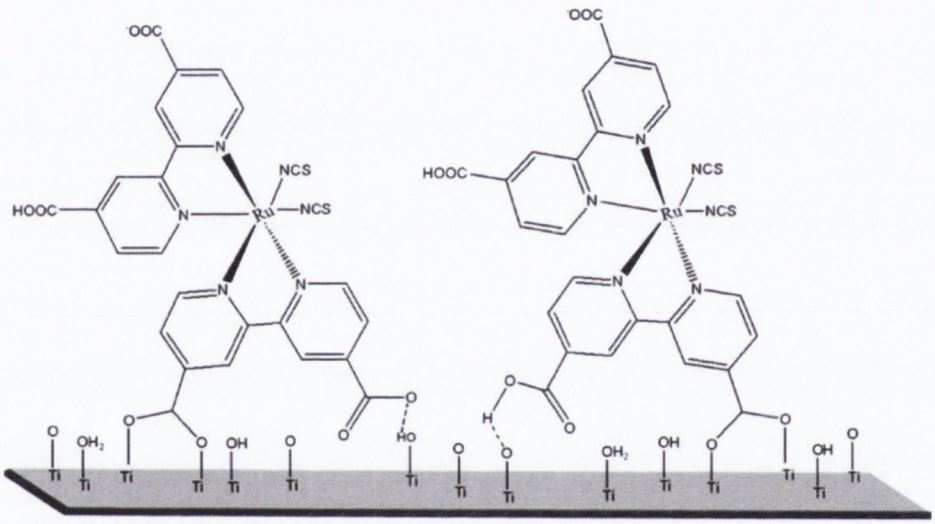

Figure 1.10 Proposed binding mechanisim for N719 on TiO_2. Image reproduced from the literature.[82]

The success of TiO_2 in DSSCs is attributed to its ability to accept electrons from the sensitiser, the injection of electrons form the sensitizer to the conduction band of the semi-conductor falls on the order of picoseeconds (ps) or femtoseconds (fs), as discussed earlier. The material is also cheap, abundant and non-toxic, which is highly advantageous when considering scale up. The mesoporous TiO_2 working electrode in DSSCs can be prepared via a number of routes. The deposition most commonly involves the preparation of a paste containing TiO_2 nanoparticles and the application of the paste to a TCO through the doctor blade method or screen printing. It is also possible to disperse TiO_2 in a liquid medium and form an electrode through spin coating. Once deposited, the electrode is heat treated in a process known as sintering. This process takes place at around 450 ^{O}C to 500 ^{O}C,

depending on the characteristics of the paste being employed. The sintering process serves to thermally decompose the organic constituents of the paste, and allows for adhesion of the TiO_2 to the substrate. This process also allows for a process known as necking to occur, whereby the individual particles fuse together and create interconnects between particles, which allows for facile electron transport throughout the depth of the film.

The TiO_2 photoanode is usually fabricated to have a post sintering thickness between 12 - 16 μm. In order to create high efficiency DSSCs the photoanode is usually fabricated to produce the TiO_2 ''double layer''. This type of photoanode contains a light absorption layer composed of 20 nm TiO_2 nanoparticles and a light scattering layer, which is composed of TiO_2 nanoparticles with a size range between 100 – 400 nm. The light absorption layer is primarily responsible for the generation of photocurrent, while the scatter layer functions to re-scatter light which has not been absorbed and results in increased levels of light capture.

1.7 Graphene and its application in dye sensitized solar cells

Graphene is the name given to a flat monolayer of sp^2 hybridized carbon atoms tightly packed into a two-dimensional (2-D) honeycomb crystal lattice. Graphene is the basic building block for graphitic materials of all other dimensionalities. Such graphitic materials include 0-D fullerenes, 1-D nanotubes and 3-D graphite (Figure 1.11).[83] Individual graphene layers are found in the form of graphite where layers stack on top of each other to form the bulk material. The current interest in graphene can be attributed to several reasons. Theoretical and experimental studies of graphene predict that graphene and graphene based materials may possess superior mechanical and electrical properties.[84] Electron transport in graphene can be described by the Dirac equation which allows access to quantum electrodynamics and novel graphene based nano-devices. Graphene is also mechanically and chemically stable and has remarkable properties when extended to bilayer and multilayer form, these properties make this material very valuable for the production of various composites with a range of potential applications.[87]

Figure 1.11 Graphene is the 2D building block for carbon materials (sp^2) of all other dimensions. Graphene can be wrapped into 0D fullerenes, rolled into 1D nanotubes or stacked into 3D graphite.[83]

Reported methods of graphene production include graphitization of SiC[86] micromechanical cleavage[87] solution exfoliation in organic solvents and surfactant solutions[88-92] and through deposition from gaseous precursors through CVD[93,94] The electronic properties, transparency and flexibility of graphene offer several applications to solar cell components which have been heavily investigated in recent times.[96-98]

One of the most promising applications of graphene for solar energy devices is as a replacement material for transparent conducting oxides (TCOs). The most widely used TCOs are indium doped tin oxide (ITO) and fluorine doped tin oxide (FTO). Both materials offer optical transparency in the visible region of the spectrum and extremely good conductivity when deposited on glass or polymer (PET,PEN) substrates. The conductivity of both materials is generally on the order of 5-30 $\Omega\square^{-1}$, depending on the layer thickness. The use of such materials for TCOs does have some drawbacks. Indium is

a finite resource and costs are expected to rise as natural stores are depleted, both ITO and FTO are instable in the presence of acid or base and they are characterised by limited transparency in the IR region of the spectrum.[99] A large body of work has focused on the application of graphene as a replacement materials for TCOs. In order for graphene to be employed as a substitute material for TCOs, it is generally accepted that the conductivity of the layer should be below 100 $\Omega\square^{-1}$ and have an optical transparency of 90% or greater in the visible.

Several routes have been proposed for the fabrication of transparent and conductive graphene-based composites on polymers or silica. Solution phase mixing of exfoliated phenyl isocyanate – treated graphite oxide with polystyrene, followed by a chemical reduction has been shown to produce electrically conductive graphene - polymer nanocomposite materials.[84] Graphene loadings of 2.5% vol. increases composite conductivity from 10^{-14} S m^{-1} at 0.1% vol. to ~ 1 S m^{-1}. Similar methods have been employed to produce chemically inert graphene silica composites which are compatible with glass and SiOx/silicon substrates.[100] These composite films are produced by incorporation of individual graphene oxide sheets into silica sols followed by spin coating, chemical reduction and thermal curing. The transmittance of the films remains as high as 0.94-0.96 over the 380-1000nm wavelength at 11% graphene loading, while the bulk conductivity of spun-cast films was recorded at 0.45 S cm^{-1}. Although these conductivity values don't compare well to that of ITO (~$1x10^4$ S cm^{-1}),[101-103] the films are robust, simple to make and should not encounter ion diffusion problems which is common place in ITO.[104]

Graphene-based transparent and conductive thin films fabricated by the thermal reduction of graphite oxide displayed very similar electronic and structural properties as highly oriented pyrolytic graphite (HOPG) but has the advantage over HOPG which cannot be easily processed into thin films.[105] Weber et al. have produced graphene-based optically transparent electrodes for spectroelectrochemistry in the UV-Vis region. Highly conductive, ultrathin graphene films on quartz substrates exhibited optical transparency over a broad frequency range. Their ability to outperform ITO is enhanced when comparing transparencies in the UV region where ITO exhibits significant absorption.[106] Wang fabricated transparent, conductive and ultrathin graphene films for use in DSSC applications. The graphene was produced from exfoliated graphite oxide. The GO sheets were deposited on a hydrophilic substrate, such as pretreated quartz, by dip coating of the

GO dispersion. The thickness of the film can be monitored by changing the dipping repetition and the temperature of the GO dispersion. The GO film was reduced into graphene via the thermal treatment under argon or hydrogen flow. These graphene films displayed high chemical and thermal stabilities and had a conductivity of 550 S cm^{-1} and a transparency of > 70 %. [107]

Graphene has also been incorporated successfully as a promising CE electrode material in DSSCs. The advantage of using graphene in this manner lies in the fact that a CE can be created solely from graphene, whereby the material acts as both the conductive electrode and the catalytic agent. This was shown effectively by Ahmed et al. who found that FTO free counter electrodes could be fabricated using a hybrid of graphene nanoplatelets, carbon nanotubes and Pedot:PSS as a conductive filler, which showed a device efficiency of 2.5% .Wang et al. have demonstrated a facile approach for deposition of graphene on a varied array of substrates for use as a CE material.[108] This approach proves to be a very useful technique as it eliminates the need for high deposition temperatures, usually associated with CVD and the thermal reduction of graphene oxide. These high temperatures are not compatible with conductive substrates or flexible polymer based materials.

The technique is based upon using a graphene film deposited on a mixed cellulose ester membrane. This then allowed the film to be dried onto and subsequently adhered to a substrate of choice at room temperature. The cellulose ester membrane could then be stripped away leaving a well adhered graphene film deposited on the substrate of choice. The thickness of the films could easily be controlled through varying the concentration of the graphene dispersion before film formation under vacuum

DSSC tests showed that the higher concentration graphene films showed best results when compared to Pt, however results obtained were quite low with η of 0.51% and FF of 0.11 compared to 3.7% and 0.63 using the Pt CE. The reasons for these poor values lie in the large charge transfer rates (R_{CT}) for the graphene film compared to that of the Pt. This large R_{CT} corresponds to the lower Jsc value obtained of 6.68 mA cm^{-2}.

Aksay et al. reasoned that the catalytic activity in graphene may be due to the oxygen containing functional groups (hydroxyls, epoxides and carbonyls) which are located on the edges of pristine grapheme sheets.[109] Through controlling the amount of oxygen functional groups via thermal processing they could examine the effect that the functional groups had on the catalytic potential of these functionalised graphene sheets (FGS). It was found that

through increasing the concentration of oxygen functional groups the catalytic ability of the material was enhanced. At a C/O ratio of 1:3 the DSSC showed peak η of 4.99% compared to 5.48% for the Pt cell. The group also demonstrated how FGS based inks cast onto a nonconductive plastic can be used effectively as a counter electrode eliminating the need for a conductive substrate and achieved values ~10% lower than that of the Pt CE.

One of the major bottlenecks in DSSCs is the transport of the photo-generated electrons across the TiO_2 network. This process competes with charge recombination. There are several main strategies to suppress the recombination and improve the electron transport. Such strategies include using composite metal oxides as the semiconductor material, which in turn have varying bandgaps. These ideas are outlined in the review by Kong et al.[110] One of the proposed approaches involves the addition of 1-D nanostructured charge carries to direct the photo-generated electrons. SWNTs are 1-D nano-objects, which have been adopted as conducting scaffolds in a TiO_2 based photo-electrochemical cell. TiO_2 nanoparticles were dispersed on SWNT films in order to improve the photo-induced charge separation and transport of carriers to the collecting electrode surface (Figure 1.12). There was an indication of Fermi level equilibration between the SWNT and the TiO_2 due to a shift of approximately 100 mV. The overall photo-conversion efficiency was improved by a factor of two.[111] Transient absorption and emission measurements indicate that a SWNT scaffold will not display any noticeable influence on the charge injection process from a ruthenium sensitizer into TiO_2 particles. SWNTs also show an enhancement in the photocurrent generation but this improvement is neutralised at a lower photo-voltage as the apparent Fermi level of the TiO_2 and SWNT composite becomes more positive than that of pristine TiO_2.[112]

TiO_2/MWNT nanocomposite photoanodes were obtained by a modified acid-catalyzed sol-gel procedure. Using these photoanodes in DSSC applications the TiO_2/MWNT nanocomposite photoanodes enabled the improvement of the physicochemical properties of the solar cell. The MWNTs enhanced the roughness factor and reduced the charge recombination of electron/hole pairs. These changes lead to larger adsorbed dye quantities allowing higher photocurrent and improved DSSC cell performance. However, a higher loading of MWNTs also causes light-harvesting competition that affects the light absorption of the dye-sensitizer, and consequently reduces the cell efficiency. Therefore an optimal suggested loading of 0.3 wt % MWNTs was proposed.[113]

The addition of carbon nanotubes however, only enables small increases in the efficiency of the cells; this is likely to be due to the poor point contact between the round TiO_2 and the straight nanotubes, as shown in Figure 1.12. By contrast, 2-D graphene may benefit the charge separation, as it has not only excellent conductivity but has a good surface contact with the titanium dioxide due to intermolecular forces such as physisorption, electrostatic binding or charge transfer interactions between the graphene and the TiO_2.[114] Therefore graphene was introduced as 2-D bridging material into the nanocrystalline photoanode of dye-sensitized solar cells. Overall, it performed better than the corresponding CNT-TiO_2 electrodes. In small quantities, 0.6 wt. %, the graphene led to a faster electron transport and a lower recombination, together with a higher light scattering. On the basis of these advantages, the short-circuit current density was increased by 45 % without sacrificing the open-circuit voltage, and the total conversion efficiency was 6.97 %, which was increased by 39%, compared to the nanocrystalline titanium dioxide photoanode.[115]

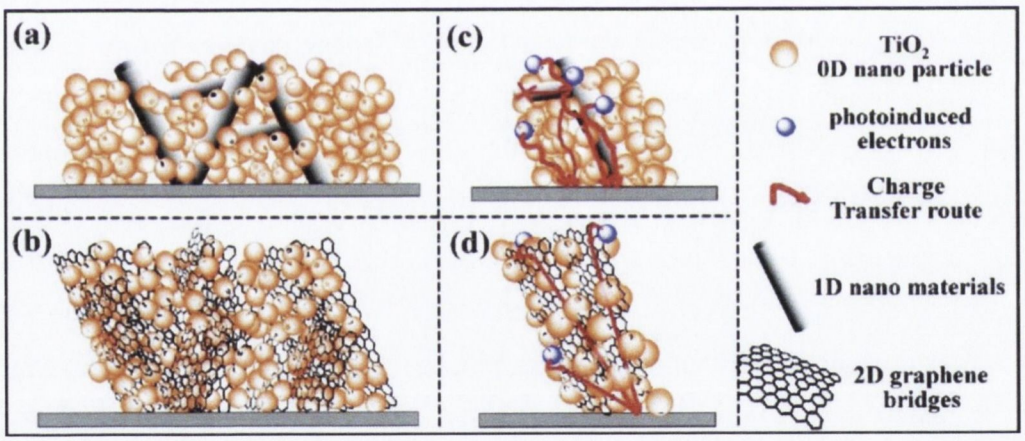

Figure 1.12 Differences between (a,c) 1-D and (b,d) 2-D nanomaterials composite electrodes. In 2-D nanomaterials composite electrodes (graphene bridges), the TiO_2 nanoparticles can anchor better around the graphene. [115]

In another work modified DSSCs were fabricated using graphene-TiO_2 composite photoanodes. The graphene-TiO_2 nanocomposites were prepared using the heterogeneous coagulation between Nafion-coated graphene and commercial TiO_2 (P25) nanoparticles, which ensured a tight interfacial binding between them. The DSSC incorporating 0.5 wt % graphene in the TiO_2 photoanode demonstrated a power conversion efficiency of 4.28 %,

which is 59 % higher than that without graphene. It was also found that the incorporated graphene caused both increased dye adsorption and significant longer electron lifetime.[116] Thus graphene has been proven to be an attractive candidate for improving the performance of the DSSC.

1.7 Graphene oxide

Graphene oxide (GO) is a structurally different form of graphene produced through chemical modification of graphite. The structure of graphene oxide has been investigated by scientists for almost a century. The material has proven difficult to characteise fully, this is due to the variability of the material from sample to sample, the amorphous nature of the graphene oxide and the non-stoichiometric atomic composition. Initiall atempts to characterise GO were carried out by Hofmann and Holst. In this work they suggested that GO contained epoxy groups spread across the basal planes of the GO sheets and that the material had a molecular formula C_2O.[117] Ruess developed this idea further in 1946, suggesting that hydroxy groups were also present along basal planes, which would account for the presence of hydrogen content observed.[118] In 1969 Scholz proposed a model that completly removed the epoxide and hydroxyl moities on the basal planes and substited these with a regular and repeating quinodial structure along the basal plane.[119] The limitation and ultimately the lack of success of these models stemed from the fact that GO was considered to be a structure based upon repeating lattice units. More recent attempts of characterising the material have focused on considering GO as an amorphous non-stoichiometric material. Lerf and Klinowski have propsed a model for GO which is currently the most cited in the literature. In order to develop there model they used solid state nuclear magnetic resonance spectrroscopy (ssNMR) as a means of evaluating the structure. There results have proposed two variations in the model for the structure of GO. The difference between both models concerns the presence or absence of carboxcylic moities on the edges of GO sheets.[120]

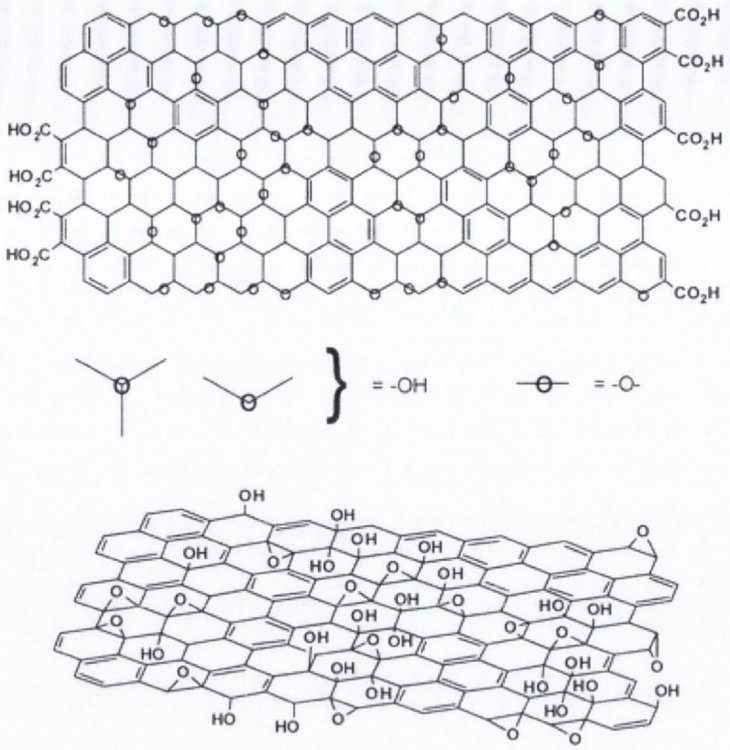

Figure 1.13 Variations in the model of graphene oxide proposed by Lerf and Klinowski. Image reproduced from Lerf and Klinowski.[121]

Figure 1.13 above is a schamatic for the proposed structure of GO based on studies by Lerf and Klinowski. The conversion of the parent graphite crystal to graphene oxide results in the functionalistion of the graphene oxide sheet with carboxyl, epoxide and alcohol moieties. Several methods exsit for producing graphene oxide. The Hummers method is the oldest and most widely employed synthetic route for the oxidation of graphite.[122] This method has a notecable disadvantage due to the formation of the volatile dimanganese heptoxide (Mn_2O_7) species in solution, which acts as a strong oxidising agent to the graphite crystal.[121] As a result of this several methods have been developed based upon modification of the Hummers protocol.[123-125]

The remarkable properties of pristine graphene are attributed to the delocalised π-π network that arises from orbitals that lie perpendicular to the plane of the graphene sheet.[126] When considering routes towards functionalization it is necessary to disrupt this π -π network in order to introduce functional groups onto the surface of the sheet. It is these functional groups that allow for chemistry to be performed on the 2D support but at the cost of losing some of the remarkable properties usually associated with pristine graphene

sheets. When introducing chemical functionality onto pristine graphene the conjugated network must be disrupted. In doing so many of the attributes of graphene are lost. Most noteably the oxidation results in a drastic loss in conductivity and GO can be considered as an insulator. It has been known for some time that it is possible to reduce graphene oxide back to graphene using harsh reducing agents such as hydrazine, however these methods have been shown to introduce a level of doping into the lattice and thus the π-π network is never fully restored.[127,128] More recent research has developed novel methods for the reduction of graphene oxide to reduced graphene oxide (RGO) as this would allow for the formation of a more graphene like material in the liquid phase, and in large quantities. Shin et al. have shown that a hydride reduction with $NaBH_4$ can be an extremely effective route towards creating RGO.[129] The conductivites measured for the RGO films prepared in this manner far exceeded that for hydrazine RGO and closely approaced conductivitiess obtained for films of pristine graphene flakes. Thermal treatment of GO was found to simultaneously reduce and exfoliate graphene oxide. Schniepp et al found that when graphite oxide is heated rapidly to 1050 ^{O}C , CO_2 is released from the oxide functionality.[130] The relese of the gas at elevated temperatures causes rapid expansion of the interlayer spacing which casuse the material to exfoliate.

Using GO does afford some advantages which aid processing and further functionalisation of the material. Functionality on the sufrace allows for GO to be dispersed readily in water and many polar solvents.[131,132] The functional groups also allow for GO sheets to be coupled to polymers,[133,134] and used as a support material for a wide range of nano-particles.[135-137] Thus using GO opens up routes to a large variety of new nano carbon composite materials which can't be realised through the use of pristine graphene

1.8 Graphene oxide metal composites

The area of nano carbon metal nanoparticle assemblies has received much research attention in recent times. Carbon nanotubes (CNT) were initially investigated as a support material for metallic,[138,139] semiconducting,[140,141] and catalytically active nanoparticles.[142] Applications of these materials range from glucose bio sensing,[143,144] fuel cell electrode materials,[145,146] water splitting reactions[147] and DSSCs.[148] The cost of carbon nanotubes

and recently introduced legislation has limited the application of these nano composites in consumer devices.

Graphene and graphene like materials have the potential to overcome some of the issues associated with CNT NP composites. Graphene is cheaper to produce, has a higher surface area (~2600 m^2g^{-1})[149] is considered safe and most importantly offers similar chemistry to that of CNTs. Therefore, routes towards functionalization of these materials can largely follow those set out for CNTs.

The functionality on the surface of GO can be used to covalently link the graphene substrate to various types of polymers,[133,150] porphyrins,[151,152] and fullerenes.[153] The functionality also offers routes towards anchoring particles onto the GO sheets with the aim of creating high surface area 2D composite materials. Variation in particle choice opens up the possibilities of several new composite materials. Metallic,[154] [155,156]semiconducting,[114,137] catalytically active particles[157] and particles with interesting optical properties such as quantum dots[158] can all be bound to the surface of graphene oxide

1.8 Carbon nanomaterials for modification of DSSC counter electrodes

The counter electrode (CE) is typically composed of a TCO layer on top of which is deposited a 2-3 nm layer of catalyst, which is normally platinum due to its excellent electrocatalytic activity for the reduction of I_3^-. The utilisation of carbon nanomaterials in counter electrodes has attracted a great deal of interest as a replacement for highly expensive platinum and due to their activity for I_3^- reduction, electronic conductivity and easy availability. In addition, the use of carbon nanomaterials opens the possibility of using various substrates such as polyethylene terephthalate (PET) and polyethylene naphthalate (PEN) in cell design and assembly as high temperature treatment of carbon is not required. The variety of carbon nanostructures also allows for tuning of important features such as electrode thickness, surface area, porosity and abundance of defect rich planes which all play an important role in the reduction of I_3^-.

There have been several reports on the utilisation of carbon black and activated carbon as counter electrodes in DSCCs. The use of carbon black as a CE was investigated by Grätzel *et al.*[159] Given that carbon black has low crystallinity and consequently many edges, it was reasoned that this material would show promising results as a catalyst for I_3^- reduction in DSSCs. A carbon paste which contained 93% carbon and 7% TiO_2 (w/w) was applied to FTO glass through the doctor blade method and this CE was compared to the commonly used Pt based CE. Results indicated that the thickness of the carbon layer had no effect on short-circuit current density (Jsc) while open circuit voltage (Voc) decreased with increasing layer thickness. The fill factor (FF) of the cells increased from 46% to 76% with increasing layer thickness up to 10μm while the best cell efficiency (η) was measured at 9.1% for a layer thickness of 14.5μm. Impedance spectra also showed that the charge transfer resistance of the CE dropped from 118 to 0.74Ω cm^{-2}.

Further work was performed by Takahasi and co-workers, who devolved a similar system but aimed to eliminate the 30% drop in efficiency which they attribute to the higher electrical resistance of the carbon powder/TiO_2 CE.[160] Using activated carbon increased the roughness factor of the carbon electrode through increasing the surface area of the activated carbon. It was expected that the redox reaction per unit of geometrical area would increase with increasing carbon roughness factor (RFc) of the counter electrode. Due to the porous nature of the activated carbon, I_3^- ions could enter the pores of the CE and be reduced more effectively. The pore size of the activated carbon was calculated to be 8Å which allows for entry of the I_3^- ions, which have been calculated to measure 3Å in diameter and 6Å in length in acetonitrile.[161] The specific resistivity of the carbon based CE was 4-5 orders of magnitude greater than that of the Pt sputtered electrode which was used as a reference and thus the internal resistance of the DSSC with the carbon based electrode was larger than that of the Pt sputtered cell. Overall this lead to a reduction in the Jsc of the device, however it was found that Jsc value did increase as the roughness factor of the CE increased. These results are largely in line with what would be expected for these carbon based electrodes. Using this approach the most promising results obtained with an electrode thickness of 153μm, yielding an efficiency value of 3.89%. This value was obtained with a high roughness factor of carbon (RFc = 64700).This result compares favourably to that of the sputtered Pt electrode which was shown to give an efficiency value of 3.61%. However when these results were compared to the literature preparation of Pt CE's the results obtained were 4.30%.

Activated carbon has also been utilised as a catalytic material on an industrial flexible graphite substrate. Meng et al have found that using an all carbon counter electrode allows for good adhesion of the catalytic activated carbon to the graphitic substrate.[162] The advantages of adopting a system such as this is that the substrate shows good electrical conductivity, flexibility, high temperature resistance and a low coefficient of thermal expansion, while the catalyst still retains a high surface area for tri-iodide reduction. Implementing systems such as this also opens up new routes towards the development of flexible and portable solar devices. The DSSC devices fabricated using these all carbon CEs demonstrated better performance than thermally deposited Pt/FTO glass devices. The all carbon CEs demonstrated a low sheet resistance when compared to the electrode with the FTO substrate. This lead to an improved FF and thus and improved η for the devices. DSSCs fabricated with an active area of 0.15 cm^2 showed a FF of 70.2% and η of 6.46% for the all carbon CE, while values for FTO/Pt cell showed a FF of of 66.1% and η of 6.37%. Increasing the size of the device to 1 cm^2 resulted in the doubling of the η value for the carbon CE device when compared to Pt/FTO.

Most recently a large and varied amount of work has focused on the use of SWCNT, MWCNT, nanohorns, bamboo like carbon nanostructures and metallic composites of these materials as effective catalytic materials for DSSC applications. The advantage of using these materials lies in the fact that they show promising electrical conductivity and display extremely large and tuneable surface area. The varied amount of these nanostructures also allows for the control and use of defect-rich edge plane materials which facilitate the electron kinetics associated with the reduction of I_3^-.

Lee et al adopted this approach and examined the possibility of exploiting bamboolike-structured MWCNTs.[163] Through taking advantage of the defect-rich edge planes along the tube fast electron kinetics at the electrode-electrolyte interface could be facilitated. Results showed that a CE based upon these bamboolike tubes were comparable to that obtained when a Pt CE was employed. The catalytic performance of the CE was examined through the rate of charge transfer (Rct) across the CE. Values for this electrode dropped from 1.8 Ω cm^{-2} (Pt) to 0.82 Ω cm^{-2}. The reasons for such high catalytic activity has been attributed to the high surface area of the CE and the defect rich basal plane, it has also been debated that this may also be attributed to residual catalyst particles located in the nanotubes.[164]

Overall the device performed well and achieved an efficiency of 7.67% which compared to 7.83% for the Pt based cell. This decrease in efficiency was reasoned to be due to the drop in value of Jsc as the CE did not reflect light in the same manner as Pt.

Metallic nanotube composites have recently been shown to have extremely promising results for CE applications in DSSCs. Taking advantage of the high surface area of MWCNTs and the catalytic properties of both Pt and MWCNTs has led to the development of MWCNT/Pt composite materials for DSSC's by Ho et al.[165] Pt nanoparticles dispersed on MWCNTs were shown to have η of 8.00 ± 0.23% compared to η of 6.92 ± 0.07% for the Pt cell. The enhancement in the efficiency of these devices is attributed to the higher Jsc value obtained which increased from 14.62 ± 0.19 to 18.01 ± 0.91 mA cm^{-2}. From examination of the surface morphologies it was concluded that the PtNP/MWCNT-CE had a rougher surface and hence a higher catalytic activity than that of the Pt-CE.

Composites of graphene and Pt NPs have also showed promising results, as DSSC CEs. The use of graphene instead of CNTs is also expected to reduce cost significantly. Gong et al. have shown that composites of graphene and Pt NPs can be used as a CE for DSSCs with high efficiencies of 6.09 % compared to 6.23 % for a Pt CE.[166] While it has been demonstrated by Misra that these materials could outperform Pt by 45 %.[167]

1.9 Carbon nanomaterials for use in the electrolyte

The electrolyte serves as one of the key components of the DSSC. The role of the electrolyte is to act as a medium for dye regeneration through an electron transfer from a redox species in the electrolyte. The oxidised component of the redox couple is in turn reduced at the counter electrode. The electrolyte must fulfil some key characteristics in order to work efficiently in the cell. These characteristics include high viscosity, high conductivity, excellent thermal stability, negligible vapour pressure and ease of sealing within the cell.

Traditional DSSC technology is based upon the use of volatile organic solvent electrolytes. These electrolytes have shown efficiency values of ~ 11-13 %[21,39] but they are also characterised by low viscosity and caustic components such as iodine and organic solvents.

These factors lead to several problems for industrial applications including leakage of the electrolyte from the cell, sealant corrosion, electrolyte degradation over extended periods of time, and poor temperature stability. These drawbacks, as well as the fact that the solvents permeate plastics, are serious obstacles for large-scale outdoor application of DSSCs and their integration into flexible structures. In the past years several research groups have tried to address the problems by developing quasi-solid state electrolytes based on polymer composites [168] or ionic liquids (IL's).[169]

Ionic liquids are solvents which are composed entirely of ions. They are commonly referred to room temperature molten salts. As ionic liquids are made up of two components, (anion and cation) they can be tailored or designed with a particular end use in mind, hence the term ''designer solvent'' has become common place.[170] The interest in ionic liquids as a potential solvent is a result of the unpredictable kinetics and thermodynamics of reaction carried out in this medium.[171] The molten nature of ILs is caused by a reduction in lattice energy of the crystalline form of the salt caused by the large size of one or both of the ions and the low degree of symmetry of the cation. Both these factors lower the melting point on the salt significantly and result in molten salts at room temperature.[172] For example the first discovered IL ([EtNH3][NO3]) had a melting point of 12 ^{O}C.[173]

Ionic liquids (IL's) have received particular attention as potential alternative electrolytes in DSSC's.[169] Characteristics of IL's include negligible vapour pressure, tuneable viscosity, non-volatility, and excellent thermal stability at both elevated and very low temperatures, [9, 174] high ionic conductivities and a broad electrochemical potential window. [6,175]

The use of IL's as DSSC electrolytes does not produce the same efficiency results as those obtained for the molecular solvent based electrolytes. This is largely due to the decreased diffusion of the redox couple through the more viscous IL which causes a decrease in Jsc of the device.[176] Carbon nanomaterials have been shown to improve the efficiency obtained by using IL based electrolytes. Incorporation of carbon nanomaterials in ILs can also allow for the production of quasi-solid electrolytes which reduces the need for hermetic sealing of the cells. The solid nature of these electrolytes is tuneable through addition of varying concentrations of the carbon nanomaterials. Ho et al.[177,178] have demonstrated how the incorporation of polyaniline–loaded carbon black (PACB) in the IL 1-propyl-3-methyl imidazolium iodide (PMII) can increase cell efficiency ~ 30 times in

comparison to the unmodified IL electrolyte. This increase in cell efficiency is attributed to an extended electron transfer surface (EETS) which provides a catalytic effect for the reduction of the I_3^- ions.[159,160,179,180]

The incorporation of various carbon nanomaterials in the IL 1-ethyl-3-methylimidazolium bis(trifluoromethylsulfonyl)imide (EMIm-TFSI) has been investigated as potential DSSC nanocomposite gel electrolytes by Usai et al. (figure 1.14)[181] Dispersions of multi walled carbon nanotubes (MWNT), single walled carbon nanotubes (SWNT), carbon black and carbon fibres were formed in EMIm-TFSI. These dispersions were prepared through the grinding mechanism outlined by Fukushima et al.[182] Briefly, the carbon nanomaterials and IL are ground in an agate mortar and pestle followed by a period of centrifugation. The efficiency increased for the electrolytes which contained carbon nanomaterials (mainly due to an increase in FF and *V*oc). The largest increase in overall efficiency was observed for the composite electrolyte which contained carbon fibres, this electrolyte showed an increase of 0.76%. The viscosity of these electrolytes also increased from 1.2 mPa s for EMIm-TFSI to 470 dPas and 110 dPas for MWNT and carbon black composites respectively while resistance values dropped from 76.0 Ω (EMIm-TFSI) to 8.9 Ω for the MWNT composite.[183]

Ahmead et al. have also shown that similar composites could be formed with the incorporation of liquid exfoliated graphene into ILs. The results showed that the incorporatinon of a large quantity of graphene (30 wt.%) and mixtures of graphene and CNTs in the IL layer could lead to a drastic improvement in the cell efficiency when compared to the IL without any additives. The electrolytes were also stable at elevated temperatures (> 300 ^{O}C) and showed good stability levels over the course of 1 month, when cells were fabricated in an open cell configuration. The slight decrease in efficiency is most likely attributed to water absorption from the hygroscopic IL over time.

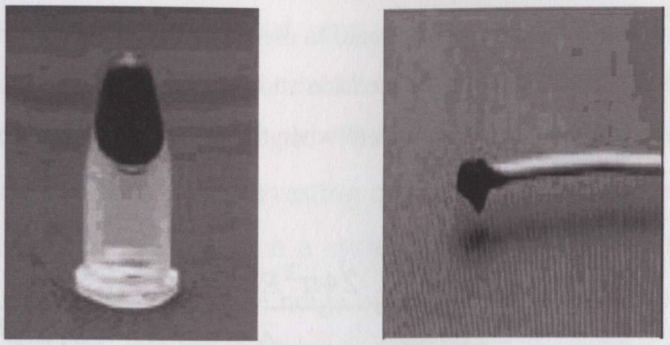

Figure 1.14 Quasi-solid ionic nanocomposite gels containing MWNT's and EMIm-TFSI.[181]

1.10 Surface plasmon resonance and its application in solar energy harvesting

Surface plasmon resonance (SPR) is a feature of many metals, based upon the collective oscillation of nanoparticles conduction band electrons which results in the generation of an evanescent wave of electrons on the metals surface.[184] Considering that a nanoparticles size is much smaller than the wavelength of light, it can be reasoned that all the electrons in the nanoparticle will be subjected to the same electromagnetic field at a given time; this is referred to as the quasi-static hypothesis.[185] The nanoparticle's conduction band electrons will resonate once the frequency of the incident light matches the natural frequency of the surface electrons against the restoring force that the positively charged nucleus. At this resonant frequency the nanoparticles will strongly absorb and scatter the incident light and result in a strong extinction co-efficient for the material. The displacement of the metals electron cloud at the plasmon resonance will cause a concentration of surface charges. These charges will be positive where electron density is lacking and negative where electron density is concentrated. The absorption of light at the nanoparticles resonance frequency is known as the surface plasmon band (SPB). The size, shape and position of a nanoparticles SPB is dependent on numerous factors: the dielectric constant of the surrounding medium, the size, shape and mono dispersity of the nanoparticles and also the interactions between the nanoparticles surface and the stabilizing ligands which can affect the electron density within the nanocrystal. The conditions under which the electron cloud will resonate have been postulated by many scientists.[186-188] It is generally accepted that Mie theory most accurately describes the conditions upon which resonance will occur as it accounts for particle size and the dielectric constant of both the metal and the surrounding medium.[189] The Mie theory (eqn 1) approaches the idea of resonance as a scattering phenomenon and the theory describes the scattering cross section

(C_{ext}) which is directly proportional to the scattering intensity of the material. (R; particle radius, εm; dielectric constant of the medium and $\varepsilon(\omega) = \varepsilon_1(\omega) + i\varepsilon_2(\omega)$ the dielectric constant of the metal. Plasmon resonance corresponds to when the cross section is maximal.

$$Cext = \frac{24\pi^3 R^3 \varepsilon_m^{2/3}}{\lambda} \frac{\varepsilon_2}{(\varepsilon_1 + 2\varepsilon_m)^2 + \varepsilon_2^2} \qquad (1)$$

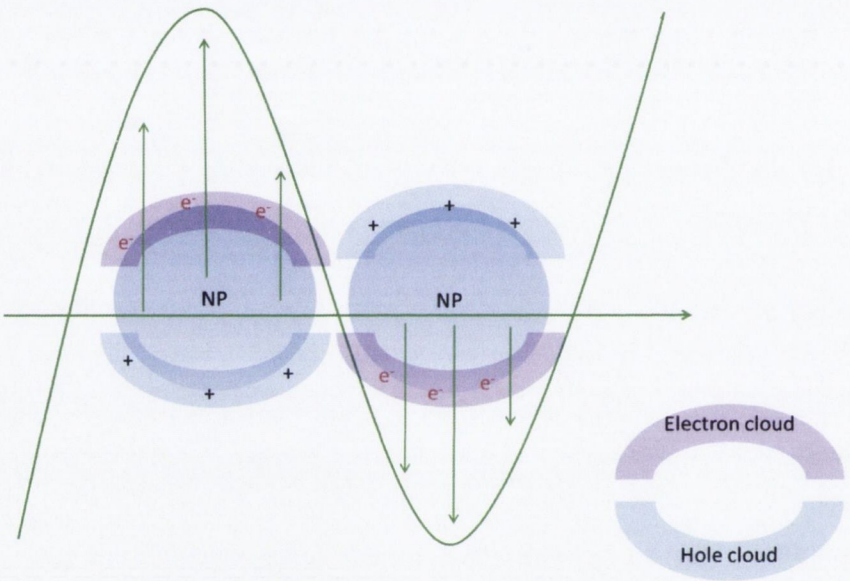

Figure 1.15 Schematic representation of the electron cloud resonance in a plasmonic nanoparticle when subjected to an electromagnetic wave.

SPR has been the subject of intense research in recent times due to the variety of potential important applications in areas such as imaging,[190,191] photonics[192] and sensing.[193-195] Recently SPR has attracted a great deal of attention as a plausible tool for increasing the efficiency of solar energy conversion devices. SPR has several potential applications in solar energy devices which range from decreasing the thickness of the absorber layer material in order to decrease bulk recombination currents, increasing the optical path of incident light in the absorber layer and as efficient mechanisms for light coupling into solar cells.[196-200] Recent research attention has focused on the use of plasmonic particles as the principle absorber for the generation of photocurrent in solar energy devices. It has been demonstrated that excitation of a metal nanoparticles plasmon can cause a charge

separation of electrons and holes at a metal semiconductor interface.[201-206] The resulting injection of "hot" electrons into the semiconductor can generate a substantial photocurrent being observed at the plasmon wavelength. These observations infer that plasmonic particles can serve as a potential light harvesting mechanism, enabling the generation of photocurrent. The advantage of using such a system lies in the fact that the plasmonic particles are highly tuneable across a wide range of wavelengths and are extremely stable and robust materials for solar energy harvesting. In addition metal nanoparticles can absorb light much more efficiently compared to semiconductors and dye molecules. Therefore, the use of photo-excited plasmonic electrons is potentially very attractive for applications in photochemistry and photo-catalysis,[207-210] solar energy harvesting (solar cells)[34,196-200,204,211] and optoelectronics.[212-217] For example, in their ground-breaking work Halas et al. have demonstrated that photons coupled into a metallic nanoantenna can excite resonant plasmons, which decay into energetic "hot" electrons injected over a potential barrier at the nanoantenna-semiconductor interface, producing a photocurrent.[214] This research opened up a range of potential applications including the use in on-chip silicon photonics, silicon light-harvesting devices, such as silicon-based solar cells, photodetectors and many other optoelectronic devices. In another work the same group reported that a metallic nanoantenna, can inject hot electrons into a nearby graphene structure, effectively doping the material. [213] The "hot" electron-doped graphene is a new type of hybrid material that is very promising for optoelectronic device applications such as optical switches and photodetectors and optically induced electronics. The same group has also demonstrated that nanoscale antennas can be sandwiched between two graphene monolayers yielding a photodetector with an 800% enhancement of the photocurrent relative to the analogous antenna-free graphene device. It was shown that the antenna can contribute to the photocurrent in two ways: by the transfer of hot electrons generated in the antenna structure upon plasmon decay, and by direct plasmon-enhanced excitation of intrinsic graphene electrons. This allows them to produce a graphene-based photodetector achieving up to 20% internal quantum efficiency in the visible and near-infrared regions of the spectrum. [212]

Several groups have studied the effect of plasmonic metal nanoparticles on the optical properties of TiO_2. Tatsuma et al. first reported on the mechanism and applications of plasmon–induced charge separation when loaded with gold nanoparticles.[201] They reported that plasmonic charge transfer from Au to TiO_2 occurred with a quantum efficiency of 26%

when excited at the plasmon frequency, however closer inspection of the spectra suggest that this result is an order of magnitude greater than the actual efficiency. Kamat and co-workers have reported that the incorporation of Au nanoparticles into TiO_2 films results in a substantial increase in photocurrent when excited with UV radiation.[218] They suggest that this result is due to decreased levels of recombination in TiO_2 when in the presence of Au NPs.

Au NPs have also been tested as modifying agents in DSSCs. Henry Sniath and his group reported that Au NPs could be employed to increase the quantum efficiency of DSSC.[204] IPCE values were shown to increase from 15% to 20% when Au NPs were incorporated with the N719 sensitizer. Peng Wang *et al* have shown extremely promising results using Au NPs and a TiO_2-photonic crystal substrate.[203] They found that the SPR of the Au NP receive a remarkable boost from the photonic crystal substrate and consequently boosts the hot electron injection from Au to TiO_2. The material was shown to have an IPCE on ~8%, which is the highest reported for such systems.

"Hot" electrons can also be used in photocatalysis. For example, it was reported that the H_2 molecule can dissociate on gold nanoparticles at the room temperature under visible light. In this case surface plasmons excited in the Au nanoparticles decay into "hot" electrons which are transfered into a Feshbach resonance of a dihydrogen molecule on the Au nanoparticle surface, causing the H_2 dissociation.[209] Thus there is a great technological potential in the use of "hot" electron based systems. However, there are many challenges in achieving an efficient extraction of energetic electrons and holes. The main limiting factors are the short lifetime of excited carriers in a metal, the slow transfer of momentum from a nanoparticle to plasmonic electrons and the reflection of carriers at interfaces. Previously it was reported that embedding plasmonic structures into the semiconductor results in substantial increases hot electron emission.[215] Also recently, is has been theoretically shown that the efficiency of generation and injection of plasmonic carriers can be increased by choosing appropriate sizes, geometries and excitation frequencies.[205,219]

References

(1) Petroleum, B. **2013**.

(2) Joshi, P.; Xie, Y.; Ropp, M.; Galipeau, D.; Bailey, S.; Qiao, Q. *Energy & Environmental Science* **2009**, *2*, 426.

(3) Hersch, P.; Zweibel, K. *Basic photovoltaic principles and methods*, Solar Energy Research Inst., Golden, CO (USA), 1982.

(4) Grätzel, M. *Nature* **2001**, *414*, 338.

(5) Grätzel, M. *Inorganic Chemistry* **2005**, *44*, 6841.

(6) Evaluation, A. S. f. T. a. M. A. T. R. S. f. P. P.

(7) Bequerel, E. *C.R. Acad. Sci.* **1839**, *9*, 145.

(8) Smith, W. *Nature* **1873**, *7*, 303.

(9) Einstein, A. *Annalen der Physik* **1905**, *322*, 132.

(10) A., M. R. *Phys. Rev. Lett.* **1916**, *7*, 355.

(11) Fritts, C. *Van Nostrands Engineering Magazine* **1885**, *32*, 388.

(12) Chapin, D. M.; Fuller, C. S.; Pearson, G. L. *Journal of Applied Physics* **1954**, *25*, 676.

(13) Shockley, W.; Queisser, H. J. *Journal of Applied Physics* **1961**, *32*, 510.

(14) De Vos, A. *Journal of Physics D: Applied Physics* **1980**, *13*, 839.

(15) Tao, M. *The Electrochemical Society Interface* **2008**, *17*, 30.

(16) Shaheen, S. E.; Ginley, D. S.; Jabbour, G. E. *MRS bulletin* **2005**, *30*, 10.

(17) Kippelen, B.; Brédas, J.-L. *Energy & Environmental Science* **2009**, *2*, 251.

(18) Kim, K.; Liu, J.; Namboothiry, M. A.; Carroll, D. L. *Applied Physics Letters* **2007**, *90*, 163511.

(19) Arango, A. C.; Johnson, L. R.; Bliznyuk, V. N.; Schlesinger, Z.; Carter, S. A.; Hörhold, H.-H. *Adv. Mater.* **2000**, *12*, 1689.

(20) http://www.nrel.gov/ncpv/pdfs/cell_efficiency_explanatory_notes.pdf. (Downloaded July 2014)

(21) Oregan, B.; Grätzel, M. *Nature* **1991**, *353*, 737.

(22) Nazeeruddin, M. K.; Kay, A.; Rodicio, I.; Humphrybaker, R.; Muller, E.; Liska, P.; Vlachopoulos, N.; Grätzel, M. *Journal of the American Chemical Society* **1993**, *115*, 6382.

(23) Kroon, J. M.; Bakker, N. J.; Smit, H. J. P.; Liska, P.; Thampi, K. R.; Wang, P.; Zakeeruddin, S. M.; Grätzel, M.; Hinsch, A.; Hore, S.; Wurfel, U.; Sastrawan, R.; Durrant, J. R.; Palomares, E.; Pettersson, H.; Gruszecki, T.; Walter, J.; Skupien, K.; Tulloch, G. E. *Progress in Photovoltaics* **2007**, *15*, 1.

(24) Grätzel, M. *Comptes Rendus Chimie* **2006**, *9*, 578.

(25) Kamat, P. V.; Fox, M. A. *Chemical Physics Letters* **1983**, *102*, 379.

(26) Clark, W. D. K.; Sutin, N. *Journal of the American Chemical Society* **1977**, *99*, 4676.

(27) Fan, F.-R. F.; Bard, A. J. *Journal of the American Chemical Society* **1979**, *101*, 6139.

(28) Houlding, V. H.; Grätzel, M. *Journal of the American Chemical Society* **1983**, *105*, 5695.

(29) Kalyanasundaram, K.; Vlachopoulos, N.; Krishnan, V.; Monnier, A.; Graetzel, M. *The Journal of Physical Chemistry* **1987**, *91*, 2342.

(30) Vogel, R.; Pohl, K.; Weller, H. *Chemical Physics Letters* **1990**, *174*, 241.

(31) Ellingson, R. J.; Beard, M. C.; Johnson, J. C.; Yu, P.; Micic, O. I.; Nozik, A. J.; Shabaev, A.; Efros, A. L. *Nano letters* **2005**, *5*, 865.

(32) Nozik, A. J. *Chemical Physics Letters* **2008**, *457*, 3.

(33) Jin, Z.; Masuda, H.; Yamanaka, N.; Minami, M.; Nakamura, T.; Nishikitani, Y. *The Journal of Physical Chemistry C* **2009**, *113*, 2618.

(34) Kim, H.-S.; Ko, S.-B.; Jang, I.-H.; Park, N.-G. *Chemical Communications* **2011**, *47*, 12637.

(35) Boschloo, G.; Hagfeldt, A. *Accounts of chemical research* **2009**, *42*, 1819.

(36) Palomares, E.; Clifford, J. N.; Haque, S. A.; Lutz, T.; Durrant, J. R. *Journal of the American Chemical Society* **2002**, *125*, 475.

(37) Hagfeldt, A.; Grätzel, M. *Chemical Reviews* **1995**, *95*, 49.

(38) Kim, M.-J.; Lee, C.-R.; Jeong, W.-S.; Im, J.-H.; Ryu, T. I.; Park, N.-G. *The Journal of Physical Chemistry C* **2010**, *114*, 19849.

(39) Mathew, S.; Yella, A.; Gao, P.; Humphry-Baker, R.; CurchodBasile, F. E.; Ashari-Astani, N.; Tavernelli, I.; Rothlisberger, U.; NazeeruddinMd, K.; GrÃ¤tzel, M. *Nat Chem* **2014**, *6*, 242.

(40) Tachibana, Y.; Moser, J. E.; Grätzel, M.; Klug, D. R.; Durrant, J. R. *The Journal of Physical Chemistry* **1996**, *100*, 20056.

(41) Hannappel, T.; Burfeindt, B.; Storck, W.; Willig, F. *The Journal of Physical Chemistry B* **1997**, *101*, 6799.

(42) Ellingson, R. J.; Asbury, J. B.; Ferrere, S.; Ghosh, H. N.; Sprague, J. R.; Lian, T.; Nozik, A. J. *The Journal of Physical Chemistry B* **1998**, *102*, 6455.

(43) Asbury, J. B.; Hao, E.; Wang, Y.; Ghosh, H. N.; Lian, T. *The Journal of Physical Chemistry B* **2001**, *105*, 4545.

(44) Haque, S. A.; Tachibana, Y.; Klug, D. R.; Durrant, J. R. *The Journal of Physical Chemistry B* **1998**, *102*, 1745.

(45) Barnes, P. R. F.; Anderson, A. Y.; Koops, S. E.; Durrant, J. R.; O'Regan, B. C. *The Journal of Physical Chemistry C* **2008**, *113*, 1126.

(46) Usui, H.; Matsui, H.; Tanabe, N.; Yanagida, S. *Journal of Photochemistry and Photobiology A: Chemistry* **2004**, *164*, 97.

(47) Ahmad, I.; Khan, U.; Gun'ko, Y. K. *Journal of Materials Chemistry* **2011**, *21*, 16990.

(48) Brennan, L. J.; Barwich, S. T.; Satti, A.; Faure, A.; Gun'ko, Y. K. *Journal of Materials Chemistry A* **2013**, *1*, 8379.

(49) Berginc, M.; Hočevar, M.; Opara Krašovec, U.; Hinsch, A.; Sastrawan, R.; Topič, M. *Thin Solid Films* **2008**, *516*, 4645.

(50) Wu, J. H.; Hao, S. C.; Lan, Z.; Lin, J. M.; Huang, M. L.; Huang, Y. F.; Fang, L. Q.; Yin, S.; Sato, T. *Advanced Functional Materials* **2007**, *17*, 2645.

(51) Park, N.-G. *The Journal of Physical Chemistry Letters* **2013**, *4*, 2423.

(52) Kazim, S.; Nazeeruddin, M. K.; Grätzel, M.; Ahmad, S. *Angewandte Chemie International Edition* **2014**, *53*, 2812.

(53) Fujishima, A.; Honda, K. *Nature* **1972**, *238*, 37.

(54) Fisher, M. B.; Keane, D. A.; Fernández-Ibáñez, P.; Colreavy, J.; Hinder, S. J.; McGuigan, K. G.; Pillai, S. C. *Applied Catalysis B: Environmental* **2013**, *130–131*, 8.

(55) Choi, H.; Stathatos, E.; Dionysiou, D. D. *Applied Catalysis B: Environmental* **2006**, *63*, 60.

(56) Han, C.; Pelaez, M.; Likodimos, V.; Kontos, A. G.; Falaras, P.; O'Shea, K.; Dionysiou, D. D. *Applied Catalysis B: Environmental* **2011**, *107*, 77.

(57) Aguado, J.; van Grieken, R.; López-Muñoz, M. J.; Marugán, J. *Catalysis Today* **2002**, *75*, 95.

(58) Dubrovinskaia, N. A.; Dubrovinsky, L. S.; Ahuja, R.; Prokopenko, V. B.; Dmitriev, V.; Weber, H. P.; Osorio-Guillen, J. M.; Johansson, B. *Physical Review Letters* **2001**, *87*, 275501.

(59) Muscat, J.; Swamy, V.; Harrison, N. M. *Physical Review B* **2002**, *65*, 224112.

(60) Diebold, U. *Surface Science Reports* **2003**, *48*, 53.

(61) Norifusa, S.; Toshio, N.; Kimihisa, Y. *Scientific Reports* **2013**, *3*.

(62) Asahi, R.; Morikawa, T.; Ohwaki, T.; Aoki, K.; Taga, Y. *Science* **2001**, *293*, 269.

(63) Linsebigler, A. L.; Lu, G.; Yates, J. T. *Chemical Reviews* **1995**, *95*, 735.

(64) Choi, W.; Termin, A.; Hoffmann, M. R. *The Journal of Physical Chemistry* **1994**, *98*, 13669.

(65) Cherepy, N. J.; Liston, D. B.; Lovejoy, J. A.; Deng, H.; Zhang, J. Z. *The Journal of Physical Chemistry B* **1998**, *102*, 770.

(66) Gregg, B. A.; Pichot, F.; Ferrere, S.; Fields, C. L. *The Journal of Physical Chemistry B* **2001**, *105*, 1422.

(67) Campbell, W. M.; Burrell, A. K.; Officer, D. L.; Jolley, K. W. *Coordination Chemistry Reviews* **2004**, *248*, 1363.

(68) Tan, Q.; Zhang, X.; Mao, L.; Xin, G.; Zhang, S. *Journal of Molecular Structure* **2013**, *1035*, 400.

(69) Hsieh, C.-P.; Lu, H.-P.; Chiu, C.-L.; Lee, C.-W.; Chuang, S.-H.; Mai, C.-L.; Yen, W.-N.; Hsu, S.-J.; Diau, E. W.-G.; Yeh, C.-Y. *Journal of Materials Chemistry* **2010**, *20*, 1127.

(70) Lin, C.-Y.; Lo, C.-F.; Luo, L.; Lu, H.-P.; Hung, C.-S.; Diau, E. W.-G. *The Journal of Physical Chemistry C* **2008**, *113*, 755.

(71) Plass, R.; Pelet, S.; Krueger, J.; Grätzel, M.; Bach, U. *The Journal of Physical Chemistry B* **2002**, *106*, 7578.

(72) Grätzel, M. *Inorganic Chemistry* **2005**, *44*, 6841.

(73) Yu, P.; Zhu, K.; Norman, A. G.; Ferrere, S.; Frank, A. J.; Nozik, A. J. *The Journal of Physical Chemistry B* **2006**, *110*, 25451.

(74) Jun, H. K.; Careem, M. A.; Arof, A. K. *Renewable and Sustainable Energy Reviews* **2013**, *22*, 148.

(75) Hetsch, F.; Xu, X.; Wang, H.; Kershaw, S. V.; Rogach, A. L. *The Journal of Physical Chemistry Letters* **2011**, *2*, 1879.

(76) Perez Leon, C.; Kador, L.; Peng, B.; Thelakkat, M. *The journal of physical chemistry. B* **2006**, *110*, 8723.

(77) Falaras, P. *Solar Energy Materials and Solar Cells* **1998**, *53*, 163.

(78) Finnie, K. S.; Bartlett, J. R.; Woolfrey, J. L. *Langmuir* **1998**, *14*, 2744.

(79) Shklover, V.; Ovchinnikov, Y. E.; Braginsky, L. S.; Zakeeruddin, S. M.; Grätzel, M. *Chemistry of Materials* **1998**, *10*, 2533.

(80) Galoppini, E. *Coordination Chemistry Reviews* **2004**, *248*, 1283.

(81) Lee, K. E.; Gomez, M. A.; Elouatik, S.; Demopoulos, G. P. *Langmuir* **2010**, *26*, 9575.

(82) Lee, K. E.; Gomez, M. A.; Regier, T.; Hu, Y.; Demopoulos, G. P. *The Journal of Physical Chemistry C* **2011**, *115*, 5692.

(83) Geim, A. K.; Novoselov, K. S. *Nature Materials* **2007**, *6*, 183.

(84) Stankovich, S.; Dikin, D. A.; Dommett, G. H. B.; Kohlhaas, K. M.; Zimney, E. J.; Stach, E. A.; Piner, R. D.; Nguyen, S. T.; Ruoff, R. S. *Nature* **2006**, *442*, 282.

(85) Ferrari, A. C.; Meyer, J. C.; Scardaci, V.; Casiraghi, C.; Lazzeri, M.; Mauri, F.; Piscanec, S.; Jiang, D.; Novoselov, K. S.; Roth, S.; Geim, A. K. *Physical Review Letters* **2006**, *97*, 187401.

(86) Forbeaux, I.; Themlin, J. M.; Debever, J. M. *Physical Review B* **1998**, *58*, 16396.

(87) Novoselov, K. S.; Jiang, D.; Schedin, F.; Booth, T. J.; Khotkevich, V. V.; Morozov, S. V.; Geim, A. K. *Proceedings of the National Academy of Sciences of the United States of America* **2005**, *102*, 10451.

(88) Hernandez, Y.; Nicolosi, V.; Lotya, M.; Blighe, F. M.; Sun, Z. Y.; De, S.; McGovern, I. T.; Holland, B.; Byrne, M.; Gun'ko, Y. K.; Boland, J. J.; Niraj, P.; Duesberg, G.; Krishnamurthy, S.; Goodhue, R.; Hutchison, J.; Scardaci, V.; Ferrari, A. C.; Coleman, J. N. *Nature Nanotechnology* **2008**, *3*, 563.

(89) Lotya, M.; Hernandez, Y.; King, P. J.; Smith, R. J.; Nicolosi, V.; Karlsson, L. S.; Blighe, F. M.; De, S.; Wang, Z. M.; McGovern, I. T.; Duesberg, G. S.; Coleman, J. N. *Journal of the American Chemical Society* **2009**, *131*, 3611.

(90) Lotya, M.; King, P. J.; Khan, U.; De, S.; Coleman, J. N. *ACS nano* **2010**, *4*, 3155.

(91) Coleman, J. N. *Accounts of chemical research* **2012**, *46*, 14.

(92) Khan, U.; O'Neill, A.; Lotya, M.; De, S.; Coleman, J. N. *Small* **2010**, *6*, 864.

(93) Kumar, S.; McEvoy, N.; Lutz, T.; Keeley, G. P.; Nicolosi, V.; Murray, C. P.; Blau, W. J.; Duesberg, G. S. *Chemical Communications*, *46*, 1422.

(94) Liu, W.; Chung, C. H.; Miao, C. Q.; Wang, Y. J.; Li, B. Y.; Ruan, L. Y.; Patel, K.; Park, Y. J.; Woo, J.; Xie, Y. H. *Thin Solid Films*, *518*, S128.

(95) Bae, S.; Kim, H.; Lee, Y.; Xu, X. F.; Park, J. S.; Zheng, Y.; Balakrishnan, J.; Lei, T.; Kim, H. R.; Song, Y. I.; Kim, Y. J.; Kim, K. S.; Ozyilmaz, B.; Ahn, J. H.; Hong, B. H.; Iijima, S. *Nature Nanotechnology*, *5*, 574.

(96) Wang, X.; Zhi, L.; Müllen, K. *Nano letters* **2008**, *8*, 323.

(97) Wu, J.; Becerril, H. A.; Bao, Z.; Liu, Z.; Chen, Y.; Peumans, P. *Applied Physics Letters* **2008**, *92*, 263302.

(98) Hong, W.; Xu, Y.; Lu, G.; Li, C.; Shi, G. *Electrochemistry Communications* **2008**, *10*, 1555.

(99) Pang, S.; Hernandez, Y.; Feng, X.; Müllen, K. *Adv. Mater.* **2011**, *23*, 2779.

(100) Watcharotone, S.; Dikin, D. A.; Stankovich, S.; Piner, R.; Jung, I.; Dommett, G. H. B.; Evmenenko, G.; Wu, S. E.; Chen, S. F.; Liu, C. P.; Nguyen, S. T.; Ruoff, R. S. *Nano Letters* **2007**, *7*, 1888.

(101) Betz, U.; Olsson, M. K.; Marthy, J.; Escola, M. F.; Atamny, F. *Surface & Coatings Technology* **2006**, *200*, 5751.

(102) Ow-Yang, C. W.; Spinner, D.; Shigesato, Y.; Paine, D. C. *Journal of Applied Physics* **1998**, *83*, 145.

(103) Granqvist, C. G.; Hultaker, A. *Thin Solid Films* **2002**, *411*, 1.

(104) Aziz, H.; Popovic, Z. D. *Chemistry of Materials* **2004**, *16*, 4522.

(105) Vollmer, A.; Feng, X. L.; Wang, X.; Zhi, L. J.; Mullen, K.; Koch, N.; Rabe, J. P. *Appl. Phys. A-Mater. Sci. Process.* **2009**, *94*, 1.

(106) Weber, C. M.; Eisele, D. M.; Rabe, J. P.; Liang, Y. Y.; Feng, X. L.; Zhi, L. J.; Mullen, K.; Lyon, J. L.; Williams, R.; Bout, D. A. V.; Stevenson, K. J. *Small* **2010**, *6*, 184.

(107) Wang, X.; Zhi, L. J.; Mullen, K. *Nano Letters* **2008**, *8*, 323.

(108) Wan, L.; Wang, S.; Wang, X.; Dong, B.; Xu, Z.; Zhang, X.; Yang, B.; Peng, S.; Wang, J.; Xu, C. *Solid State Sciences* **2011**, *13*, 468.

(109) Roy-Mayhew, J. D.; Bozym, D. J.; Punckt, C.; Aksay, I. A. *Acs Nano* **2010**, *4*, 6203.

(110) Kong, F.-T.; Dai, S.-Y.; Wang, K.-J. *Advances in OptoElectronics* **2007**, 75384.

(111) Kongkanand, A.; Dominguez, R. M.; Kamat, P. V. *Nano Letters* **2007**, *7*, 676.

(112) Brown, P.; Takechi, K.; Kamat, P. V. *Journal of Physical Chemistry C* **2008**, *112*, 4776.

(113) Yen, C. Y.; Lin, Y. F.; Liao, S. H.; Weng, C. C.; Huang, C. C.; Hsiao, Y. H.; Ma, C. C. M.; Chang, M. C.; Shao, H.; Tsai, M. C.; Hsieh, C. K.; Tsai, C. H.; Weng, F. B. *Nanotechnology* **2008**, *19*.

(114) Williams, G.; Seger, B.; Kamat, P. V. *Acs Nano* **2008**, *2*, 1487.

(115) Yang, N. L.; Zhai, J.; Wang, D.; Chen, Y. S.; Jiang, L. *Acs Nano* **2010**, *4*, 887.

(116) Sun, S. R.; Gao, L.; Liu, Y. Q. *Applied Physics Letters* **2010**, *96*.

(117) Hofmann, U.; Holst, R. *Berichte der deutschen chemischen Gesellschaft (A and B Series)* **1939**, *72*, 754.

(118) Ruess, G. *Montash. Chem* **1946**, *76*, 381.

(119) Scholz, W.; Boehm, H. P. *Zeitschrift für anorganische und allgemeine Chemie* **1969**, *369*, 327.

(120) Lerf, A.; He, H.; Forster, M.; Klinowski, J. *The Journal of Physical Chemistry B* **1998**, *102*, 4477.

(121) Dreyer, D. R.; Park, S.; Bielawski, C. W.; Ruoff, R. S. *Chemical Society Reviews* **2010**, *39*, 228.

(122) Hummers Jr, W. S.; Offeman, R. E. *Journal of the American Chemical Society* **1958**, *80*, 1339.

(123) Marcano, D. C.; Kosynkin, D. V.; Berlin, J. M.; Sinitskii, A.; Sun, Z.; Slesarev, A.; Alemany, L. B.; Lu, W.; Tour, J. M. *ACS Nano* **2010**, *4*, 4806.

(124) Chen, J.; Yao, B.; Li, C.; Shi, G. *Carbon* **2013**, *64*, 225.

(125) Kovtyukhova, N. I.; Ollivier, P. J.; Martin, B. R.; Mallouk, T. E.; Chizhik, S. A.; Buzaneva, E. V.; Gorchinskiy, A. D. *Chemistry of Materials* **1999**, *11*, 771.

(126) Geim, A. K.; Novoselov, K. S. *Nat Mater* **2007**, *6*, 183.

(127) Park, S.; Hu, Y.; Hwang, J. O.; Lee, E.-S.; Casabianca, L. B.; Cai, W.; Potts, J. R.; Ha, H.-W.; Chen, S.; Oh, J. *Nature communications* **2012**, *3*, 638.

(128) Park, S.; An, J.; Potts, J. R.; Velamakanni, A.; Murali, S.; Ruoff, R. S. *Carbon* **2011**, *49*, 3019.

(129) Shin, H. J.; Kim, K. K.; Benayad, A.; Yoon, S. M.; Park, H. K.; Jung, I. S.; Jin, M. H.; Jeong, H. K.; Kim, J. M.; Choi, J. Y. *Advanced Functional Materials* **2009**, *19*, 1987.

(130) Schniepp, H. C.; Li, J.-L.; McAllister, M. J.; Sai, H.; Herrera-Alonso, M.; Adamson, D. H.; Prud'homme, R. K.; Car, R.; Saville, D. A.; Aksay, I. A. *The Journal of Physical Chemistry B* **2006**, *110*, 8535.

(131) Paredes, J. I.; Villar-Rodil, S.; Martínez-Alonso, A.; Tascón, J. M. D. *Langmuir* **2008**, *24*, 10560.

(132) Li, D.; Müller, M. B.; Gilje, S.; Kaner, R. B.; Wallace, G. G. *Nature nanotechnology* **2008**, *3*, 101.

(133) Satti, A.; Larpent, P.; Gun'ko, Y. *Carbon* **2010**, *48*, 3376.

(134) Xu, Y.; Hong, W.; Bai, H.; Li, C.; Shi, G. *Carbon* **2009**, *47*, 3538.

(135) Lightcap, I. V.; Kosel, T. H.; Kamat, P. V. *Nano letters* **2010**, *10*, 577.

(136) Zhou, X.; Huang, X.; Qi, X.; Wu, S.; Xue, C.; Boey, F. Y.; Yan, Q.; Chen, P.; Zhang, H. *The Journal of Physical Chemistry C* **2009**, *113*, 10842.

(137) Kamat, P. V. *The Journal of Physical Chemistry Letters* **2009**, *1*, 520.

(138) Wildgoose, G. G.; Banks, C. E.; Compton, R. G. *Small* **2006**, *2*, 182.

(139) Kim, B.; Sigmund, W. M. *Langmuir* **2004**, *20*, 8239.

(140) Georgakilas, V.; Gournis, D.; Tzitzios, V.; Pasquato, L.; Guldi, D. M.; Prato, M. *Journal of Materials Chemistry* **2007**, *17*, 2679.

(141) Kongkanand, A.; Martínez Domínguez, R.; Kamat, P. V. *Nano letters* **2007**, *7*, 676.

(142) Yoon, B.; Wai, C. M. *Journal of the American Chemical Society* **2005**, *127*, 17174.

(143) Lim, S. H.; Wei, J.; Lin, J.; Li, Q.; KuaYou, J. *Biosensors and Bioelectronics* **2005**, *20*, 2341.

(144) Wei, G.; Xu, F.; Li, Z.; Jandt, K. D. *The Journal of Physical Chemistry C* **2011**, *115*, 11453.

(145) Mu, Y.; Liang, H.; Hu, J.; Jiang, L.; Wan, L. *The Journal of Physical Chemistry B* **2005**, *109*, 22212.

(146) Li, W.; Liang, C.; Zhou, W.; Qiu, J.; Zhou, Z.; Sun, G.; Xin, Q. *The Journal of Physical Chemistry B* **2003**, *107*, 6292.

(147) Dai, K.; Peng, T.; Ke, D.; Wei, B. *Nanotechnology* **2009**, *20*, 125603.

(148) Li, G. r.; Wang, F.; Jiang, Q. w.; Gao, X. p.; Shen, P. w. *Angewandte Chemie International Edition* **2010**, *49*, 3653.

(149) Zhu, Y.; Murali, S.; Cai, W.; Li, X.; Suk, J. W.; Potts, J. R.; Ruoff, R. S. *Adv. Mater.* **2010**, *22*, 3906.

(150) Villar-Rodil, S.; Paredes, J. I.; Martinez-Alonso, A.; Tascon, J. M. D. *Journal of Materials Chemistry* **2009**, *19*, 3591.

(151) Karousis, N.; Sandanayaka, A. S. D.; Hasobe, T.; Economopoulos, S. P.; Sarantopoulou, E.; Tagmatarchis, N. *Journal of Materials Chemistry* **2011**, *21*, 109.

(152) Xu, Y.; Liu, Z.; Zhang, X.; Wang, Y.; Tian, J.; Huang, Y.; Ma, Y.; Zhang, X.; Chen, Y. *Adv. Mater.* **2009**, *21*, 1275.

(153) Yang, J.; Heo, M.; Lee, H. J.; Park, S.-M.; Kim, J. Y.; Shin, H. S. *ACS Nano* **2011**, *5*, 8365.

(154) Seger, B.; Kamat, P. V. *The Journal of Physical Chemistry C* **2009**, *113*, 7990.

(155) Zhang, N.; Qiu, H.; Liu, Y.; Wang, W.; Li, Y.; Wang, X.; Gao, J. *journal of materials chemistry* **2011**, *21*, 11080.

(156) Muszynski, R.; Seger, B.; Kamat, P. V. *The Journal of Physical Chemistry C* **2008**, *112*, 5263.

(157) Li, Y.; Gao, W.; Ci, L.; Wang, C.; Ajayan, P. M. *Carbon* **2010**, *48*, 1124.

(158) Dong, H.; Gao, W.; Yan, F.; Ji, H.; Ju, H. *Analytical Chemistry* **2010**, *82*, 5511.

(159) Murakami, T. N.; Ito, S.; Wang, Q.; Nazeeruddin, M. K.; Bessho, T.; Cesar, I.; Liska, P.; Humphry-Baker, R.; Comte, P.; Pechy, P.; Gratzel, M. *Journal of The Electrochemical Society* **2006**, *153*, A2255.

(160) Imoto, K.; Takahashi, K.; Yamaguchi, T.; Komura, T.; Nakamura, J.; Murata, K. *Solar Energy Materials and Solar Cells* **2003**, *79*, 459.

(161) Sakane, H.; Mitsui, T.; Tanida, H.; Watanabe, I. *Journal of Synchrotron Radiation* **2001**, *8*, 674.

(162) Chen, J.; Li, K.; Luo, Y.; Guo, X.; Li, D.; Deng, M.; Huang, S.; Meng, Q. *Carbon* **2009**, *47*, 2704.

(163) Lee, W. J.; Ramasamy, E.; Lee, D. Y.; Song, J. S. *ACS Appl. Mater. Interfaces* **2009**, *1*, 1145.

(164) Šljukić, B.; Banks, C. E.; Compton, R. G. *Nano Letters* **2006**, *6*, 1556.

(165) Huang, K.-C.; Wang, Y.-C.; Dong, R.-X.; Tsai, W.-C.; Tsai, K.-W.; Wang, C.-C.; Chen, Y.-H.; Vittal, R.; Lin, J.-J.; Ho, K.-C. *Journal of Materials Chemistry* **2010**, *20*, 4067.

(166) Gong, F.; Wang, H.; Wang, Z.-S. *Physical Chemistry Chemical Physics* **2011**, *13*, 17676.

(167) Bajpai, R.; Roy, S.; Kumar, P.; Bajpai, P.; Kulshrestha, N.; Rafiee, J.; Koratkar, N.; Misra, D. S. *ACS Appl. Mater. Interfaces* **2011**, *3*, 3884.

(168) Stathatos, E.; Lianos, P.; Lavrencic-Stangar, U.; Orel, B. *Adv. Mater.* **2002**, *14*, 354.

(169) Papageorgiou, N.; Athanassov, Y.; Armand, M.; Bonhote, P.; Pettersson, H.; Azam, A.; Grätzel, M. *Journal of The Electrochemical Society* **1996**, *143*, 3099.

(170) Freemantle, M. *Chemical & Engineering News Archive* **1998**, *76*, 32.

(171) Earle Martyn, J.; Seddon Kenneth, R. In *Clean Solvents*; American Chemical Society: 2002; Vol. 819, p 10.

(172) Seddon, K. R. *Molten Salt Forum: Proceedings of 5th International Conference on MoltenSalt Chemistry and Technology* **1998**, *5–6*, 53.

(173) Walden, P. *Bull. Acad. Imper. Sci. (St. Petersburg)* **1914**, *1800*.

(174) Rogers, R. D.; Seddon, K. R. *Science* **2003**, *302*, 792.

(175) Fukushima, T.; Aida, T. *Chemistry-a European Journal* **2007**, *13*, 5048.

(176) Kubo, W.; Kambe, S.; Nakade, S.; Kitamura, T.; Hanabusa, K.; Wada, Y.; Yanagida, S. *Journal of Physical Chemistry B* **2003**, *107*, 4374.

(177) Chen, P. Y.; Lee, C. P.; Vittal, R.; Ho, K. C. *Journal of Power Sources*, *195*, 3933.

(178) Lee, C. P.; Chen, P. Y.; Vittal, R.; Ho, K. C. *Journal of Materials Chemistry*, *20*, 2356.

(179) Suzuki, K.; Yamaguchi, M.; Kumagai, M.; Yanagida, S. *Chemistry Letters* **2003**, *32*, 28.

(180) Saito, Y.; Kubo, W.; Kitamura, T.; Wada, Y.; Yanagida, S. *Journal of Photochemistry and Photobiology a-Chemistry* **2004**, *164*, 153.

(181) Usui, H.; Matsui, H.; Tanabe, N.; Yanagida, S. *Journal of Photochemistry and Photobiology a-Chemistry* **2004**, *164*, 97.

(182) Fukushima, T.; Kosaka, A.; Ishimura, Y.; Yamamoto, T.; Takigawa, T.; Ishii, N.; Aida, T. *Science* **2003**, *300*, 2072.

(183) Noda, A.; Hayamizu, K.; Watanabe, M. *Journal of Physical Chemistry B* **2001**, *105*, 4603.

(184) Kelly, K. L.; Coronado, E.; Zhao, L. L.; Schatz, G. C. *The Journal of Physical Chemistry B* **2002**, *107*, 668.

(185) Kreibig, U. V. M.; Springer, Berlin, 1995; Vol. 25.

(186) Maxwell-Garnett, J. C. *Philos. Trans. R. Soc. A* **1904**, *203*, 385.

(187) Maxwell-Garnett, J. C. *Philos. Trans. R. Soc. A* **1905**, *205*, 237.

(188) Debye, P. *Ann. Phys. (Leipzig)* **1909**, *30*, 57.

(189) Mie, G. *Ann Phys (Leipzig)* **1908**, *25*, 377.

(190) Jordan, C. E.; Corn, R. M. *Analytical Chemistry* **1997**, *69*, 1449.

(191) Nelson, B. P.; Grimsrud, T. E.; Liles, M. R.; Goodman, R. M.; Corn, R. M. *Analytical Chemistry* **2000**, *73*, 1.

(192) Ozbay, E. *Science* **2006**, *311*, 189.

(193) Nylander, C.; Liedberg, B.; Lind, T. *Sensors and Actuators* **1982**, *3*, 79.

(194) Liedberg, B.; Nylander, C.; Lunström, I. *Sensors and Actuators* **1983**, *4*, 299.

(195) Homola, J.; Yee, S. S.; Gauglitz, G. *Sensors and Actuators B: Chemical* **1999**, *54*, 3.

(196) Catchpole, K. R.; Polman, A. *Opt. Express* **2008**, *16*, 21793.

(197) Ferry, V. E.; Munday, J. N.; Atwater, H. A. *Adv. Mater.* **2010**, *22*, 4794.

(198) Nakayama, K.; Tanabe, K.; Atwater, H. A. *Applied Physics Letters* **2008**, *93*, 121904.

(199) Pala, R. A.; White, J.; Barnard, E.; Liu, J.; Brongersma, M. L. *Adv. Mater.* **2009**, *21*, 3504.

(200) Ferry, V. E.; Verschuuren, M. A.; Li, H. B. T.; Verhagen, E.; Walters, R. J.; Schropp, R. E. I.; Atwater, H. A.; Polman, A. *Opt. Express* **2010**, *18*, A237.

(201) Tian, Y.; Tatsuma, T. *Journal of the American Chemical Society* **2005**, *127*, 7632.

(202) Wu, K.; Rodríguez-Córdoba, W. E.; Yang, Y.; Lian, T. *Nano Letters* **2013**.

(203) Zhang, Z.; Zhang, L.; Hedhili, M. N.; Zhang, H.; Wang, P. *Nano Letters* **2012**, *13*, 14.

(204) Brown, M. D.; Suteewong, T.; Kumar, R. S. S.; D'Innocenzo, V.; Petrozza, A.; Lee, M. M.; Wiesner, U.; Snaith, H. J. *Nano Letters* **2010**, *11*, 438.

(205) Govorov, A. O.; Zhang, H.; Gun'ko, Y. K. *The Journal of Physical Chemistry C* **2013**, *117*, 16616.

(206) Nishijima, Y.; Ueno, K.; Yokota, Y.; Murakoshi, K.; Misawa, H. *The Journal of Physical Chemistry Letters* **2010**, *1*, 2031.

(207) Singh, V.; Beltran, I. J. C.; Ribot, J. C.; Nagpal, P. *Nano Letters* **2014**, *14*, 597.

(208) Thrall, E. S.; Steinberg, A. P.; Wu, X. M.; Brus, L. E. *Journal of Physical Chemistry C* **2013**, *117*, 26238.

(209) Mukherjee, S.; Libisch, F.; Large, N.; Neumann, O.; Brown, L. V.; Cheng, J.; Lassiter, J. B.; Carter, E. A.; Nordlander, P.; Halas, N. J. *Nano Letters* **2013**, *13*, 240.

(210) Mukherjee, S.; Zhou, L. A.; Goodman, A. M.; Large, N.; Ayala-Orozco, C.; Zhang, Y.; Nordlander, P.; Halas, N. J. *Journal of the American Chemical Society* **2014**, *136*, 64.

(211) Brown, P.; Kamat, P. V. *Journal of the American Chemical Society* **2008**, *130*, 8890.

(212) Fang, Z. Y.; Liu, Z.; Wang, Y. M.; Ajayan, P. M.; Nordlander, P.; Halas, N. J. *Nano Letters* **2012**, *12*, 3808.

(213) Fang, Z. Y.; Wang, Y. M.; Liu, Z.; Schlather, A.; Ajayan, P. M.; Koppens, F. H. L.; Nordlander, P.; Halas, N. J. *Acs Nano* **2012**, *6*, 10222.

(214) Knight, M. W.; Sobhani, H.; Nordlander, P.; Halas, N. J. *Science* **2011**, *332*, 702.

(215) Knight, M. W.; Wang, Y. M.; Urban, A. S.; Sobhani, A.; Zheng, B. Y.; Nordander, P.; Halas, N. J. *Nano Letters* **2013**, *13*, 1687.

(216) Sikora, J.; Halas, S. *Rapid Communications in Mass Spectrometry* **2011**, *25*, 689.

(217) Sobhani, A.; Knight, M. W.; Wang, Y. M.; Zheng, B.; King, N. S.; Brown, L. V.; Fang, Z. Y.; Nordlander, P.; Halas, N. J. *Nature Communications* **2013**, *4*.

(218) Chandrasekharan, N.; Kamat, P. V. *The Journal of Physical Chemistry B* **2000**, *104*, 10851.

(219) A.O. Govorov, H. Z., V. Demi, and Yurii K. Gun'ko *NanoToday DOI: 10.1016/j.nantod.2014.02.006]*.

Chapter 2 Experimental

2.1 Starting materials

All chemicals were purchased from Sigma-Aldrich unless stated otherwise. Fluorine doped tin oxide (FTO) glass (2.3 mm ; 13 $\Omega\square^{-1}$) was also purchased from Sigma-Aldrich

Graphite was purchased from Alfa Aser and used as received.

TiO_2 (P25) was purchased from Degussa and used as received.

TiO_2 pastes were purchased from Dyesol Ltd. along with the N-719 sensitizing dye ($RuLL'(NCS)_2$ (L=2,2'-bipyridyl-4,4'-dicarboxylic acid) (L'= 4,4'-dinonyl-2,2'-bipyridine).

Surlyn sealing spacer (25 μm and 60 μm) thickness was purchased from Solaronix Ltd.

1-methyl-3-propylimidazolium iodide (PMII) and 1-butyl-3-methyl imidazolium iodide (BMII) were purchased from Iolitec Ltd.

All optical equipment for assembly of IPCE electrical rig was purchased from Thor labs

Screen printing holder was supplied by A.W.T world Trade Inc. while the screen printing mesh was supplied by Serigraf Ltd.

All electrodes for use in electrochemical investigations were purchased from IL cambria scientific Ltd.

Theoretical calculations and modelling (chapter 6) was performed by Prof. A. Govorov (Athens University, USA).

2.2. General procedures for DSSC assembly

2.2.1 Assembly of Dye Sensitized Solar Cells

TiO_2 electrodes were soaked in a 0.3 mM solution of $RuLL'(NCS)_2$ (L=2,2'-bipyridyl-4,4'-dicarboxylic acid) (L'= 4,4'-dinonyl-2,2'-bipyridine) dye in a 1:1 ratio of tert-butanol and acetonitrile for a period of 16 hours. The process allows for the adsorption of a monolayer of the light harvesting dye onto the mesoporous electrode. Upon removal from the dye solution, the electrodes were washed with ethanol in order to remove any unadsorbed dye molecules from the surface. Once dry a surlyn sealant (25/60 μm) was placed around the active area of the electrode and the CE was placed on top. The device was sealed using a hot press heated to 130 °C. At this temperature the surlyn seal melts and once cooled acts as a sealant between both electrodes. The electrolyte was introduced into the chamber between both electrodes under vacuum. 25μL of electrolyte was placed over a $1mm^2$ hole drilled into the back of the counter electrode and when placed under vacuum the electrolyte was driven into the cell. The hole in the CE was sealed using a small portion of surlyn and a piece of glass.

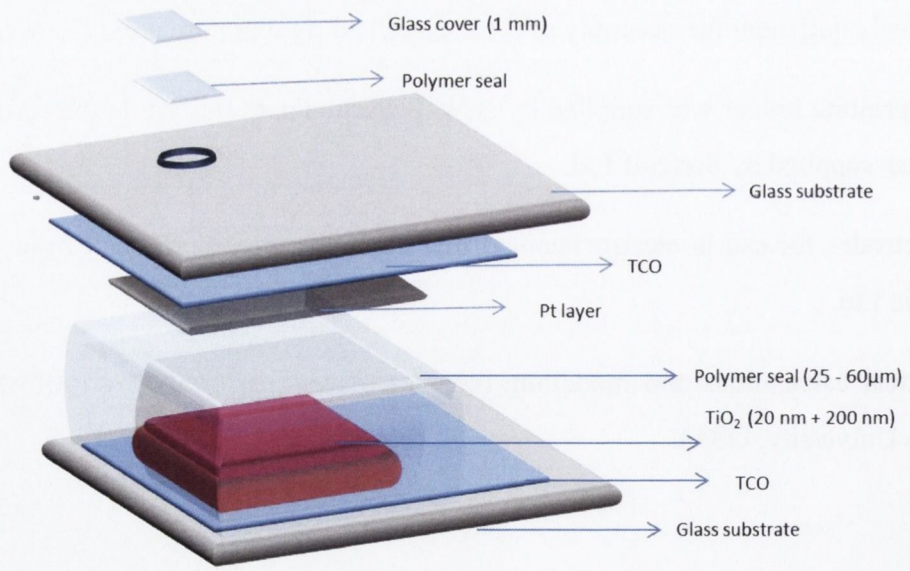

Figure 2.1 Assembly mechanism of for the dye sensitized solar cell

2.2.2 Organic iodide/tri-iodide electrolyte formulation

The organic electrolyte used in this work is based upon the following formulation. 0.6M 1-Butyl-3-methyl imidazolium iodide, 0.03 M iodine, 0.10 M guandinium thiocyanate and 0.5M 4-tert-Butylpyridine in a solvent mixture of acetonitrile and valeronitrile (85;15 vol.)

2.3 Experimental Procedures for Chapter 3

2.3.1 Fabrication of TiO_2 screen printing paste

TiO_2 screen printing paste was formulated from commercial P25 TiO_2 from Degussa. The procedure for paste preparation followed a modified method that was outlined by Ito et al.[1] This procedure allowed for the preparation of a stable paste at room temperature, containing TiO_2 nanoparticles between 20-25 nm in size. The TiO_2 paste was prepared using a ceramic mortar and pestle. The TiO_2 paste formulation followed the following scheme.

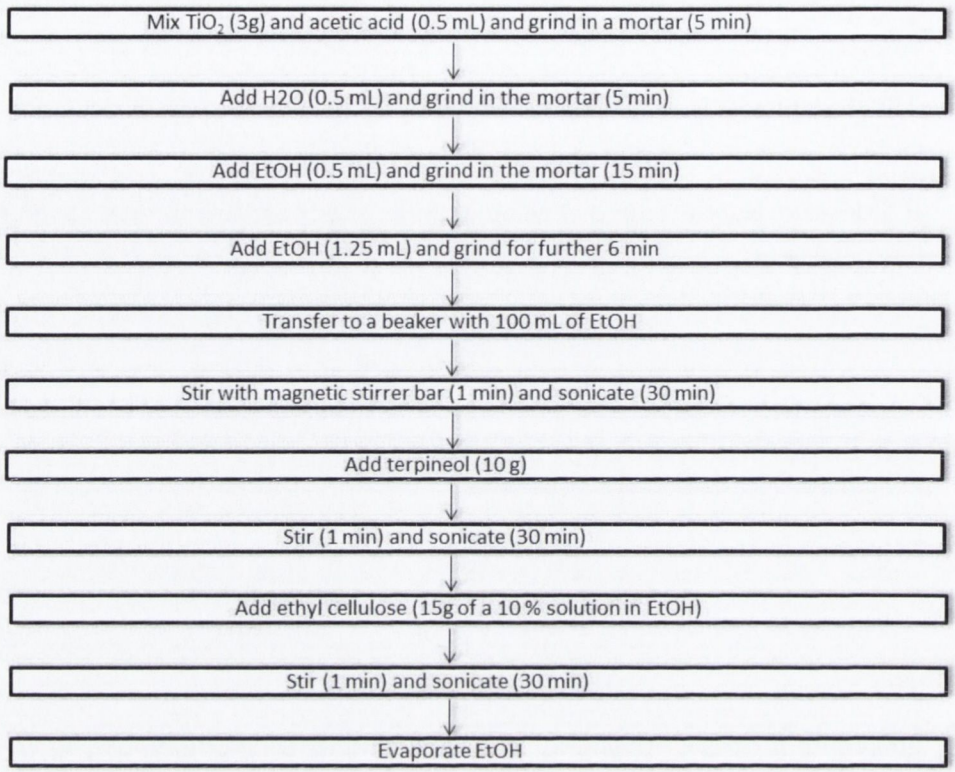

Figure 2.2 Fabrication scheme of screen-printing paste from a nanocrystalline-TiO_2 powder

2.3.2 Preparation of TiO_2 photoanodes

TiO_2 electrodes were prepared on FTO coated glass substrates. Glass substrates were cleaned in a detergent solution with ultra-sonication for 15 minutes followed by sonication in ethanol (10 min) and acetone (10 min). A bulk TiO_2 layer was applied to the FTO coated glass from a 40 mM aqueous hydrolysed $TiCl_4$ solution. FTO glass plates were submerged in the hydrolysed $TiCl_4$ solution at 70 °C for 30 minutes. Once removed, the glass was washed with water and alcohol. In order to form the mesoporous electrode TiO_2 paste was applied to FTO coated substrates using the screen printing method. TiO_2 pastes were fabricated according to the procedure outlined in section 2.2.2. Electrodes were produced

with several coatings of the prefabricated paste onto FTO substrates until a thickness of 12–13 μm was achieved. Following this, 2 layers of light scattering TiO_2 (150–200 nm particle size) (Dyesol WERO-2) was deposited. TiO_2 working electrodes were treated to a sintering profile which consisted of a drying period at 125 °C for 6 minutes, ramping to 350 °C and holding for 15 minutes, ramping to 450 °C and holding for 15 minutes and finally sintering at 500 °C for 15 minutes. A ramping rate of 8 °C min^{-1} was used for all ramping steps. Once cooled the electrodes were immersed into a 40 mM aqueous $TiCl_4$ solution and heated to 70 °C for 30 minutes. Upon removal from the bath, electrodes were cleaned with water and alcohol and treated to a second sintering step at 500 °C for 30 minutes.

2.3.3 Preparation of platinum counter electrodes

FTO coated glass was first drilled to create a hole in the glass substrate, which would allow for electrolyte filling once cell assembly was completed. The glass substrates were washed in H_2O, followed by a 0.1 M HCl solution in ethanol and cleaned through ultrasonication in acetone for 10 minutes. The substrates were then heat treated at 400 °C for 15 minutes in order to remove any residual contaminants on the surface. Once cooled, the platinum catalyst was deposited on the FTO coated substrate by drop casting a solution of chloroplatinic acid (H_2PtCl_6) in H_2O (5 mM). The heat treatment was repeated after deposition in order to form the metallic Pt film.

2.4 Experimental Procedures for Chapter 4

2.4.1 Production of Graphene

Graphite stock solutions were prepared in $CHCl_3$ at a concentration of 1mg ml^{-1}. The solutions were placed in an ultrasonic bath (Grant XB6) operated at 50-60 Hz, for 100

hours to ensure that maximum exfoliation of the graphite had occurred.[2] Following this the graphene suspensions were centrifuged at 500 RPM for 1 hour. This step allows for the unexfoliated heavier material to precipitate out from solution. The top layer of the suspension was decanted off and used for both TEM and Raman analysis. Once the analysis confirmed the successful production of graphene the material was used as an additive in IL electrolytes.

2.4.2 Preparation of graphene-ionic liquid electrolytes

Graphene-ionic liquid electrolytes were prepared by adding graphene dispersions in $CHCl_3$ to PMII at various concentrations, ranging from 0.125 wt. % to 3 wt. %. The residual chloroform was removed with vacuum assisted heating in a Schlenk vessel. The resulting PMII graphene composites were utilized as electrolytes in DSSCs.

2.5 Experimental Procedures for Chapter 5

2.5.1 Graphene oxide synthesis

Graphene oxide (GO) was prepared from bulk graphite *via* the Hummers method[3], 1g of graphite, 0.5g of sodium nitrate and 23 ml of sulphuric acid (H_2SO_4) was added to a 500 ml round bottomed flask and stirred at 4 °C for 15 minutes. 3g of potassium permanganate ($KMnO_4$) was added slowly with vigorous stirring. Once all the $KMnO_4$ was added the ice bath was removed and the suspension heated to 35 °C for 30 minutes. This afforded a murky brownish grey solution. Following this 46 ml of water was added and the suspension was set to stir for 15 minutes. The solution was then treated with 140 ml of hydrogen peroxide (H_2O_2) in order to reduce residual permanganate and manganese dioxide to the colourless, soluble manganese sulphate. The solution was washed through centrifugation up to 10 times with a 10 % aqueous solution of hydrochloric acid (HCl) followed by copious amounts of water. The resulting GO was suspended in H_2O at a

concentration of 1mg ml^{-1} and filtered under vacuum onto an omnipore 200 nm membrane and washed with 1L of H_2O. The presence of GO was confirmed with FT-IR, Raman and UV-Vis spectroscopies, along with SEM and TEM analysis.

2.5.2 Synthesis of graphene oxide, platinum nanocomposites

GO (20 mg) was dissolved in H_2O (20 ml) and ultra-sonicated for 1 hour in order to ensure maximum dispersion of GO and hence largest viable surface area. After ultra-sonication the aqueous GO suspension was added to a round bottomed flask and set to stir at room temperature for 30 min. 90μL(24 x 10^{-4} mol) of an 8% aqueous solution of $H_2PtCl_6.6H_2O$ (24 x 10^{-4} mol) was added to the suspension and left to stir for another 30 minutes. The solution was reduced with 10 mL of an aqueous solution of $NaBH_4$ (20μM) which was added drop wise to the reaction vessel. The solution was left to stir for 1 hour. Following this the composite was washed several times with water through a high speed centrifugation at 3000 RPM for 10 minutes.

2.5.3 Synthesis of graphene oxide, gold nanocomposites

The synthetic procedure for the AurGO composite followed that of the PtrGO composite, using molar equivalents of $HAuCl_4.3H_2O$ instead of $H_2PtCl_6.6H_2O$.

2.5.4 Electrophoretic deposition of GO, AurGO and PtrGO

Solutions of GO, AurGO and PtrGO were prepared in NMP at a concentration of 0.1 mg ml^{-1} for EPD. Samples were ultra-sonicated in NMP for 1 hour to allow for a homogeneous dispersion of the material into solution. Both electrodes were immersed into a solution of NMP with the desired material. Deposition was carried out by applying a DC voltage of

250V across both of the electrodes for 15 minutes. Following deposition the electrodes were dried in atmosphere and heat treated at 200 ^{O}C for 1 hour.

2.6 Experimental Procedures for Chapter 6

2.6.1 Synthesis of 4-(dimethylamino)pyridine (DMAP) stabilized gold nanoparticles

DMAP stabilised, water soluble gold nanoparticles particles were synthesied according to a previously published method.[4] In short, hydrogen tetrachloroaurate (III) trihydrate (0.150g) was dissolved in water (12 ml). To this solution a solution of DMAP (0.250g) in chloroform (12 ml) was added and stirred vigorously. The solution turned bright orange after a period of about 20 minutes, indicating the phase transfer and complexation of the DMAP ligand to the gold complex. After a further 2 hours of stirring the phases were separated and the aqueous phase was reduced with 700 µl of a solution of sodium borohydride (0.1g) in water (10 ml). The resulting ruby red solution was stirred for a further hour before analysis and further use.

2.6.2 Phase transfer of DMAP stabilized gold nanoparticles to the organic phase

The phase transfer of the water soluble gold nanoparticles to chloroform ($CHCl_3$) followed the following procedure.[4] 2 ml of the gold nanoparticle stock solution were dissolved in Millipore water (10 ml). This diluted dispersion (12 ml) was added to $CHCl_3$ (10 ml) containing dodecanthiol (DDT) (830 µmol). The two phases were stirred vigorously for approximately 30 minutes, after which the organic phase began to turn brown, indicating

the phase transfer of the particles to the organic phase. The solution was left to stir for a further 2 hours to ensure complete transfer of the particles to the organic phase.

2.6.3 Electrophoretic deposition (EPD) of gold nanoparticles into nanoporous TiO_2 films

EPD was carried out by assembling a 2 electrode sandwich configuration with an insulating spacer (4 mm) using a TiO_2 electrode and a bare FTO counter electrode. The assembly was immersed in a solution of the gold nanoparticles in $CHCl_3$. Both electrodes were connected to a power supply (TTi PLH 250 DC power supply). Nanoparticles were assembled in TiO_2 electrodes by applying a voltage of 250V across both electrodes for 15 minutes, causing the particles to migrate under the influence of the DC field. After EPD the electrodes were rinsed in propanol in order to remove any excess gold or solvent from the surface of the electrode.

2.6.4 Synthesis of $[Co(II)(bpy)_3](PF_6)_2$ and $[Co(III)(bpy)_3](PF_6)_3$

The cobalt complex, $[Co(II)(bpy)_3](PF_6)_2$ and the oxidised form $[Co(III)(bpy)_3](PF_6)_3$ were synthesised following the literature procedure.[5] $CoCl_2.6H_2O$ (1.0g, 4.12 mmol) and 2,2'-bipyridyl (2.2g, 13.94 mmol) were dissolved in methanol (100 ml) and refluxed for 2 hours. After the resulting solution was cooled to room temperature ammonium hexafluorophosphate (NH_4PF_6) (3.4 g, 20.86 mmol) was added to the reaction mixture. The resulting yellow precipitate was filtered and washed with water, ethanol and ether and dried under vacuum. Oxidation of $[Co(bpy)_3](PF_6)_2$ (500 mg) was carried out using nitrosonium tetrafluoroborate ($NOBF_4$) (107 mg, 0.916 mmol) in acetonitrile (15 ml) at room temperature for 30 minutes. The complex was precipitated with NH_4PF_6 (502 mg) and filtered and washed and dried as above.

2.6.5 Organic cobalt(II/III) electrolyte formulation

The cobalt redox electrolyte consisted of 0.22 M $[Co(II)bpy_3](PF_6)_2$, 0.03 M $[Co(III)bpy_3](PF_6)_3$, 0.1 M $LiClO_4$ and 0.5 M tert-butyl pyridine in acetonitrile.

2.7 Instrumental techniques and procedures

2.7.1 Raman Spectroscopy

The quantum theory treats monochromatic radiation of frequency *v0* as a stream of photons having energy *hv0*, where h is a Planck's constant. When light is scattered from a molecule or crystal, most photons are elastically scattered with the same frequency (*v0*) as the incident photons. However, a small fraction of light (approximately 1 x 10^{-7} photons) is scattered at optical frequencies different from the frequency of the incident photons. The scattered radiation occurs in all directions and may also have observable changes in its polarization along with its wavelength. The Raman effect can be described using an energy diagram shown in figure 2.3. The incident photon raises energy of the molecule from the ground state to a 'virtual state'. The virtual state is not a stationary energy state of the molecule in the quantummechanical sense, but rather a distortion of the electron distribution of a covalent bond.

The molecule immediately relaxes back to the original electronic state by emitting a photon. If the molecule returns to the vibrational energy level from which it started, as shown in figure 2.3) the emitted photon has the same energy, and therefore, the same wavelength as the initial photon. No energy is transferred to the molecule. This is mentioned before Rayleigh scattering. The Stokes Raman scattering occurs if the molecule returns to a higher vibrational level. The emitted photon has less energy, and therefore a longer wavelength than the initial photon. The vibrational energy of the molecule is

increased. If the molecule returns to a lower vibrational level, the emitted photon has more energy, and therefore a shorter wavelength than the initial photon. The vibrational energy of the molecule is decreased. This event corresponds to anti-Stokes Raman scattering. In general discussion, Raman scattering is usually assumed to be Stokes Raman scattering unless it is labelled as anti-Stokes.

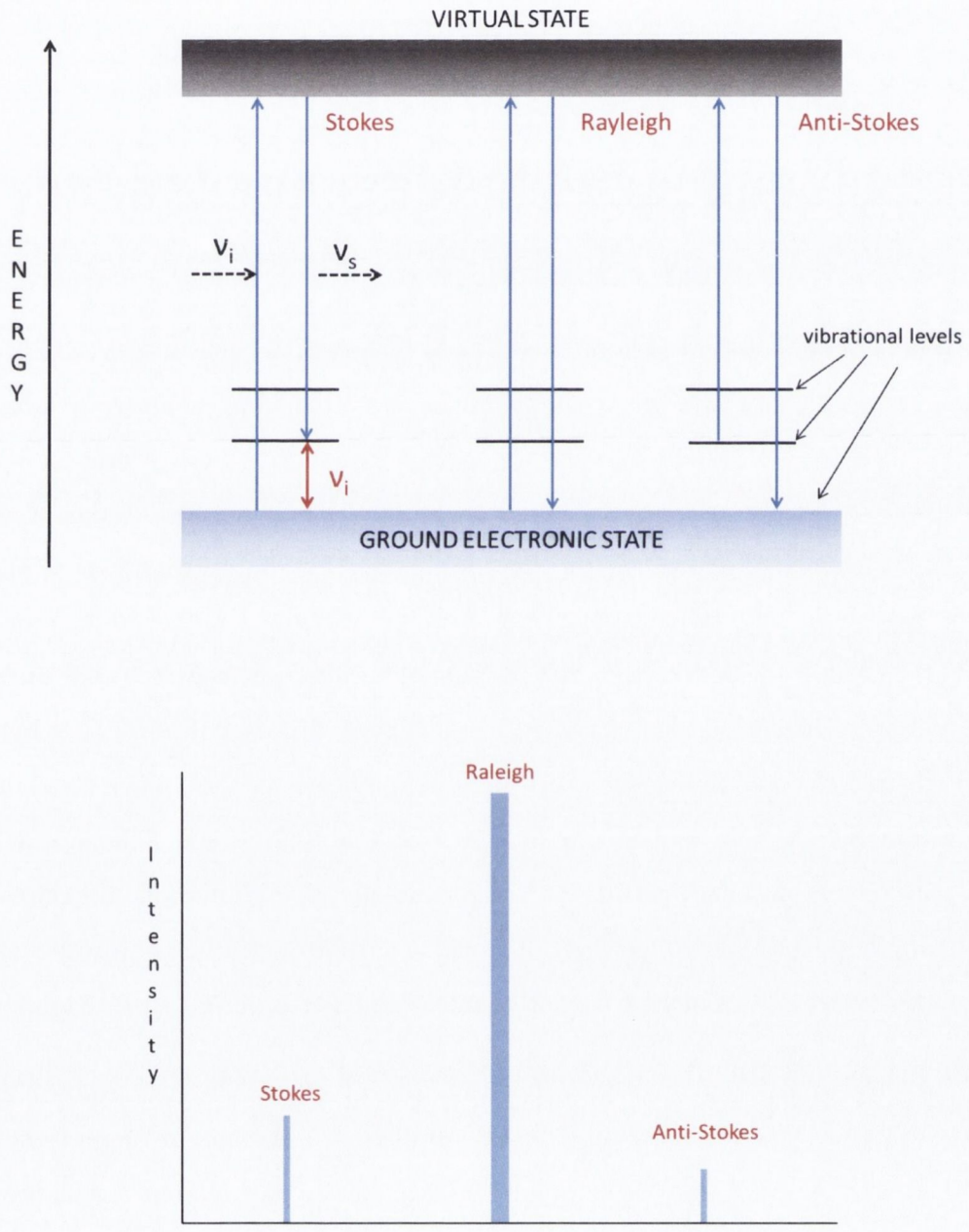

Figure 2.3 Raman energy level diagram (top) and Raman intensities for the Stokes, Raleigh and anti-Stokes Raman scattering (bottom)

Raman spectra were recorded using a Renishaw 1000 micro-Raman system fitted with a Leica microscope and Grams Research™ analysis software. The excitation wavelength was 633 nm (unless stated otherwise) from a Renishaw RL633 HeNe laser. The 50X objective lense of the Leica microscope was capable of focusing the beam to a spot size of ~2-3 μm in diameter. The spectrometer was calibrated before use using a reference Si wafer centred at 520 cm^{-1}

2.7.2 Atomic force microscopy

AFM is a type of scanning probe microscopy. The AFM can provide a high resolution 3D profile of a surface by measuring the forces between a sharp probe (AFM tip) which is mounted on an oscillating cantilever spring.[6] The amount of force between the probe and the sample is dependent on the spring constant of the cantilever. This force can be described using Hooke's law where F = -k.x (F= force (N); k = spring constant (Nm^{-1}); and x = cantilever deflection (m)). The position of the tip relative to the surface is controlled using a piezoelectronic scanner. The piezoelectric scanner allows for extremely accurate length changes to be controlled with the application of a voltage across the piezoelectric material. As the tip scans across a surface, the deflection of the cantilever is measured using a laser which is coupled to a photodiode. The photodiode measures the intensity of the frequency dependant laser as it reflects from the oscillating cantilever. The measured cantilever deflections are used to create a detailed map of the surface topography.

Figure 2.4 below shows the operating principle of the AFM. It is possible to operate the AFM in 3 modes, 1) contact mode AFM 2) Semi-contact or tapping mode and 3) non-contact mode AFM. The type of AFM employed depends on the nature of the material under investigation and the resolution required. Contact mode AFM maintains a constant force between the probe and the sample in order to obtain images. Contact mode AFM is generally used for generating images of rough surfaces with fast scanning speeds. The main disadvantage of using contact mode in AMF is the damage that can be caused to the

tip and the sample during extended contact. Tapping mode AFM is similar to the contact mode. However, in tapping mode the cantilever is oscillated over the sample at its resonant frequency. The tip gently taps the surface and probes the surface topography. Tapping mode AFM can be employed to produce high resolution images of samples that may be damaged in full contact mode. Non-contact mode does not contact the sample surface during sample scanning. Changes in the cantilever amplitude are a result of attractive Van der Waals forces between the sample and the tip. This method of AFM can be used to image extremely delicate samples; however, images are generally of lower resolution than that obtained from contact mode or tapping mode AFM. Contaminants absorbed on the surface can also interfere with the oscillation of the cantilever spring and hence operation in ultra-high vacuum (UHV) is often required.

AFM images were recorded in tapping mode using both the inverted and upright configuration of the NTEGRA Spectra (NT-MDT). Images were recorded with NCH tips (nanoworld) at a resonance frequency of ~ 295kHz.

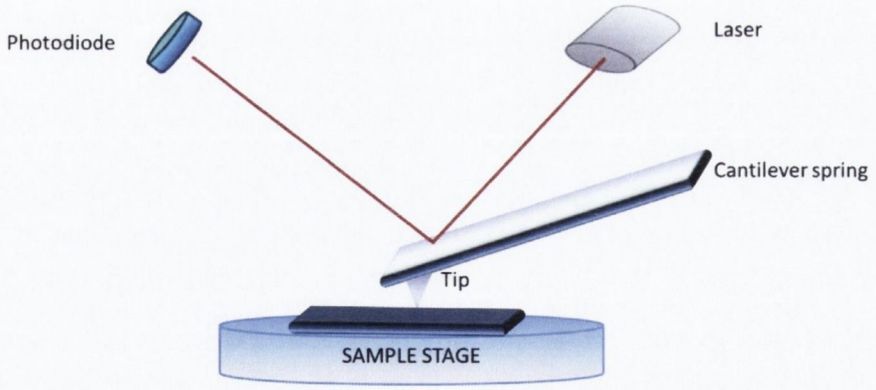

Figure 2.4 The operating principle of an AFM

2.7.3 Transmission electron microscopy

Transmission electron microscopy (TEM) is an imaging technique which produces detailed images of a sample by illuminating the sample with an electron beam. The electron beam is accelerated down an evacuated tube from an electron source. The source of the high energy electrons is generally from a thermionic or field emission gun. The electrons that are transmitted through the sample are detected with a charge coupled device (CCD) camera and can be used to generate a detailed image of the sample. As the wavelength of electrons is much smaller that the wavelength of light, the possible resolution of the TEM is several orders of magnitude greater than that of an optical microscope.

All low resolution transmission electron microscopy images were recorded using a Jeol 2100 TEM at an operating voltage of 200 KeV. High resolution TEM images were recorded with an FEI-Titan TEM, at an operating voltage of 300 KeV. Samples for TEM were prepared by suspending the material under investigation into an appropriate solvent and drop casting onto copper coated TEM grids.

2.7.4 Scanning electron microscopy

A Scanning electron microscopy (SEM) uses a focused beam of electrons to scan over the surface of a sample in a raster fashion. The focused electrons can interact with the sample in a number of different ways, providing complementary information regarding the samples topography and composition. Secondary electrons, which are emitted from excited atoms which have interacted with the focused electron beam. A detector is used to collect the secondary electrons and generate an image of the surface topography. Back-scattered electrons (BSEs) (i.e. beam electrons which are reflected from the sample) can often be employed to gain an insight into the elemental composition of the sample, as the BSEs intensity is strongly related to the atomic number present in the sample.

Scanning electron microscopy was carried out with a Zeiss ultra plus field emission scanning electron microscope equipped with wavelength dispersive X-ray microanalysis.

2.7.5 Scanning transmission electron microscopy

Scanning Transmission Electron Microscopy (STEM) combines the scanning capabilities of an SEM with the transmission capability of the TEM. A focused electron beam is scanned over a sample in a raster fashion. The STEM employs a high angle detector to capture secondary electrons from the surface of the sample. The intensity of these electrons is related to the atomic number (Z) of the elements in the sample and this allows the STEM to produce high quality Z-contrast images.

2.7.5 Profilometry

Profilometry measurements were taken with the help of Mr. Neal Leddy (Centre for microscopy and analysis, TCD) using an omniscan MicroXamWhite-light interferometer.

2.7.6 X-ray diffraction

X-ray diffraction was performed using Siemens-500 X-ray diffractometer. X-ray diffraction is a technique which is used to obtain information about the structure of crystalline materials, based upon their diffraction pattern.[7] When a beam from a monochromatic X-ray interacts with a crystalline material the X-rays undergo constructive and destructive interference, in a process known as diffraction. The diffraction of X-rays by a crystal can be described by Bragg's Law ($n\lambda=2d\sin\theta$). Most materials are not single crystals, but are polycrystalline in nature; hence the X-ray beam sees all the inter-atomic planes due to this polycrystallinity. During an XRD experiment the experimental angle is changed, (2θ angles) so that all the possible diffraction peaks from the material can be detected.

2.7.7 Electrochemistry

All electrochemical investigations were carried out using an Autolab III potentiostat controlled through NOVA 1.10 software and are described in detail below.

2.7.8 UV-Vis absorption spectroscopy

UV-Vis absorption spectra were recorded using an Agilent technologies, Cary 60 Uv-Vis scanning spectrometer. All samples were examined in a 1 cm quartz cell using an appropriate solvent.

2.7.9 Sintering Oven

The oven used for electrode sintering was elite thermal systems limited BMF 11/7 with a temperature controller supplied by Eurotherm limited.

2.7.10 Ultra-Sonication

Ultra-sonication was carried out using a GEX-600 ultrasonic horn, which employed a tapered titanium tip and was operated at variable power. The ultra-sonic bath used was a Grant ultrasonic bath operated with a frequency between 50-60 Hz.

2.7.11 Thermogravimetric analysis

TGA allows for the mass of a sample to be monitored as a function of temperature and plotted as a TGA or derivative TGA (DTGA) curve. TGA is commonly used to determine thermal characteristics of materials and the contents of components that exhibit mass loss or gain.[8] A modern TGA instrument consists of a number of parts. Mass loss is monitored using a sensitive thermo balance. A digital recorder records variation in weight during a TGA scan. A heating furnace made from a ceramic material, which can withstand high temperature. The temperature is precisely controlled by a temperature programmer and a computer monitor displays the output data.

Thermogravimetric analysis was carried out using a Perkin Elmer Pyrus 1 TGA equiped with an ultra-micro balance with a sensitivity of 0.1 microgram.

2.7.12 Screen printing setup

The manual screen printer used in the work was composed of a moveable screen positioner and holder, a printing screen made from a 90T polyester mesh and a manual squeegee used for ink application and spreading. The screen holder was supplied by A.W.T World Trade Inc. while the screens and squeegee was supplied by Serigraph Ltd. Screen templates were designed using the Inkscape software package.

2.7.13 DC power supply

The DC power supply used for electrophoretic deposition was a TTi PLH250 DC power supply.

2.7.14 Spray deposition

Spray deposition was performed by filling graduated reservoir with the material to be deposited (in an appropriate solvent). The reservoir was attached to a Harden and Steinback Evolution airbrush. This was then integrated into a Janome JR 2300N automatic robot system along with a pressurised N_2 hose. FTO substrates were cut to required sizes and thoroughly washed using soapy water followed by thorough rinsing with acetone and iso-propanol (IPA) and dried under ambient conditions. The cleaned glass substrates were placed on the hotplate set to an elevated temperature, depending on the solvent being employed. The robotic arm and moveable tray was set to spray the desired 8 cm x 8 cm area on the FTO substrates by activating the airbrush trigger releasing a fine controllable jet of solution (at 40 psi air pressure) onto the substrate. This process resulted in the formation of composite films. The thickness of the films can be controlled by altering the number of layers sprayed i.e. the amount of solution deposited.

2.7.15 Fourier transform infra-red spectroscopy

Fourier transform infra-red spectroscopy was carried out with a Perkin Elmer Spectrum One NTS with ATR Sampling Accessory.

2.7.16 Solar I-V measurements

Solar I-V measurements were performed using a digital source meter (Keithley 2400) and a full spectrum solar simulator (Newport 96000), fitted with a xenon arc discharge lamp which operated at 150W, and was equipped with an air mass (AM) 0 and 1.5D filter. The AM 0 filter acts to remove the xenon emission lines from the spectrum and closely match that of solar radiation. The 1.5D filter acts to mimic the solar spectrum at 48.2° from the suns zenith angle. At this angle the radiation path length, measured in units of Air Mass, is

1.5 times the radiation path length at the zenith angle of 0 °. The solar simulator was calibrated with a silicon-based reference cell before testing. All cells were tested at 1 sun (1000 Wm^{-2}) unless otherwise stated. The testing area of the cells was 0.2 cm^{-2} (unless otherwise stated) and was defined by a mask.

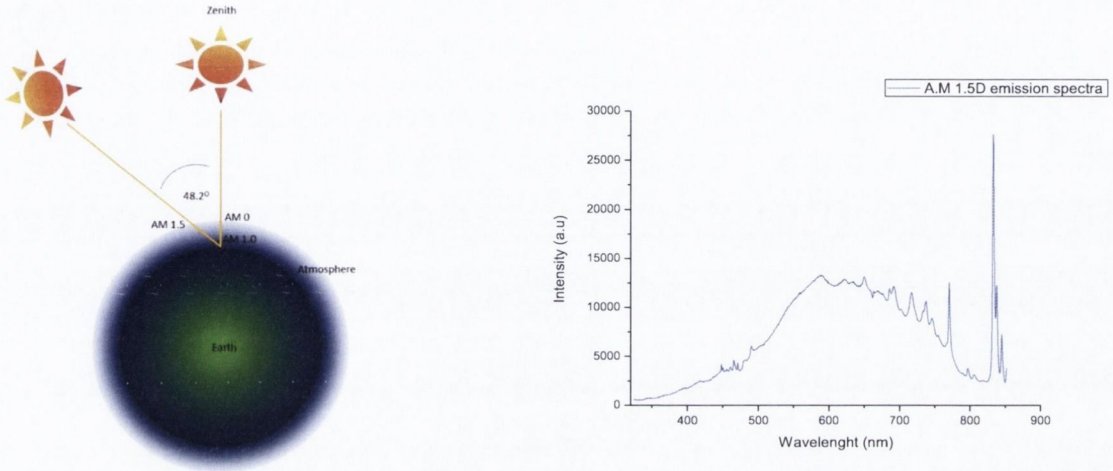

Figure 2.5 Diagram of solar air masses and spectral output from xenon arc lamp fitted with AM 0 and AM 1.5D filters

Solar cells were tested at AM 1.5D conditions by running a current-voltage (I-V) sweep across the devices under illumination. The resulting I-V curve was used to analyse the properties of the solar cells, and ultimately there quantum efficiency. IV curves provide 3 parameters which can be used to calculate overall cell efficiency. The short-circuit current (Isc) is the device current measured at short circuit conditions, i.e. at 0V, and flows with zero external resistance. The value of Isc provides an insight into the photocurrent produced by the device when illuminated. The open circuit voltage (Voc) is the voltage across both electrodes when the resistance in the cell is large, i.e. at 0A. The fill factor (FF) can be calculated as the ratio of Pmax to the area of the rectangle formed by Isc and Voc (where $Pmax=Isc_{max}.Voc_{max}$) An ideal FF of 100% (FF = 1) describes a right angle between Voc and the Isc, where the maximum power is equal to the theoretical power (Pmax = Pt),

however this FF is not possible as resistive losses are always present in a solar cell. An efficient device will generally operate with a FF of ~ 80% (FF=0.8).

$$FF = \frac{Pmax}{Isc.Voc} \qquad (1)$$

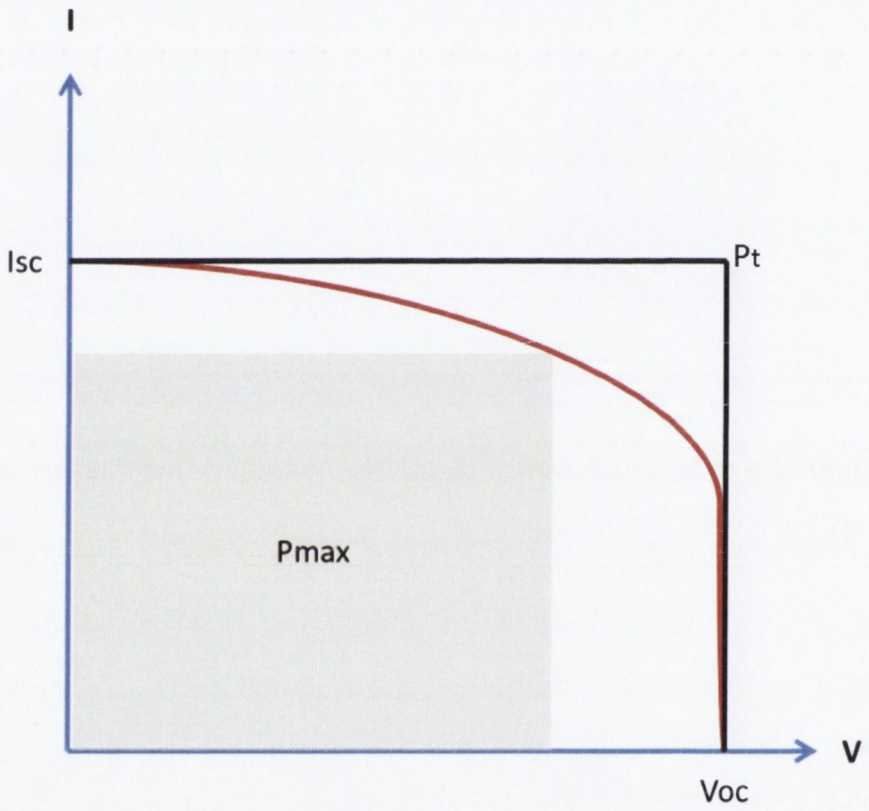

Figure 2.6 Example I-V curve of a solar cell under illumination

The resistive losses in a solar cell can be categorised as either series resistance (Rs) or shunt resistance (Rsh). Rs refers to the combined resistance of all the materials that lie in the path of the photocurrent. As Rs increases the IV curve begins to change shape and the current value begins to drop at lower applied voltage. The Rsh is the resistance across the junctions in the device, mainly due to current leakage across the charge separation area. The Rsh value should be as high as possible; this ensures that current travels the correct route around the circuit, through the load rather than short circuiting across the junction. A

low value of Rsh will cause a low Voc while maintaining the Isc. The values of Rs and Rsh can be estimated by using the inverse of the IV curve slope at Isc and Voc respectively.[9]

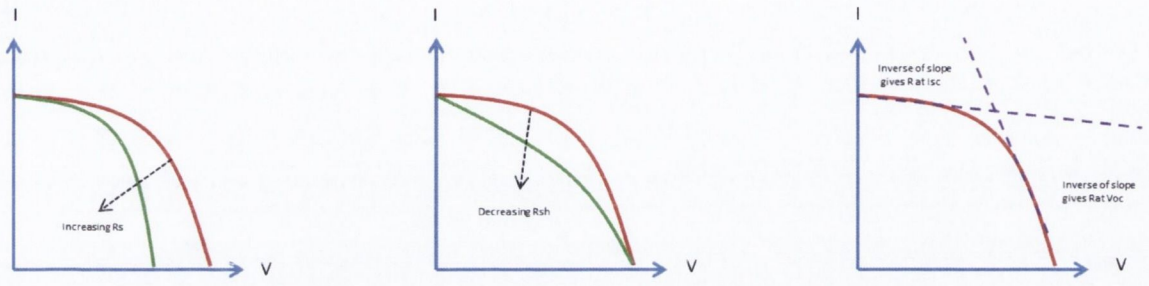

Figure 2.7 IV curves showing the effect of increasing Rs (left) decreasing Rsh (middle) and how to estimate the magnitude of Rs and Rsh from the inverse of the slope at Isc and Voc (right)

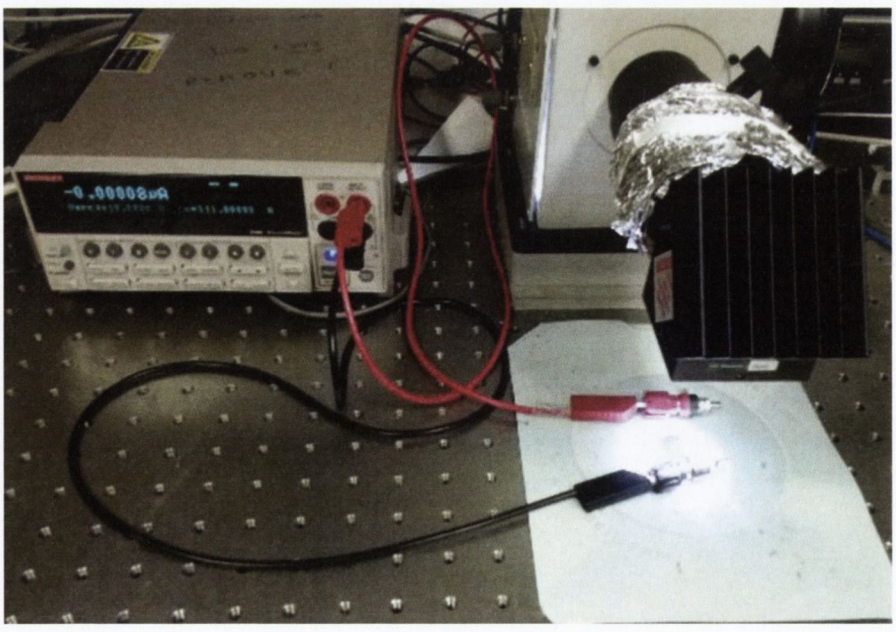

Figure 2.8 Photographic image of full spectrum solar simulator in operation

The overall quantum efficiency of the solar cell is the ratio of optical power density (W m^{-2}) to output electrical power delivered to the load. The quantum efficiency of a solar cell can be calculated using the following expression, where η is the overall quantum efficiency (%), Isc is the short circuit current (A) Voc is the open circuit voltage (V), FF is the fill factor (expressed as a percentage of 1) P is the incident power (W) and A is the active area of the cell.

$$\eta\,(\%) = \frac{Pcell}{Plight} = \frac{Isc.Voc.FF}{P.A} \qquad (2)$$

2.7.17 Photoaction spectra

Photoaction spectra were obtained using a specifically designed experimental setup. The components consisted of a Autolab(III) potentiostat controlled with the NOVA 1.10 software package, a light source of known emission and power and a non-transparent screen. The technique is also known as amperometric I-t analysis, as the photocurrent is monitored as a function of time. Removal of the non-transparent screen allows the short circuit current (at zero bias) of the electrodes to be monitored directly with the potentiostat. Replacement of the screen blocks the incident light and the current falls to zero. Amperometric I-t curves allow for quick evaluation of photoactive electrodes without the need for building a full device. The electrolyte scavenges photo generated holes and allows for the electrode stability to be monitored over extended periods of time.

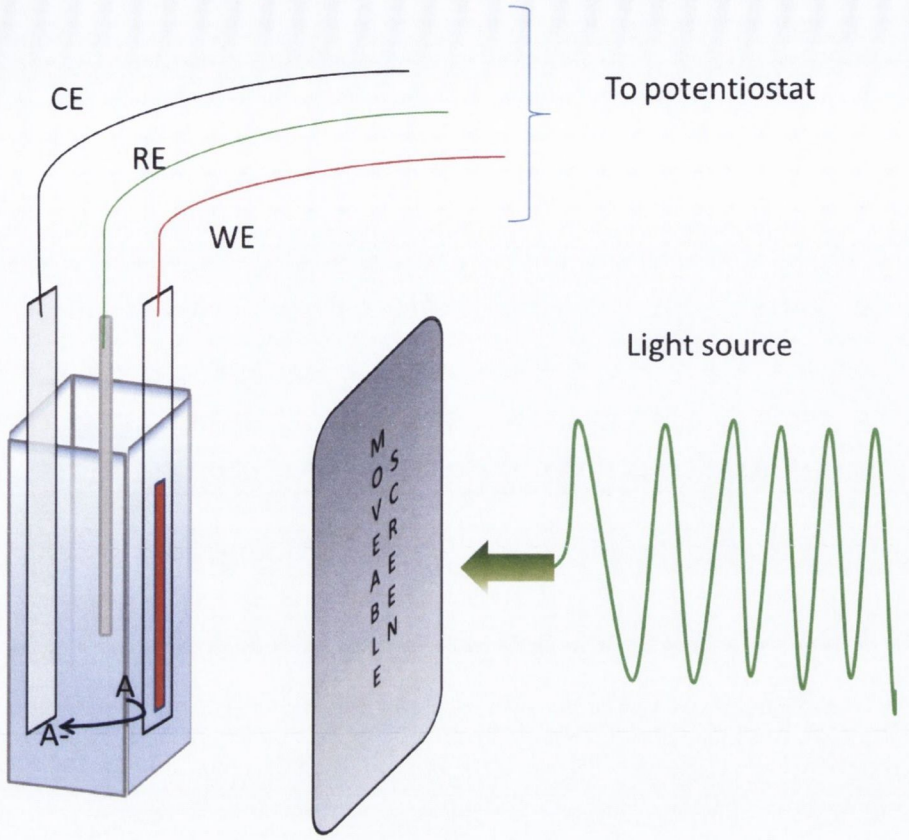

Figure 2.9 Experimental setup for recording photoaction spectra

2.7.18 Design and building of Incident Photon to conversion efficiency experimental setup (IPCE)

Incident photon to current efficiency (IPCE) is a technique which allows for one to calculate the quantum efficiency of a photosensitive device. The technique is also known as the external quantum efficiency (EQE). The quantum efficiency of a solar cell is the ratio between the number of photons hitting the surface of the solar cell and the amount of charge carriers that are created. IPCE is measured over a range of wavelengths and produces a spectrum which shows how the photovoltaic cell performs throughout the tested spectral range.

Using an IPCE it is possible to monitor the response of the solar cell to monochromatic light and this provides information about how the cell performs over a wide range of

wavelengths. The IPCE value is generally expressed as a percentage of photons that are absorbed by the solar cell and are converted to electrons, as a function of the incident wavelength. The IPCE value provides information about how efficiently the cell responds over a range of frequencies. The IPCE does not allow the total power conversion of the solar cell to be calculated and therefor differs to the conventional AM1.5 test. In order to calculate the total conversion efficiency of a solar cell it is necessary to know the operating voltage of the device. In IPCE the test is run at short circuit conditions (0V) however through integration of the IPCE spectrum it is possible to obtain an estimate of the total conversion efficiency of the solar cell.

The diagram below outlines two experimental setups that were designed and built for testing IPCE values for solar cells that were fabricated. The first experimental setup allows for IPCE values to be calculated for fully assembled cells, while the second setup allows for the solar cell electrodes to be tested in a photo electrochemical regime which does not require the solar cells to be fully assembled but rather allows for them to be tested in a conventional 3 electrode electrochemical cell.

The device built utilizes a 150 W xenon arc discharge lamp (Oriel instruments) a monochromator, a spectrograph, optical chopper, a lock-in-amplifier (LIA) and a digital sourcemeter (Kiethley 2400).

The lock-in-amplifier serves as a method of recovering the signal from the solar cell in the presence of a large background, and can be used to produce a signal with a very high signal to noise ratio. The main function of the LIA is to provide a DC output signal which is proportional to an AC input signal. The AC-DC conversion is performed by a phase-sensitive detector (PSD), its function is to rectify the signal of interest while suppressing the effect of noise or interfering components which may accompany the signal. The PSD works by multiplying two signals together as can be seen in figure 2.10. The two signals are the AC input signal, generated by the solar cell in response to chopped light and the internal reference signal which is generated by the PSD. The internal reference signal is generated in the same phase as the input sinusoidal signal from the solar cell, The product of the two signals is output as a sinusoidal signal but since there is no phase shift between both input signals, the sinusoidal output signal has a mean positive value. The mean DC

value for the output sinusoidal is isolated using a low-pass filter. The filtered output is the measured using conventional DC voltmeter techniques.

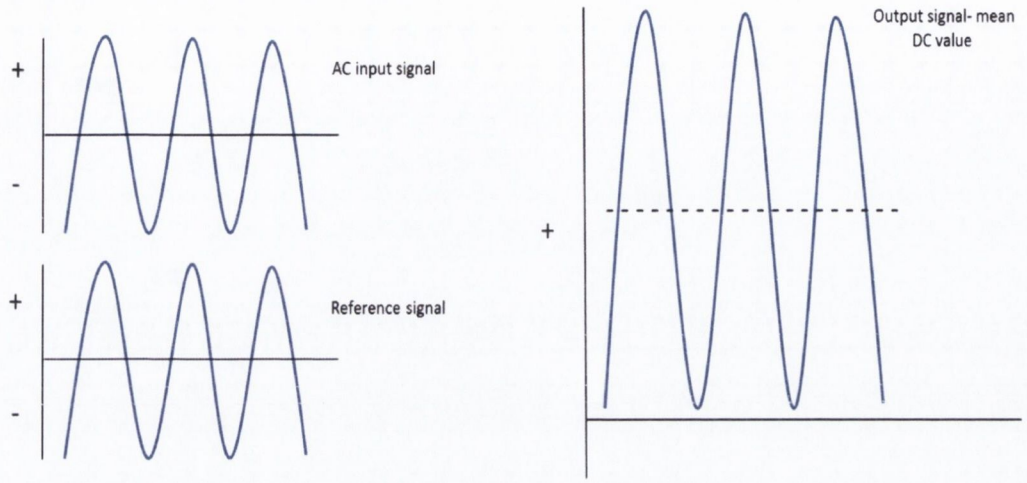

Figure 2.10 Signal processing in the lock-in-amplifier - AC to DC conversion

As seen in the diagram below (figure 2.11), light from the xenon lamp enters the monochromator and is diffracted into its component colours. A piston located in the monochromator allows for the mirror position to be changed and this allows for selection of the various wavelengths. Light exiting the monochromator is passed through an optical chopper and this creates a light source with a frequency component. The frequency of the light response is controlled by the optical chopper frequency control. The optical chopper is used to create a square wave which contains a sharp on/off response. To test the nature of this on/off response the optical chopper was allowed to chop light incident on a silicon photodiode. The Si photodiode was connected to an oscilloscope and the square wave response was monitored.

The optical chopper is connected to the LIA, the function of the LIA is 2-fold. The LIA 'locks in' to the frequency established by the optical chopper and will actively search for an input signal from a device containing this frequency. Using the LIA allows for a IPCE spectrum to be calculated with an extremely high signal to noise ratio, given that the LIA will only output a signal from a device that contains a frequency component matching

exactly that of the input frequency, defined by the chopper. This ensures that any frequencies incident on the solar cell will not be included in the IPCE as they will not have the predefined frequency component. The optical chopper frequency was always set at frequency which was a non-multiple of 50Hz, this ensured that the LIA would not 'lock on' to other devices operating at the terrestrial frequency.

Once the frequency component of the light source was established the light was passed through a beam splitter (THOR Labs). The beam splitter allowed for 8% of the light to be sent to the spectrograph, while 92% of the beam was sent through the optical diffuser.

The spectrograph (Oriel instruments) was calibrated using a series of laser optical filters and was used to monitor the frequency of the light incident on the solar cell

The optical diffuser takes the sharp monochromatic line of light and diffuses this light over a wider area, allowing for cells to be tested under a larger, more uniform light source.

In order to calculate the IPCE value for each cell, 2 individual measurements must be taken. The first measurement uses a photodiode to analyse the number of photons incident upon the testing area. The photodiode has its own inherent IPCE response, so this must be taken into account when calculating the photons incident on the diode, as the diode does not perform with an IPCE of 100% throughout the entire spectrum. Once the power (P) incident on the photodiode is known it is possible to test the current response (Isc) of the solar cell at short circuit conditions (0V). When the current response of the cell has been calculated the IPCE can be created using the following expression.

$$IPCE(\%) = \frac{Isc(A)}{P(W)} \times \frac{1240}{\lambda(nm)} \times 100 \qquad (3)$$

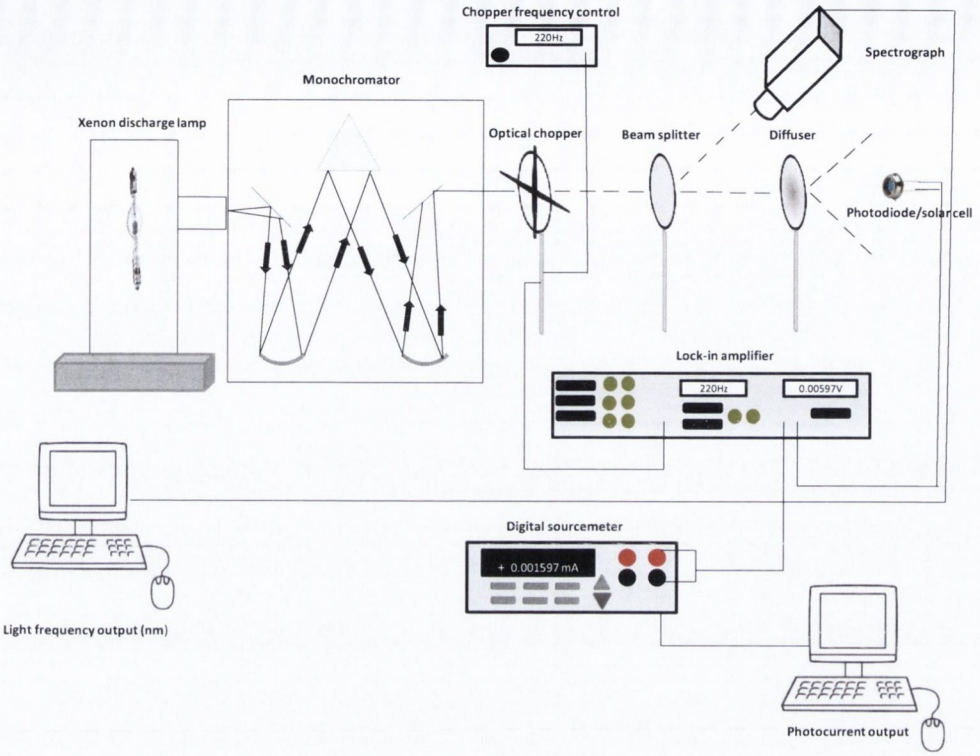

Figure 2.11 Design plan for Incident Photon to Conversion Efficiency experimental setup

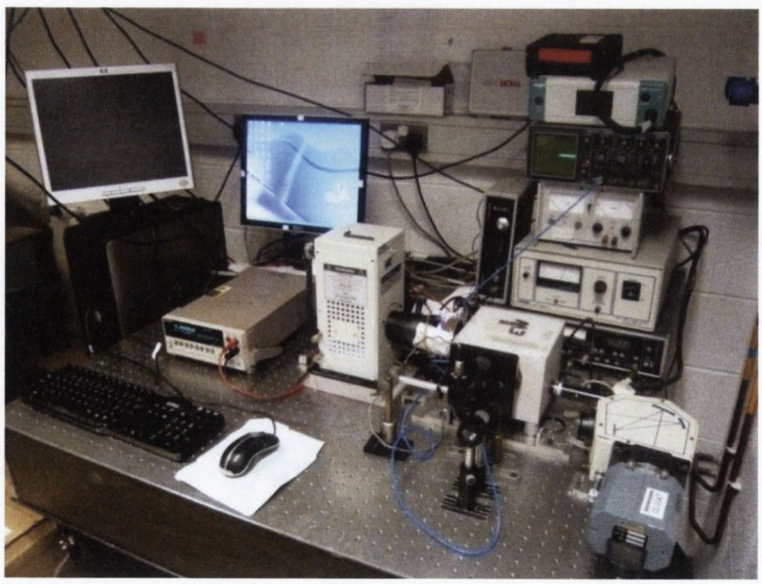

Figure 2.12 Photographic image of the IPCE setup once built.

The second IPCE setup differs to that explained above. In this experimental setup photoanodes are tested for their current response in a photo electrochemical setup using a potentiostat. This test allows for photoanodes to be tested without the need for full cell fabrication. This setup does not employ the LIA as a means of increasing the signal to noise ratio, as the LIA can only be employed in a two electrode configuration. Photoanodes are testes in a standard 3 electrode electrochemical cell containing a working electrode (WE) which is the photoandoe, a counter electrode (CE) which is FTO coated glass and a saturated calomel reference electrode (SCRE). Current generated by the photoanode is recorded by the potentiostat which is run in chronoampommertry mode. In chronoampometry the current is measured as a function of time. The experiments are run over 90 seconds as the light frequency is scanned from 950 nm to 400 nm while the photocurrent is recorded by the potentiostat. This technique has some advantages over the first IPCE setup as the current is constantly being recorded by the potentiostat as the frequency is changed and this allows for extremely detailed spectra to be recorded.

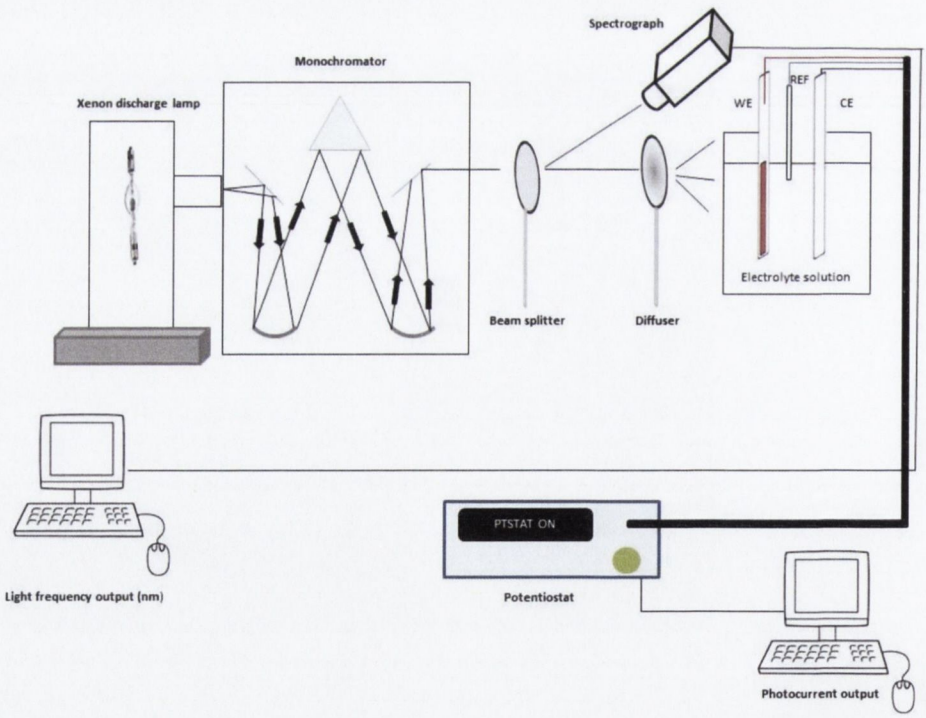

Figure 2.13 Alternative design setup for IPCE run in chronoamperometry mode

References

(1) Ito, S.; Chen, P.; Comte, P.; Nazeeruddin, M. K.; Liska, P.; Péchy, P.; Grätzel, M. *Progress in Photovoltaics: Research and Applications* **2007**, *15*, 603.

(2) O'Neill, A.; Khan, U.; Nirmalraj, P. N.; Boland, J.; Coleman, J. N. *The Journal of Physical Chemistry C* **2011**, *115*, 5422.

(3) Hummers Jr, W. S.; Offeman, R. E. *Journal of the American Chemical Society* **1958**, *80*, 1339.

(4) Griffin, F.; Fitzmaurice, D. *Langmuir* **2007**, *23*, 10262.

(5) Kim, H.-S.; Ko, S.-B.; Jang, I.-H.; Park, N.-G. *Chemical Communications* **2011**, *47*, 12637.

(6) Binnig, G.; Quate, C. F.; Gerber, C. *Physical Review Letters* **1986**, *56*, 930.

(7) Otwinowski, Z.; Minor, W. *Methods enzymol* **1997**, *276*, 307.

(8) Coats, A.; Redfern, J. *Analyst* **1963**, *88*, 906.

(9) Ginley, D. S. C., D. *Cambridge University Press* **2011**.

Chapter 3

Graphene – ionic liquid electrolytes for iodine free dye sensitized solar cells

3.1 Introduction

The electrolyte is one of the key components of DSSCs. The function of the electrolyte is to transfer charge from the counter electrode (CE) to the dye which is anchored onto the mesoporous TiO_2 charge collection layer. In order to work effectively the electrolyte must fulfil some key characteristics including thermal stability, high diffusion coefficient and suitable viscosity which will allow for ease of sealing without impeding the transfer of charge.[1,2] Traditional DSSC technology has focused on the use of organic solvent based electrolytes which cause a number of problems during manufacturing. These problems include leakage of the electrolyte, degradation of the polymer seal and evaporation of the solvent which all limit cell lifetime and hence long-term applications. These disadvantages are serious obstacles that face the successful commercialization of DSSC technology, in particular the large scale development of flexible modules.

In order to resolve these problems, several alternative electrolyte compositions have been studied. Ionic liquids (ILs) have received much attention in recent years as a potential substitute to the organic solvent based electrolytes currently employed in DSSCs. Room temperature ILs are molten salts with characteristics highly suitable for DSSC electrolytes.[3-6] Some of these characteristics include tuneable viscosity, non-volatility, ionic conductivity, excellent thermal stability, a broad electrochemical potential window and negligible vapour pressure.[7-9] Unfortunately the conversion efficiencies achieved with ILs at full air mass (AM 1.5) does not match that of solvent electrolytes. This is due to the fact that the diffusion coefficient of the redox pair in the IL or viscous molten salt is generally 1-2 orders of magnitude lower than that of ionic diffusion in an organic solvent.[10]

The highest reported DSSC efficiency obtained using an IL electrolyte stands at 8.2 %.[11] This result was achieved by combining 3 individual ILs to form a eutectic melt which contained characteristics of each of the individual IL components. Several approaches have been investigated towards designing an IL electrolyte which retains the characteristics of the IL but yet achieves conversion efficiency closer to that of the solvent based electrolytes. Such approaches have included the incorporation of various nanocomponents,[12-14] the use of polymer IL composites,[15,16] organic/inorganic gel electrolytes,[14] hole conducting materials[17] and carbon nanomaterials.[18]

Gratzel et al has reported that the incorporation of nanoparticles of SiO_2 at 5 wt.% into the IL 1-propyl-3-methyl-imidazolium iodide (PMII) could effectively solidify the electrolyte and produce efficiencies of 7%.[12] It was found that the presence of silica nanoparticles in the electrolyte had no effect on the IL regeneration efficiency for the oxidised sensitizer and the electrolyte had the advantage of being free from leakage.[12,15]

The addition of carbon nanomaterials, in particular carbon nanotubes (CNTs) to ILs has been shown to form a composite material known as a bucky gel. The addition of CNTs to ILs has been shown to be responsible for the molecular ordering of the organic molten salt. Work by Aida et al. has shown that when pristine CNTs are ground into ILs containing the imidazolium cation, the CNT bundles untangle within the gel to form much finer CNT bundles.[19] The grinding of the CNTs into the IL caused a phase transfer and it was found that the change in material properties was a result of the physical cross-linking of the nanotube bundles, which was mediated by local molecular ordering of the IL. It was reasoned that the non–covalent π-mediated interaction between the imidazolium cations and the CNT surface allowed for the formation of a highly gelatinous material which displays both ionic and electronic conductivity.[9] The electronic conductivity is attributed to the presence of the pristine CNTs while the ionic conductivity is due to the presence of the IL ions. The conductivity of the material could be controlled by choosing appropriate ratios of CNT to IL and also by tailoring the functional groups of the IL cation.[20]

Investigations by Li et al. showed both experimentally and theoretically that the interaction between pristine CNTs and imidazolium containing ILs was actually caused by Van der Waals interactions, rather than the previously assumed cation – π interaction.[21] Using both vibrations spectroscopy and molecular simulation they found that the dispersion mechanism was similar to that observed for the dispersion of CNTs in sodium

dodecyl sulphate (SDS) dispersed systems, which is commonly used to disperse CNTs into solution.[22,23]

This work was further extended to graphite exfoliation in ILs. It was discovered by Loh et al. that graphite could successfully be exfoliated into ILs using an electrochemical approach, whereby a graphite rod, placed in a IL solution could decomposed into IL functionalised graphene nanosheets.[24] The group further expanded on this work to produce carbon nanoparticles and fluorescent carbon nanoribbons in ILs with the application of 15V across the graphite rod [25] placed in a solution of imidazolium based IL and water. It was found that the IL/water ratio is an important parameter influencing the properties of the graphene produced.

The applications of such bucky gel materials are widespread. Polymerisation of ILs in the presence of CNTs is known to produce mechanically reinforced electro-conductive polymers. A 7% loading of SWCNTs in a metacrylate functionalised imidazolium IL has been shown to have conductivity as high as 1S cm^{-1} and a Young's modulus 120 times that of the un-doped IL.[20] Watanabe et al. found the CNT containing buck gels can be used as an electrolyte component in electrical double layer capacitors[26] and it has also been observed that the bucky gel materials can also serve as an actuator,[27] whereby electrical energy applied across the actuator is converted into mechanical energy. The use of bucky gels in electrochemical solar cells has also been reported. These quasi solids gels have been shown to work effectively as an electrolyte layer in DSSCs. Work by Usui et al.[13] explored the potential of using carbon nanotubes as an IL additive for DSSC electrolytes. The reported results showed that the addition of CNTs (single and multi-walled) led to an overall increase in device efficiency. The increase in efficiency was attributed to the decrease in resistance of the composite electrolytes. The effect of adding carbon black (CB) to an ionic liquid electrolyte was investigated by Lee and co-workers.[28] In this work polyaniline-loaded CB (PACB) was used to increase device efficiency form 0.6% to 5.81%. This large increase in efficiency was attributed to the charge mediation properties afforded by the PACB. It was also observed that cells operated fully (but at decreased efficiency) without the use of a Pt catalyst. This indicated that the presence of PACB acted as a catalyst for the redox reactions in the electrolyte in the form of an EETM (extended electron transfer mechanism)

As a material for DSSCs, composites of ILs and CNTs/graphene have shown promising results when used as electrolytes. Lee et al. reported on a quasi-solid electrolyte for DSSCs using an IL (1-ethyl-3methyl-imidazolium iodide) and SWCNTs (10 wt. %) as a filler.[29]

They showed that moderate efficiencies of 1.88 % could be achieved when compared to the unmodified IL, which showed an efficiency of 0.41 %. Ikeda et al. used a similar approach and incorporated both SWCNTs and MWCNTs (6.97 wt. % for both) to the IL 1,3-diethyleneoxide derivative of imidazolium iodide and obtained power conversion efficiencies of 1.63% and 1.01% respectively.[30] These cells have the notable advantage of stability with respect to sealing and temperature, however a major drawback for these electrolytes is the high cost associated with the CNTs. A cost effective alternative to using CNTs for these applications is to use graphene. Given the similar chemical and electronic structure of graphene to CNTs it was reasoned that 2D graphene could be used to form similar bucky gels to that described above for CNTs. The extended 2D π network should provide a good surface for the interaction with the imidazolium ions and allow for a stable dispersion of exfoliated graphene in the IL.

Previous work from our group has demonstrated that very viscous quasi-solid state electrolytes can be prepared by the incorporation of large amounts of graphene(~ 30 wt. %) or carbon nanotubes to ionic liquids.[18] Using these new electrolytes, significant increases in light conversion efficiencies of DSSCs have been achieved and the electrolytes have also been shown to be stable to both high temperature and use over extended time periods.

In this work two dimensional graphene flakes were used to prepare new electrolytes for dye sensitized solar cells (DSSC). Small amounts (up to 3 wt. %) of graphene flakes were suspended into the ionic liquid (IL) 1-propyl-3-methyl imidazolium iodide (PMII) to produce new electrolytes. Graphene was produced following the solvent exfoliation technique outlined in by O'Neill et al.[27] The exfoliation of the graphene in a low boiling point solvent allowed for graphene to be added to the IL in the liquid phase and the solvent could then be removed from the IL post addition. This allowed for an increased level of interaction between the surface of the graphene sheet and the IL when compared to the addition of graphene in the solid phase. When added to the IL in the solid phase the graphene requires a large amount of grinding, ultra-sonication and centrifugation in order to form the stable IL-graphene composite, however addition in the liquid phase allows for

an in-situ formation of the composite material or ''bucky gel'', upon removal of the solvent. The formation of the graphene was confirmed with Raman spectroscopy, transmission electron microscopy and atomic force microscopy. The conversion efficiency

of these electrolytes was examined through the fabrication of 'closed' DSSCs, whereby the finished cell is sealed from outside atmospheric conditions. The effect of graphene addition to the redox activity on the IL electrolytes was also examined through cyclic voltammetric experiments.

The use of these electrolytes in DSSCs resulted in more than twenty five times improvement of the solar cell efficiency, increasing efficiency form 0.10 % to 2.60%, upon addition of 1 wt.% of graphene. The increase in efficiency can be attributed to two primary reasons. Graphene can act as an efficient charge transfer agent in the viscious IL and also as a catalyst for the electrochemical reduction of I_3^- in the electrolyte layer. In addition, $\pi - \pi$ and Van der Waals interactions between the graphene sheets and IL imidazolium cation lead to the formation of self-organised assemblies or networks, similar to those observed for carbon nanotubes[19,31] and which has also been observed for imidazolium containing ILs used for the functionalization of graphene sheets.[32] These factors not only provide an efficient electron transfer network through the electrolyte but also allow for the formation of stable and quasi solid electrolytes, at higher graphene concentrations.

3.2 Graphene preparation and characterisation

Exfoliation of the graphite to prepare graphene followed the procedure similar to that outlined by O' Neill et al.[33] Briefly the graphite was dispersed in chloroform at a concentration of 1 mg ml^{-1}. The solution was then placed in an ultrasonic bath and ultrasonicated for a period of ~ 100 hours to ensure maximum exfoliation of the graphite. After this process the solution was centrifuged at 500 RPM for 1 hour. Following this the supernatant was decanted off leaving the unexfoliated graphite in the precipitate. The resulting dark coloured suspension was deposited onto holey carbon grids for TEM analysis (figure 3.2). The graphene solutions were vacuum filtered onto omnipore (0.2μm) membranes. The graphene dispersions were then added to PMII at various concentrations ranging from 0.125 wt.% to 3 wt.% and the residual chloroform was removed with vacuum

assisted heating under Schlenk conditions. The resulting PMII graphene composites were utilized as electrolytes in DSSCs.

Raman spectroscopy was used to investigate the nature and quality of the graphene after sonication in $CHCl_3$. Raman spectroscopy is commonly used for the characterisation of carbon materials such as graphite,[34,35] CNTs,[36,37] graphene[38-40] and fullerenes[41,42], as these materials show strong Raman signals. Raman spectroscopy is a non-destructive and fast characterisation technique which enables one to determine the number of graphene layers present in a sample and also there quality. Graphene samples for Raman analysis were prepared from dispersions in $CHCl_3$ at a concentration of 1 mg ml^{-1}. The dispersions were filtered using vacuum assisted filtration, onto an omnipore membrane which had a pore size of 0.2μm. After filtration onto the membrane the samples were dried with vacuum assisted heating.

The Raman spectra of graphitic materials are composed of 3 distinct peaks. The D peak located at ~1350 cm^{-1} gives an insight into the level of disorder in the sample. Disorder in the sample may be caused by a disrupted π network, defects in the lattice, or a large amount of flake edges, this is known as the edge effect.[43] The G peak located at ~ 1580 cm^{-1} and the 2D located at ~2700 cm^{-1} are always present in graphitic samples. The shape of these peaks and the relationship between there intensities can be used very effectively to gain an insight into the level of exfoliation in a graphitic sample.[40]

Raman spectroscopy (Figure 3.1) clearly demonstrated that solvent exfoliation of graphite resulted in the production of a highly exfoliated multi-layered graphene. The Raman spectra obtained for a graphite film prepared from chloroform without any ultra-sonication are shown in figure 3.1a). A small D band can be observed at ~ 1350 cm^{-1}, this peak is an indication of defects in the sample most likely caused by the edges of the graphite flakes present.

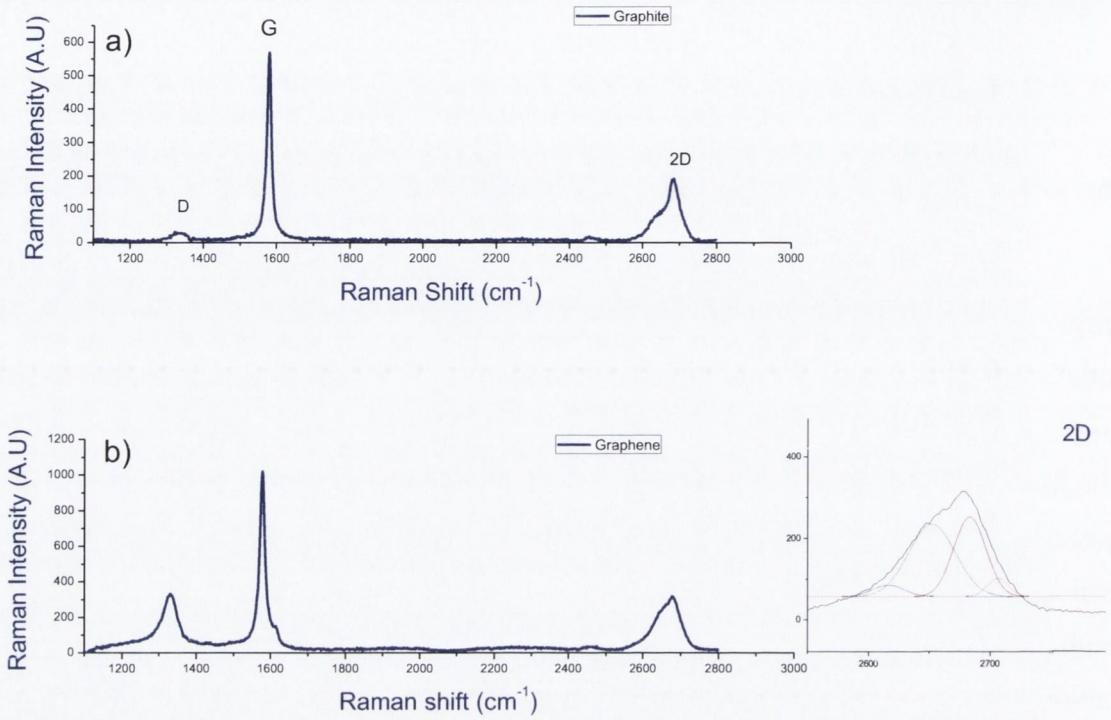

Figure 3.1 Comparative Raman spectra recorded for a) graphite and b)graphene film prepared through vacuum filtration of exfoliated graphene solution. The inset shows the four component peaks of the 2D graphene peak

The relationship in intensity between the G and 2D peak (4:1) clearly show that the sample is composed of bulk graphite. This is further confirmed by the shape of the 2D peak where the shoulder located at ~ 2650 cm^{-1} is indicative of graphite. Figure 3.1b above displays the Raman spectra recorded for the film prepared after a 100 hour sonication in chloroform. Ten individual scans were taken of this film and the data obtained was averaged and presented as the Raman spectra above. Clear differences in the size and shape of the graphitic peaks show the presence of exfoliated graphite. Monolayer graphene can't be expected to be observed using this sample preparation. The filtration process will inevitably cause exfoliated flakes to restack on top of each other, however it is expected that the flakes will not accumulate in the same orientation as that found in bulk graphite. This effect is known as turbostatic graphite and results from the flakes not stacking in A-B formation.[40] The Raman spectra recorded shows an intense D peak which can be attributed

to the larger number of flake edges present in the exfoliated sample, it may also be indicative of some disturbance in the π network after such an extended sonication period.[44] The change in shape of the 2D peak is the clearest indication of exfoliated graphite. The broad shoulder observed in bulk graphite is no longer observed and this is consistent with what is expected from a graphene film which has not aggregated back into the bulk form.[45] The 2D peak of the graphene film is composed of 4 distinct peaks $2D_{1B}$ (blue) $2D_{1A}$ (green) $2D_{2A}$(red) and $2D_{2B}$ (orange) which give an indication into the extent of exfoliation in the sample. This feature is not observed in our graphite 2D band, which consists solely of D_1 and D_2 component peaks.[40]

TEM analysis confirmed the presence of highly exfoliated multilayered graphene (Figure 3.2). Images B,C and D show the presence of multiple graphene layers. The folding edge of the sheet in image B is a common feature associated with graphene sheets. Graphene layers can be observed in images B,C and D and show the extent of exfoliation when compaered to the bulk graphite (A). Significant exfoliation of the parent graphite crystal to graphene layers was also observed through analysis of atomic force microscopy (AFM) images obtained before and after exfoliation.

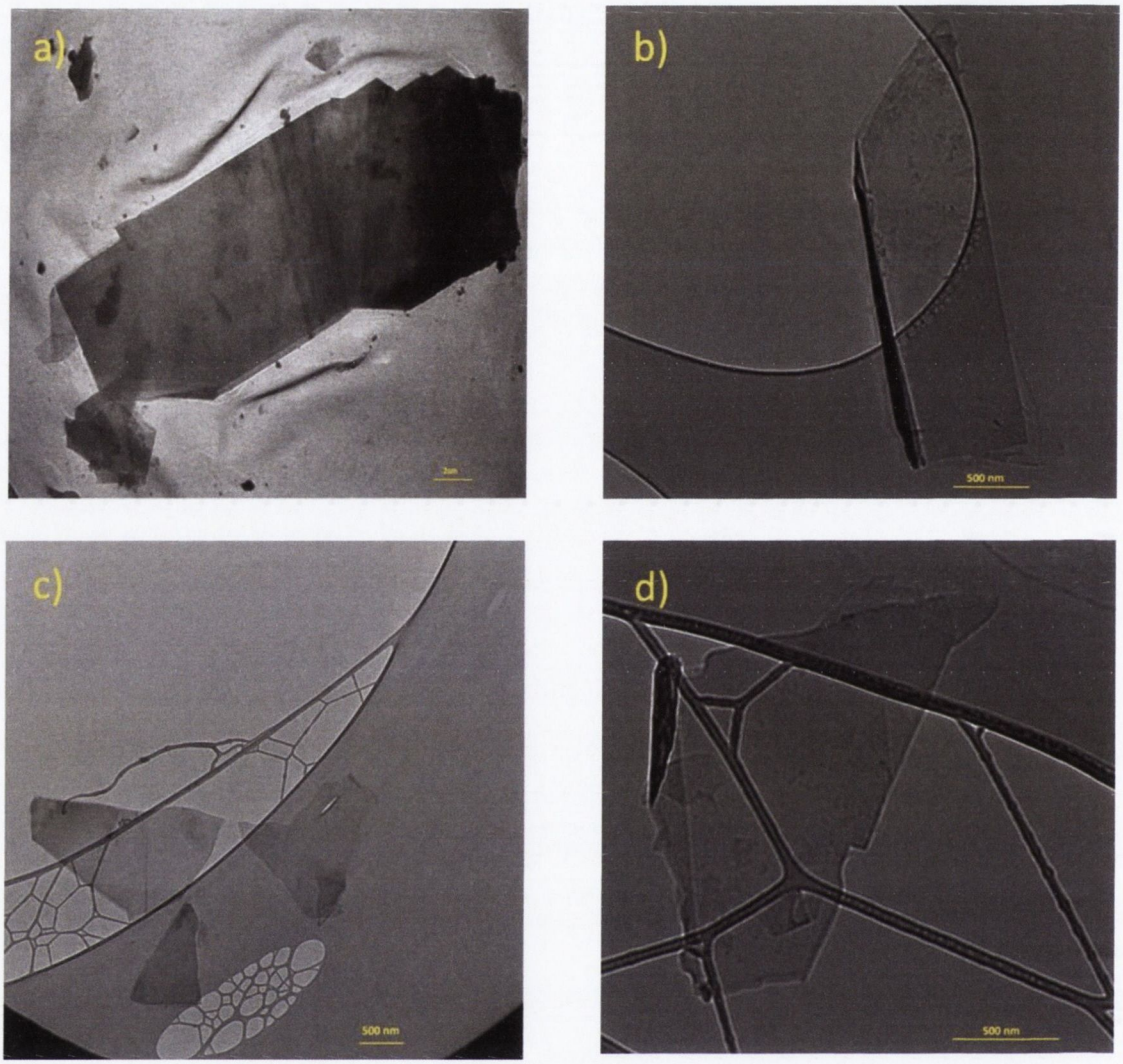

Figure 3.2 Transmission electron microscope images of a) graphite and b-d) graphene exfoliated in chloroform at a concentration of 1 mg ml^{-1}.

3.3 Electrochemical analysis of graphene ionic liquid electrolytes

In order to gain an insight into the effect of graphene on the redox activity of the ionic liquid we carried out cyclic voltammetry (CV) studies. Figure 3.3 shows the CV curves obtained for the I^-/I_3^- system with and without the presence of varying concentrations of graphene. CV scans were studied over a potential window of -0.4 to 1.18 V vs. a saturated (KCl) calomel reference electrode.

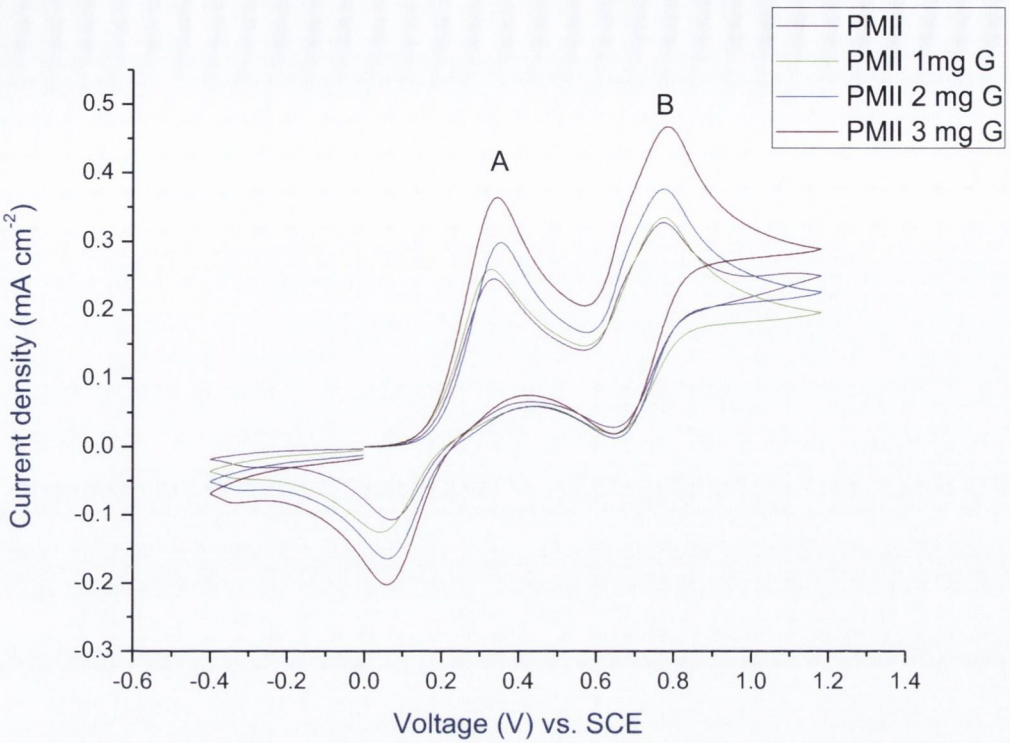

Figure 3.3 Cyclic voltammograms recorded for PMII (black line) and PMII with increasing graphene concentration (green-blue-red). CV curves were obtained at a scan rate of 75 mV s^{-1}. The electrochemical cell consisted of a gold working electrode (3 mm^2) and a Pt wire counter electrode. A saturated calomel (KCl) reference electrode was employed for all scans. The stock electrolyte consisted of a 0.1M tetraethylammonium tetrafluoroborate (supporting electrolyte) and 1.0 mM PMII in acetonitrile. Graphene was added incrementally from 1mg to 3 mg.

The cyclic voltammogram of the I^-/I_3^- redox couple consists of a pair of redox waves, as can be seen below. Redox wave A, which is located from 0.0 – 0.3 V, holds most intrest for studying electron transfer mechanisims in DSSCs, as it corresponds to the oxidation (anodic peak) and reduction (cathodic peak) of I_3^- via the following electron transfer reaction[46,47]

(A) $$I_3^- + 2e^- \longleftrightarrow 3I^-$$

Redox peak B (0.7 – 0.8 V) is attributed to the electron transfer mechanisim below:

(B) $$3I_2 + 2e^- \longleftrightarrow 2I_3^-$$

One proposed mechanism for our observed increase in solar cell efficiency is the development of an extended electron transfer surface which allows for tri-iodiode reduction to occur on graphene sheets which are located in the electrolyte. We believe that the presense of graphene reduces the diffusion length of the species in the viscious ionic liquid and thus results in an increase in solar cell efficiency. The CV results show a clear increase in the current response obtained in the presence of graphene located in the electrolyte. Examination of the first redox wave (A) shows a clear increase in both the oxidation current response and the reduction current response when graphene is added to the system. This would suggest that the graphene is serving as a catalyst for this redox reaction in the liquid phase and allows for an increase in current response. Figure 3.5 below shows the extent of the current response for redox reaction (A) in the presence of increasing graphene concentrations.

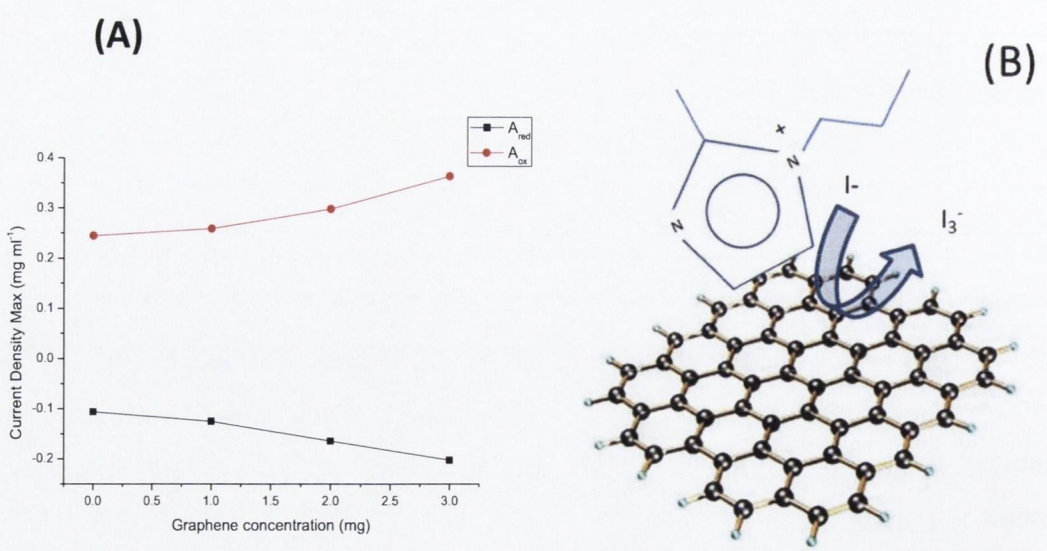

Figure 3.4 (A) Increase in oxidation and reduction current for I_3^- in the presence of liquid exfoliated graphene; (B) Schematic of the proposed mechanism for the extended electron

transfer surface

3.4 Electrolyte preparation and fabrication and testing of DSSCs

Graphene dispersions in $CHCl_3$ were added to PMII at various concentrations ranging from 0.125 wt.% to 3 wt.%. The chloroform was allowed to evaporate from the IL over a period of 4-5 hours under Schlenk conditions. The concentration of graphene added to the IL was monitored using UV-Vis spectroscopy (figure 3.6) where the characteristic featureless graphene absorption spectra followed Beer-Lambert behaviour. The photograph of ionic liquids with varying concentrations of graphene is shown in figure 3.5. The graphene-ionic liquid composite electrolytes were then utilized to fabricate DSSCs. The fabrication mechanism for DSSCs utilising these graphene-IL electrolytes differs slightly than that used for DSSCs employing conventional electrolytes. The presence of graphene in the ionic liquid alters the charge transfer properties of the electrolyte, charge transfer in the electrolyte can be considered as both ionic (the I^-/I_3^- redox couple) and electronic (conductive graphene sheets). When sealing the devices with the surlyn gasket it is important to create a tight seal around the active area of the device. Failure to do so will result in the electrolyte touching both FTO plates and the electronic conductivity of the electrolyte will cause the device to short circuit. Essentially the graphene will act as a wire between both conductive plates.

It is also necessary to ensure that the hole created in the CE for the purpose of electrolyte filling is ~3 times larger than that used in conventional device architectures. If the CE hole is any smaller the force of the vacuum used during electrolyte filling can separate the solid graphitic component from the IL. This causes a non-homogenous dispersion to be drawn into the cell which is composed mainly of IL.

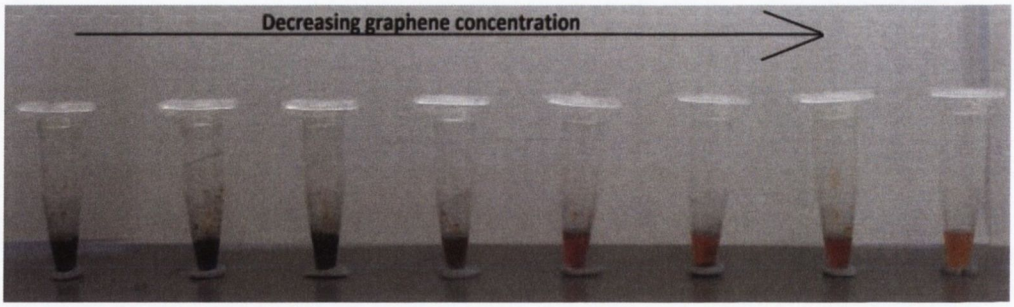

Figure 3.5 Photographic image of graphene ionic liquid electrolytes showing increasing graphene concentration.

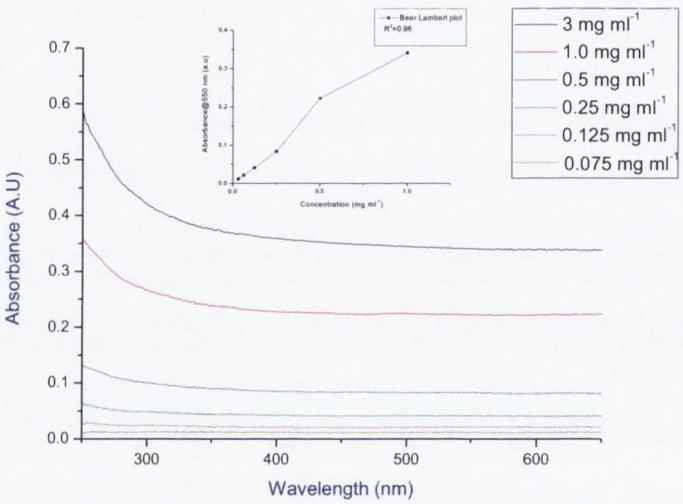

Figure 3.6 UV-Vis spectra recorded for graphene dispersions in $CHCl_3$ at varying concentrations.

3.5 Thermal stability of graphene IL composite electrolytes

The stability of the graphene IL electrolytes was investigated using thermogravametric analysis (TGA). The samples were heated from 25 ^{o}C to 900 ^{o}C at a rate of 10 ^{o}C min^{-1}. TGA and derivative TGA (DTGA) curves are shown in figure 3.7. The DTGA curve of PMII showed 3 distinct peaks at 73 ^{o}C, 324 ^{o}C and 373 ^{o}C. The loss of 2.61 wt. % at 73 ^{o}C

is most likely due to the removal of moisture from the IL, which is hygroscopic in nature and may absorb atmospheric moisture while being placed in the TGA pan. The majority of the mass (92.97 %) was lost at 302 °C, which is in the region for the decomposition of PMII as it has a boiling point between 301-304 °C. The small loss of mass at 373 °C (4.02 wt. %) may be due to residual carbon derived from the decomposition of the IL and the presence of a small concentration of graphene (1 wt. %). This indicates that the electrolyte shows excellent thermal stability when compared to solvent based electrolytes, which show evaporation at temperatures below 100 °C. The lack of mass loss in this low temperature region also shows that the removal of $CHCl_3$ from the electrolyte using Schlenk techniques was successful.

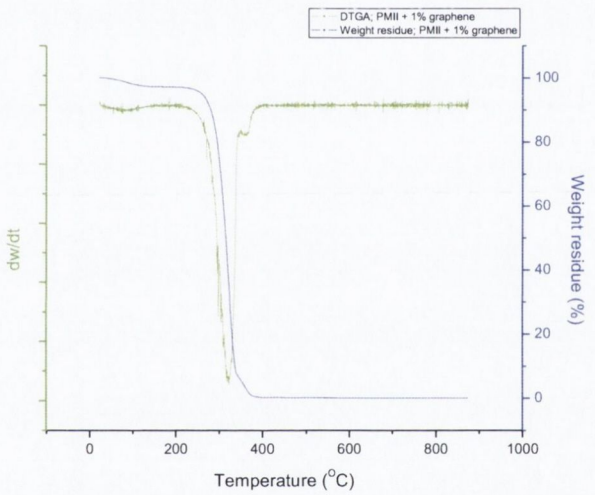

Figure 3.7 TGA and DTGA curves recorded for the graphene IL composite electrolyte at 1 wt. % added graphene

3.6 Photovoltaic testing of graphene IL electrolytes

The prepared graphene ionic liquid composite electrolytes have been tested at a range of graphene concentrations. The presence of graphene in any concentration led to an increase in the efficiency of the DSSC when compared to the results obtained for PMII alone. PMMI showed an efficiency of 0.10 % which agrees well with that found in the literature.

[14] The highest efficiency achieved for the composite electrolytes was 2.60% which was observed when an electrolyte was prepared at a concentration 1.0 wt%. At graphene concentrations greater than 3 wt.% the electrolyte begins to show behaviour similar to that of a quasi-solid based system. It is interesting to note that as the viscosity of these electrolytes increases they can still outperform the unmodified electrolyte. It is was found that at graphene concentrations greater than 1.0 wt% excess amounts of graphene begin to

impede the transfer of ions through the electrolyte and thus a drop in cell efficiency is noted (1.74 % at 3 wt.%). Analysis of the Jsc obtained from these devices shows that upon addition of graphene an increase in the Jsc can be observed, when compared to PMII. The increase in Jsc can be attributed to the increased conductivity of the electrolyte, caused by a decrease in the charge diffusion length of the redox species as a result of the catalytic graphene sheets in the electrolyte. The Jsc for the highest efficiency cell (1.0 wt% graphene added) was found to be 8.58 mA cm^{-2}. The Jsc was observed to fall at graphene concentrations higher than 1 wt% and this can be attributed to the development of quasi-solid based systems at this concentration which impede the transport of ions through the electrolyte layer. The FF of the cells was also increased from 0.30 for the IL without the addition of any graphene to 0.63 for the highest concentration of graphene added (3 wt. %) this indicates that the presence of graphene in the electrolyte is reducing the internal electrical resistance, or shunt resistance (Rsh) of the devices. Figure 3.9 displays the J-V curves showing a peak efficiency of 2.60 % at 1000 W m^{-2}.

These results are rather different from our previous work for ionic liquids with a very high graphene content [18] and here we demonstrate that an increased efficiency can be achieved with much lower graphene concentrations. We believe that this is due to the electrolyte preparation and cell fabrication procedures. In the present work graphene is added to the IL in the liquid phase (dispersed in $CHCl_3$) rather than as a solid additive. In contrast to our previous work, where very viscous gel-like electrolytes (with up to 30 wt.% of graphene) was deposited on one of the electrodes in open air before the cell was sealed,[18] in our current work we use liquid graphene-IL based electrolyte having a maximum 3.0 wt. % of graphene and we used a "closed cell" approach, where the cell was initially sealed and then the electrolyte was introduced into the cell under vacuum and then sealed with surlyn. This approach enabled us to achieve much better efficiencies at low concentration of graphene (up to 2.6 % at 1 wt. % of graphene content).

Graphene conc. (wt%)	Voc (V)	Jsc(mA cm^{-2})	FF	η(%)
0	0.57	0.59	0.31	0.10
0.125	0.52	2.41	0.25	0.31
0.25	0.55	4.11	0.28	0.64
0.50	0.60	3.85	0.44	1.03
1.0	0.61	8.58	0.49	2.60
3.0	0.61	4.47	0.63	1.74

Table 3.1 Photovoltaic parameters obtained for DSSCs using graphene ionic liquid composite electrolytes (Voc - open-circuit voltage; Jsc -short-circuit current density, FF-Fill Factor and η- efficiency

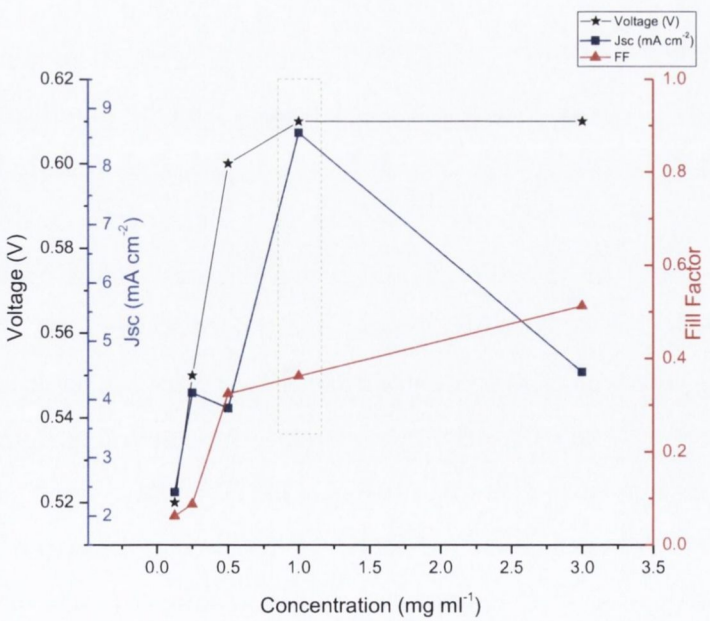

Figure 3.8 Graphical representation of the data contained in table 4.1. The highlighted region corresponds to the best performing electrolyte.

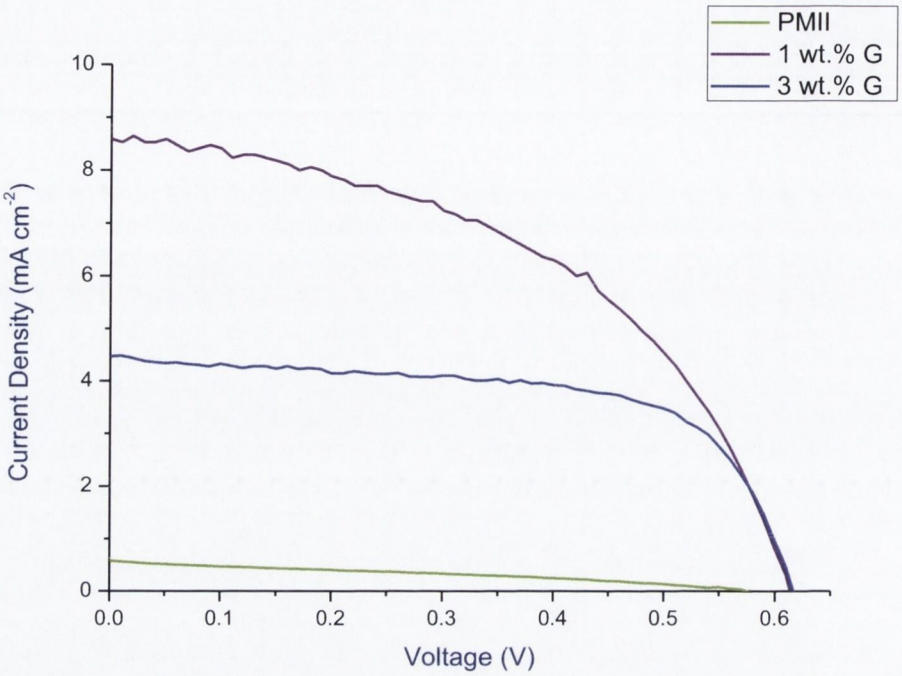

Figure 3.9 J-V curves obtained for PMII and graphene IL composite electrolytes.

3.7 Conclusions

In conclusion, this work has resulted in the development of new electrolytes for DSSCs. These electrolytes were prepared by incorporating small amounts of liquid exfoliated graphene (< 3 wt. %) into the IL 1-propyl-3-methyl imidazolium iodide. We have demonstrated that the addition of 1.0 wt. % of graphene to ionic liquid based electrolytes results in a significant improvement of DSSC efficiency, increasing the power conversion efficiency from 0.18 % to 2.60 %. Crucially, these electrolytes are free from any added iodine, as the only source of iodine in the device is from the IL anion. This feature is expected to greatly increase the stability of these devices as the low levels of iodine present will limit degradation of the sealing materials. The addition of liquid phase graphene to the IL allows for a greater interaction between the IL and the graphene sheets. This increased level of interaction can facilitate a facile π-π network to develop between the graphene and the IL. This enables us to perform the preparation of extremely uniform and stable dispersions of graphene in the IL, upon removal of residual solvent. The resulting composite electrolyte shows thermal stability at elevated temperatures, unlike conventional organic solvent based electrolytes, usually containing acetonitrile and valeronitrile. The

resulting electrolyte can be considered as a composite liquid rather than an IL modified with solidifying agents.

We believe that the addition of graphene nanosheets also allows for an augmented electron pathway through the viscious IL electrolyte, owing primarily to the remarkable electronic properties of graphene It is also expected that the graphene affords an EETM in the electrolyte, which facilitates the electrochemical reduction of I_3^- in the electrolyte and thus lowers the diffusion length of the redox couple through the electrolyte. These results show that the addition of small amounts of graphene offers a viable route towards the preparation of ionic liquid composite electrolytes, which are more advanced than conventional solvent based systems.

References

(1) Wu, J.; Lan, Z.; Lin, J.; Huang, M.; Li, P. *Journal of Power Sources* **2007**, *173*, 585.

(2) Wei, D. *International Journal of Molecular Sciences* **2010**, *11*, 1103.

(3) Armel, V.; Pringle, J. M.; Forsyth, M.; MacFarlane, D. R.; Officer, D. L.; Wagner, P. *Chemical Communications* **2010**, *46*, 3146.

(4) Jhong, H.-R.; Wong, D. S.-H.; Wan, C.-C.; Wang, Y.-Y.; Wei, T.-C. *Electrochemistry Communications* **2009**, *11*, 209.

(5) Wang, P.; Zakeeruddin, S. M.; Exnar, I.; Gratzel, M. *Chemical Communications* **2002**, 2972.

(6) Kawano, R.; Matsui, H.; Matsuyama, C.; Sato, A.; Susan, M. A. B. H.; Tanabe, N.; Watanabe, M. *Journal of Photochemistry and Photobiology A: Chemistry* **2004**, *164*, 87.

(7) Rogers, R. D.; Seddon, K. R. *Science* **2003**, *302*, 792.

(8) Earle Martyn, J.; Seddon Kenneth, R. In *Clean Solvents*; American Chemical Society: 2002; Vol. 819, p 10.

(9) Fukushima, T.; Aida, T. *Chemistry – A European Journal* **2007**, *13*, 5048.

(10) Gorlov, M.; Kloo, L. *Dalton Transactions* **2008**, 2655.

(11) Bai, Y.; Cao, Y. M.; Zhang, J.; Wang, M.; Li, R. Z.; Wang, P.; Zakeeruddin, S. M.; Gratzel, M. *Nature Materials* **2008**, *7*, 626.

(12) Wang, P.; Zakeeruddin, S. M.; Comte, P.; Exnar, I.; Grätzel, M. *Journal of the American Chemical Society* **2003**, *125*, 1166.

(13) Usui, H.; Matsui, H.; Tanabe, N.; Yanagida, S. *Journal of Photochemistry and Photobiology A: Chemistry* **2004**, *164*, 97.

(14) Stathatos, E.; Lianos, P.; Zakeeruddin, S. M.; Liska, P.; Grätzel, M. *Chemistry of Materials* **2003**, *15*, 1825.

(15) Wang, P.; Zakeeruddin, S. M.; Grätzel, M. *Journal of Fluorine Chemistry* **2004**, *125*, 1241.

(16) Wang, P.; Zakeeruddin, S. M.; Moser, J. E.; Nazeeruddin, M. K.; Sekiguchi, T.; Gratzel, M. *Nat Mater* **2003**, *2*, 402.

(17) Bach, U.; Lupo, D.; Comte, P.; Moser, J. E.; Weissortel, F.; Salbeck, J.; Spreitzer, H.; Gratzel, M. *Nature* **1998**, *395*, 583.

(18) Ahmad, I.; Khan, U.; Gun'ko, Y. K. *Journal of Materials Chemistry* **2011**, *21*, 16990.

(19) Fukushima, T.; Kosaka, A.; Ishimura, Y.; Yamamoto, T.; Takigawa, T.; Ishii, N.; Aida, T. *Science* **2003**, *300*, 2072.

(20) Fukushima, T.; Kosaka, A.; Yamamoto, Y.; Aimiya, T.; Notazawa, S.; Takigawa, T.; Inabe, T.; Aida, T. *Small* **2006**, *2*, 554.

(21) Wang, J.; Chu, H.; Li, Y. *ACS Nano* **2008**, *2*, 2540.

(22) O'Connell, M. J.; Bachilo, S. M.; Huffman, C. B.; Moore, V. C.; Strano, M. S.; Haroz, E. H.; Rialon, K. L.; Boul, P. J.; Noon, W. H.; Kittrell, C.; Ma, J.; Hauge, R. H.; Weisman, R. B.; Smalley, R. E. *Science* **2002**, *297*, 593.

(23) Moore, V. C.; Strano, M. S.; Haroz, E. H.; Hauge, R. H.; Smalley, R. E.; Schmidt, J.; Talmon, Y. *Nano Letters* **2003**, *3*, 1379.

(24) Liu, N.; Luo, F.; Wu, H.; Liu, Y.; Zhang, C.; Chen, J. *Advanced Functional Materials* **2008**, *18*, 1518.

(25) Lu, J.; Yang, J.-x.; Wang, J.; Lim, A.; Wang, S.; Loh, K. P. *ACS Nano* **2009**, *3*, 2367.

(26) Katakabe, T.; Kaneko, T.; Watanabe, M.; Fukushima, T.; Aida, T. *Journal of The Electrochemical Society* **2005**, *152*, A1913.

(27) Maleki, N.; Safavi, A.; Tajabadi, F. *Analytical Chemistry* **2006**, *78*, 3820.

(28) Lee, C. P.; Chen, P. Y.; Vittal, R.; Ho, K. C. *Journal of Materials Chemistry*, *20*, 2356.

(29) Lee, C.-P.; Yeh, M.-H.; Vittal, R.; Ho, K.-C. *Journal of Materials Chemistry* **2011**, *21*, 15471.

(30) Ikeda, N.; Miyasaka, T. *Chemistry Letters* **2007**, *36*, 466.

(31) Fukushima, T.; Aida, T. *Chemistry-a European Journal* **2007**, *13*, 5048.

(32) Liu, N.; Luo, F.; Wu, H. X.; Liu, Y. H.; Zhang, C.; Chen, J. *Advanced Functional Materials* **2008**, *18*, 1518.

(33) O'Neill, A.; Khan, U.; Nirmalraj, P. N.; Boland, J.; Coleman, J. N. *The Journal of Physical Chemistry C* **2011**, *115*, 5422.

(34) Tuinstra, F.; Koenig, J. L. *The Journal of Chemical Physics* **1970**, *53*, 1126.

(35) Reich, S.; Thomsen, C. *Philosophical Transactions of the Royal Society of London. Series A: Mathematical, Physical and Engineering Sciences* **2004**, *362*, 2271.

(36) Dresselhaus, M. S.; Dresselhaus, G.; Saito, R.; Jorio, A. *Physics Reports* **2005**, *409*, 47.

(37) Dresselhaus, M. S.; Dresselhaus, G.; Jorio, A.; Souza Filho, A. G.; Saito, R. *Carbon* **2002**, *40*, 2043.

(38) Malard, L. M.; Pimenta, M. A.; Dresselhaus, G.; Dresselhaus, M. S. *Physics Reports* **2009**, *473*, 51.

(39) Kudin, K. N.; Ozbas, B.; Schniepp, H. C.; Prud'homme, R. K.; Aksay, I. A.; Car, R. *Nano Letters* **2007**, *8*, 36.

(40) Ferrari, A. C.; Meyer, J. C.; Scardaci, V.; Casiraghi, C.; Lazzeri, M.; Mauri, F.; Piscanec, S.; Jiang, D.; Novoselov, K. S.; Roth, S.; Geim, A. K. *Physical Review Letters* **2006**, *97*, 187401.

(41) Bethune, D. S.; Meijer, G.; Tang, W. C.; Rosen, H. J. *Chemical Physics Letters* **1990**, *174*, 219.

(42) Bethune, D. S.; Meijer, G.; Tang, W. C.; Rosen, H. J.; Golden, W. G.; Seki, H.; Brown, C. A.; de Vries, M. S. *Chemical Physics Letters* **1991**, *179*, 181.

(43) Khan, U.; O'Neill, A.; Lotya, M.; De, S.; Coleman, J. N. *Small* **2010**, *6*, 864.

(44) Dresselhaus, M. S.; Jorio, A.; Saito, R. *Annual Review of Condensed Matter Physics* **2010**, *1*, 89.

(45) Hernandez, Y.; Nicolosi, V.; Lotya, M.; Blighe, F. M.; Sun, Z.; De, S.; McGovern, I. T.; Holland, B.; Byrne, M.; Gun'Ko, Y. K.; Boland, J. J.; Niraj, P.; Duesberg, G.; Krishnamurthy, S.; Goodhue, R.; Hutchison, J.; Scardaci, V.; Ferrari, A. C.; Coleman, J. N. *Nat Nano* **2008**, *3*, 563.

(46) Rogers, E. I.; Streeter, I.; Aldous, L.; Hardacre, C.; Compton, R. G. *The Journal of Physical Chemistry C* **2008**, *112*, 10976.

(47) Popov, A. I.; Geske, D. H. *Journal of the American Chemical Society* **1958**, *80*, 1340.

Chapter 4

Metal nanoparticle- graphene oxide composites for solar cell applications

4.1 Introduction

The counter electrode (CE) of the DSSC in generally composed of a thin layer of Pt (1-3 nm) deposited onto FTO/ITO conducting glass substrates.[1] The role of the counter electrode is to regenerate the oxidised species in the electrolyte, which in turn regenerates the oxidised dye, anchored to the oxide charge collection layer.[2] The utilisation of Pt as a counter electrode material is due to its ability to reduce the iodide redox couple with relative ease, allowing for fast electron transfer across the electrode.

A large and varied amount of work has focused on the use of SWCNTs,[16] MWCNTs,[17] nanohorns,[18] and metallic composites[19] of these materials as effective catalytic materials for DSSC applications. The advantage of using these materials lies in the fact that they show promising electrical conductivity and an extremely large and tuneable surface area. The varied amount of these nanostructures also allows for the control and use of defect-rich edge plane materials which facilitate the electron kinetics associated with the reduction of I_3^-.[20] Metallic nanotube composites have recently been shown to have extremely promising results for CE applications in DSSCs. Taking advantage of the high surface area of MWCNTs and the catalytic properties of both Pt and MWCNTs has led to the development of MWCNT/Pt composite materials for DSSCs by Ho et al.[21] Pt nanoparticles dispersed on MWCNTs were shown to have enhanced efficiency when compared to thermally evaporated platinum CEs. Unfortunately, the large cost associated with the production and processing of CNTs and MWCNTs will most likely limit their incorporation into consumer devises. Similar high efficiencies have also been observed for composites of graphene and Pt nanoparticles.[22,23]

The recent development in graphene production and the emergent understanding of its remarkable electronic, optical, thermal and mechanical properties has led to incorporation of this monoatomic carbon layer as a CE material for DSSC's.[9,11,24,25] The review by Wang

et al. has discussed recent advances in graphene based materials for DSSCs.[24] Graphene polymer composites,[10,25,26] hybrids of graphene and CNTs[27,28] and graphene metallic composites[22,29,30] have all been shown to display promising catalytic activity for the reduction of the tri-iodide ion in DSSCs and corresponding high efficiencies have been demonstrated.

Clearly there is large scope for employing carbon nanomaterials as CE materials for DSSCs. These materials may open up new approaches for cheaper, flexible, transparent and more robust CEs for DSSCs. This will greatly aid the development of high end roll-to-roll mass production of this technology and use as a viable solar energy source.

Graphene oxide (GO) is a modified form of graphene produced through chemical modification of graphite. The conversion of graphite to graphene oxide results in the functionalistion of the graphene oxide sheet with carboxyl, epoxide and alcohol moieties.[31,32] There are several advantages in using this material when compared to graphene, however there are also some noteable disadvantages which must be considered.

The remarkable properties of graphene are attributed to the delocalised π-π network that arises from orbitals that lie perpendicular to the plane of the graphene sheet.[33] When considering routes towards functionalization it is necessary to disrupt this π-π network in order to introduce functional groups onto the surface of the sheet. It is these functional groups that allow for chemistry to be performed on the 2D support but at the cost of losing some of the remarkable properties usually associated with pristine graphene sheets. When introducing chemical functionality onto pristine graphene the conjugated network must be disrupted. In doing so many of the attributes of graphene are lost. It is possible to reduce graphene oxide back to graphene using harsh reducing agents such as hydrazine,[34,35] however these methods have been shown to introduce a level of nitrogen doping into the lattice and thus the π-π network is never fully restored.[36]

Using GO does afford some advantages which aid processing and further functionalisation of the material. Functionality on the surface allows for GO to be dispersed readily in water and many solvents.[37] The functional groups also allow for GO sheets to be coupled to polymers[38,39] and used as a support material for a wide range of nano-particles.[40,41] Thus, using GO opens up routes to a large variety of new nano carbon composite materials which can't be realised through the use of pristine graphene.

In this work graphene oxide was used as a template for the deposition of platinum and gold nanoparticles. It was found that platinum and gold nanoparticles could be sucsefully deposited, with a small size distribution and in high concentration onto the surface of GO. Multiple techniques were investigated for the deposition of these materials onto FTO glass substrates. The main aim was the formation of a stable and catalyticlly active electrode on FTO glass substrates. Such an electrode could then be tested electrochemically and in DSSCs and potentially offer new routes towards fabrication of low cost solar energy devices.

4.2 Synthesis and characterisation of GO and metal nanoparticle - GO composites

The oxidation of graphite to graphene oxide (GO) via the Hummer's method (see section 2.2.3) causes disruption in the extended π-π network and introduces oxygen containing functional groups onto the surface of the graphite. These oxygen containing functional groups are believed to be composed of hydroxyl, carboxylic acid and epoxide moieties, as proposed by Lerf and Klinowski.[32] The oxidation process can be monitored through FT-IR spectroscopy as these functional groups absorb IR radiation efficiently. Figure 4.1 below shows the FT-IR spectra recorded for both graphite and GO. As can be seen from figure 4.1, the oxidation cause the introduction of carboxyl, hydroxyl and epoxide functionality onto the surface of the material. The broad peak at ~ 3400 cm^{-1} is attributed to O-H stretching vibrations, while stretching vibrations from C=O can be observed at 1600 cm^{-1}. C-OH stretching can be seen at 1060 cm^{-1}, while O-H bending vibrations can also be seen around 1450 cm^{-1}. Stretching of in plane C=C bonds is observed at 1526 cm^{-1}.

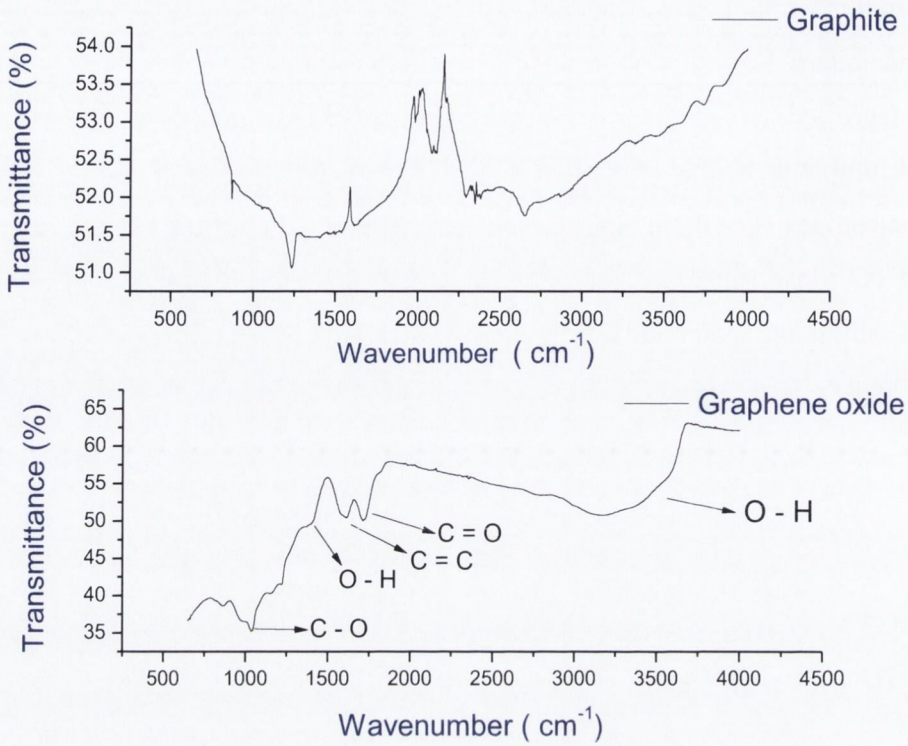

Figure 4.1 FT-IR spectra recorded for both graphite and graphene oxide

The Uv-Vis. spectra (figure 4.2) recorded for graphene oxide was prepared at a concentration of 0.01 $mgml^{-1}$ in water. The UV-vis. spectra contains two bands resulting from electronic transitions within the functional groups in GO. This differs greatly from the featureless spectrum usually seen for graphite. The spectrum contains a maximum at 231 nm which corresponds to π-π^* transitions of aromatic C=C bonds, and a small shoulder located at ~300 nm which can be attributed to n-π^* transitions in C=O bonds.[37]

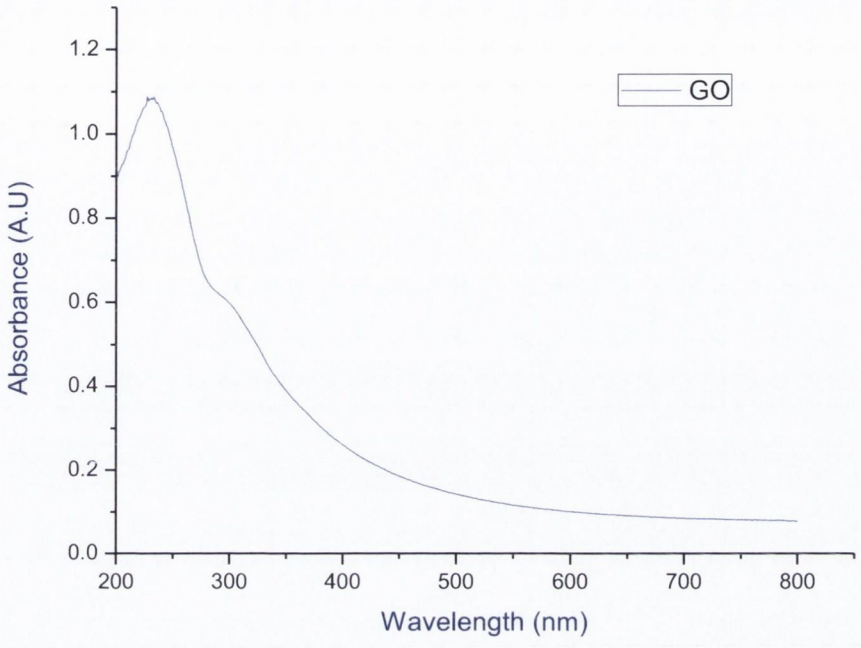

Figure 4.2 UV-vis. spectra recorded for graphene oxide dispersed in H_2O

Raman spectroscopy has also been employed to characterise graphene oxide samples. Figure 4.3) below shows the Raman spectra recorded for graphite and GO. Changes observed in the Raman spectra of GO are due to the disruption of the delocalised π-π network that extends across the graphene oxide layer. Graphitic films were prepared through vacuum assisted filtration of aqueous dispersions of both graphite and graphene oxide onto omnipore 200 μm membranes. The as prepared films were allowed to dry overnight at 70 ^{o}C before spectra were recorded

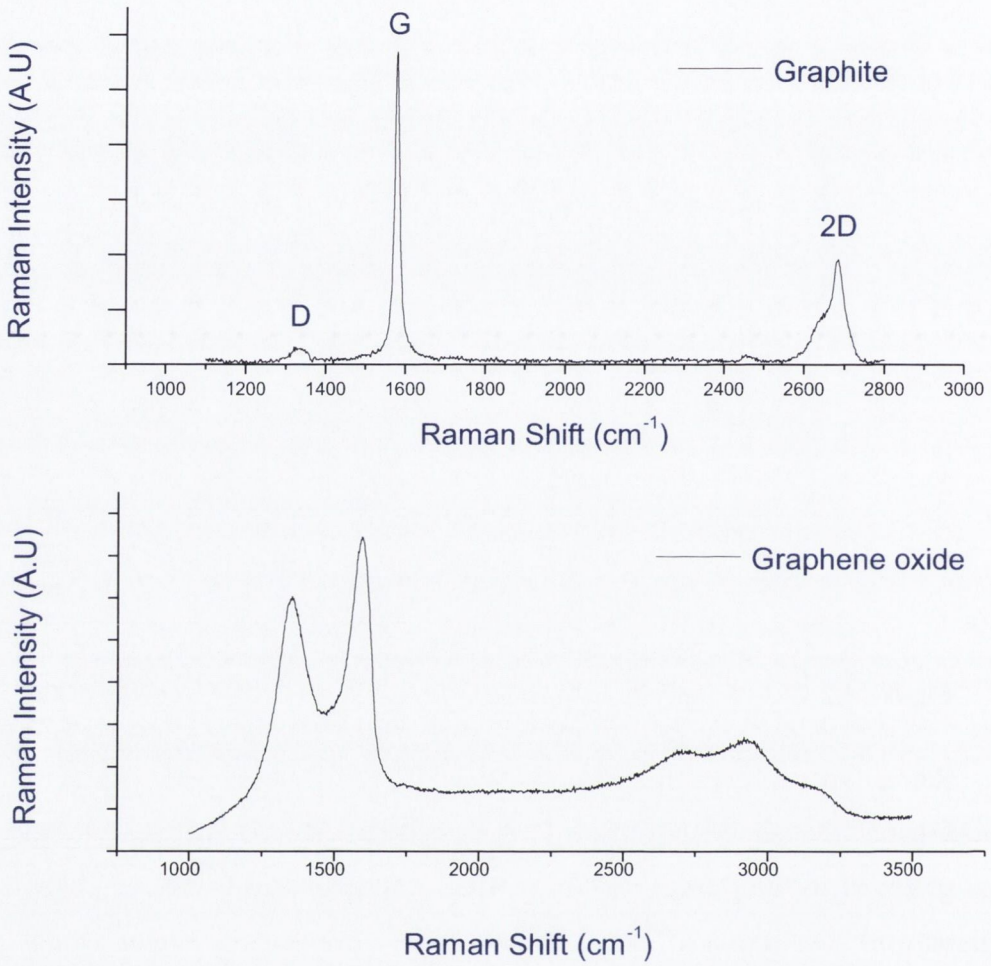

Figure 4.3 Raman spectra recorded for graphite and graphene oxide films

The prominent change in spectral response of GO can be attributed to the extensive breakdown of the delocalised π-π network during the oxidation process. The D band in the Raman spectra of GO is seen to broaden and increase in intensity, thus confirming the increased extent of disorder in the film caused by epoxide, hydroxyl and carboxyl functionality. The G band of GO also broadens and blue shifts by ~10 cm^{-1}. The broadening of the G band can be explained by the increased level of disorder in the film. The shift in G band position can be attributed to the amorphization of graphite. The literature points to some possible explanations of this trend, which include a merging of the G band of GO with that of the 2D band.[42] Another explanation offered is that the isolation of carbon–carbon double bonds in GO causes resonance at a higher frequency. [43]

Raman mapping was also employed for characterising GO. Figure 4.4 and 4.5 shows Raman mapping was recorded for the D band and G band of a single GO flake deposited on a Si/SiO_2 substrate. Raman mapping is a very useful technique for generating detailed images which are based upon the Raman spectrum of a sample. Each pixel in the image represents an individual Raman spectrum. The Raman spectra for the maps below were recorded with a 514 nm excitation source, at 100% laser power, with 10 accumulations for each scan and each scan recorded for 10 seconds. The maximum intensities for the D band and G band were extracted from the spectra and used to generate the false colour images shown in figure 4.4 and 4.5.

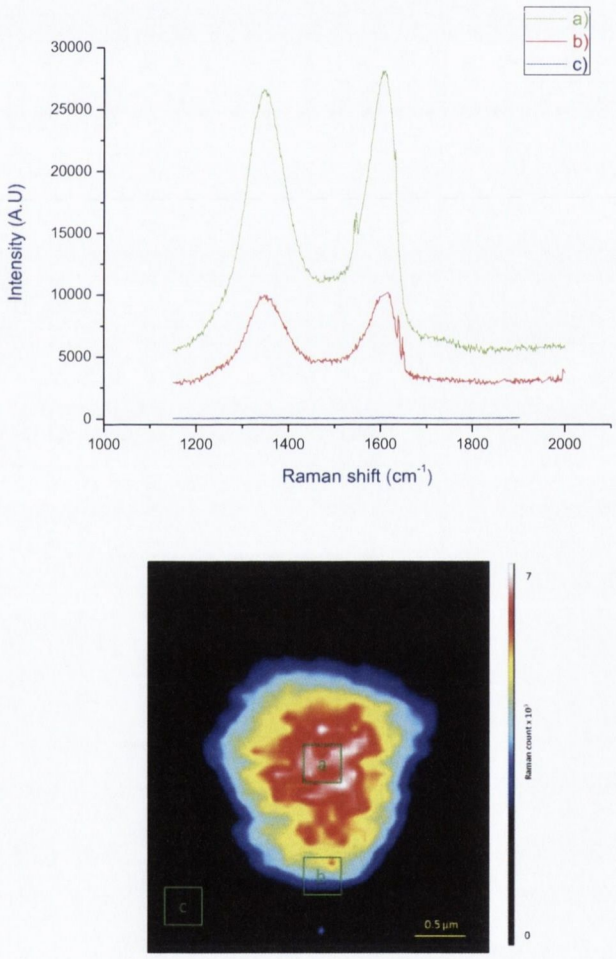

Figure 4.4 Top- Raman spectra recorded for spots a, b and c on the Raman map. Bottom- Raman mapping of GO, G band intensity.

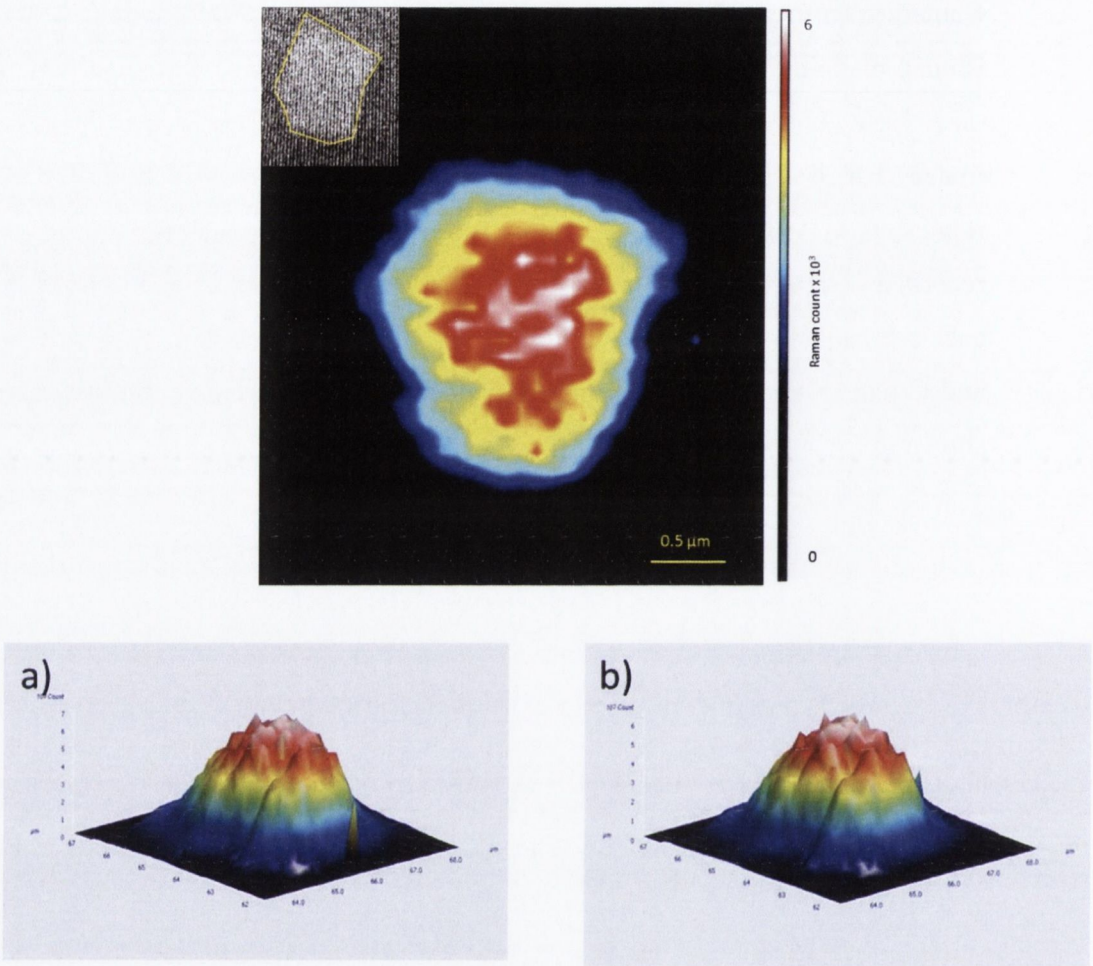

Figure 4.5 Top- Raman mapping of GO D band intensity, the inset shows a filtered optical image of the GO flake deposited on a Si/SiO_2 wafer. Bottom – 3D plots of G and D band intensity

As can be seen for the Raman mapping experiments the greatest Raman intensity is located within the centre of the GO flake. The Raman intensity is observed gradually decreasing towards the flake edges. This indicates that the centre of the flake contains a greater concentration of carbon-carbon double bonds, as these bonds are known to have high Raman intensities.[44] The mapping experiments would also suggest that the flake edges contain high defect concentrations, caused by the oxidations process, which is represented by the decrease in Raman intensity observed in this region of the GO flake.

Figure 4.6) below shows the Raman spectra recorded for the D band and G band for all of the materials under investigation (GO, rGO, PtrGO and AurGO) The materials were

prepared via s borohydride reduction of GO in the presence of gold and platinum salts, as described in section 2.5.2 and 2.5.3. The rGO was prepared through a reduction with $NaBH_4$, without the presence of any metal salt. A highlight of the Raman G band for the materials is shown in figure 4.7) and the corresponding G band positions are represented in Table 5.1). It can be observed from Table 5.1) that the G band position for graphite and GO shifts significantly to the red upon oxidation (1578 .80 cm^{-1} to 1583.88cm^{-1}) (an explanation for this trend is given above). Upon reduction of GO with $NaBH_4$ the G band position shits back to the position of graphite (1578.25 cm^{-1}) indicating an increased level of graphitisation in the material. This shift is also observed for AurGO and PtrGO, but not to the same extent. This is most likely due to $NaBH_4$ acting as a co-reducing agent for both the metal salts and the GO simultaneously. Hence, a less significant blue shift is observed.

The ration of I_D/I_G (D band intensity/G band intensity) is often used as a gauge for measuring the extent of disorder caused by defects in carbon nanomaterials. Generally it is assumed that a higher I_D/I_G indicates greater level of disorder in these materials however some results in the literature do not support this argument. The prominent increase in the D band intensity is related to a reduction in size of the in-plane sp^2 domains. The reduction of GO to rGO does not significantly alter the I_D/I_G ratio (0.971 and 0.976 respectively). After deposition of the metallic nanoparticles I_D/I_G increases slightly to 1.002 for AurGO and 1.040 for PtrGO. The increase in the I_D/I_G ration has been linked to the creation of new graphitic domains, which are smaller in size than that present in GO but more numerous in number.

The 2D band in the Raman spectrum of graphene oxide is seen to broaden and decrease in intensity, as seen in figure 4.8). This is a result of the increase presence of defects in the material. The return of the 2D band after the reduction with $NaBH_4$ indicates that it can successfully partially restore the sp^2 nature of the lattice.[35,38]

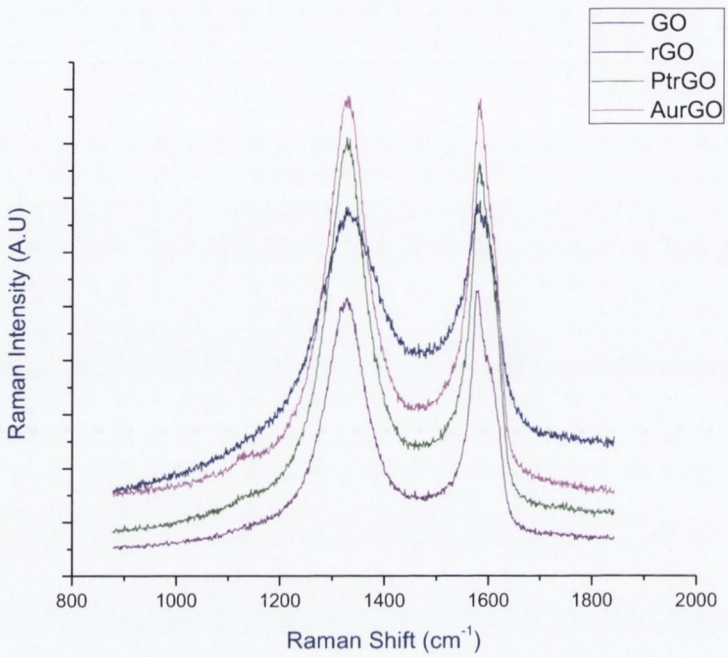

Figure 4.6 Raman spectra of D and G band for GO, rGO, AurGO and PtrGO

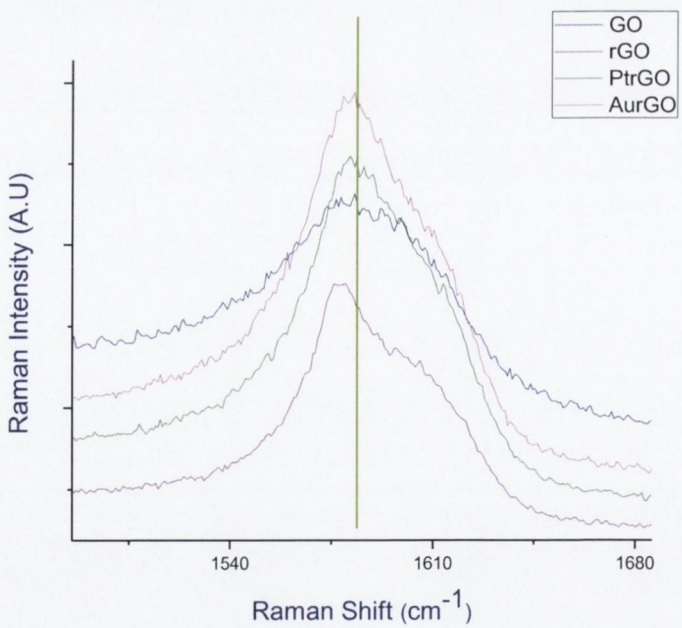

Figure 4.7 Highlight of Raman G band from figure 4.6

Material	G band (cm^{-1})
Graphite	1578.80
rGO	1578.25
AurGO	1581.45
PtrGO	1581.46
GO	1583.86

Table 4.1 Shift in position of Raman G band for graphite, rGO, AurGO, PtrGO and GO

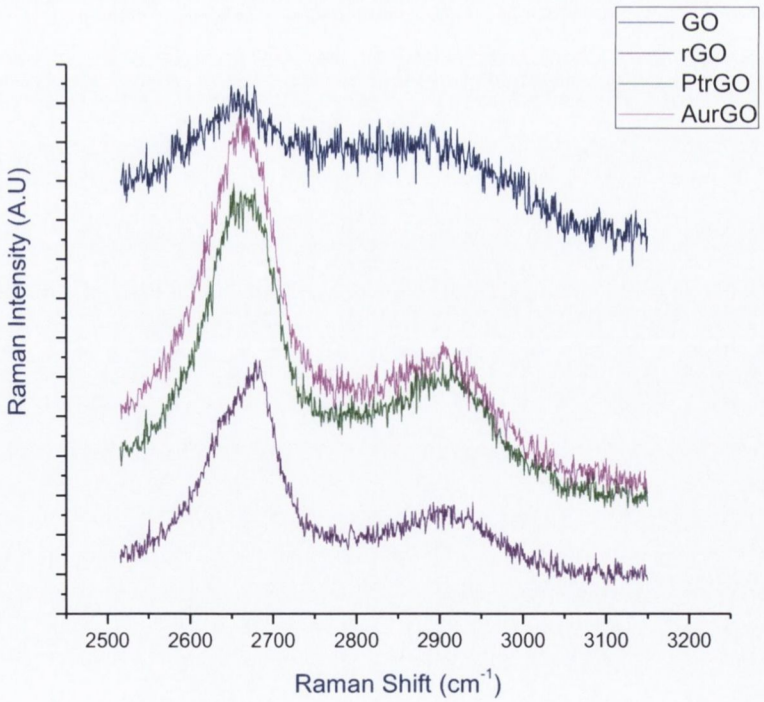

Figure 4.8 Raman spectra of 2D band of GO, rGO, AurGO and PtrGO

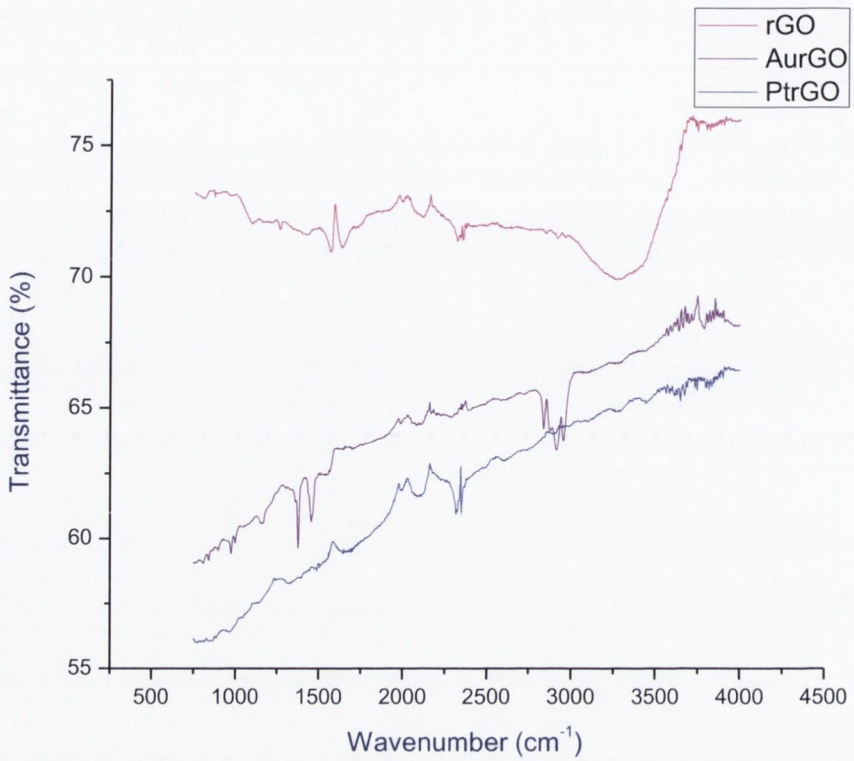

Figure 4.9 FT-IR spectra recorded for rGO, AurGO and PtrGO

FT-IR spectra ware recorded for AurGO PtrGO and also rGO. These spectra can be compared to those presented in figure 4.1. The reduction of GO to rGO with $NaBH_4$ seems to be an effective method or removing some of the functionality introduced during the oxidation process. It can be seen the vibrations associated with carboxyl and epoxide functionality is largely removed from the material. OH functionality can still be observed at ~ 3400 cm^{-1} which suggests that the reduction with $NaBH_4$ is not successful at removing these functional groups. This OH vibration is removed from the material after the deposition of both Au and Pt NPs, suggesting that the NPs are located on defect sites where there is prominent areas of hydroxyl functionality.

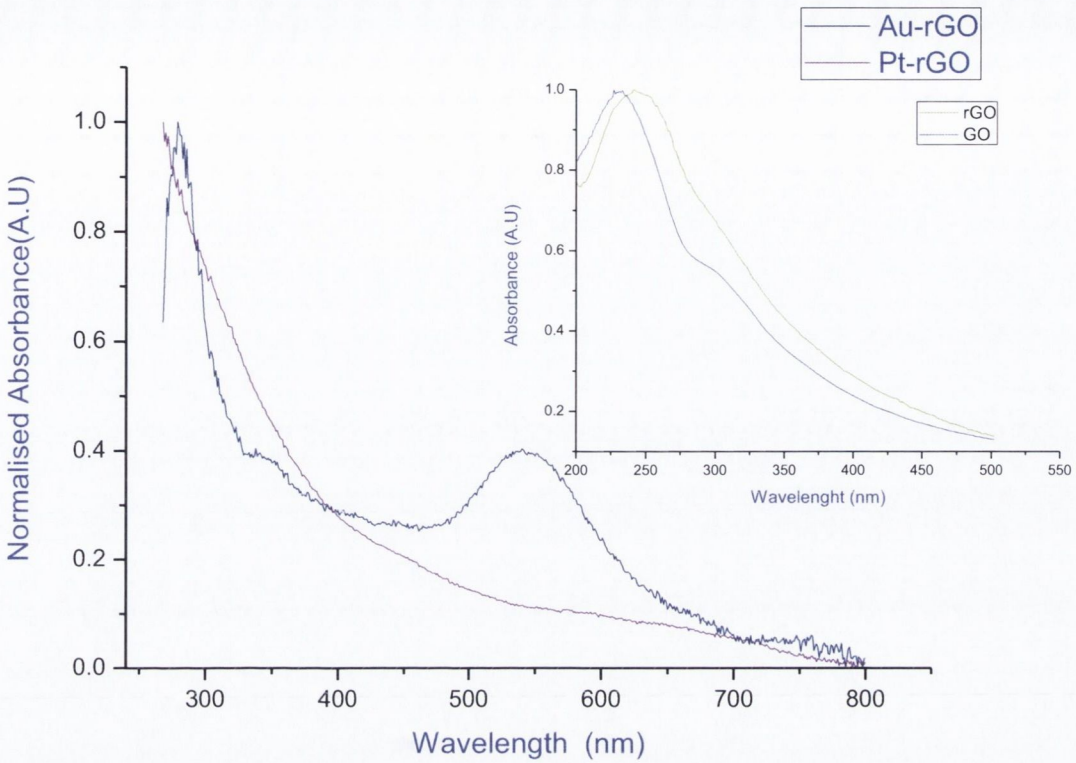

Figure 4.10 UV-vis spectra recorded for AurGO and PtrGO. The inset compares the absorption features of GO and rGO.

The reduction of GO with $NaBH_4$ is known to effectively restore the aromaticity of the lattice and significantly increase the conductivity of the material. This process can be observed by monitoring the shift in the peak absorption band of GO.[45] As aromaticity is restored, the peak absorption band is shifts to the red and the band located at ~ 300 nm, which is associated with C=O bonds, is removed from the spectrum. The inset in figure 4.10 above compares the absorption characteristics of GO and rGO, which was prepared via reduction with $NaBH_4$. The peak absorption band for rGO is observed to shift from 230 nm to 241 nm and the band at 300 nm is no longer present. This indicates that the hydride reduction allows for the removal of functional groups and increases the in plane aromaticity of the material. This observation is in agreement with results obtained through FT-IR.

The spectral features observed in the UV-vis spectra recorded for both AurGO and PtrGO showed the characteristic absorbance associated with these metallic nanoparticles. A large

plasmon band was observed at 540 nm for the AurGO composite. This band is indicative of the plasmon resonance of the Au NPs anchored onto the surface of the GO sheet. The absorption band at ~300 nm is due to the GO absorption. This band is shifted significantly to the red when compared to the unmodified GO. This shift in GO absorbance is known to be associated with the restoration of the π-π lattice of the GO. This is likely due to the reduction with $NaBH_4$, which is known to offer significant reduction of GO.

The spectrum of the PtrGO composite is dominated by the absorbance of the Pt NPs into the UV region of the spectrum. The strong Pt absorption in the UV is seen to dominate the absorption of the GO in this region and masks the spectral features associated with GO.

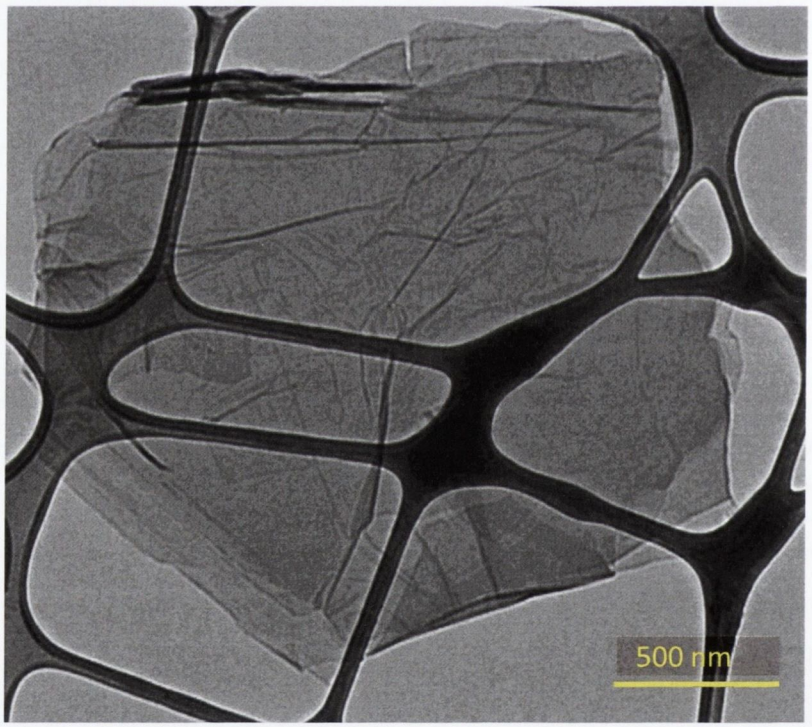

Figure 4.11 TEM images of graphene oxide

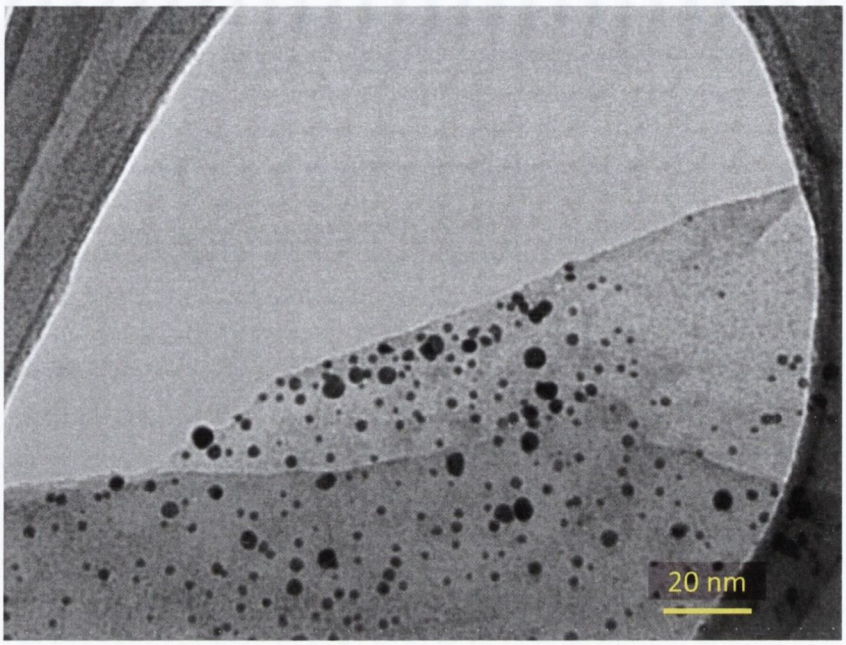

Figure 4.12 TEM images of Au NPs on reduced graphene oxide

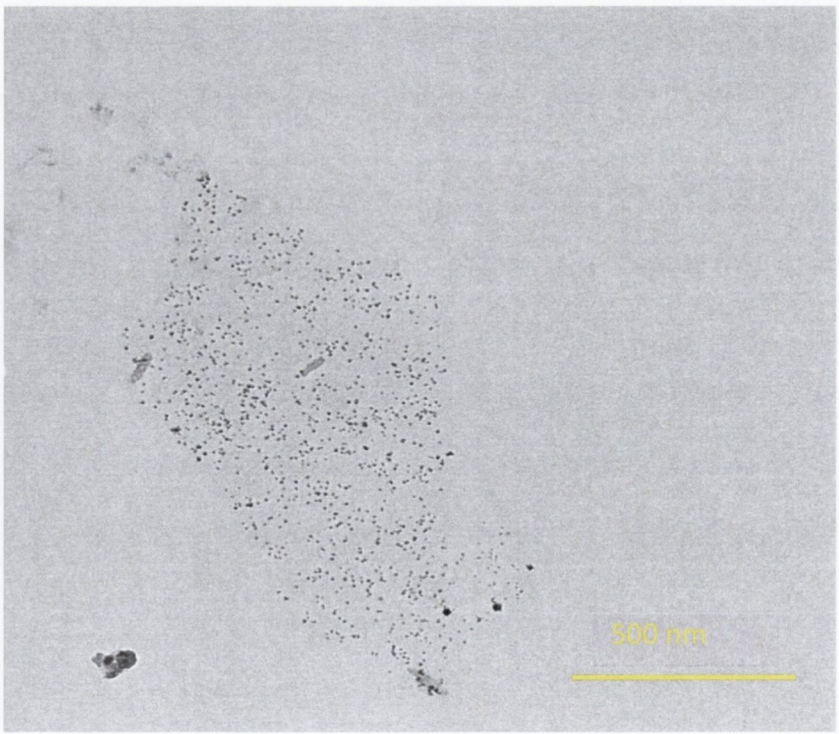

Figure 4.13 TEM image of Pt NPs on reduced graphene oxide

TEM imaging provides comprehensive evidence for the successful synthesis of GO coated with Pt and Au nanoparticles. Samples for TEM analysis were prepared from an aqueous dispersion of Pt and Au functionalised GO, drop-cast onto lacy carbon grids. TEM analysis showed a large concentration of monolayer GO flakes coated with a high concentration of uniformly distributed platinum and gold nanoparticles. Flake sizes ranged from 200nm to large GO domains, several microns in size. The TEM images above (figure 4.11) show GO, monolayer GO coated with Au NPs, (figure 4.12). Figure 4.13 shows Pt NP deposition onto GO.

The TEM images also show that pre mentioned synthesis allows for the formation of NPs with uniform deposition on the surface of the GO sheet and produces particles with a narrow size distribution between 6-10 nm.

SEM analysis of Pt functionalised GO films was employed to further confirm the succcesful synthesis of the Pt GO nanocomposite material. Samples were prepared for SEM through a vacuum assisted filtration process of an aqueous dispersion of the composite onto a 200 μm omnipore membrane. After drying the sample at 70°C overnight, they were subjected to SEM. A film of non-functionalised GO was also prepared in order to act as a control for the imaging experiment. The images below further confirm the succesful synthesis of the composite and coincide well with those obtained from TEM analysis.

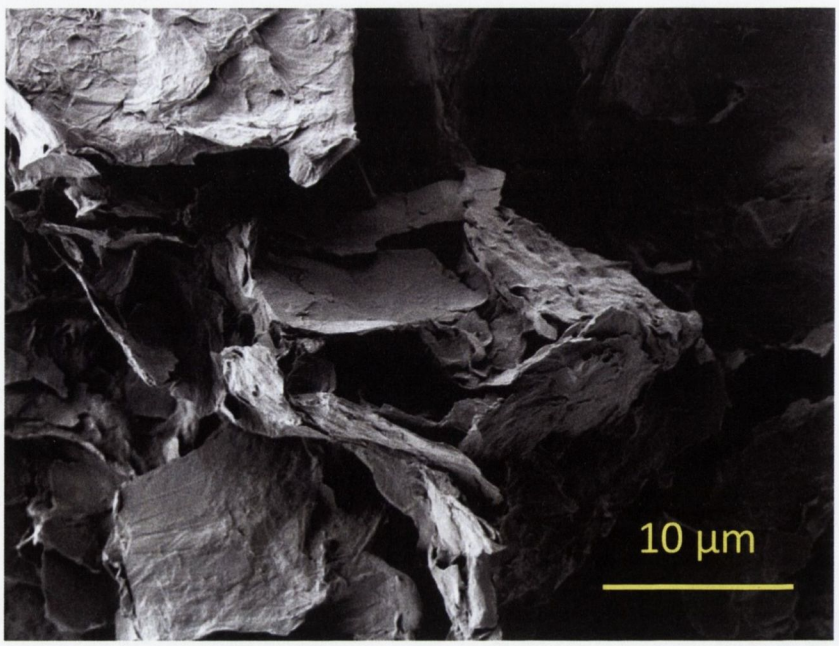

Figure 4.14 SEM image of graphene oxide

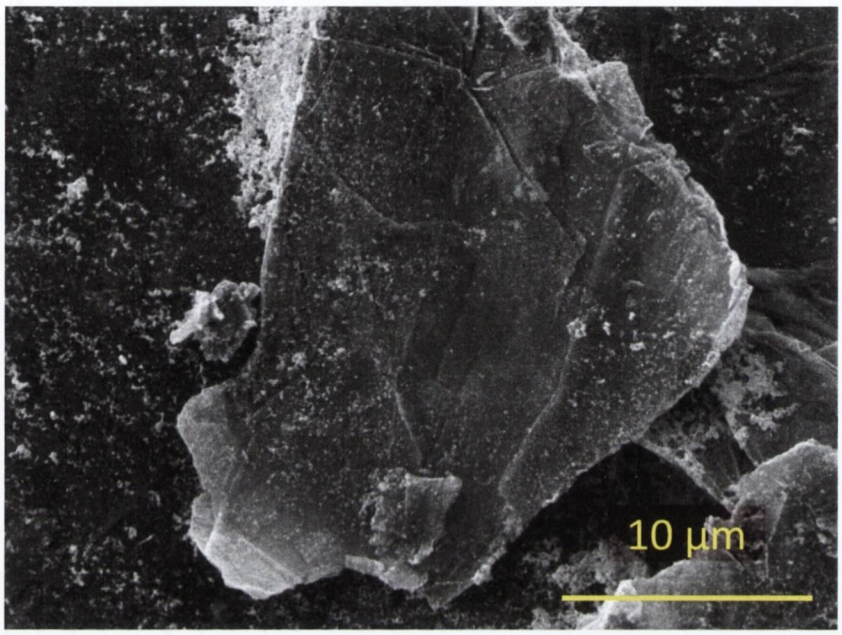

Figure 4.15 SEM image of Au NPs on reduced graphene oxide

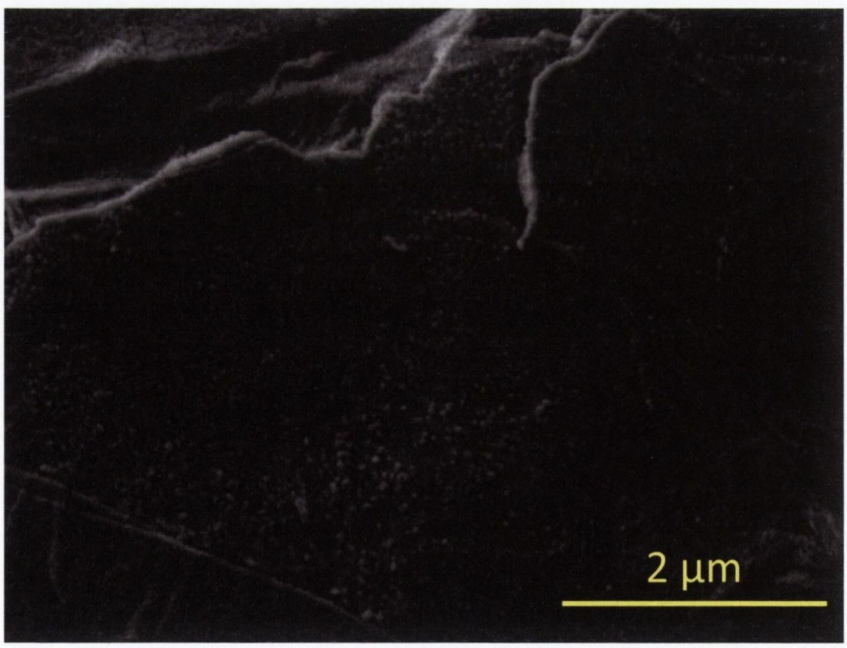

Figure 4.16 SEM image of Pt NPs on reduced graphene oxide

XRD patterns were recorded for GO, rGO, PtrGO and AurGO and are presented in figure 5.14) below. Figure 4.14 a) shows the XRD pattern for GO, which is composed of 2 distinct peaks located at $2\theta = 10.89^{\circ}$ and 26.68°, the first peak is due to the diffraction cause by GO while the second peak is attributed to graphite. This peak most likely arises from areas of un-oxidised regions in the sample. Upon reduction of GO to rGO the peak located at 10.89° disappears completely from the diffraction pattern, thus indicating the reduction of the functional groups on the GO surface (figure 4.14 b). The peak associated with graphite diffraction remains. The co-reduction of GO with metal salts to form AurGO and PtrGO causes diffraction peaks associated with both Au and Pt to appear. Figure 4.14 c) shows the diffraction pattern recorded for PtrGO. Pt peaks at $2\theta = 39.3^{\circ}$, 46.2°, 67.9°, and 81.4° can be assigned to the (111), (200), (220) and (311) crystalline planes of Pt. This indicates that the deposition of Pt onto GO allows for the formation of NPs that are composed of pure crystalline Pt. Figure 4.14 d) shows the diffraction pattern recorded for AurGO. The diffraction peaks are similar to that of pure Au, with peaks at $2\theta = 33.26^{\circ}$, 44.60°, 64.67°, 77.54° and 82.35° assigned to (111), (200), (311) and (222) crystalline planes of gold.

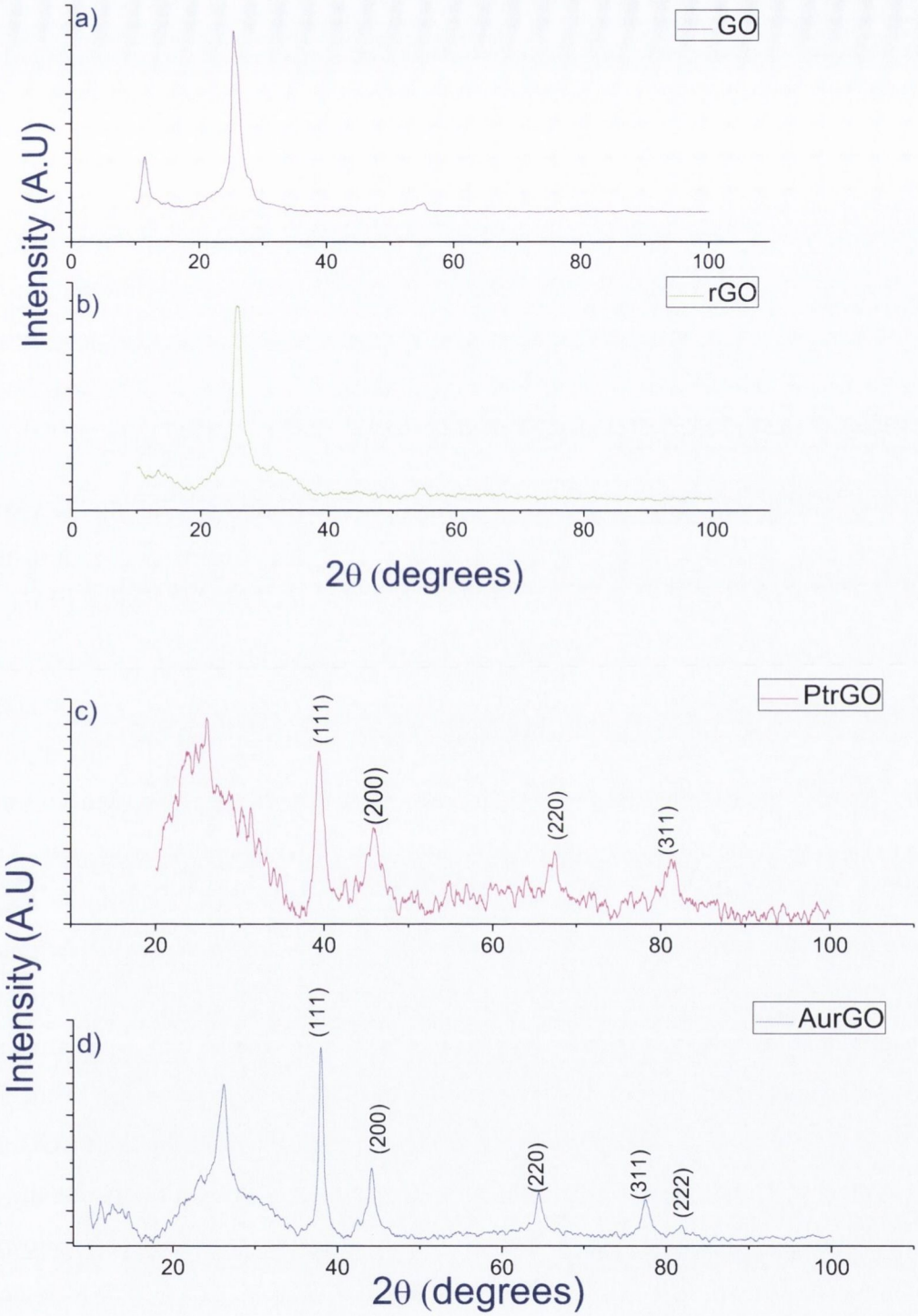

Figure 4.16 XRD pattern recorded for a) GO b) rGO c) PtrGO d) AurGO

4.2 Deposition of GO and metal functionalised GO onto FTO glass substrates

Deposition of GO and metal NP coated GO onto FTO substrates was necessary in order to form electrodes from these materials. This allowed for the materials stability for device applications to be examined, as well as the materials electrochemical activity towards the reduction of the tri-iodide ion to be studied. Multiple deposition routes were examined for the deposition of the materials.

Drop-casting of the material was examined as the first route for the deposition of the materials. The drop-casting method allows for thin films to be formed from materials when suspended in a liquid. Deposition of the solution allows for thin films of the suspended material to be formed on a chosen substrate upon evaporation of the solvent. In order to form films of GO and Au/Pt coated GO upon FTO it was necessary to suspend the material in a solvent with ultra-sonication. H_2O was chosen as the solvent for this approach as GO is readily suspended in H_2O. H_2O did not allow for the Au/Pt coated GO to be easily suspended, even when sonication was employed for extended time periods. This is most likely due to the metal NPs sitting on defect sites on the surface of the GO sheet. These defect sites are known to contain high concentrations of functional groups (COOH,CO,OH), which allow for GO to be suspended in water. In order to suspend the material in water, small amounts of the conducting polymer Poly(3,4-ethylenedioxythiophene) Polystyrene sulfonate (Pedot:PSS) was added to the suspension. Pedot:PSS is a water soluble polymer, and it's interaction with the Au/PtrGO allowed for the material to be suspended into the aqueous layer. This is most likely due the interaction of thiophene units in the Pedot chain with the surface of the metal NPs, allowing for the increased stability of the material in water. Once suspended in water, at a concentration of 1 $mgml^{-1}$, the materials were drop-cast onto FTO coated glass substrates. Once the water had evaporated from the surface of the substrate, the films were heated at 80 ^{o}C for 2 hours.

As a means of decreasing the sheet resistance of the electrodes after deposition, the electrodes were treated to a dipping process in methanol. This allowed for the insulating PSS to be removed from the film and for the conductive Pedot to remain as the conductive

filler.[46] AFM phase imaging (figure 4.17 below) was used to investigate this process. AFM phase imaging is a particularly useful tool for investigating the morphology and constituents of a blended polymer film. Phase imaging is useful here as it can clearly identify the difference between two mixed polymers as opposed to topographical imaging. This is due to the interaction of the AFM tip with regions of changing material properties (i.e. the change in areas of films with more or less of a particular polymer). Figure 4.17) shows the phase images of untreated (a & b) and methanol treated (a & c) films. The images show there is a clear microstructure change in the films upon treatment with methanol. The untreated films (figure 4.17 a) show a greater degree of phase change in the film morphology. This is due to changing areas of PSS and PEDOT rich grains in the films. After treatment the films exhibit a much lower degree of phase contrast in the film (figure 4.17 b). This is due to the removal of PSS from the film (mostly from the surface) and conformational change in the PEDOT chains to a more linear formation thus resulting in a more even PEDOT distribution in the film and a lower degree of phase shift in the AFM tapping oscillation.

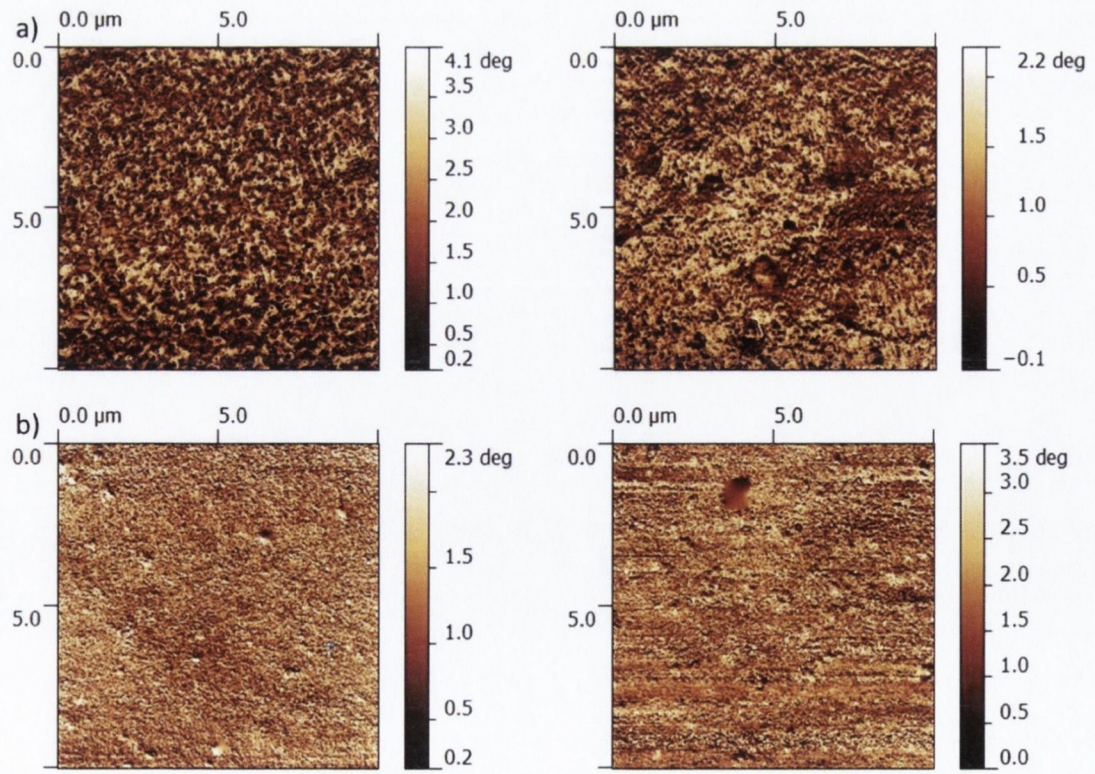

Figure 4.17 AFM phase imaging of A) Pedot:Pss and B) Pedot:Pss after methanol treatment

Unfortunately, this deposition method did not allow for the formation of stable and reproducible films on the FTO substrate. Films frequently peeled off the glass substrates during the drying process and this method was thus deemed unsuitable for further use.

Spray deposition was used as the second method of forming films from these materials. The spray deposition was achieved using a customised spraying setup. The spray setup consisted of an automated mechanical horizontal system and adjustable vertical position with a pneumatic arm that activates and engages the spray gun (figure 5.16). The system (X-Y coordinates, speed of movement and arm activation) were all controlled using the programmable controller. The spray system, such as the height of the spray gun above the substrate, nozzle aperture and air pressure were set up accordingly to optimally produce a uniform thin film over the sprayed area. The steady fine spray jet deposits the material solution onto the heated substrate whereupon the fine droplets spread and rapidly evaporate when in contact with the substrate. The most concentrated part of the spray cone is optimised to the spray pattern programmed into the system so that the trace pattern forms an even coat over the sprayed area. Diluting the stock solution allows for an even coating to be built up over a number of passes on the spray area and also for a greater degree of control over the film thickness deposited as desired. Solutions were prepared in N-methyl pyrolidone (NMP). NMP allowed for GO, AurGO and PtrGO to be readily suspended in the solvent. This is most likely due to the excellent exfoliation ability of NMP towards 2 dimensional materials, in particular graphene.[47]

Figure 4.18 Spray set up of the Janome JR 2300N automatic robot showing; 1: airbrush with compressed air feed attached 2: mechanical robot with pneumatic arm 3: hotplate where substrate is placed 4: programmable controller.

This deposition method allowed for the formation of extremely uniform and stable films upon the FTO substrate. It was also possible to control the film thickness through optimisation of solution concentrations and deposition time. The main drawback of this method is the time taken to produce the films. To produce one batch of 4, 1 cm x 1 cm films took between 4-5 hours and thus was unsuitable for producing large quantities of films for analysis.

The third method of deposition used was electrophoretic deposition (EPD) of the materials from suspensions in NMP. This method proved to be the most successful for producing large quantities of electrodes. The electrode thickness was easily controlled with variation of the deposition time. Figure 4.19 below shows the UV-Vis spectra recorded for GO deposited onto FTO substrates with increasing deposition time. As can be seen, increasing the deposition time increases the quantity of GO deposited into the substrate. The films produced were visually very even and had excellent coverage on the substrate. The film quality was akin to that produced with the spray system but in a time scale of 15 minutes per electrode, compared to over 4 hours for the spray deposition method.

Deposition through EPD was also advantageous as it allowed for GO and metal functionalised GO to be separated under the influence of the electric field. GO migrated and deposited on the positive electrode while AurGO and PtrGO deposited on the negative electrode. Hence, when depositing AurGO and PtrGO, material in solution which was not coated with metal NPs would be deposited on the opposite electrode. This was extremely advantageous as it insured that the electrodes only contained the material of interest and were not a blend of metal functionalised GO and unmodified GO.

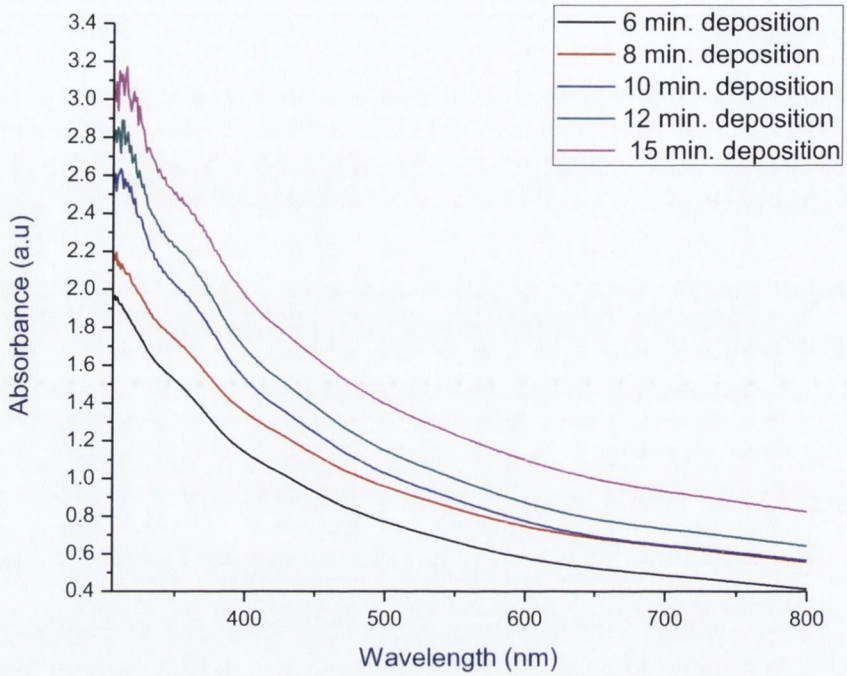

Figure 4.19 UV-Vis spectra of GO deposited on FTO through EPD.

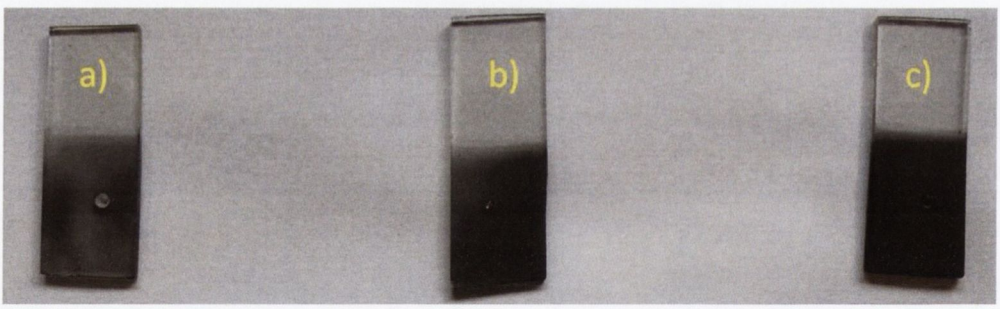

Figure 4.20 Photographic images of PtrGO deposited through EPD a) single depositon b) double deposition c) triple deposition

4.3 Electrochemical analysis of GO and metal functionalisedGO electrodes

The electrochemical activity of PtrGO electrodes towards the reduction of tri-iodide was examined using cyclic voltammetry(CV). PtrGO, AurGO and GO electrodes were fabricated on pre-cleaned FTO glass substrates (13 $\Omega\square^{-1}$) using EPD, as described above. Cyclic voltogramms were recorded between ~ -0.2 to 1.3 V (depending on the material) at varying scan rates. A standard 3 electrode electrochemical cell was employed using an

FTO counter electrode and the fabricated composite electrodes on FTO substrates as the working electrodes. A saturated calomel referance electrode (KCl) was used for all scans. The electrolyte consisted of 0.1 M tetraethylammonium tetrafluoroborate (supporting electrolyte) and 10μM 1-propyl 3-methyl imidazolium iodide (PMII) in acetonitrile. The cyclic voltammogram of the I^-/I_3^- redox couple consists of two redox peaks attributed to the two following reactions occurring at the working electrode surface.[48]

a) $$I_3^- + 2e^- \longleftrightarrow 3I^-$$

b) $$3I_2 + 2e^- \longleftrightarrow 2I_3^-$$

The first redox wave (A), which is located at lower potential, holds most interest for studying electron transfer mechanisms in DSSCs, as it corresponds to the oxidation (anodic peak) and reduction (cathodic peak) of the I_3^- ion.

It can be seen from figure 5.19 a) that the Pt electrode catalyses both reaction A (lower potential) and reaction B (higher potential) registering a high current response in the anodic and cathodic sweep. Analysis of the redox activity of the I^-/I_3^- system was examined on both platinum and PtrGO electrodes. The effect of a double deposition of PtrGO through EPD was also examined, as it was reasoned that increasing the amount of the material on the electrode surface would increase the electrochemical capability.

Through varying the scan rates a change in the position of the anodic and cathodic peak positions was observed for Pt and PtrGO. This indicates the quasi reversible nature of the redox couple. For a reversible couple, no change in peak position would be expected at varying scan rates. Similar redox activity has been observed for this couple on a polished gold electrode and is discussed in chapter 4. Analysis of the peak separation, ΔEp (ΔEp = Ipa-Ipc) through various scan rates, shows an increase in the ΔEp with increasing scan rate value, also evidence for the quasi reversible nature of this reaction.

The CVs recorded for all electrodes are presented in figure 5.19 below. It is clear that both the Pt electrode and both the PtrGO electrodes (single and double deposition) register high

activity towards the reduction and oxidation of the iodide/tri-iodide redox couple. As a control, the catalytic activity of a GO electrode prepared through EPD was also examined (figure 4.21 d). It can clearly be observed that the GO does not support the reduction or oxidation of the redox couple, even when the potential window is expanded considerably. This indicates that the presence of Pt NPs on the surface of GO drastically increases the catalytic ability of the material towards I^-/I_3^- reduction and oxidation. Comparison of the CVs recorded for the Pt and PtrGO electrodes reveals that the Pt electrode displays a sharper response for all oxidation and reduction peaks; this indicates a faster and more facile electron transfer mechanism from the bulk metal film to the active species in the electrolyte. The PtrGO electrodes demonstrate a more sluggish response, as indicated by the broadened oxidation and reduction peaks.

Figure 4.21 e) below shows that the PtrGO, deposited through EPD, can form a stable electrode, which can effectively oxidise and reduce the couple over multiple scanning cycles. The CV presented was recorded over 55 scanning cycles (at 200 mVs^{-1}) and show no observable change in the magnitude or position of the peak oxidation and reduction currents.

Tafel polarization curves of the electrode materials were also obtained (figure 4.12 f). The Tafel analysis can be used to examine the electrochemical activity of the electrode materials towards the I^-/I_3^- couple. The Tafel analysis was carried out by fabricating ''dummy cells'' from the electrode materials. A ''dummy cell'' consists of 2 electrodes, fabricated from the same material, sandwiched together, with an electrolyte in the space between the electrodes. Application of a voltage across the cell, yields a current response, which is related to the catalytic capability of the material under investigation. A plot of thelog of the current density versus the applied potential yields a Tafel curve. The exchange current density (*Jo*) at the electrode-electrolyte interface can be estimated from the slope of the anodic or cathodic branch of the Tafel curve. The larger the slope, the larger the exchange current density at the interface. The actual value of Jo can be obtained from the rate of charge (R_{CT}) transfer at the interface using the following equation:

$$Jo = \frac{RT}{nFR_{CT}} \qquad (1)$$

where R is the gas constant, T is the temperature, F is Faraday's constant and R_{CT} is the charge transfer resistance. Unfortunately R_{CT} is calculated from electrochemical impedance spectroscopy, and we did not have the facilities to carry out such measurements, hence Jo can only be estimated from the Tafel polarization curves. From the Tafel plots it can be seen that the slopes of the anodic and cathodic branches of the polarization curves are in the order: PtrGO > Pt > AurGO > GO > FTO. This indicates that the exchange current density at the PtrGO electrode is higher than that of the Pt electrode. This increase Jo is attributed to the increased surface area of the nano structured PtrGO electrode, afforded by the Pt nanoparticles on the surface of GO. The presence of the Pt nanoparticles allows for the tri-iodide reduction to occur on an increased amount of reaction sites, hence an increase in the exchange current density is observed.

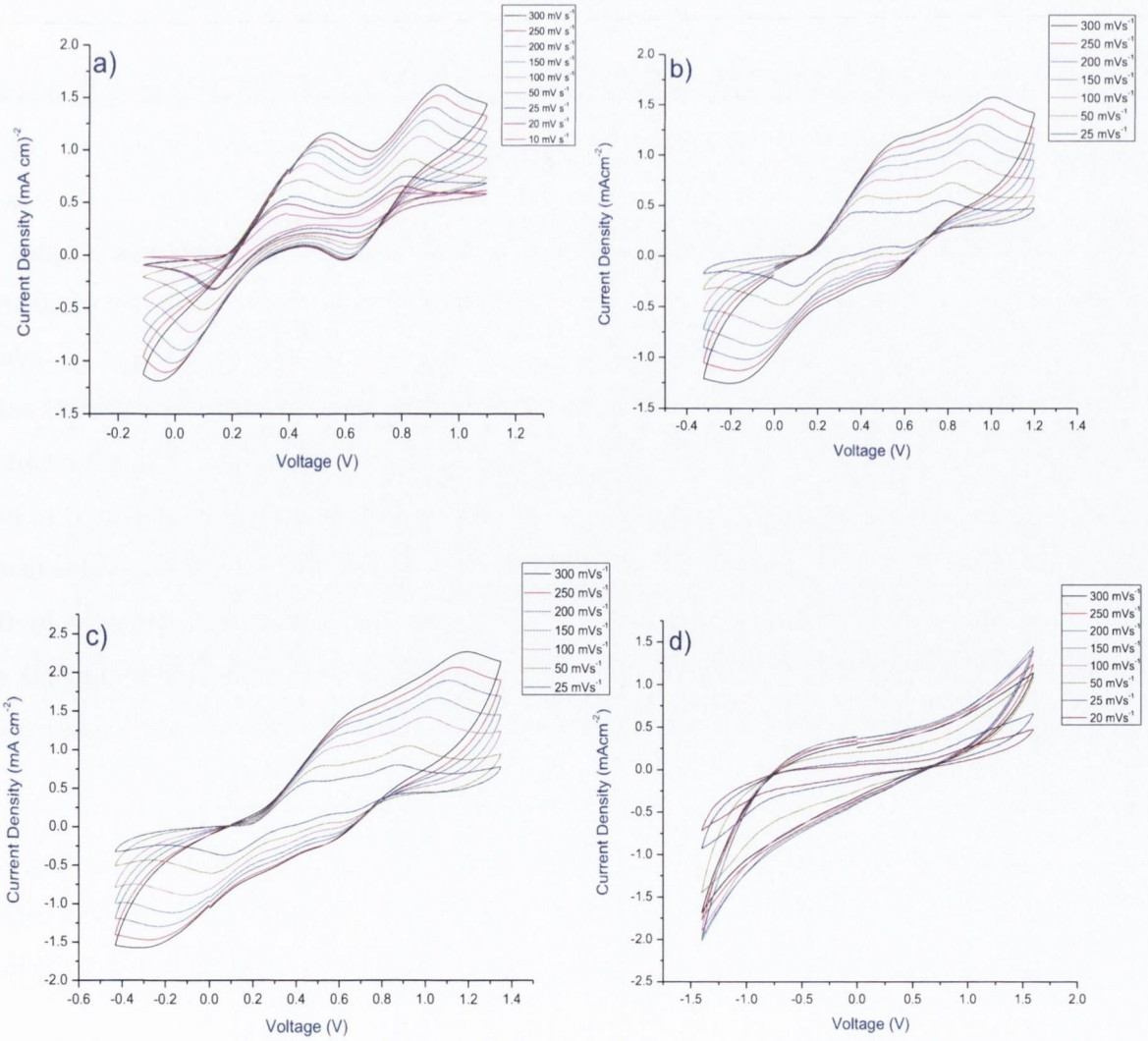

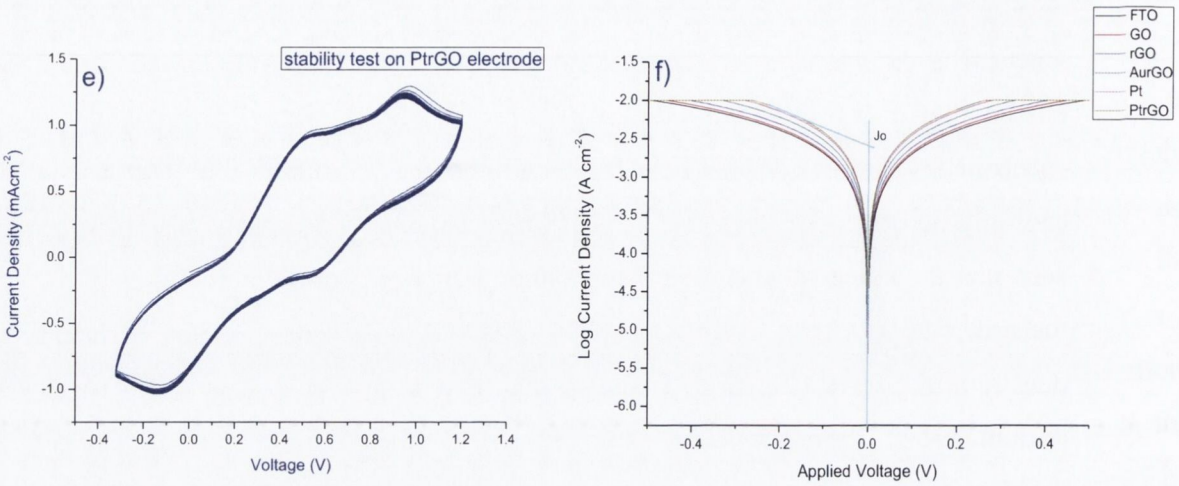

Figure 4.21 a) CV recorded for a) Pt electrode b) single deposition of PtrGO c) double deposition of PtrGO d) single deposition of GO e) stability test on a single deposition PtrGO electrode (200 mVs^{-1} ; 55 scans) f) Tafel polarization curves of counter electrodes in dummy cell configuration using the commercial Dyesol Ltd. EL-100 electrolyte

As a means of directly comparing the catalytic ability of the electrode materials, it is useful to compare the CVs obtained for the electrodes, under identical conditions (i.e. the same scan rate and electrolyte concentration, with careful consideration taken to the electrode area). This allows direst comparisons to be made between the materials. Figure 4.21) below highlights the CVs obtained for Pt and PtrGO electrodes at a scan rate of 200 mV s^{-1}. It can be seen that the Pt electrode registers a high current response for I_3^- reduction ($Imax_{red}$) at a potential of ~ 0 V, against the SCE. The single deposition of PtrGO exhibits a slightly reduced value for $Imax_{red}$, but still shows high catalytic ability towards this reaction. Deposition of a second layer of PtrGO onto the first layer can be used to further increase the catalytic response of the electrode and produce a higher $Imax_{red}$ value than that obtained for the Pt electrode. It is believed that the high surface area afforded by the Pt NPs on the GO creates a larger number of reaction sites, when compared to the bulk metal film and can result in an increased current response for the tri-iodide reduction, at appropriate PtrGO loadings.

A noticeable shift in the $Imax_{red}$ potential can be observed between the Pt and PtrGo electrodes. This shift in peak position (0 V to -0.12 V) would be expected to result in a slight drop in the device Voc, however if the current response for this reduction is

increased (as can be seen for the double deposition) the effect of this shift in peak position may be somewhat limited.

The inset in figure 4.22) shows the CV response recorded for a single deposition GO electrode. As can be seen the electrode shows a negligible response towards I^-/I_3^- oxidation and reduction.

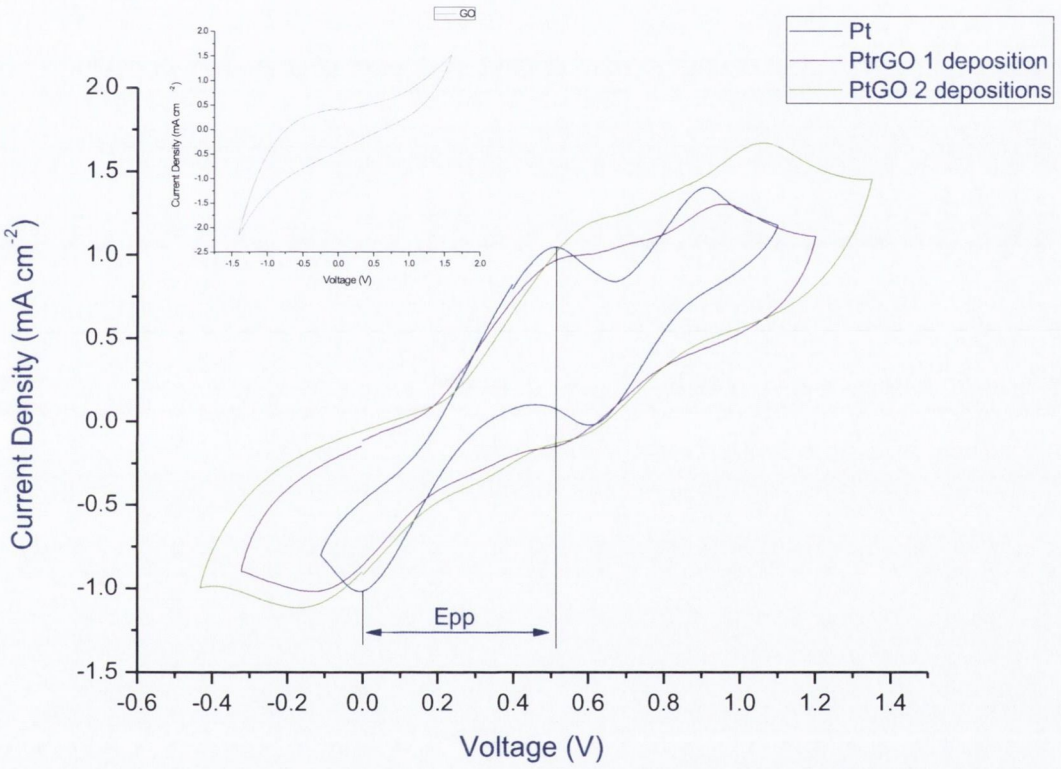

Figure 4.22 Comparative CVs recorded for Pt and PtrGO electrodes at 200 mVs^{-1} vs. SCE

The peak to peak separation potential (Epp) for a redox pair is inversely correlated with the rate constant of a redox reaction. The Epp values recorded for Pt and PtrGO for reaction A are 0.51 V and 0.78 V respectively (at 200 mVs^{-1}). This indicates that the reduction rate constant of the Pt electrode is faster in comparison to the PtrGO electrode.

From analysis of the electrochemical investigations it appears that there are noticeable advantages and disadvantages to employing the PtrGO electrode as a potential CE in DSSCs. The PtrGO electrode can be used to achieve higher a higher current response for

the tri-iodide reduction and this response can be tailored by choosing appropriate material loadings on the electrode, through EPD. The increased current response which can be obtained would be expected to lead to a corresponding increase in the current response for a fully assembled DSSC. The increased current response and also the increased exchange current density (Tafel polarization curves) can be attributed to the large surface area available for reduction and oxidation reactions, due to the presence of Pt nanoparticles. CVs of PtrGO show larger peak separation values and less sharps oxidation and reduction peaks, when compared to Pt. This indicates a more sluggish electron transfer reaction across the interface, the shift of the I_3^- cathodic peak to a more negative potential will also be expected to decrease device Voc.

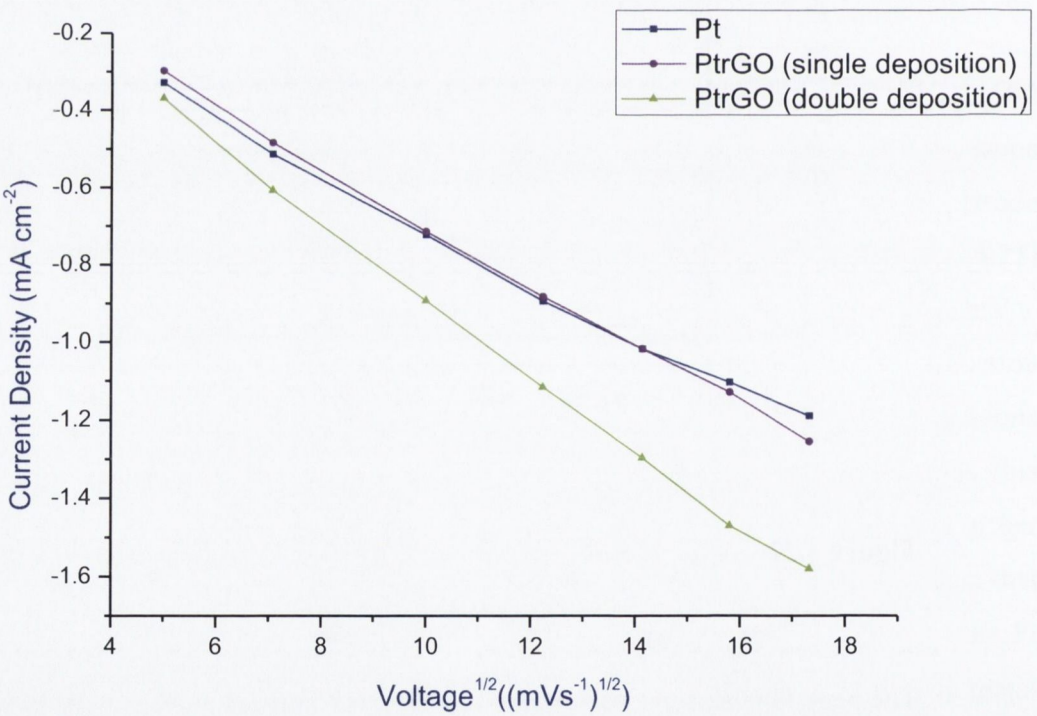

Figure 4.23 Plot of $V^{1/2}$ vs. maximum current response for reaction A, cathodic sweep ($Imax_c$)

The maximum current response for the reduction of I_3^- (reaction A; cathodic sweep)($Imax_{red}$) was monitored and plotted as a function of the square root of the scan rate ($V^{1/2}$) in order to gain an insight into the process occurring at the electrode surface. Figure 4.31 above shows the linear relationship observed between $V^{1/2}$ and $Imax_c$ suggests that the redox reactions occurring on the electrode surface are controlled by ionic diffusion of the redox active species in the electrolyte and may also be related to the migration of the iodide ions out of the porous electrode surface.[49]

4.4 Fabrication and testing of DSSCs

DSSCs were fabricated following the procedure outlined in section 2.2.6. All cells were tested at a light intensity of 100 mW cm^{-2} and with an area of 0.2 cm^2 which was defined by a mask. The results obtained from solar I-V analysis are presented in table 5.2.

CE material	Jsc ($mAcm^{-2}$)	Voc (V)	FF	η (%)
Pt	12.35	0.72	0.45	4
GO	0.007	0.69	0.20	0.09
AurGO (1 deposition)	7.2	0.65	0.25	1.17
AurGO (2 depositions)	7.6	0.66	0.33	1.65
AurGO (3 depositions)	13.2	0.64	0.36	3.04
PtrGO (1 deposition)	8.55	0.70	0.26	1.55
PtrGO (2 depositions)	10.3	0.70	0.26	1.87
PtrGO (3 depositions)	14.05	0.70	0.60	5.90

Table 4.2 Photovoltaic parameters obtained for DSSCs using graphene various CE materials (Voc - open-circuit voltage; Jsc -short-circuit current density, FF- Fill Factor and η- efficiency

As can be seen from the results presented in table 5.2) the standard DSSC utilising a conventional thermally evaporated Pt CE registered an overall efficiency on 4% when illuminated. The effect of using GO as a CE material was also examined and the results proved to be very poor, with an efficiency of 0.09%. The deposition of metallic nanoparticles onto the surface of the GO resulted in the formation of a catlytically active material towards I_3^- reduction. CEs fabricated from AurGO through EPD showed a maximum efficiency of 3.04 %. The same cells fabricated using PtrGO showed a dramatic increase in efficiency when compared to Pt. Using PtrGO as a CE material it was possible to increase DSSC efficiency by 47.5%, from 4 % (Pt) to 5.90 % (PtrGO ; triple deposition). This large increase in efficiency is attributed to the nano-structured nature of the CE, when compared to the metallic Pt film. The results for the PtrGO CEs agree well with the finding from our electrochemical studies. As the number of depositions of PtrGO increases, we observe a large increase in the photocurrent response (from 8.55 mA cm^{-2} to 14.05 mA cm^{-2}). This effect was also observed in CV studies whereby a large increase in cathodic current was observed with increasing deposition number. The shift in the cathodic peak in the CVs to a higher overpotential can also be observed from the results obtained through I-V analysis. The Voc of the Pt CE shows a slightly higher voltage (0.72V) when compared to that obtained for the PtrGO electrode (0.70 V), however this slight drop in voltage seems to be largely negligible when considering the overall efficiency increase (figure 4.24) and the increase in output power (figure 4.25).

DSSCs built using the AurGO electrode showed promising results. As expected the cells did not perform as well as Pt. This is due to the large overpotential for tri-iodide reduction which can be observed in the CVs of this material (-1.5 V vs SCE for tri-iodide reduction). This can also be observed in the power density curves (figure 4.25) for the electrodes. The AurGO electrodes show a maximum power point (Pmax) at 0.31 V, while the Pt electrode and the PtrGO electrode show an increase in the Pmax voltage at 0.45 V and 0.48 V respectively. Once again it was observed that increasing the materials loading on the electrode through multiple EPD cycles proved to be an effective method of increasing the efficiency of the cells built using this CE. Jsc values increased from 7.2 mA cm^{-2} to 13.2 mA cm^{-2} aftter 3 EPD cycles, resulting in an increase in efficiency form 1.17% to 3.04%.

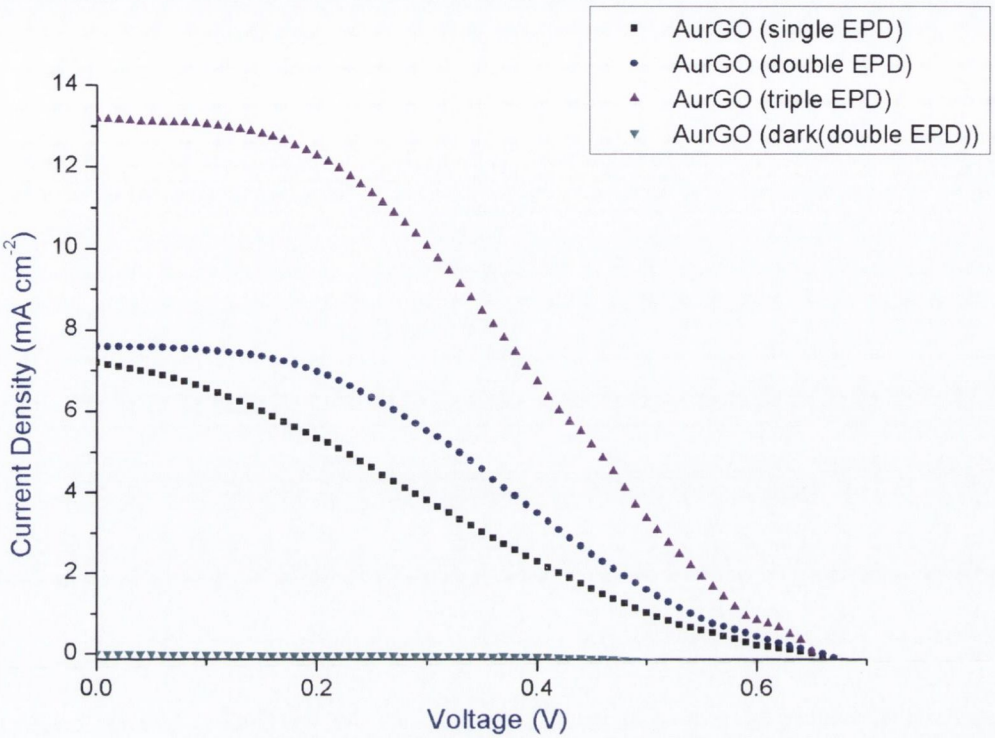

Figure 4.24 J-V curves recorded for DSSCs using AurGO CEs

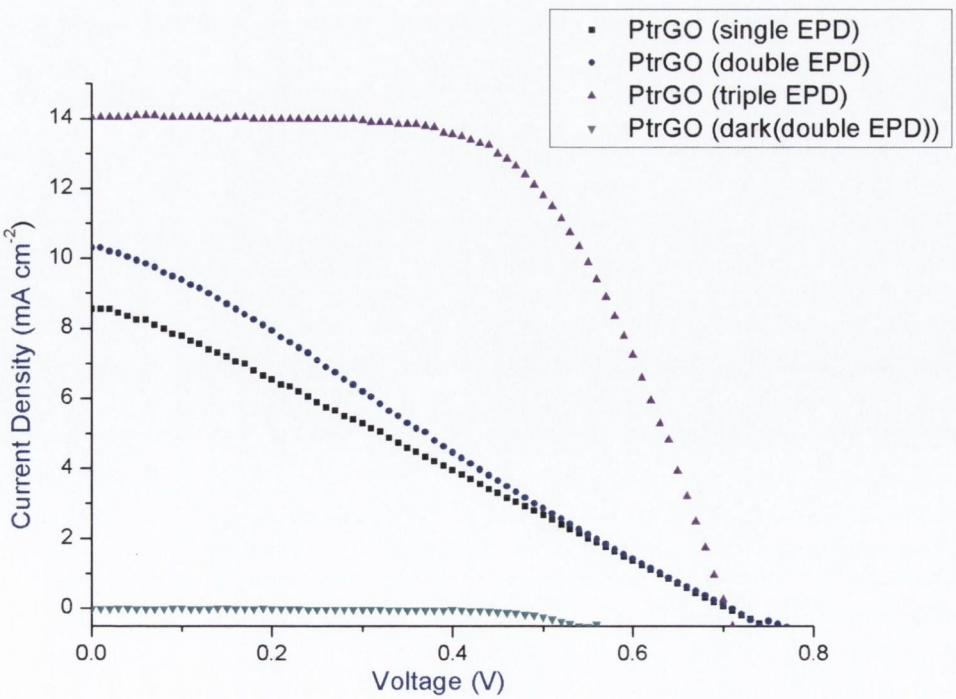

Figure 4.25 J-V curves recorded for DSSCs using PtrGO CEs

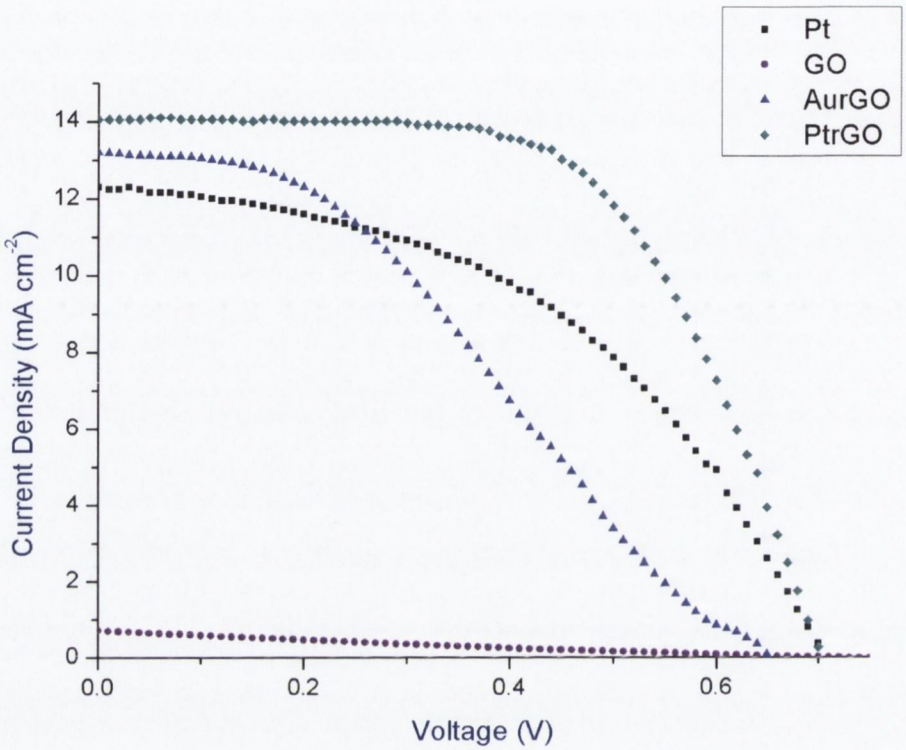

Figure 4.26 J-V curves recorded for DSSCS comparing the various CEs

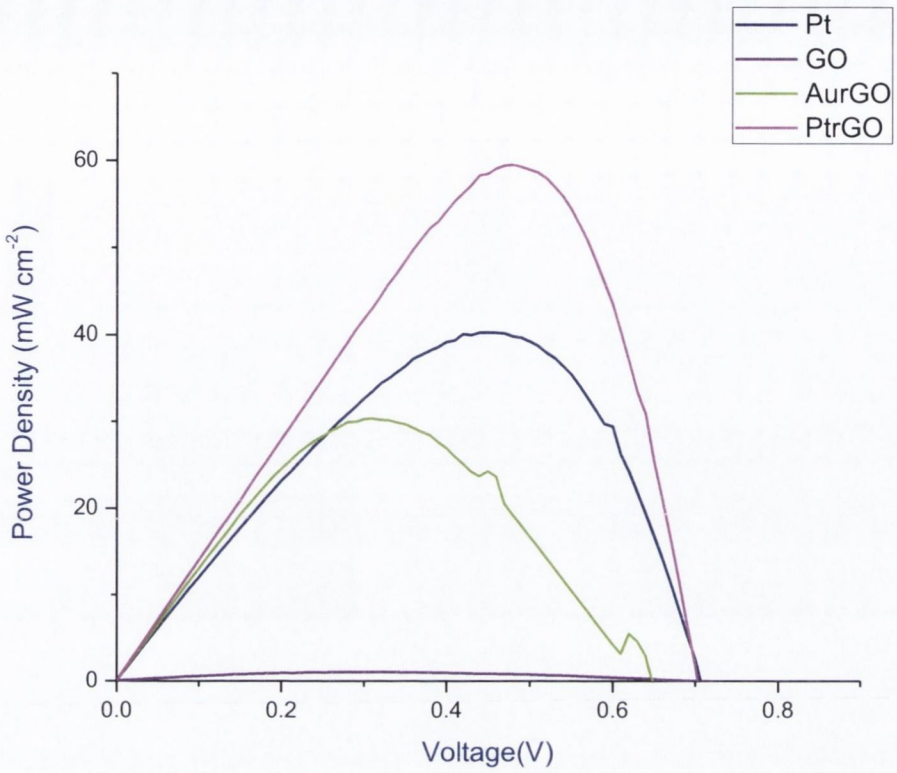

Figure 4.27 Comparison of the power density obtained for the CEs investigated

4.5 Electrophoretic deposition as a route for fabricating GO metal composite electrodes

As an alternative method for fabricating GO metal composites a 2 step electrophorectic deposition process was investigated. Blank FTO electrodes were submerged into solutions of GO in NMP (as was done for CE formation). After removal from the GO suspension the FTO was coated with a layer of GO, approximately 700 nm thick. Following a drying step, the GO coated FTO electrode was then submerged into a solution of Au NPs in $CHCl_3$, at varying concentrations, for the second EPD. The second EPD allowed for Au NPs to migrate into the porous GO film and result in the production of an AuGO composite electrode.

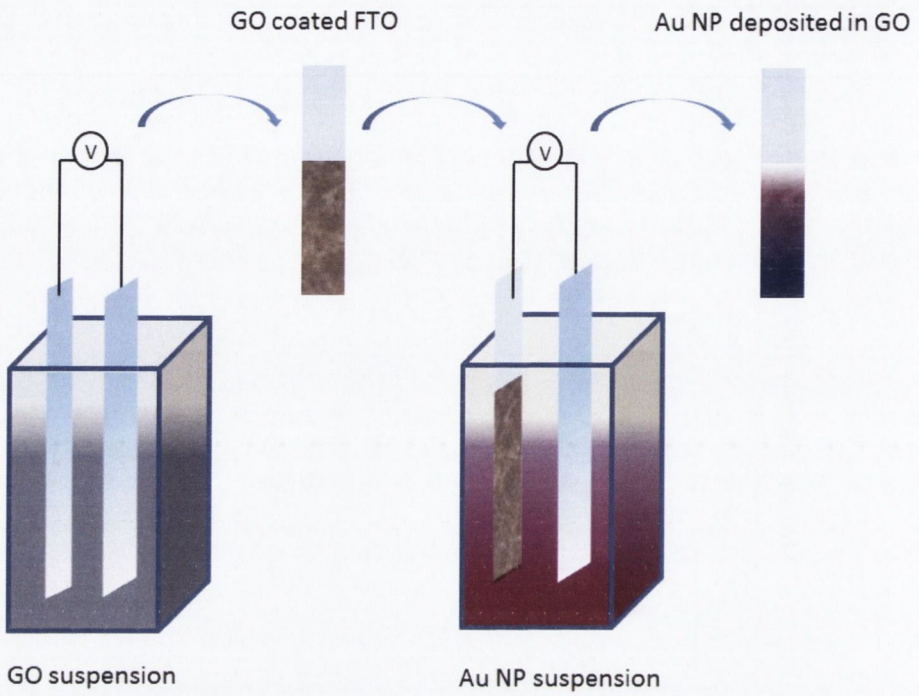

Figure 4.28 Schematic of the EPD process used to create the AuGO composite electrodes

The presence of Au NPs in the GO films was confirmed was UV-Vis spectroscopy, by following the evolution of the plasmon band which is associated with Au NP absorbance. As can be seen from figure 4.29 below. The deposition of Au NPs into the porous GO electrode results in a significant increase in the optical absorbance of the films. The presence of the Au NP plasmon resonance can be observed by examining the Δabsorbance, whereby Δabsorbance = AuGO absorbance - GO absorbance. Figure 4.30) shows the Δabsorbance recorded from 4 separate depositions of Au NPs from varying solution concentrations. The presence of a large plasmon resonance is indicative of Au NPs imbedded into the GO film. Figure 4.30 d) shows the Δabsorbance recorded for a GO electrode soaked in a solution of Au NPs, without the application of an electric field. As can be seen from figure 4.30 a-c) the influence of the electric field is crucial for increasing the NP loading within the GO electrode.

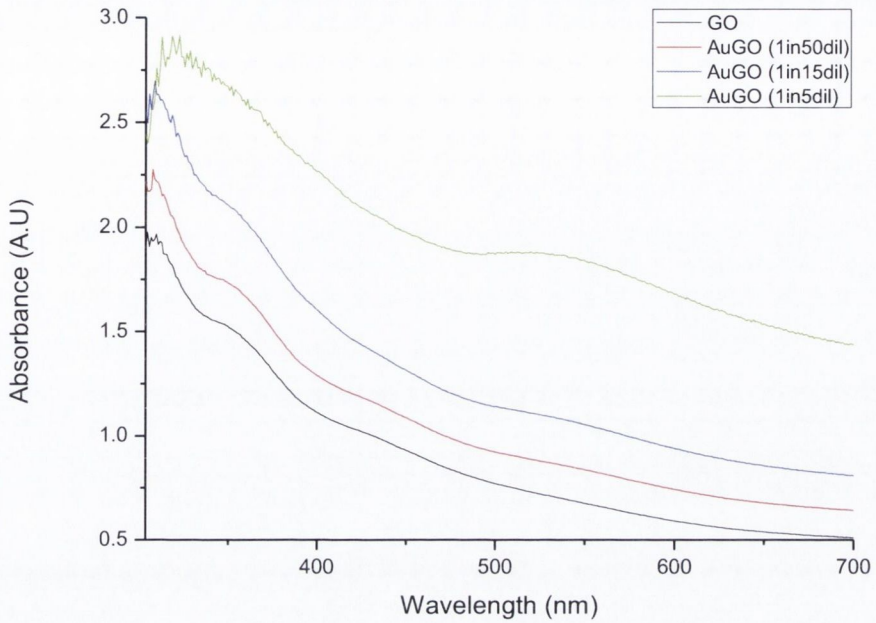

Figure 4.29 UV-Vis spectra of GO and AuGO deposited electrophoretically

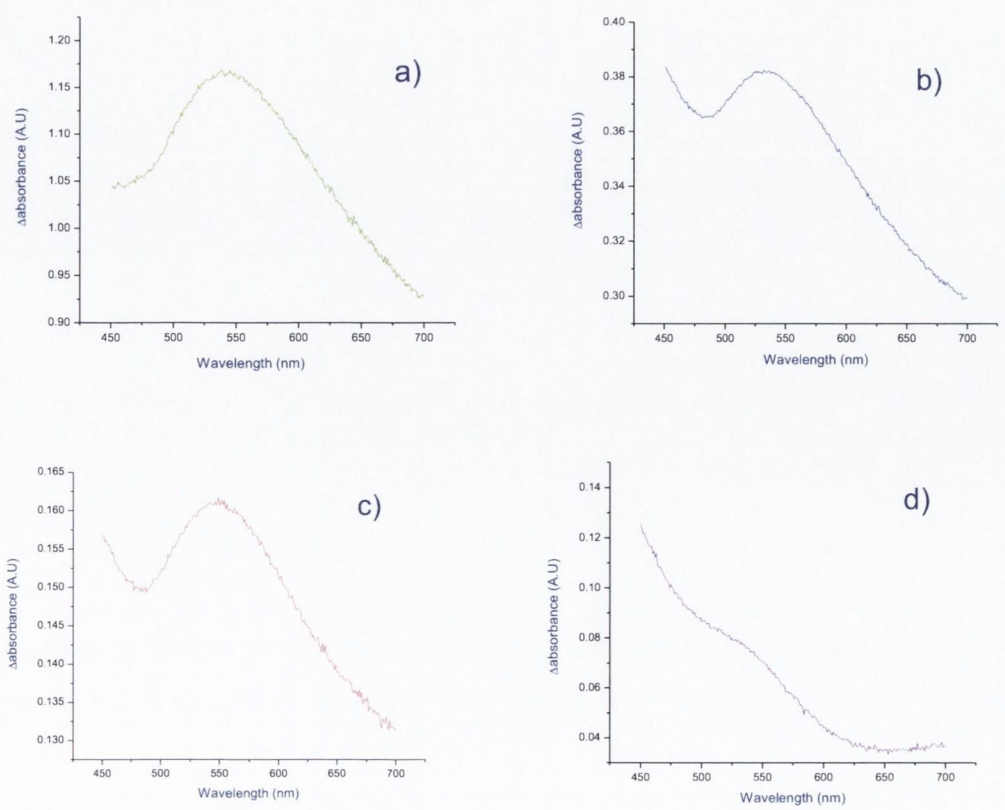

Figure 4.30 Δabsorbance spectra recorded for a-c) Au NPs in GO deposited through EPD and d) Δabsorbance recorded for a GO film soaked in a Au NP solution without an electric field

Elemental mapping of the electrodes was carried out in order to confirm that Au NPs have deposited throughout the GO electrode and did not form a bulk gold film on top of the GO. Figure 4.31 below shows the elemental map recorded for an AuGO electrode deposited from a solution concentration of 2 mM. As can be seen the presence of Au (green) can be observed throughout the GO electrode. The red colouration represents the presence of Sn, from the TCO layer upon which the material has been deposited

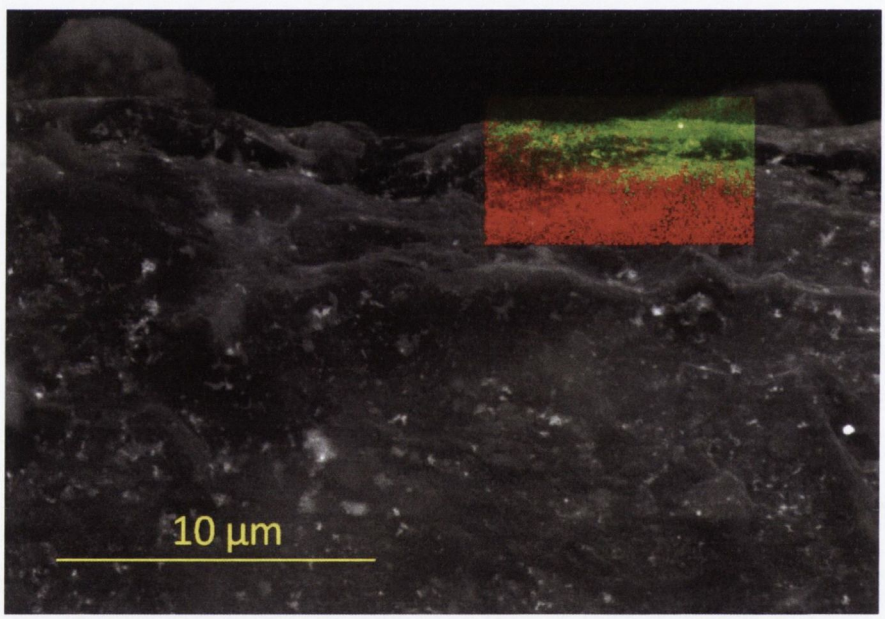

Figure 4.31 Elemental mapping recorded for an AuGO electrode deposited from a Au NP solution concentration of 2 mM. The prewsance of gold (green) and tin (red) is clearly observed

Previous studies with 2D materials have shown that they can be used as materials for photo detection[50,51] and sensing.[52,53] It has also been shown by Halas et al. that plasmonic nano-antennas coupled to graphene can act as extremely efficient plasmonic photo sensors.[54] Considering that plasmonic Au NPs show strong optical responses it was reasoned that

theses electrodes, formed through EPD, may also show interesting photo sensing and photo detection properties. Devices from these electrodes were fabricated according to the design template shown in figure 4.32 Back contacts were thermally evaporated from metallic silver wire.

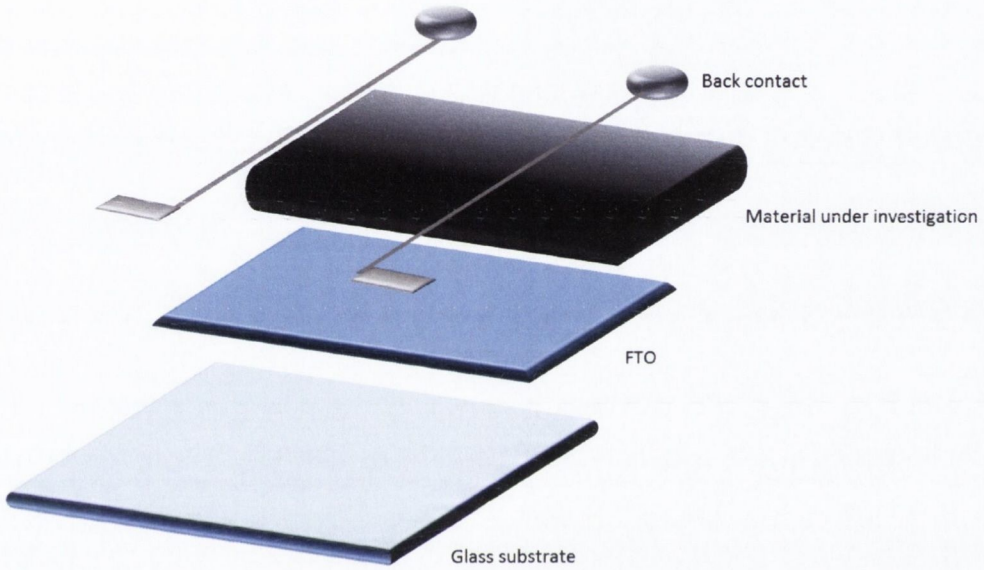

Figure 4.32 calculated differential absorption spectra recorded for gold NPs electrophoretically deposited into electrophoretically deposited GO films.

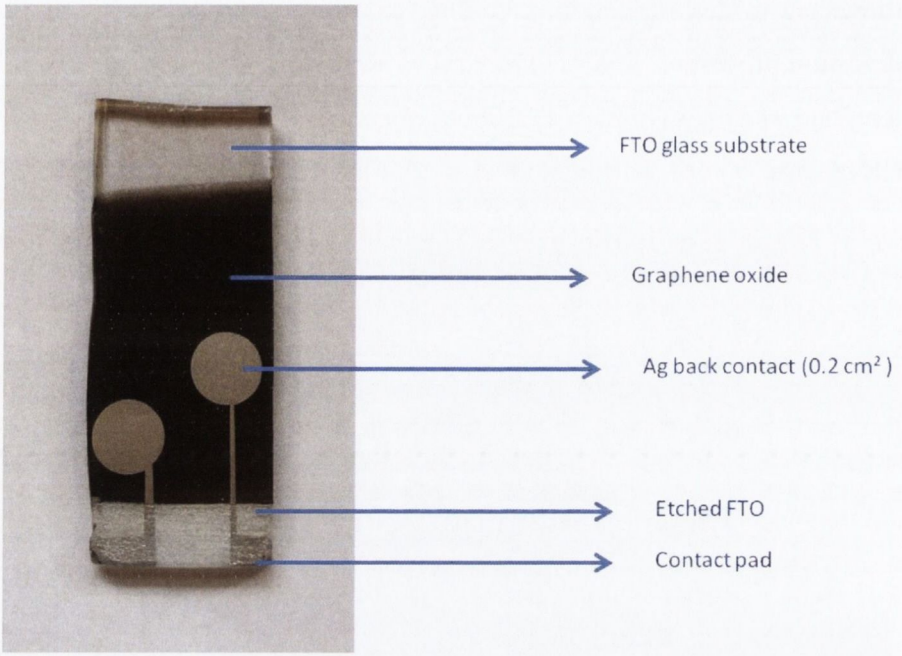

Figure 4.33 Photographic image of photo sensing device fabricated electrophoretically from GO and Au NPs

Results obtained from these investigations were poor. It was found that thermal evaporation of silver as the back contact material consistently shorted the devices. The porous nature of the electrodes allows the silver vapour to penetrate the electrode and make contact with the FTO substrate and hence causes a short circuit. Future work will aim to solve this problem, which will allow for optical testing of these devices.

4.6 Conclusions

In conclusion, this work has resulted in the development of new materials and methodologies for the development of new CEs for DSSCs. These CEs were prepared through EPD of composites of metallic nanoparticles (gold and platinum) on reduced graphene oxide. New synthetic methods for PtrGO and AurGO composites were successfully developed in this work, and crucially we show that metallic NPs can be deposited onto 2D substrates without the need for stabilising ligands. It is believed that the

lack of such stabilising ligands on the surface of the metallic nanoparticles increases the catalytic potential of these systems, as the particle surface is free to interact with redox species in solution.

The electrophoretic approach allowed for fine control over the material deposition and hence the catalytic ability of the electrodes. It was also observed that EPD could effectively separate GO from AurGO and PtrGO under the influence of an electric field. Electrochemical investigations revealed that PtrGO deposited on FTO could potentially be a suitable replacement for metallic Pt films in DSSC. AurGO did not perform as well in electrochemical studies.

DSSCs fabricated using these materials performed well. It was found that AurGO CEs could reach efficiencies 76% that of Pt. Results obtained with PtrGO were even more promising. After 3 EPD cycles, PtrGO CEs reached as efficiency of 5.90 %, 47.5% greater than that of the Pt electrode. We believe that this increase in efficiency is attributed to the nanostructured nature of the CE, which offers an extremely high surface area. Hence, there are more available reaction sites for the reduction of the tri-iodide ion in solution. This results in an increase in the current response of the cells, as can be seen in J-V measurements and through cyclic voltammograms.

These results show that by utilising a nanostructured electrode it is possible to obtain extremely high efficiencies when compared to conventional approaches. We believe that such composites of 2D materials and metallic nanoparticles may have a range of potential applications, which can take advantage of both the extremely high surface area offered by 2D materials and the catalytic and plasmonic properties of metal nanostructures.

This work has also shown that GO Au NP composite electrodes can be prepared using a two-step electrophotretic approach. Elemental analysis and spectroscopic studies have shown that Au NPs infiltrate the porous GO film and retain their optical characteristics after deposition. Optical devices have been fabricated from these materials and we aim to analyse the potential of using these devices as plasmonic optical sensors in the near future.

References

(1) O'Regan, B.; Grätzel, M. *Nature* **1991**, *353*, 737.

(2) Grätzel, M. *Nature* **2001**, *414*, 338.

(3) Smestad, G.; Bignozzi, C.; Argazzi, R. *Solar Energy Materials and Solar Cells* **1994**, *33*, 253.

(4) Yen, M.-Y.; Yen, C.-Y.; Liao, S.-H.; Hsiao, M.-C.; Weng, C.-C.; Lin, Y.-F.; Ma, C.-C. M.; Tsai, M.-C.; Su, A.; Ho, K.-K.; Liu, P.-L. *Composites Science and Technology* **2009**, *69*, 2193.

(5) Brennan, L. J.; Byrne, M. T.; Bari, M.; Gun'ko, Y. K. *Advanced Energy Materials* **2011**, *1*, 472.

(6) Wang, X.; Zhi, L.; Mullen, K. *Nano Letters* **2007**, *8*, 323.

(7) Eda, G.; Fanchini, G.; Chhowalla, M. *Nat Nano* **2008**, *3*, 270.

(8) Yang, N.; Zhai, J.; Wang, D.; Chen, Y.; Jiang, L. *Acs Nano* **2010**, *4*, 887.

(9) Choi, H.; Kim, H.; Hwang, S.; Han, Y.; Jeon, M. *Journal of Materials Chemistry* **2011**, *21*, 7548.

(10) Hong, W.; Xu, Y.; Lu, G.; Li, C.; Shi, G. *Electrochemistry Communications* **2008**, *10*, 1555.

(11) Roy-Mayhew, J. D.; Bozym, D. J.; Punckt, C.; Aksay, I. A. *Acs Nano* **2010**, *4*, 6203.

(12) Ahmad, I.; Khan, U.; Gun'ko, Y. K. *Journal of Materials Chemistry* **2011**, *21*, 16990.

(13) Brennan, L. J.; Barwich, S. T.; Satti, A.; Faure, A.; Gun'ko, Y. K. *Journal of Materials Chemistry A* **2013**, *1*, 8379.

(14) Wang, X.; Zhi, L.; Müllen, K. *Nano letters* **2008**, *8*, 323.

(15) Murakami, T. N.; Ito, S.; Wang, Q.; Nazeeruddin, M. K.; Bessho, T.; Cesar, I.; Liska, P.; Humphry-Baker, R.; Comte, P.; Péchy, P. *Journal of the Electrochemical Society* **2006**, *153*, A2255.

(16) Suzuki, K.; Yamaguchi, M.; Kumagai, M.; Yanagida, S. *Chemistry Letters* **2003**, *32*, 28.

(17) Ramasamy, E.; Lee, W. J.; Lee, D. Y.; Song, J. S. *Electrochemistry Communications* **2008**, *10*, 1087.

(18) Costa, R. D.; Feihl, S.; Kahnt, A.; Gambhir, S.; Officer, D. L.; Wallace, G. G.; Lucio, M. I.; Herrero, M. A.; Vázquez, E.; Syrgiannis, Z. *Adv. Mater.* **2013**, *25*, 6513.

(19) Xiao, Y.; Wu, J.; Yue, G.; Lin, J.; Huang, M.; Lan, Z. *Electrochimica Acta* **2011**, *56*, 8545.

(20) Lee, W. J.; Ramasamy, E.; Lee, D. Y.; Song, J. S. *ACS Appl. Mater. Interfaces* **2009**, *1*, 1145.

(21) Bourlinos, A. B.; Georgakilas, V.; Zboril, R.; Steriotis, T. A.; Stubos, A. K. *Small* **2009**, *5*, 1841.

(22) Yen, M.-Y.; Teng, C.-C.; Hsiao, M.-C.; Liu, P.-I.; Chuang, W.-P.; Ma, C.-C. M.; Hsieh, C.-K.; Tsai, M.-C.; Tsai, C.-H. *journal of Materials Chemistry* **2011**, *21*, 12880.

(23) Bajpai, R.; Roy, S.; Kumar, P.; Bajpai, P.; Kulshrestha, N.; Rafiee, J.; Koratkar, N.; Misra, D. *ACS Appl. Mater. Interfaces* **2011**, *3*, 3884.

(24) Wang, H.; Hu, Y. H. *Energy & Environmental Science* **2012**, *5*, 8182.

(25) Wang, G.; Zhuo, S.; Xing, W. *Materials Letters* **2012**, *69*, 27.

(26) Bourdo, S. E.; Viswanathan, T. *Carbon* **2005**, *43*, 2983.

(27) Battumur, T.; Mujawar, S. H.; Truong, Q. T.; Ambade, S. B.; Lee, D. S.; Lee, W.; Han, S.-H.; Lee, S.-H. *Current Applied Physics* **2012**, *12, Supplement 1*, e49.

(28) Zhu, G.; Pan, L.; Lu, T.; Xu, T.; Sun, Z. *Journal of Materials Chemistry* **2011**, *21*, 14869.

(29) Gong, F.; Wang, H.; Wang, Z.-S. *Physical Chemistry Chemical Physics* **2011**, *13*, 17676.

(30) Bajpai, R.; Roy, S.; Kumar, P.; Bajpai, P.; Kulshrestha, N.; Rafiee, J.; Koratkar, N.; Misra, D. S. *ACS Appl. Mater. Interfaces* **2011**, *3*, 3884.

(31) Dreyer, D. R.; Park, S.; Bielawski, C. W.; Ruoff, R. S. *Chemical Society Reviews* **2010**, *39*, 228.

(32) Lerf, A.; He, H.; Forster, M.; Klinowski, J. *The Journal of Physical Chemistry B* **1998**, *102*, 4477.

(33) Geim, A. K.; Novoselov, K. S. *Nat Mater* **2007**, *6*, 183.

(34) Park, S.; An, J.; Potts, J. R.; Velamakanni, A.; Murali, S.; Ruoff, R. S. *Carbon* **2011**, *49*, 3019.

(35) Stankovich, S.; Dikin, D. A.; Piner, R. D.; Kohlhaas, K. A.; Kleinhammes, A.; Jia, Y.; Wu, Y.; Nguyen, S. T.; Ruoff, R. S. *Carbon* **2007**, *45*, 1558.

(36) Park, S.; Hu, Y.; Hwang, J. O.; Lee, E.-S.; Casabianca, L. B.; Cai, W.; Potts, J. R.; Ha, H.-W.; Chen, S.; Oh, J. *Nature communications* **2012**, *3*, 638.

(37) Paredes, J. I.; Villar-Rodil, S.; Martínez-Alonso, A.; Tascón, J. M. D. *Langmuir* **2008**, *24*, 10560.

(38) Stankovich, S.; Dikin, D. A.; Dommett, G. H. B.; Kohlhaas, K. M.; Zimney, E. J.; Stach, E. A.; Piner, R. D.; Nguyen, S. T.; Ruoff, R. S. *Nature* **2006**, *442*, 282.

(39) Satti, A.; Larpent, P.; Gun'ko, Y. *Carbon* **2010**, *48*, 3376.

(40) Zhou, X.; Huang, X.; Qi, X.; Wu, S.; Xue, C.; Boey, F. Y. C.; Yan, Q.; Chen, P.; Zhang, H. *The Journal of Physical Chemistry C* **2009**, *113*, 10842.

(41) Lightcap, I. V.; Kosel, T. H.; Kamat, P. V. *Nano Letters* **2010**, *10*, 577.

(42) Kudin, K. N.; Ozbas, B.; Schniepp, H. C.; Prud'homme, R. K.; Aksay, I. A.; Car, R. *Nano Letters* **2007**, *8*, 36.

(43) Ferrari, A. C.; Robertson, J. *Physical Review B* **2000**, *61*, 14095.

(44) Ferrari, A. C.; Meyer, J. C.; Scardaci, V.; Casiraghi, C.; Lazzeri, M.; Mauri, F.; Piscanec, S.; Jiang, D.; Novoselov, K. S.; Roth, S.; Geim, A. K. *Physical Review Letters* **2006**, *97*, 187401.

(45) Shin, H. J.; Kim, K. K.; Benayad, A.; Yoon, S. M.; Park, H. K.; Jung, I. S.; Jin, M. H.; Jeong, H. K.; Kim, J. M.; Choi, J. Y. *Advanced Functional Materials* **2009**, *19*, 1987.

(46) McCarthy, J. E.; Hanley, C. A.; Brennan, L. J.; Lambertini, V. G.; Gun'ko, Y. K. *Journal of Materials Chemistry C* **2014**, *2*, 764.

(47) Hernandez, Y.; Nicolosi, V.; Lotya, M.; Blighe, F. M.; Sun, Z. Y.; De, S.; McGovern, I. T.; Holland, B.; Byrne, M.; Gun'ko, Y. K.; Boland, J. J.; Niraj, P.; Duesberg, G.; Krishnamurthy, S.; Goodhue, R.; Hutchison, J.; Scardaci, V.; Ferrari, A. C.; Coleman, J. N. *Nature Nanotechnology* **2008**, *3*, 563.

(48) Boschloo, G.; Hagfeldt, A. *Accounts of chemical research* **2009**, *42*, 1819.

(49) Saito, Y.; Kubo, W.; Kitamura, T.; Wada, Y.; Yanagida, S. *Journal of Photochemistry and Photobiology A: Chemistry* **2004**, *164*, 153.

(50) Mueller, T.; Xia, F.; Avouris, P. *Nature Photonics* **2010**, *4*, 297.

(51) Loh, K. P.; Bao, Q.; Eda, G.; Chhowalla, M. *Nature chemistry* **2010**, *2*, 1015.

(52) Cunningham, G.; Khan, U.; Backes, C.; Hanlon, D.; McCloskey, D.; Donegan, J. F.; Coleman, J. N. *Journal of Materials Chemistry C* **2013**, *1*, 6899.

(53) Perea-López, N.; Elías, A. L.; Berkdemir, A.; Castro-Beltran, A.; Gutiérrez, H. R.; Feng, S.; Lv, R.; Hayashi, T.; López-Urías, F.; Ghosh, S. *Advanced Functional Materials* **2013**, *23*, 5511.

(54) Fang, Z.; Liu, Z.; Wang, Y.; Ajayan, P. M.; Nordlander, P.; Halas, N. J. *Nano Letters* **2012**, *12*, 3808.

Chapter 5

Generation of enhanced photo-current from plasmonic gold nanoparticles in nanoparticulate TiO_2 films.

5.1 Introduction

This chapter focuses on the preparation and photophysical studies of a gold nanoparticle - titanium dioxide composite system. The material was prepared by the electrophoretic deposition of gold nanoparticles into a porous nanoparticulate titanium dioxide film, creating a photoactive electrode. The work aims to evaluate the effect of the Au NPs on the optoelectronic and photo- physical properties of TiO_2. A theoretical description of the process occurring at the Au/TiO_2 interface is also provided. The results obtained through theoretical modeling are in extremely close agreement with those obtained through experiment.

Surface plasmon resonance (SPR) is a feature of many metal nanostructures, based upon the collective oscillation of nanoparticles conduction band electrons, when excited at the particles plasmon resonance frequency.[1] SPR has been the subject of intense research in recent times due to the variety of potential important applications in areas such as imaging, [2,3] photonics[4] and sensing[5-7]. SPR is a highly tuneable process and can be observed from the UV to the near-IR region of the electromagnetic spectrum, with plasmon resonance dependent upon the material used, the surrounding medium of the particles and the size and shape of the particular nanostructure. Recently SPR has attracted a great deal of attention as a plausible tool for increasing the efficiency of solar energy conversion devices. SPR has several potential applications in solar energy devices which range from decreasing the thickness of the absorber

layer material in order to decrease bulk recombination currents, increasing the optical path of incident light in the absorber layer and as efficient mechanisms for light coupling into solar cells.[8-12] Recent research attention has focused on the use of plasmonic particles as the principle absorber for the generation of photocurrent in solar energy devices. It has been demonstrated that excitation of a metal nanoparticles plasmon can cause a charge separation of electrons and holes at a metal semiconductor interface.[13-18] The resulting injection of "hot" electrons into the semiconductor can generate a substantial photocurrent being observed at the plasmon wavelength. These observations infer that plasmonic particles can serve as a potential light harvesting mechanism, enabling the generation of photocurrent. The advantage of using such a system lies in the fact that the plasmonic particles are highly tuneable across a wide range of wavelengths and are extremely stable and robust materials for solar energy harvesting. In addition metal nanoparticles can absorb light much more efficiently compared to semiconductors and dye molecules. Therefore, the use of photo-excited plasmonic electrons is potentially very attractive for applications in photochemistry and photo-catalysis,[19-22] solar energy harvesting (solar cells)[8-12,16,23,24] and optoelectronics.[25-30] there are many challenges in achieving an efficient extraction of energetic electrons and holes. The main limiting factors are the short lifetime of excited carriers in a metal, the slow transfer of momentum from a nanoparticle to plasmonic electrons and the reflection of carriers at interfaces. Previously it was reported that embedding plasmonic structures into a semiconductor results in a substantial increase in hot electron emission. [28] Also recently, it has theoretically been shown that the efficiency of generation and injection of plasmonic carriers can be increased by choosing appropriate particle sizes, geometries and excitation frequencies.[17,31]

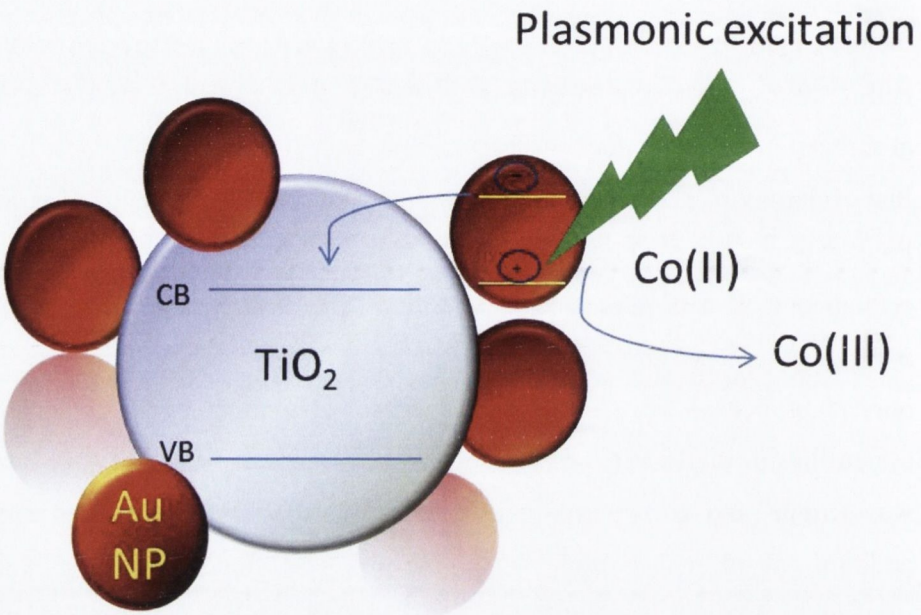

Figure 5.1 Proposed mechanism for the generation of plasmonic photocurrent

In this work we offer an approach to produce new $AuTiO_2$ nanocomposites with high efficiency of "hot" electron injection and provide theoretical modelling of electron generation mechanisms and calculations of "hot" carrier contributions. We demonstrate that gold nanoparticles can be deposited into TiO_2 films using an electrophoretic approach, whereby particles migrate into the TiO_2 mesoporous electrode under the influence of an electric field. We also show that a heat treatment of the electrodes enables us to finely tune the plasmon peak position of the nanoparticles after deposition into TiO_2. In this case the heat treatment allows us to remove the stabilising insulating ligands on the surface of the gold nanoparticles and allows for a more efficient electron injection process and a resulting increase in the photocurrent response. The resulting $AuTiO_2$ composite electrodes have been investigated as potential photocurrent generators.

5.2 Preparation of photoactive gold-TiO_2 electrode

Gold nanoparticles have been initially synthesised in water and then transferred to the organic phase using a previously published method.[32] Transfer to the organic phase was necessary in order to avoid water splitting under the applied DC field during the following electrophoretic deposition. $CHCl_3$ acted as an ideal solvent for the phase transfer as its polar nature allowed for good 'wettability' and interaction with the TiO_2 substrate. Analysis of TEM images (Figure 5.2) showed that the synthesized gold nanoparticles had an average size of 5.1 nm (see figure 5.3 for histogram)

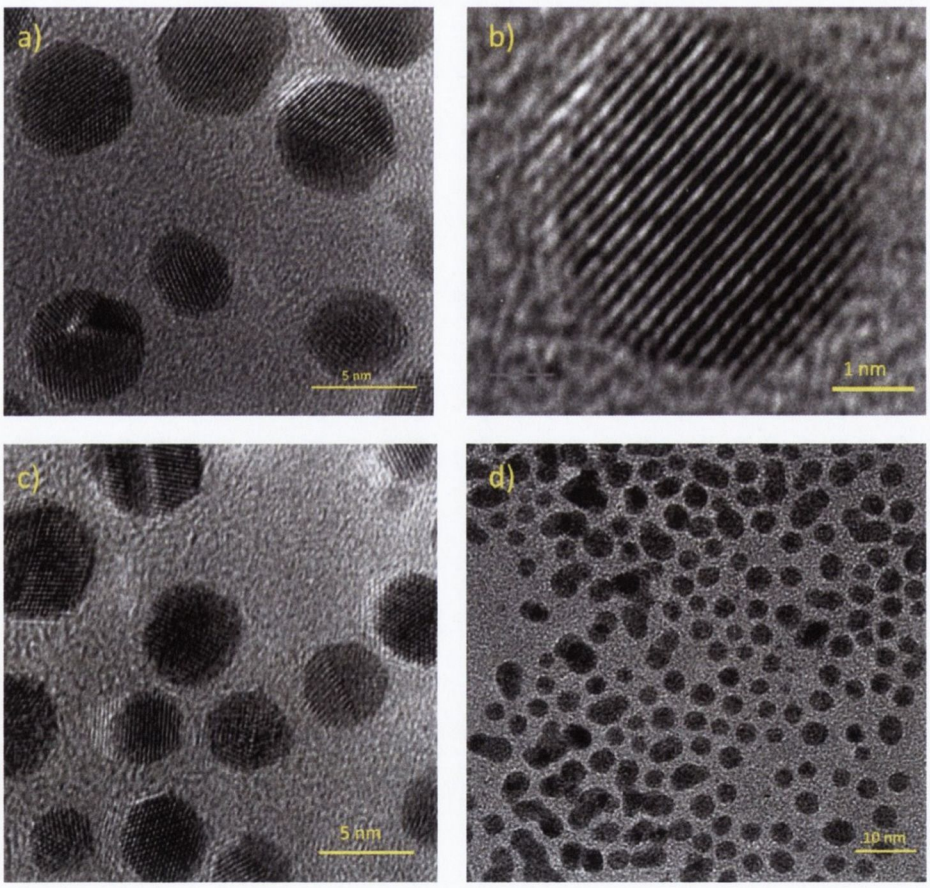

Figure 5.2 HRTEM image of a-d) gold nanoparticles (~5nm) deposited from $CHCl_3$ onto lacy carbon grid. Image b shows an individual nanoparticle showing the crystal lattice spacing

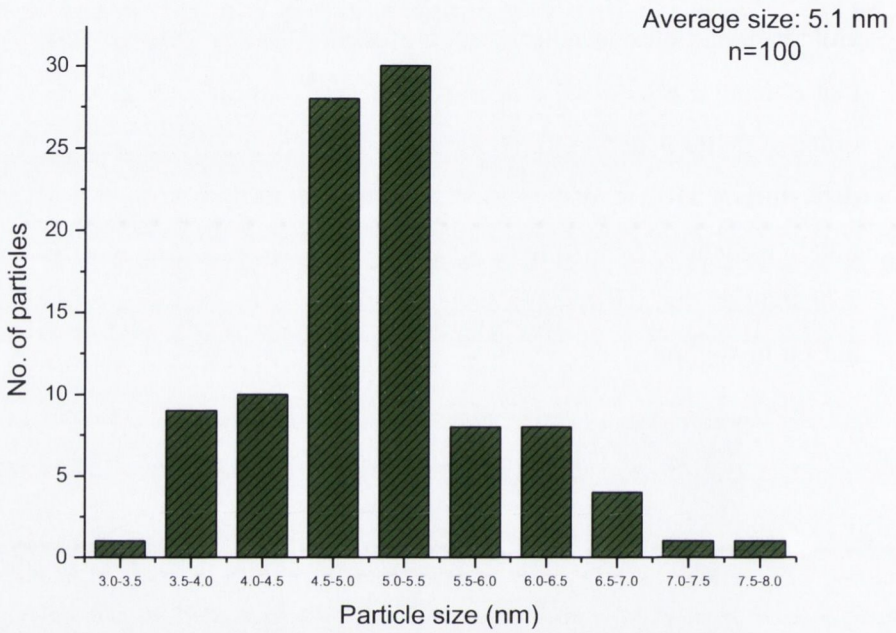

Figure 5.3 Size distribution for Au NPs determined through TEM. The average size of the particles measures 5.1 nm. Sizes of 100 individual particles were measured.

Nanoparticulate TiO_2 films were fabricated using the screen printing method onto FTO glass substrates (Sigma, 2.3 mm, 13 $\Omega\square^{-1}$). The glass was thoroughly cleaned in a detergent solution followed by washing with isopropanol prior to deposition. In order to facilitate a good adhesion of the TiO_2 nanoparticle layer, an initial bulk layer of TiO_2 was deposited through drop casting an aqueous solution of $TiCl_4$ (40mM) onto heated glass substrates. The nanoparticulate TiO_2 layer was deposited using the Dyesol 90-NRT commercial TiO_2 paste from Dyesol Ltd. using a 90T polyester mesh. A single deposition allowed for the formation of a ~3μm layer of TiO_2 onto the FTO substrates. The dimensions of the electrodes measured 1cm x 3 cm. After deposition the electrodes were treated to a sintering profile of 125 °C for 5 min, 350 °C for 15

min, 450 °C for 15 min and finally 500 °C for 15 min. A ramp rate of 8 °C min^{-1} was used for all steps. Once cooled the electrodes were used for electrophoretic deposition (EPD).

EPD was carried out by submerging a TiO_2 electrode and a blank FTO electrode into a solution of gold nanoparticles in $CHCl_3$. A DC voltage of 250 V was applied across the electrodes for 15 minutes. It was observed that gold nanoparticles were favourably deposited into the TiO_2 film (Figure 5.4) rather than on the surface of the FTO coating, which would agree with findings by Kamat et al. who have also observed this trend.[33] EPD allows for the creation of a photoactive electrode on time scales far less than that employed for dye sensitization of TiO_2, which in generally in the range of 16-24 hours.[34]

5.3 Characterisation of gold-TiO_2 photoanode

Uv-Vis spectra (Figure 5.4 (II)) of gold nanoparticles electrophoretically deposited into TiO_2 films have shown increasing plasmonic intensity with the growing concentration of nanoparticles in the deposition solution. As expected the deposition of gold nanoparticles resulted in a very large increase in the optical absorption of the TiO_2 films when studied with UV-Vis spectroscopy and visually (Figure 5.4 (IV)). The presence of a large plasmon band was also observed in the UV-Vis spectra, indicative of the presence of gold nanoparticles in the TiO_2 films. The plasmon peak position of the gold nanoparticles embedded in TiO_2 closely matched that of the plasmon position for the gold particles in the liquid phase, confirming that after the EPD the particles are still in the nanoparticulate form and have not coalesced into a bulk gold film.

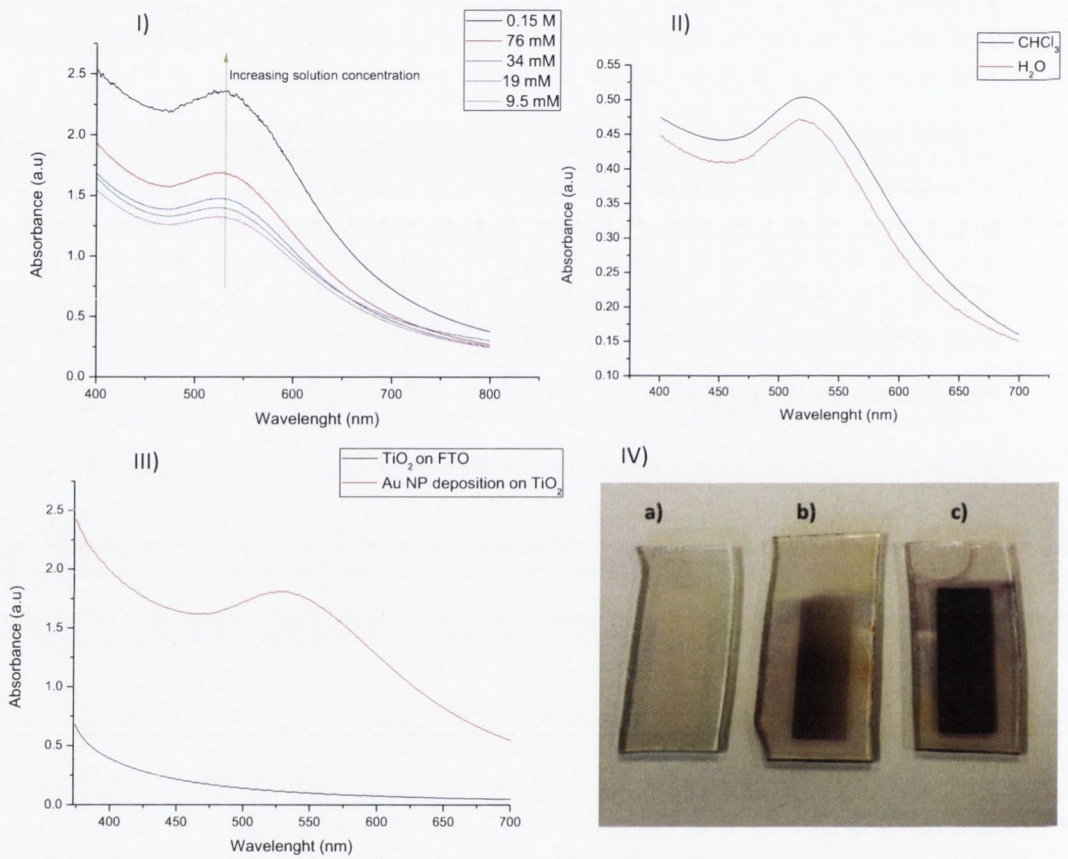

Figure 5.4 I)) Uv-Vis spectra of gold nanoparticles electrophoretically deposited into TiO_2 films from a range of $CHCl_3$ solution concentrations at 250V for 15 II) UV-Vis spectra of gold nanoparticles recorded in H_2O and after the phase transfer to $CHCl_3$ III) UV-Vis spectra of bare TiO_2 and TiO_2 after EPD of gold nanoparticles from a solution concentration of 37.9mM IV) Photographic image of a) TiO_2 b) deposition of gold nanoparticles from a solution concentration of 0.37μM c) deposition from a solution concentration of 38 mM.

In order to examine the effect of EPD on the nature of the Au NPs and the formed electrodes a rigorous microscopic and elemental analysis was undertaken. HRTEM images were taken of both the unmodified TiO_2 and the $AuTiO_2$ composite. In order to study the material in TEM it

was necessary to remove some of the material from the FTO electrode using a sharp blade. The material was then dissolved in an appropriate solvent and ultra-sonicated in order to disperse the material into the liquid phase. Following this the TEM samples were prepared through drop casting onto lacy carbon TEM grids. The TEM images (Figure56.5) below show the unmodified TiO_2 deposited from H_2O (a and b) and the Au modified TiO_2 deposited from $CHCl_3$ (c and d). It can be observed from the images that the sonication of the $AuTiO_2$ in $CHCl_3$ did not remove the Au NPs from the surface of the TiO_2. This would indicate that the Au NPs are adhered well to the oxide surface . It can also be observed that the Au NPs are still nano particulate and have not coalesced into a bulk Au film on top of the TiO_2.

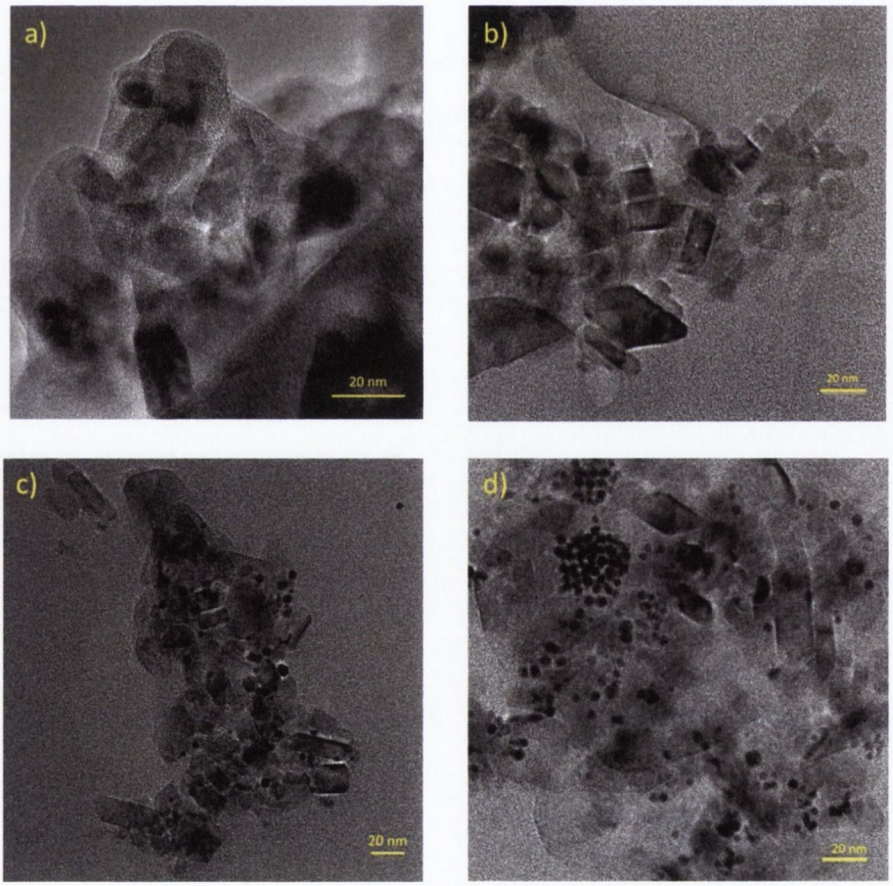

Figure 5.5 HRTEM images of TiO_2 (a and b) and $AuTiO_2$ after EPD (c and d)

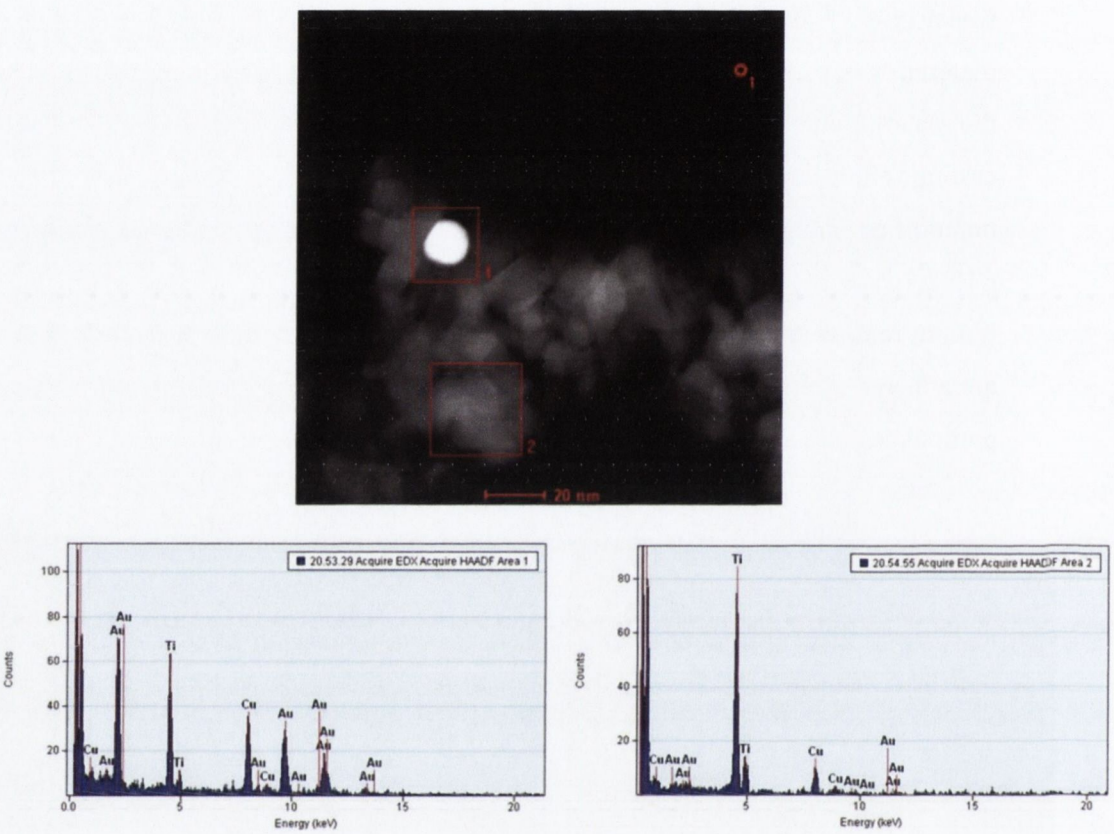

Figure 5.6 STEM image of an individual Au NP on the surface of TiO_2. The highlighted regions 1 and 2 are matched to the EDX spectra below

Scanning electron microscopy (SEM) of the composite films (Figure 5.7) clearly demonstrated that the EPD allowed for individual gold nanoparticles to be deposited into the TiO_2. Some clustering of the nanoparticles was observed in the SEM images, in particular on top of the film however throughout the film the particles seemed to be largely deposited individually.

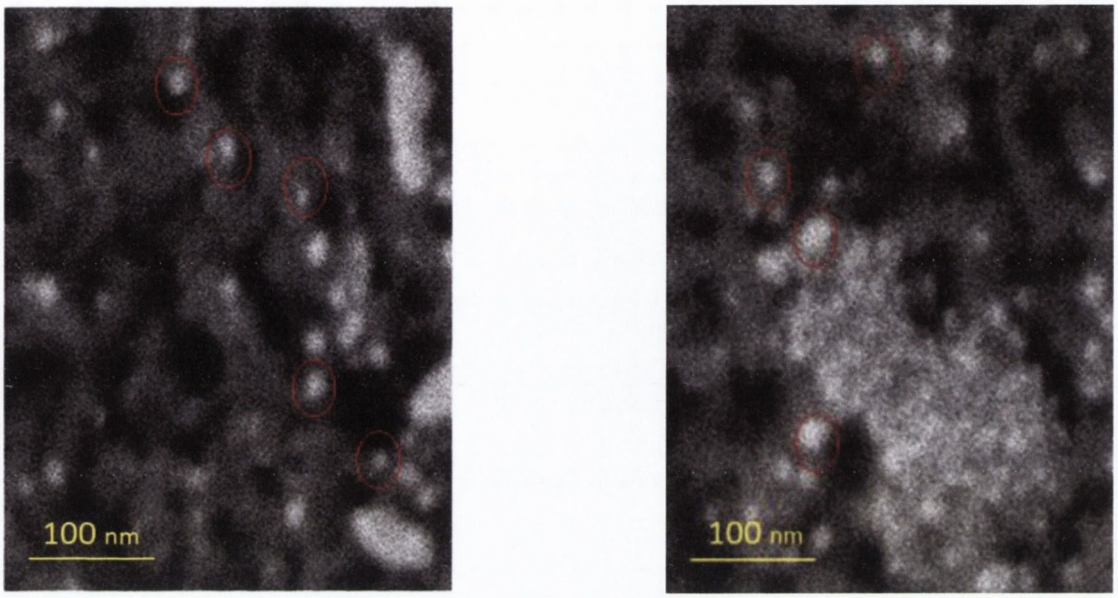

Figure 5.7 SEM images of gold nanoparticles deposited in TiO_2 through EPD

Analysis of the resulting electrodes was carried with the use of energy dispersive X-ray spectroscopy (EDX) allowing the elemental composition of the composite films to be determined. The EDX spectra (Figure 5.8) were recorded by mapping the elemental composition of the electrode with respect to depth, recording the composition from several microns above the film to the glass substrate below. From EDX data it is evident (Figure 5.8) that the gold nanoparticles are distributed evenly throughout the TiO_2, which infers that EPD of the gold nanoparticles allowed for the particles to migrate through the pores of the TiO_2 under the applied field. This is highly advantageous for processes such as plasmonic charge transfer as increasing the loading of nanoparticles throughout the film should allow for a more efficient charge separation to occur.

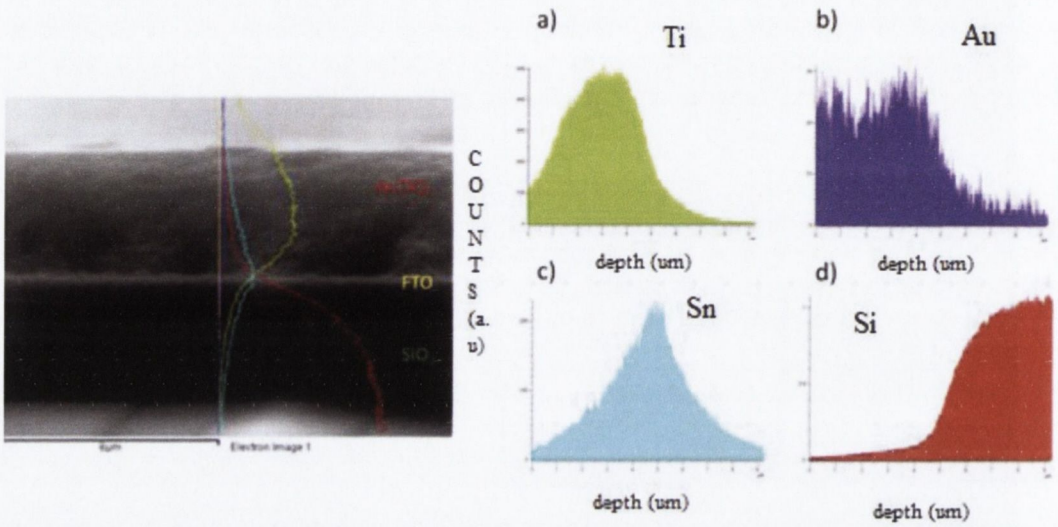

Figure 5.8 EDX line mapping recorded for a) TiO_2 b) gold c) tin and d) silicon.

Nanoparticulate TiO_2 films have been produced by the screen printing method onto FTO glass substrates and used for electrophoretic deposition (EPD). Electrophoretic deposition (EPD) is a versatile approach for depositing a wide range of materials from quantum dots, [23,35] nanoparticles [36,37], polymers[38] and carbon nanomaterials.[39-41] EPD allows for charged colloidal particles, suspended in solution, to migrate under the influence of an electric field and to be deposited onto a conductive electrode of opposite charge. This approach is an extremely versatile method for the deposition of particles into a porous TiO_2 network, allowing a range of nanoparticle deposition concentrations to be achieved, which also show an even distribution across the depth of the film. By keeping the voltage and the time of the depositions constant it is possible to vary the concentration of gold nanoparticles in the TiO_2 film by simply changing the concentration of gold nanoparticles in the deposition solution.

In order to increase the short circuit current of these electrodes under illumination, we introduced a thermal treatment of the electrodes after deposition of the nanoparticles. The thermal treatment served as a mechanism for removal of the insulating DDT ligands used to stabilize the particles in solution and allowed for gold nanoparticles to be in closer contact with the TiO_2 nanoparticles, therefore enabling a more efficient charge injection. It was observed that heat treatment of the films results in both a significant increase in the optical absorption of the films and also increases the plasmonic intensity (Figure 5.9 (I)). The plasmonic band shifts significantly to the red,(524 nm to 562 nm after 600 $^{\circ}$C treatment) suggesting that the particles undergo a thermal ripening process while in the TiO_2 films, as the gold nanoparticles grow and obtain a narrower size distribution. [42,43] This is also indicated by the full width half maximum (FWHM) values obtained for the plasmonic peaks. The FWHM value decreases from 201 nm to 108 nm after the heat treatment at 600 $^{\circ}$C. The heat treatment also serves as a versatile method of finely tuning the optical properties of the electrodes. As the temperature is increased, the gold nanoparticles grow and shift further to the red region of the spectrum. We observed that it is possible to shift the plasmonic peak position from 525 nm to 580 nm through heating the films for 1 hour, at varying temperatures. We have found that the plasmonic peak position shifts linearly with increasing temperature (Figure 5.10), therefore this can serve as a highly selective method for accurately tuning the optical absorption of the electrodes after the deposition has occurred.

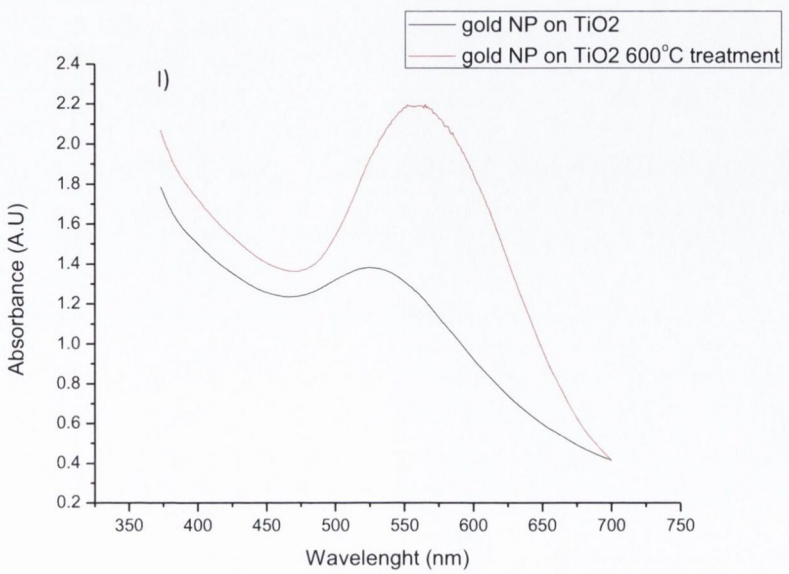

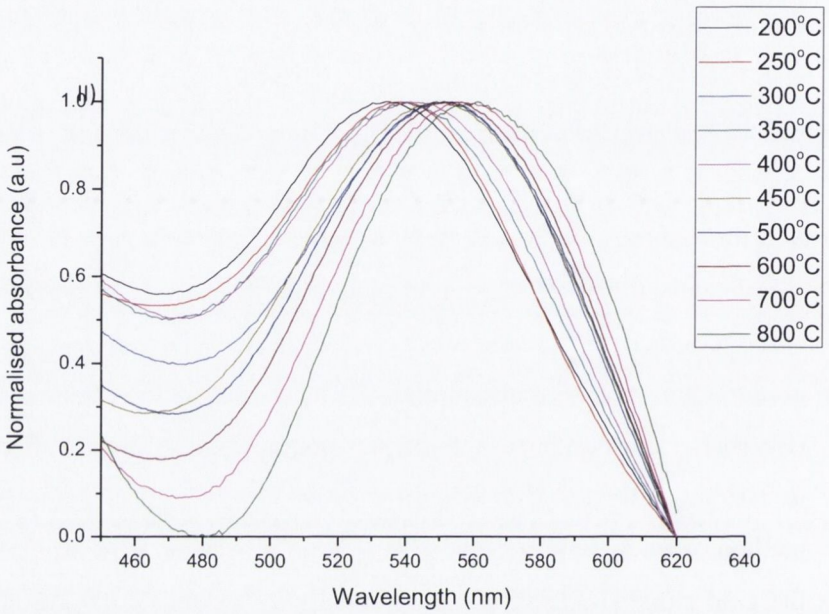

Figure 5.9 I) UV-vis spectra showing the shift in the plasmon peak position and the increase in plasmonic intensity after heat treatment of the Au-TiO_2 composite films at 600 °C. II) UV-Vis spectra showing the shift in the plasmon peak position with the heat treatment.

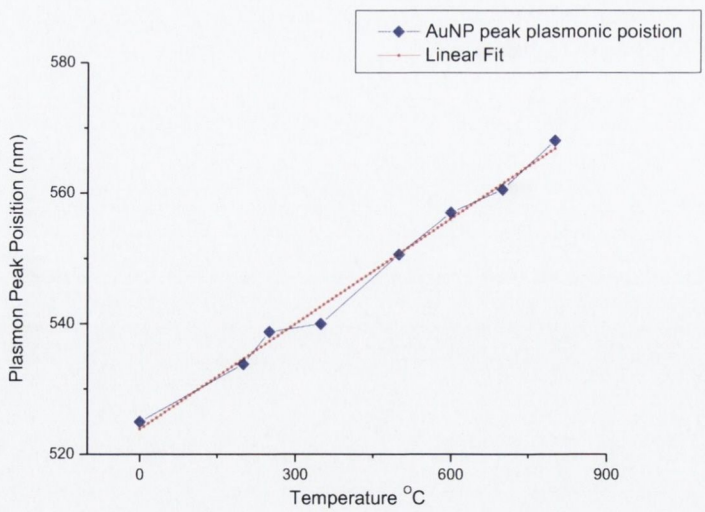

Figure 5.10 Linear relationship between increasing sintering temperature and plasmonic peak position.

In addition to removal of the insulating ligands surrounding the particles, the thermal treatment partially fuses the gold and TiO_2 particles, resulting in the partial embedding of gold nanoparticles into the titanium dioxide structure. The fusion of the particles is expected to lead to an enhanced injection of hot electrons when illuminated at the plasmonic frequency, and is partially responsible for the increased plasmonic current which is observed.

5.4 Electrochemical investigations

Photo-electrochemical (PEC) performance tests were carried out on the electrodes in order to examine this effect. All Photophysical measurements (photoaction response, PEC analysis, IV) were obtained using a 3 electrode electrochemical cell with an $AuTiO_2$ composite WE, FTO CE, and a saturated calomel reference electrode (KCl). The electrolyte used was 0.05M NaOH in water. Tests were carried out in a specially designed quartz cuvette (innovative lab supply), which allowed for the electrodes (1cm x 3 cm) to be fully immersed in the electrolyte. Data was recorded with an Autolab(III) potentiostat and the Nova 1.10 software package. CVs were recorded in a standard 3 electrode electrochemical cell utilizing a gold working electrode ($3mm^2$) a Pt wire counter electrode and a saturated calomel reference electrode (KCl).

The PEC tests were carried out in a 3 electrode electrochemical cell utilising an $AuTiO_2$ working electrode, FTO counter electrode and a saturated calomel (KCl) reference electrode. The cells were tested under visible light ($\geq$ 425 nm) illumination; the light source was chopped using an optical chopper operating at a frequency of 14Hz. PEC tests ran for 30 minutes and showed extremely reproducible behavior over this time, this indicates the that the Au NPs are stable light harvesters under such operating conditions.

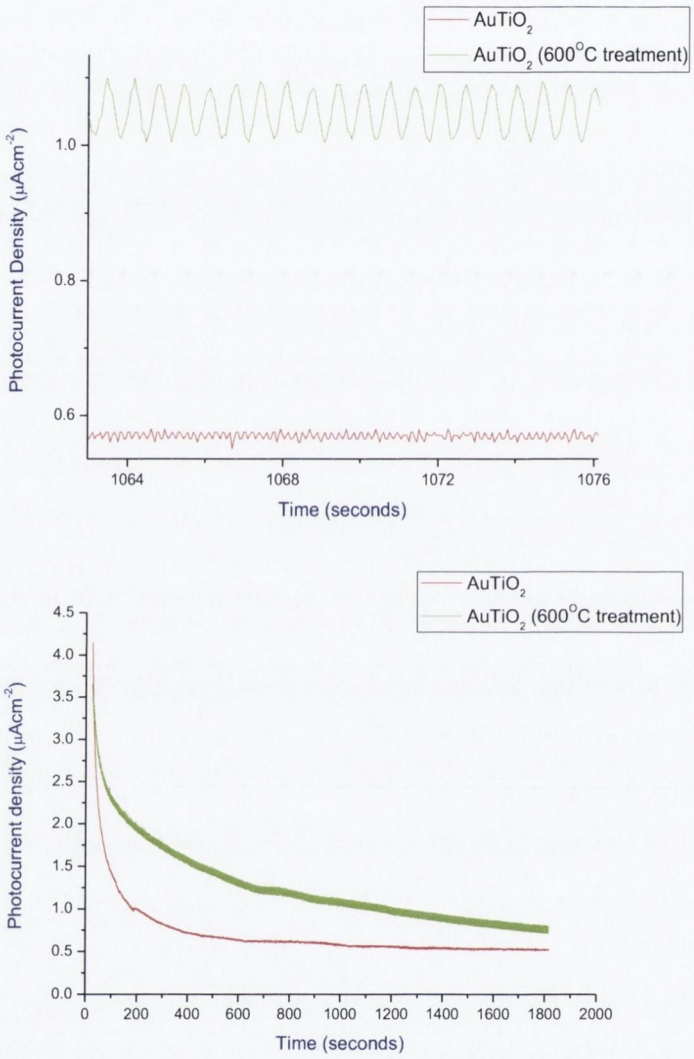

Figure 5.11 Photo electrochemical performance of heat treated (600 °C treatment) Au -TiO_2 film (green) and non-treated Au - TiO_2 film (red) under visible light illumination ($\geq 425\ nm$) (0.45 V vs. SCE) with a chopping frequency of 14 Hz.

The PEC tests revealed an extremely stable and reproducible on/off switching response to the chopped light. This stable switching response has been observed at chopping frequencies

greater than 100 Hz. which is indicative of a stable and fast injection response from gold to TiO_2. PEC tests observed above were carried out at 14 Hz for clarity. The photocurrent response for the electrodes can be calculated from the difference in photocurrent observed between the on and off states, whereby the on/off response is regulated by the optical chopper. The PEC analysis (Figure 5.11) clearly shows an increase in the photocurrent observed for the heat treated electrode, it can also be seen from the PEC data that the heat treated films produce a more regular and sharper on/off switching response which would indicate the formation of a higher quality junction between the gold and TiO_2.

It can be observed that there is also a significant increase in the magnitude of the overall current value for heat treated electrode. The current from such a device can be attributed to a) photocurrent b) electrolyte charge transfer properties, which depends largely on the viscosity, temperature and concentration of the solution and c) recombination. The change in photocurrent can be observed from the on/off switching states and it is reasoned that recombination will actually be favored for the heat treated electrode as a photo excited electron will not have to cross the insulating ligand barrier in order to interact with a positively charged hole. Hence we attribute this increase in the magnitude of the overall current response to the change in the interfacial boundary layer between the gold nanoparticles and the electrolyte. If the electrodes undergo no heat treatment then the stabilizing ligands will still sit on the particles surface and limit the interaction of the particle with the electrolyte. In this work the electrolytes employed were polar in nature (H_2O and $CHCl_3$ solvent based systems), considering that the stabilizing ligand (DDT) is a long fatty chain containing 12 carbon atoms, it can be assumed that the interaction between the particles surface and the electrolyte will be hampered by the presence of the ligands. The electrode/electrolyte boundary layer will be expected to grow over time and a current decrease will be observed. Removal of the ligands through the thermal treatment allows for a greater interaction between the particles surface and the electrolyte. The boundary layer thickness in this case is expected to decrease and for current values to increase

As a mechanism of evaluating the plasmonic photocurrent response for the electrodes we tested the photoaction response of the electrodes under illumination at 525 nm (THOR Labs LIU102)(Figure 5.12).

It can clearly be observed from the photoaction response that when electrodes are illuminated at or close to the plasmonic frequency of the particles, a large photocurrent is generated when compared to the unmodified TiO_2 (Figure 5.12). A maximum photocurrent of 0.20 μAcm^{-2} is observed for the heat treated Au - TiO_2 electrode which is a significant increase from the 0.01μAcm^{-2} observed for TiO_2. This large increase in photocurrent is attributed to the generation and injection of hot plasmonic electrons from the gold nanoparticles into the TiO_2. It can also be observed that at the plasmonic wavelength the sintered films perform significantly better than the untreated films, owing primarily to the removal of organic ligand and the creation of a higher quality junction between gold and TiO_2.

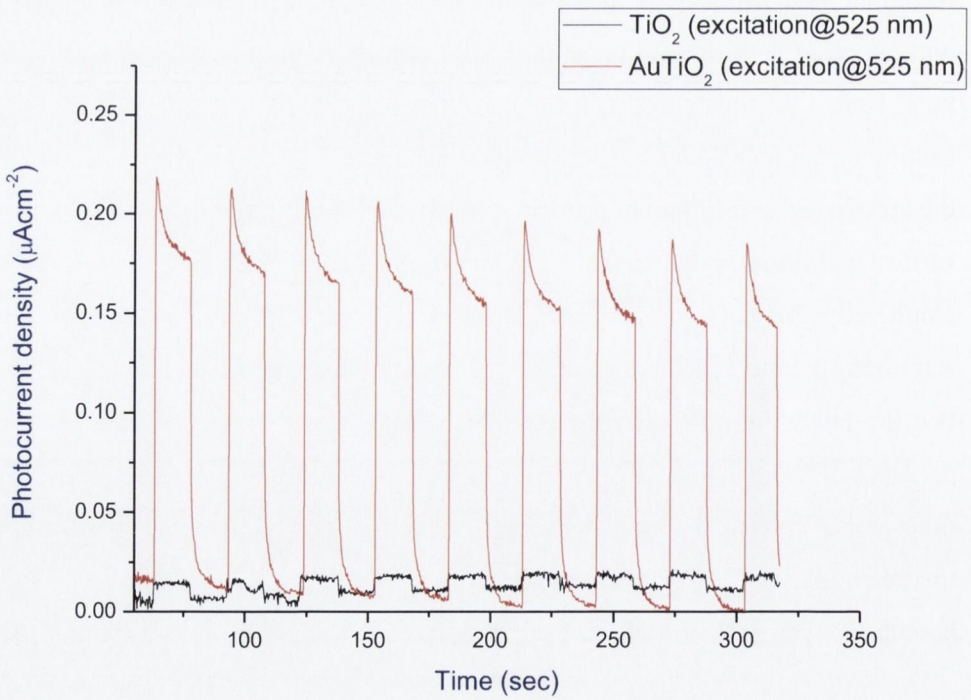

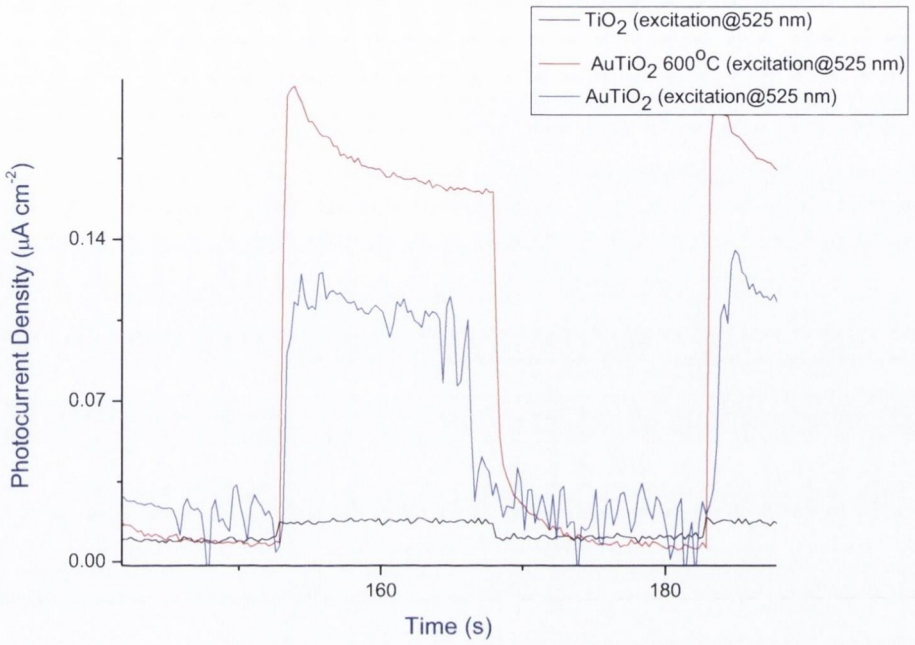

Figure 5.12 Photoaction response obtained for Au - TiO_2 electrode when illuminated at 525 nm. Photoaction results were obtained using a 3 electrode electrochemical cell with an Au - TiO_2 WE, FTO CE, and a SCRE (KCl). The electrolyte used was 0.05M NaOH in water. Tests were carried out in a specially designed quartz cuvette, which allowed for the electrodes (1cm x 3 cm) to be fully immersed in the electrolyte.

Analysis of the photoaction response for the Au-TiO_2 (600°C) and the uncalcinated $AuTiO_2$ electrode shows an initial sharp photocurrent spike (J_I), followed by a noticeable decrease in the photocurrent. After this decrease the photocurrent reaches a steady state value (Jss) (see Figure 5.16). The initial spike in the photocurrent is due to the separation of plasmonic hot electrons and holes at the Au-TiO_2 interface. Hot plasmonic electrons migrate through the TiO_2 layer and are transported to the FTO back contact. The hot holes move to the surface of the Au nanoparticles and are captured by the reduced species in the electrolyte. The decrease in the photocurrent response, following J_I, is a result of recombination processes. As holes reach the

surface of the Au NPs they may recombine with electrons in the conduction band of TiO_2. This decay of photocurrent is determined by the rate of electron capture from holes trapped at nanoparticle surface states.[44]

This effect has also been observed in colloidal TiO_2 films when simulated with light.[45,46] In this work, the photoaction current is so small when illuminated at 525 nm that it is difficult to resolve these features in the photocurrent response.

In order to calculate the quantum efficiency of the plasmonic injection from Au to TiO_2, incident photon to conversion efficiency (IPCE) spectra was recorded. The cobalt mediator was chosen for these experiments as previous work using the iodide/tri-iodide redox system caused leaching of gold from the electrodes almost immediately and was deemed unsuitable for further use. The $[Co(II/III)bpy_3](PF_6)_{2/3}$ redox couple was synthesied according to the procedure outlined by Park et al[24] and which has also been outlined in the experimental section.

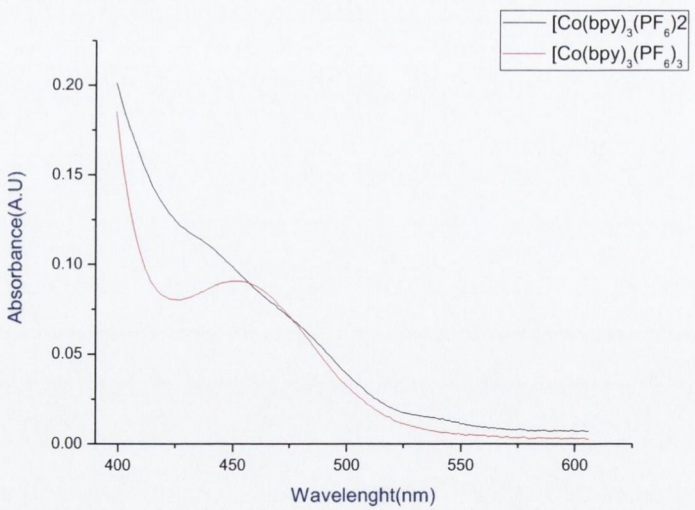

Figure 5.13 Uv-Vis spectra of $[Co(II)bpy_3](PF_6)_2$ and $[Co(III)bpy_3](PF_6)_3$

Cyclic voltammetry (Figure 6.15) recorded for the Co (II/III) couple on a gold electrode ($3mm^2$) clearly showed the reversible nature of the redox couple with increasing scan rates.

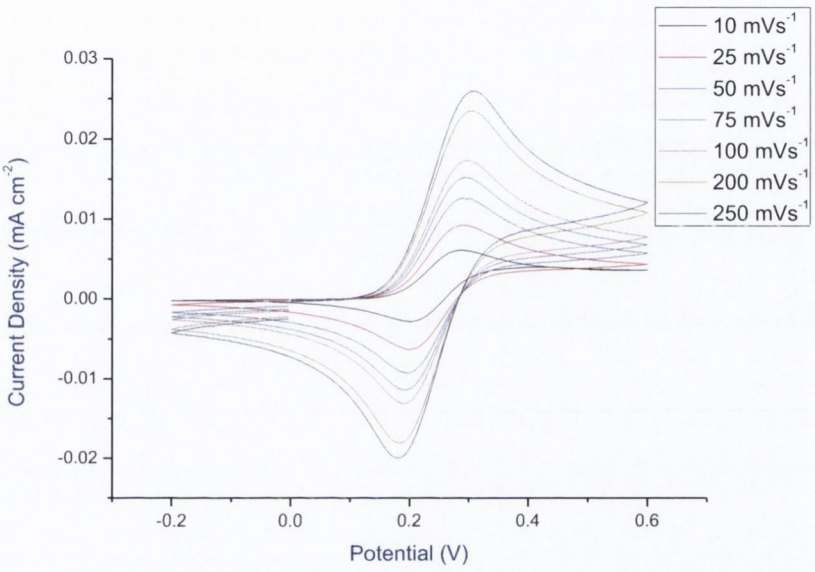

Figure 5.14 Cyclic voltammograms recorded for the Co(II/III) redox couple in acetonitrile with increasing scan rates . CVs were recorded in a standard 3 electrode electrochemical cell utilizing a gold working electrode ($3mm^2$) a Pt wire counter electrode and a saturated calomel reference electrode (KCl).

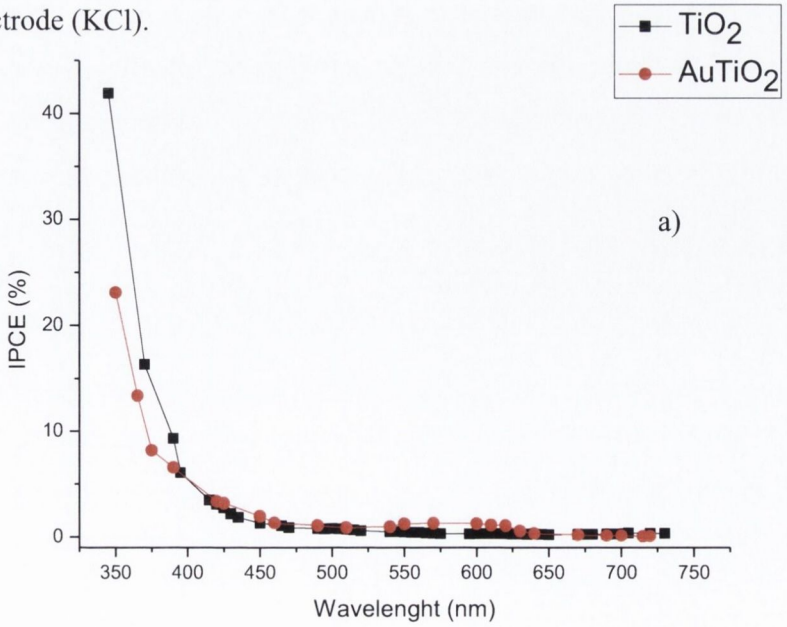

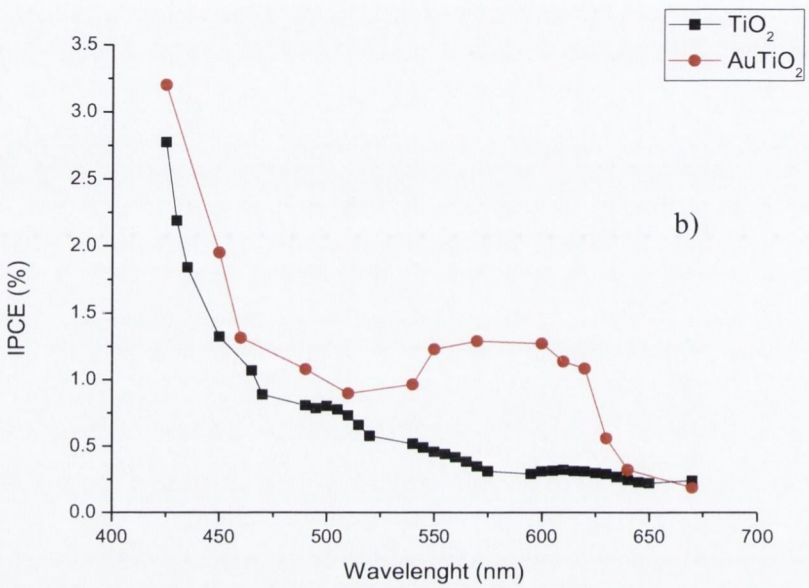

Figure 5.15 a) Full spectrum IPCE data obtained for TiO_2 and $AuTiO_2$ composite electrodes b) IPCE spectra of TiO_2 and $AuTiO_2$ in the plasmonic domain.

The IPCE data (Figure 5.15) shows clear evidence for the generation of plasmonic photocurrent. The IPCE data was recorded using a 150 W xenon discharge lamp. The output beam was passed through a monochromator followed by an optical chopper. The monochromatic light was chopped at a frequency of 90Hz and monitored using an oriel instruments spectrograph (model 77400) which was calibrated using a series of laser cut off filters (THOR Labs). The power of the frequency dependent light was calculated using a Si photodiode (Newport 818-UV-L) which output the frequency dependent signal to a lock-in-amplifier. IPCE data were recorded for both the unmodified TiO_2 electrode and the $AuTiO_2$ photoelectrode. Cells were fabricated in a sandwich configuration with a 25 μm surlyn spacer, a Pt CE prepared via deposition of H_2PtCl_6 (aq.) and a $[Co(II/III)bpy_3](PF_6)_{2/3}$ redox mediator. The electrolyte composition for IPCE experiments was as follows, 0.22 M $[Co(II)bpy_3](PF_6)_2$, 0.03 M $[Co(III)bpy_3](PF_6)_3$, 0.1M $LiClO_4$ and 0.5 M tert-butyl pyridine in acetonitrile. IPCE values were calculated using the following expression:

$$IPCE(\%) = \frac{Isc(A)}{W\,(W)} \cdot \frac{1240}{\lambda(nm)} \cdot 100 \qquad (1)$$

Upon excitation at the plasmonic wavelength the IPCE was observed to increase from 0.30% for unmodified TiO_2 to 1.27% for the Au modified system. These results are in close agreement with the photocurrent observed in the photoaction spectra (Figure 5.12) and also correlate closely with the UV-Vis spectra obtained for the Au TiO_2 composite electrode (IPCE is slightly red shifted for $AuTiO_2$), indicating that maximum photocurrent is obtained in the region of maximum plasmonic intensity. It has also been observed that the plasmonic photocurrent scales linearly with input power. Photocurrent decay experiments (Figure 5.16) carried out at the plasmonic wavelength show a direct correlation between input power and the plasmonic photocurrent.

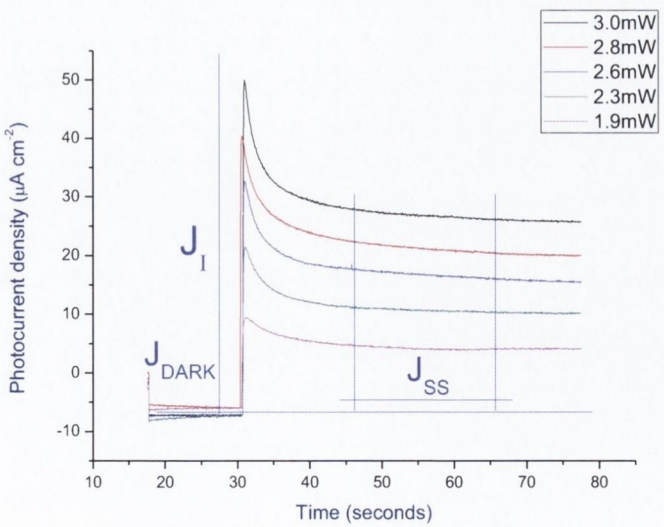

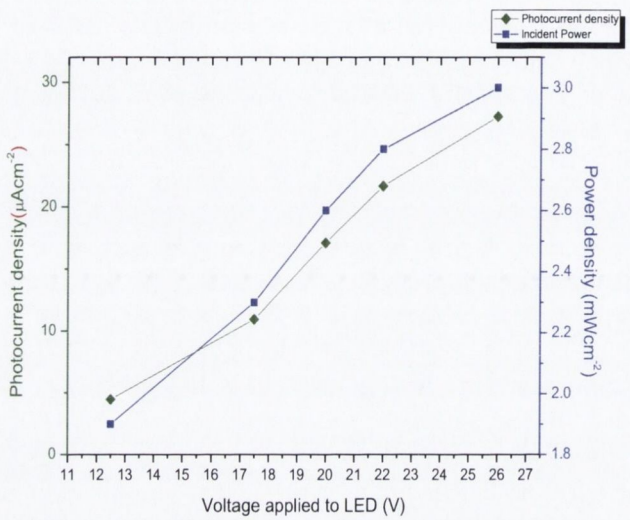

Figure 5.16 Linear relationship between input power ($mWcm^{-2}$) on plasmonic photocurrent (μA; @50 s) generation.

Analysis of the ΔIPCE spectrum (Figure 5.17), whereby ΔIPCE = $IPCEAu\text{-}TiO_2$ – $IPCETiO_2$, reveals the contribution of only the gold NPs to the overall photocurrent. The ΔIPCE shows that the gold nanoparticles affect the overall photocurrent through 3 distinct mechanisms. The first mechanism is the production of plasmonic photocurrent (discussed earlier), which can be considered as a positive contributor the photocurrent production.

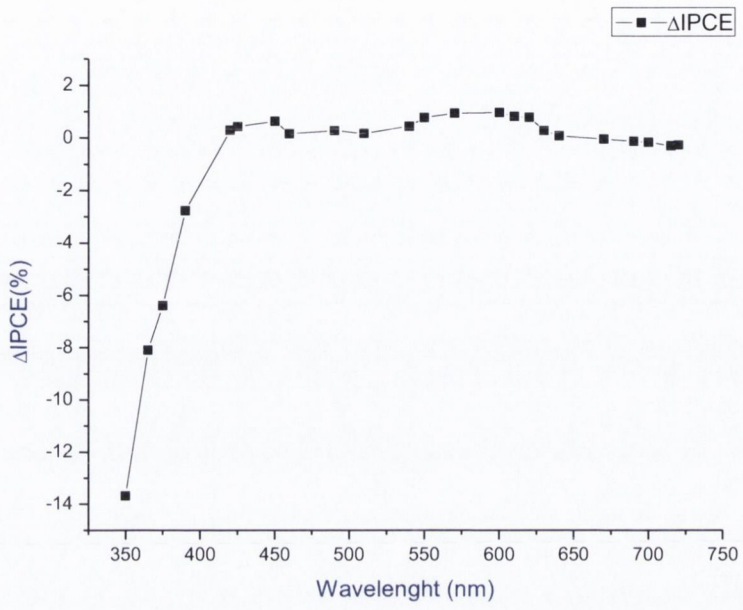

Figure 5.17 ΔIPCE spectra (ΔIPCE = IPCE$AuTiO_2$ – IPCETiO_2)

The second mechanism is the production of photocurrent through inter-band *d-sp* transitions within the gold nanoparticles. ΔIPCE spectra shows the generation of inter-band photocurrent at 449 nm, with a quantum efficiency of 0.6% which is in exceptionally good agreement with that predicted by theory (426 nm). The photocurrent resulting for inter-band transitions can also be considered as a positive contributor to the overall photocurrent.

As the excitation wavelength is extended into the UV region, the presence of AuNPs suppresses the production of current. IPCE values obtained at 345 nm show a decreased in photocurrent output from ~42% for TiO_2 to ~23% for $AuTiO_2$ composite. This substantial decrease in photocurrent (44%) is attributed to the back transfer of UV excited TiO_2 electrons to Au nanoparticles trap states, which lie on the surface of gold. The presence of Au nanoparticles can be considered as a negative contributor to overall photocurrent when illumination is in the UV region.

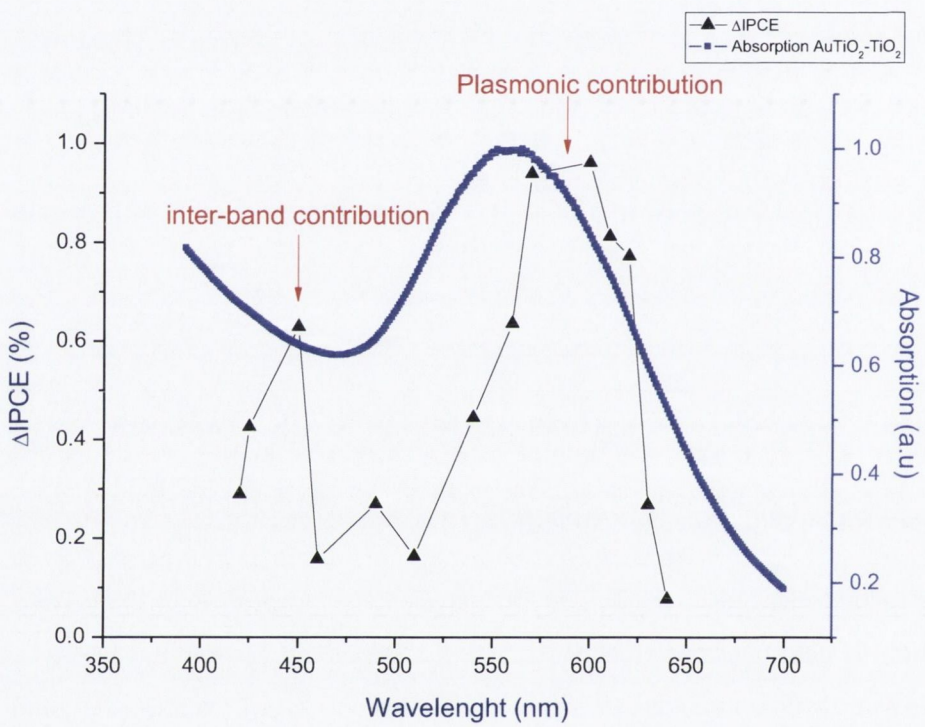

Figure 5.18 Experimental data for ΔIPCE and the comparison with the plasmon absorption peak. The absorption peak is blue-shifted

J-V characteristics (Figure 5.19) were also recorded in a 3 electrode electrochemical cell under illumination at 550 nm. The dependence of the photocurrent on the applied voltage provides important information on the processes occurring in the Au - TiO_2 electrode. The I-V data recorded shows a large increase in short circuit current for the Au modified TiO_2 when compared to the unmodified TiO_2. The Jsc value increases from ~2μA cm^{-2} to just under 30μA cm^{-2}, which is a significant increase in the photocurrent which we attribute to the plasmonic injection of hot electrons from gold NPs into TiO_2.

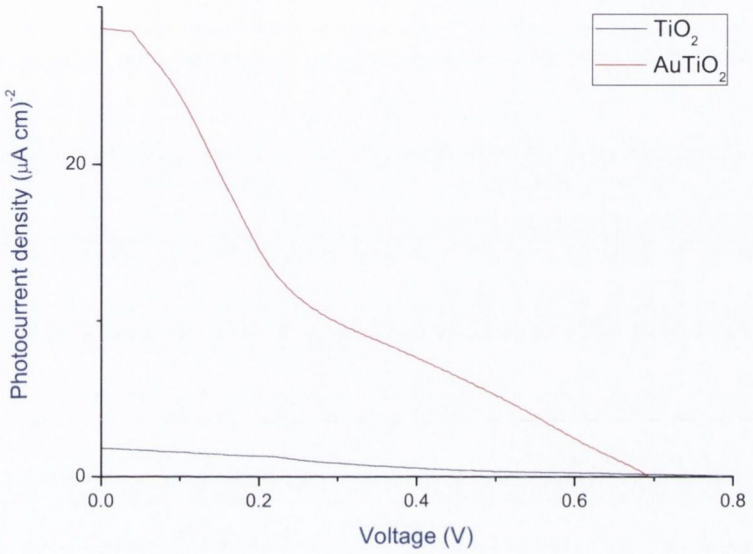

Figure 5.19 Photocurrent dependence as a function of applied voltage for TiO_2 and Au -TiO_2 under excitation at 525 nm (3.0mW)

A theoretical description for all of the above processes is outlined below. The theoretical contribution to this work was kindly performed by Prof. Alexander Govorov of Ohio State University.

5.5 Theoretical investigations

5.5.1 The contribution of the hot palsmonic electrons of Au NPs to the photocurrent

The paper[17] describess the theory of photo-generated electrons in plasmonic NPs. The rate of generation of electrons above the barrier energy, $\Delta E_{b,electrons} = 0.9eV$, is given by the following integral:

$$Rate_{NP} = Rate_{\text{excited electrons},\, \varepsilon > E_F + 0.9eV}(\omega) = \int_{E_F+0.9eV}^{+\infty} \delta Rate(\varepsilon) d\varepsilon$$

,

$$\delta Rate(\varepsilon) = \frac{4}{\hbar} \sum_{\alpha=(n,l,m)} \sum_{\alpha'=(n',l',m')} (f_{\alpha'}^0 - f_\alpha^0) \left| e \cdot \varphi_{\alpha,\alpha'} \right|^2 \Phi(\varepsilon - \varepsilon_\alpha) \left[\frac{\Gamma}{(\hbar\omega - \varepsilon_\alpha + \varepsilon_{\alpha'})^2 + \Gamma^2} + \frac{\Gamma}{(\hbar\omega + \varepsilon_\alpha - \varepsilon_{\alpha'})^2 + \Gamma^2} \right]$$

where $\delta Rate(\varepsilon)$ gives the rate of excitation of electrons to the states with the excited energy ε ; This equation is similar to the Fermi's golden rule for the transition probability. Then, we obtain the total rate of excitation above the barrier by integrating this probability. The functions $\varphi_{\alpha,\alpha'}$ are the matric element of the plasmonic electric potential between quantum states α and α' in the spherical quantum well; $\Phi(\varepsilon - \varepsilon_\alpha)$ is a numerical delta function. Then, the total rate of generation of electrons in a sample $Rate_{sample} = N_{NP} Rate_{NP}$, where N_{NP} is the number of Au NPs in a sample. The total rate of incident photons:

$$I_{photons} = \frac{I_0 \cdot A}{\hbar\omega},$$

where the sample of the area is defined as A and the incident flux is given by I_0. Then, the corresponding contribution to the IPCE is estimated as

$$\Delta IPCE_{Au-NP,\,electrons} \sim \frac{Rate_{sample}}{I_{photon}} \cdot 100\% = \rho_{s,NP} \frac{Rate_{NP}}{I_0 / \hbar\omega} \cdot 100\%,$$

where $\rho_{s,NP}$ is the surface density of NPs in the sample that was estimated for our model to be $\rho_{s,NP} \sim (12nm)^{-2}$.

5.5.2 The contribution of the hot holes of Au NPs to the photocurrent

It was identified in refs.[17] and[31] that hot plasmonic holes in Au NPs are efficiently generated via the inter-band d-sp transitions. The rate of such inter-band transitions can be estimated from the rate of inter-band absorption in Au NPs [31]. The rate of inter-band absorption is given by the Mie theory:

$$Q_{\text{inter-band}} = I_0 \cdot \sigma_{\text{abs,inter-band}} = I_0 \cdot \frac{1}{\sqrt{\varepsilon_0}} V_{NP} \omega \left| \frac{3\varepsilon_0}{2\varepsilon_0 + \varepsilon_{Au}} \right|^2 \text{Im}[\varepsilon_{\text{Au, inter-band}}],$$

where the inter-band contribution to the Au dielectric constant[31] is given by

$$\varepsilon_{\text{Au, inter-band}} = \varepsilon_{bulk\ Au}(\omega) + \frac{\omega_p^2}{\omega^2 + i\omega \cdot \Gamma_{bulk,D}}.$$

The rate of generation of holes in the d-band of Au is then calculated as $Rate_{NP,holes} = Q_{\text{inter-band}} / \hbar\omega$. The corresponding contribution to the IPCE becomes

$$\Delta IPCE_{Au-NP,\,electrons} \sim \rho_{s,NP} \frac{Rate_{NP,holes}}{I_0 / \hbar\omega} \cdot 100\% .$$

5.5.3 The contribution from the electrons and holes generated *via* inter-band absorption in TiO_2.

Here we use the bulk refractive index of TiO_2 taken from the database[47]. The rate of inter-band absorption in the TiO_2 slab can be estimated as

$$Q_{TiO_2} = I_0(1 - e^{-2 \cdot k_0 L \cdot n_2}),$$

where the symbols have been defined in the main text. Then, the rate of degeneration of electron and holes in the whole sample $Rate_{TiO_2,tot} = Q_{TiO_2} / \hbar\omega$. The effect of Au NPs comes from the probability to trap electrons and holes inside NPs removing such carriers from the photo-current,

$I_{TiO_2-Au} - I_{TiO_2} = P_{trap} \cdot Rate_{TiO_2,tot}$. The related term in the IPCE then becomes

$$\Delta IPCE_{TiO_2,\,electrons\ and\ holes} = \frac{P_{trap} Rate_{TiO_2,tot}}{I_{photon}} \cdot 100\% = P_{trap}(1 - e^{-2 \cdot k_0 L \cdot n_2}) \cdot 100\% .$$

The trapping probability, P_{trap}, is an unknown parameter and depends on a complicated dynamics of photo-generated carriers. Since the absorption rate in 3-μm TiO_2 film is very strong in the UV and starts abruptly at 391nm, our result does not depend much on the coefficient P_{trap}. Basically the contribution $\Delta IPCE_{TiO_2,\,electrons\ and\ holes}$ looks like a negative step function at 391nm (Figure 13 for $\Delta IPCE(\lambda)$). To be definitive, we took $P_{trap} = 0.3$.

It is interesting to compare the absorption and IPCE efficiency spectra (Figure 5.20). The plasmonic peak in the IPCE in both experiment and theory is red-shifted. This effect can be explained in the following way: This peak originates from the over-barrier injection of hot plasmonic carriers. The generation rate in this case is proportional to the product of the plasmon enhancement factor and a coefficient $\frac{(\hbar\omega - \Delta E_b)}{\omega^4}$ (see equation for $Rate_{NP}$ in the main text). The coefficient $\frac{(\hbar\omega - \Delta E_b)}{\omega^4}$ comes from the quantum amplitudes of optical transitions in a NC. These amplitudes and the coefficient increase with increasing the wavelength and therefore the position of the plasmonic maximum in the function $Rate_{NP}$ becomes red-shifted. This example shows that, in general, the photocurrent and absorption spectra are not proportional to each other. More discussions on this behavior can be found in refs.[17,31]

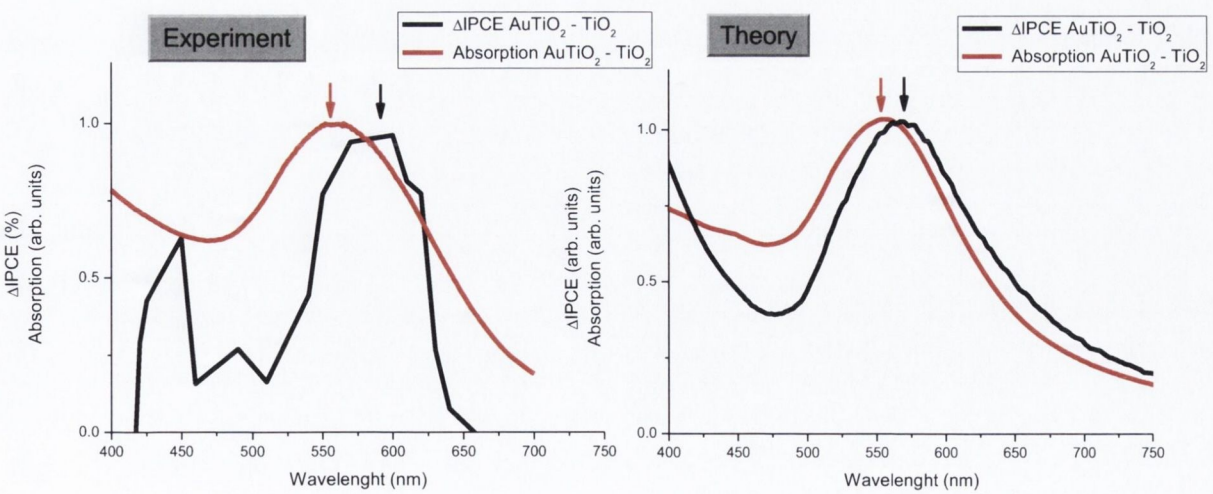

Figure 5.20 Comparison of IPCE and absorption spectra for both experiment and theory.

To understand the structure of the spectrum of $\Delta IPCE(\lambda)$ shown in figure 5.17, we now present the photo-injected current in a sample as a sum of three terms since the photocurrent has it origin in three processes:

$$I_{tot} = I_{Au-NP,\,electrons} + I_{Au-NP,\,holes} + I_{TiO_2,\,electrons\,and\,holes}, \quad (1)$$

where the first two terms describe the photocurrents coming from the injection of electrons and holes from plasmonic Au NPs, respectively, and the last term is the bulk photocurrent in the TiO_2 matrix. Figure 12 illustrates the corresponding processes. The change in the IPCE due to the presence of Au NPs is defined as

$$\Delta IPCE = IPCE_{TiO_2-Au} - IPCE_{TiO_2} = \frac{I_{tot,TiO_2-Au} - I_{tot,TiO_2}}{I_{photon}} \cdot 100\%,$$

where $I_{photon} = I_0 \cdot A / \hbar\omega$ is the rate of incident photons hitting the sample of the area A and I_0 is the incident flux. Using Eq. 1, we can now split the change of IPCE into three contributions,

$$\Delta IPCE = \Delta IPCE_{Au-NP,\,electrons} + \Delta IPCE_{Au-NP,\,holes} + \Delta IPCE_{TiO_2,\,electrons\,and\,holes}.$$

We now start with the first term, which is rate of the injection of hot plasmonic electron from the Au NPs. This term can be estimated as the rate of excitation of electrons above the barrier ΔE_B

$$\Delta IPCE_{Au-NP,\,electrons} \sim \frac{N_{NP} Rate_{NP}}{I_0 \cdot A / \hbar\omega} \cdot 100\% = \rho_{s,NP} \frac{Rate_{NP}}{I_0 / \hbar\omega} \cdot 100\%,$$

where $Rate_{NP}$ is the rate of excitation of electrons above the barrier for one NP and $\rho_{s,NP}$ is the surface density of NPs in the sample. The rate $Rate_{NP}$ should be calculated using the quantum mechanical approach based on the excitation probabilities given in supporting information.[17,31] This term is proportional to the field-enhancement factor and exhibits the plasmon resonance in a NP

$$Rate_{NP} \sim |\gamma_{NP}(\omega)|^2 \frac{(\hbar\omega - \Delta E_b)}{\omega^4} = \left| \frac{3\varepsilon_0}{3\varepsilon_0 + \varepsilon_{Au}(\omega)} \right|^2 \frac{(\hbar\omega - \Delta E_b)}{\omega^4},$$

where $\varepsilon_{Au}(\omega)$ and ε_0 are the dielectric constants of Au and matrix, respectively.[17] Since the TiO_2 matrix is highly porous, the effective dielectric constant of the matrix is expected to be lower than that of TiO_2 and should be obtained from the fitting of the plasmon peak in the absorption spectra. From this fitting, we get $\varepsilon_0 = 3$. For the Au NPs, we use the empirical dielectric constant from Ref.[48] The contribution $\Delta IPCE_{Au-NP,\,holes}$ comes from the strong hole generation from the d-band of Au NPs and it is a bulk effect.[31] This contribution can be calculated from the absorption spectrum using the bulk band structure of Au. The details are in SI. The term $\Delta IPCE_{TiO_2,\,electrons\ and\ holes}$ appear from the inter-band transitions and is proportional to the absorption rate of the TiO_2 film and the probability of trapping electron and holes by the Au NPs. It can be estimated by the equation:

$$\Delta IPCE_{TiO_2,\,electrons\ and\ holes} \sim P_{trap}(1 - e^{-2 \cdot k_0 L \cdot n_2}) \cdot 100\%,$$

where L, k_0 and n_2 are the film width, vacuum wave vector of light and imaginary part of the refractive index, respectively; P_{trap} is the trapping probability of carriers in the TiO_2 film. Figure 5.20 shows the calculated spectrum $\Delta IPCE$ and its contributions. Our calculations reproduce well the positions and signs of the contributions, but we did not attempt to calculate

the magnitude since the dynamics and trapping of electrons and holes in the Au TiO_2 composite is very complex.

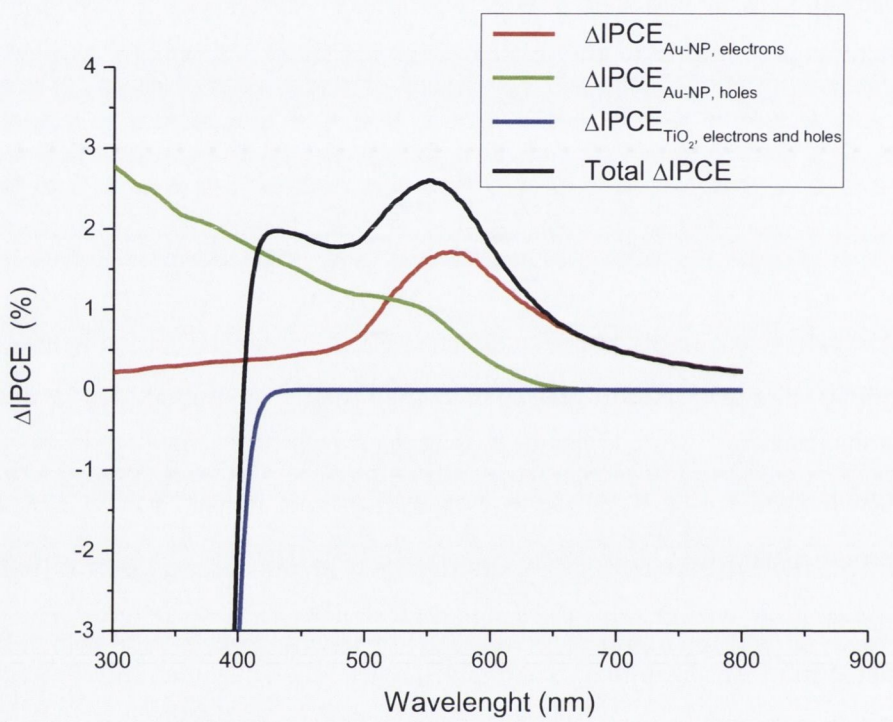

Figure 5.21 Calculated contributions to $\Delta IPCE(\lambda)$. The graph shows estimated terms $\Delta IPCE_{Au-NP,\,electrons}$, $\Delta IPCE_{Au-NP,\,holes}$, $\Delta IPCE_{TiO_2,\,electrons\ and\ holes}$ and also the calculated full spectrum $\Delta IPCE$.

Our theory also reveals the origin of the peaks in the experimental spectrum for $\Delta IPCE(\lambda)$ and explains the physical picture. In Figure 5.21, we see the following calculated features: (1) The calculated peak at 570 nm is the plasmon peak due to the generation of over-barrier electrons; this peak comes from the terms $\Delta IPCE_{Au-NP,\,electrons}$ and exhibits the plasmon peak because of the e field enhancement inside the Au nanoparticles at the plasmon wave length that correspondingly leads to an amplification of the hot electron injection; (2) The structure that

appears in the wavelengths interval $\lambda \sim 520\ nm$. This interval corresponds to the onset of the intensive inter-band generation of holes in the d-band of Au nanoparticles by the photons with $\hbar\omega > \Delta E_{holes} = 2.3eV$ (see the diagram in Figure 5.22); (3) finally, the last structure is due to the inter-band generation of electrons and holes in the TiO_2 film. This stricture is in the interval $\lambda < 390nm$ that corresponds to the inter-band absorption above the TiO_2 bandgap for photon energies $\hbar\omega > E_g = 3.2eV$.

A schematic band diagram of the Au TiO_2 system and the optical and relaxation processes involved in the photocurrent model are shown in Figure 5.22. The hot electron-hole pair can be excited in TiO_2 (the left-hand side) or in Au nanoparticles (the right-hand side of the Figure 5.22). In the case of Au nanoparticles, the hole can be excited in the *sp*-bands or in the *d*-band. The excitation of hole in the *d*-band is especially prominent since such holes have a large density of states. The vertical red arrows depict the optical excitation processes whereas the horizontal black arrows show the transport processes such as injection from a NP, trapping in a NP and electron transfer from the Co mediator.

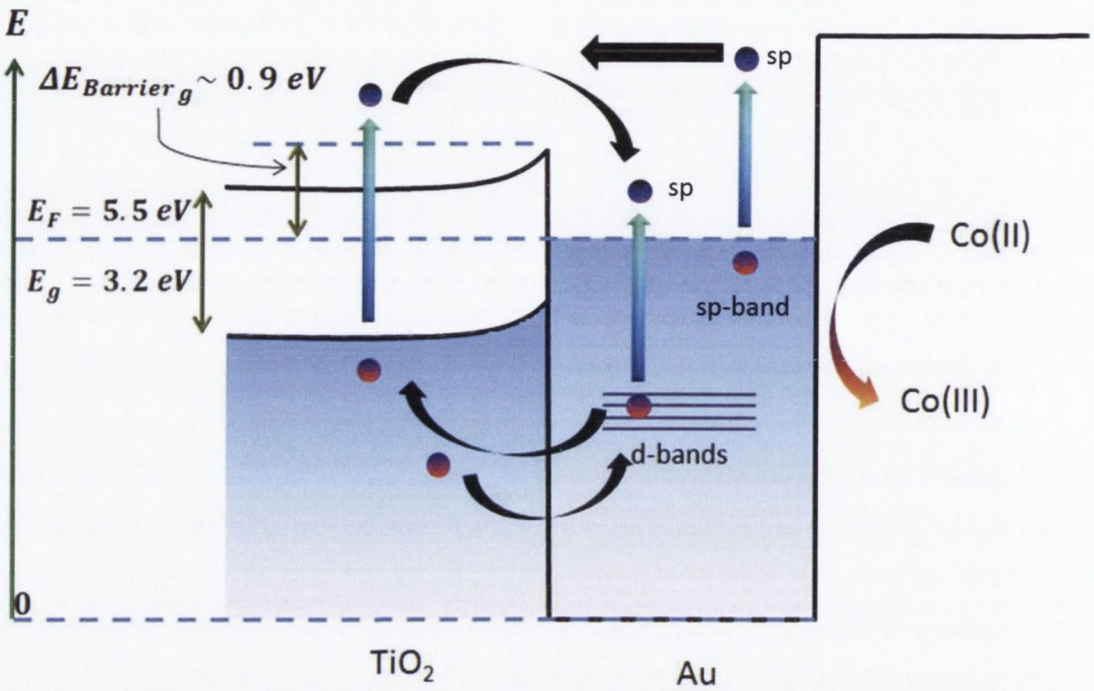

Figure 5.22 Band diagram of the Au -TiO_2 system and the optical and relaxation processes used in the photocurrent model. Blue and red dots represent photo-generated hot plasmonic electrons and holes, respectively.

5.6 Conclusions

In conclusion we have developed a new approach for introducing gold nanoparticles into nanoporous TiO_2 films. Most importantly we have demonstrated that the optoelectronic characteristics of these composite electrodes can be controlled precisely with the application of heat treatment. In addition to the control of optical characteristics, the heat treatment serves as a tool for significant increasing of the plasmonic photocurrent under illumination. We have observed plasmonic injection from Au NPs to TiO_2 with a quantum efficiency of 1.27% utilizing the $[Co(II/III)bpy_3](PF_6)_{2/3}$ redox mediator. The presence of gold inter-band transition was also observed as a positive contributor to the overall photocurrent. Importantly, our theoretical calculations accurately match the results obtained from photo- physical studies

providing a detailed explanation of the process occurring at the Au-TiO_2 interface. Our theory also reveals the origin of the peaks in the experimental spectra for $\Delta IPCE(\lambda)$ and explains the physics behind the spectral features. We expect that further improvements in photocurrent

output can be achieved through optimization of the photoactive layer thickness and its architecture. We also believe that these Au-TiO_2 nanocomposite systems may find a range of potential applications including the use as photoanode materials for solar energy harvesting and in new types of photocatalytic and optical sensing devices.

References

(1) Kelly, K. L.; Coronado, E.; Zhao, L. L.; Schatz, G. C. *The Journal of Physical Chemistry B* **2002**, *107*, 668.

(2) Jordan, C. E.; Corn, R. M. *Analytical Chemistry* **1997**, *69*, 1449.

(3) Nelson, B. P.; Grimsrud, T. E.; Liles, M. R.; Goodman, R. M.; Corn, R. M. *Analytical Chemistry* **2000**, *73*, 1.

(4) Ozbay, E. *Science* **2006**, *311*, 189.

(5) Nylander, C.; Liedberg, B.; Lind, T. *Sensors and Actuators* **1982**, *3*, 79.

(6) Liedberg, B.; Nylander, C.; Lunström, I. *Sensors and Actuators* **1983**, *4*, 299.

(7) Homola, J.; Yee, S. S.; Gauglitz, G. *Sensors and Actuators B: Chemical* **1999**, *54*, 3.

(8) Catchpole, K. R.; Polman, A. *Opt. Express* **2008**, *16*, 21793.

(9) Ferry, V. E.; Munday, J. N.; Atwater, H. A. *Adv. Mater.* **2010**, *22*, 4794.

(10) Nakayama, K.; Tanabe, K.; Atwater, H. A. *Applied Physics Letters* **2008**, *93*, 121904.

(11) Pala, R. A.; White, J.; Barnard, E.; Liu, J.; Brongersma, M. L. *Adv. Mater.* **2009**, *21*, 3504.

(12) Ferry, V. E.; Verschuuren, M. A.; Li, H. B. T.; Verhagen, E.; Walters, R. J.; Schropp, R. E. I.; Atwater, H. A.; Polman, A. *Opt. Express* **2010**, *18*, A237.

(13) Tian, Y.; Tatsuma, T. *Journal of the American Chemical Society* **2005**, *127*, 7632.

(14) Wu, K.; Rodríguez-Córdoba, W. E.; Yang, Y.; Lian, T. *Nano Letters* **2013**.

(15) Zhang, Z.; Zhang, L.; Hedhili, M. N.; Zhang, H.; Wang, P. *Nano Letters* **2012**, *13*, 14.

(16) Brown, M. D.; Suteewong, T.; Kumar, R. S. S.; D'Innocenzo, V.; Petrozza, A.; Lee, M. M.; Wiesner, U.; Snaith, H. J. *Nano Letters* **2010**, *11*, 438.

(17) Govorov, A. O.; Zhang, H.; Gun'ko, Y. K. *The Journal of Physical Chemistry C* **2013**, *117*, 16616.

(18) Nishijima, Y.; Ueno, K.; Yokota, Y.; Murakoshi, K.; Misawa, H. *The Journal of Physical Chemistry Letters* **2010**, *1*, 2031.

(19) Singh, V.; Beltran, I. J. C.; Ribot, J. C.; Nagpal, P. *Nano Letters* **2014**, *14*, 597.

(20) Thrall, E. S.; Steinberg, A. P.; Wu, X. M.; Brus, L. E. *Journal of Physical Chemistry C* **2013**, *117*, 26238.

(21) Mukherjee, S.; Libisch, F.; Large, N.; Neumann, O.; Brown, L. V.; Cheng, J.; Lassiter, J. B.; Carter, E. A.; Nordlander, P.; Halas, N. J. *Nano Letters* **2013**, *13*, 240.

(22) Mukherjee, S.; Zhou, L. A.; Goodman, A. M.; Large, N.; Ayala-Orozco, C.; Zhang, Y.; Nordlander, P.; Halas, N. J. *Journal of the American Chemical Society* **2014**, *136*, 64.

(23) Brown, P.; Kamat, P. V. *Journal of the American Chemical Society* **2008**, *130*, 8890.

(24) Kim, H.-S.; Ko, S.-B.; Jang, I.-H.; Park, N.-G. *Chemical Communications* **2011**, *47*, 12637.

(25) Fang, Z. Y.; Liu, Z.; Wang, Y. M.; Ajayan, P. M.; Nordlander, P.; Halas, N. J. *Nano Letters* **2012**, *12*, 3808.

(26) Fang, Z. Y.; Wang, Y. M.; Liu, Z.; Schlather, A.; Ajayan, P. M.; Koppens, F. H. L.; Nordlander, P.; Halas, N. J. *Acs Nano* **2012**, *6*, 10222.

(27) Knight, M. W.; Sobhani, H.; Nordlander, P.; Halas, N. J. *Science* **2011**, *332*, 702.

(28) Knight, M. W.; Wang, Y. M.; Urban, A. S.; Sobhani, A.; Zheng, B. Y.; Nordander, P.; Halas, N. J. *Nano Letters* **2013**, *13*, 1687.

(29) Sikora, J.; Halas, S. *Rapid Communications in Mass Spectrometry* **2011**, *25*, 689.

(30) Sobhani, A.; Knight, M. W.; Wang, Y. M.; Zheng, B.; King, N. S.; Brown, L. V.; Fang, Z. Y.; Nordlander, P.; Halas, N. J. *Nature Communications* **2013**, *4*.

(31) A.O. Govorov, H. Z., V. Demi, and Yurii K. Gun'ko *NanoToday DOI: 10.1016/j.nantod.2014.02.006]*.

(32) Griffin, F.; Fitzmaurice, D. *Langmuir* **2007**, *23*, 10262.

(33) Chandrasekharan, N.; Kamat, P. V. *Nano Letters* **2000**, *1*, 67.

(34) Gratzel, M. *Nature* **2001**, *414*, 338.

(35) Salant, A.; Shalom, M.; Hod, I.; Faust, A.; Zaban, A.; Banin, U. *Acs Nano* **2010**, *4*, 5962.

(36) Teranishi, T.; Hosoe, M.; Tanaka, T.; Miyake, M. *The Journal of Physical Chemistry B* **1999**, *103*, 3818.

(37) Giersig, M.; Mulvaney, P. *The Journal of Physical Chemistry* **1993**, *97*, 6334.

(38) Wang, Y.; Pang, X.; Zhitomirsky, I. *Colloids and Surfaces B: Biointerfaces* **2011**, *87*, 505.

(39) Gao, B.; Yue, G. Z.; Qiu, Q.; Cheng, Y.; Shimoda, H.; Fleming, L.; Zhou, O. *Adv. Mater.* **2001**, *13*, 1770.

(40) Boccaccini, A. R.; Cho, J.; Roether, J. A.; Thomas, B. J. C.; Jane Minay, E.; Shaffer, M. S. P. *Carbon* **2006**, *44*, 3149.

(41) Wu, Z.-S.; Pei, S.; Ren, W.; Tang, D.; Gao, L.; Liu, B.; Li, F.; Liu, C.; Cheng, H.-M. *Adv. Mater.* **2009**, *21*, 1756.

(42) Alvarez, M. M.; Khoury, J. T.; Schaaff, T. G.; Shafigullin, M. N.; Vezmar, I.; Whetten, R. L. *The Journal of Physical Chemistry B* **1997**, *101*, 3706.

(43) Lin, X. M.; Wang, G. M.; Sorensen, C. M.; Klabunde, K. J. *The Journal of Physical Chemistry B* **1999**, *103*, 5488.

(44) Yu, J.; Dai, G.; Huang, B. *The Journal of Physical Chemistry C* **2009**, *113*, 16394.

(45) Hagfeldt, A.; Lindström, H.; Södergren, S.; Lindquist, S.-E. *Journal of Electroanalytical Chemistry* **1995**, *381*, 39.

(46) Tafalla, D.; Salvador, P.; Benito, R. M. *Journal of The Electrochemical Society* **1990**, *137*, 1810.

(47) http://refractiveindex.info/legacy/?group=CRYSTALS&material=TiO2.

(48) Johnson, P. B.; Christy, R. W. *Physical Review B* **1972**, *6*, 4370.

Chapter 6

Conclusions and future work

6.1 Conclusions

In this work various photovoltaic materials have been prepared and investigated as potential candidates for increasing the efficiency of sensitized solar cells. We have focused our work on developing alternative strategies for enhancing solar cell performance by optimising the 3 main components of a dye sensitized solar cell, namely the electrolyte, the working electrode (WE) and the counter electrode (CE). We believe that the work we have presented in this thesis has successfully demonstrated the possibilities of using nanostructured materials in various parts of the DSSC.

The initial aim of this work was to develop a system for building DSSC devices reproducibly. In order to achieve this goal, it was necessary to focus our attention on the reproducible production of TiO_2 WEs. As the WE serves as the main component of the DSSC, responsible for light absorption, dye adsorption and charge separation, it was deemed necessary to optimise the procedure for fabricating nano-structured TiO_2 WEs. Our initial approach looked at using the doctor blade method for fabricating WEs from commercial TiO_2 pastes. This method worked by swiping the TiO_2 paste over a mask which was adhered to an FTO glass substrate. Once the mask was removed the electrodes we sintered and used as DSSC WEs. The doctor blade method allowed us to fabricate electrodes in large quantities. Unfortunately the majority of the electrodes fabricated using this method were very unstable and frequently cracked severely and flaked off the glass substrates after the heat treatment. This was most likely due to the fact that this method produced quite thick electrodes, approaching 30 μm in thickness. The evaporation of gaseous by-products during the sintering process was believed to be responsible for the cracking which was frequently observed in electrodes fabricated using the doctor blade approach. Therefore, in order to increase the quality and reproducibility of the WEs, we focused our attention on screen printing of TiO_2 as a possible method for fabricating WEs. The screen printing setup was specifically designed with this aim in mind. TiO_2 pastes were fabricated from Degussa P25 TiO_2 nanoparticles and this paste was used in conjunction with a 90-T polyester mesh for the printing. We introduced a pre and post

$TiCl_4$ treatment as a means of increasing the stability and efficiency of the TiO_2 WEs. We also developed a sintering profile which allowed for the formation of stable and crack free electrodes. The electrodes formed using the screen printing method consisted on 9 individual layers of 20 nm TiO_2 and 2 layers of a commercial scattering TiO_2 paste, which contained particles between 150 -200 nm in size. WEs fabricated from the screen printing method were between 13-17 μm thick, as confirmed by SEM and profilometry. The electrodes also showed extremely reproducible I-t responses when subjected on on/off illumination cycles, varying as little as 1 μAcm^{-2} between electrodes. These electrodes were thus deemed suitable for use as the WE of choice for all subsequent chapters of this thesis, unless stated otherwise.

Another goal of this research was to develop a new type of electrolyte for DSSCs. We believe that the conventional electrolyte formulation, which is based upon volatile organic solvents has numerous problems. The caustic nature of the conventional electrolyte can cause the polymer seal in these devices to degrade over time. These electrolytes are also unsuitable for high temperature applications, due to the low boiling point of acetonitrle. The use of a liquid electrolyte also causes problems during the manufacture of DSSCs as sealing a liquids layer can cause difficulties sealing.

In our work we have successfully shown that composite electrolytes based on ionic liquids (ILs) and graphene can be used as alternative electrolytes to build DSSCs which display promising efficiency and very good thermal stability. These electrolytes can also be made to be quasi solid materials, known as "bucky gels", depending on the quantity of graphene added to the IL.

Our results have shown that the addition of just 1 wt.% of graphene to the IL PMMI can increase the efficiency of the electrolyte 25 times when compared to the unmodified IL. We have demonstrated that DSSC utilising unmodified PMMI can operate with an efficiency of 0.1%, under 1 sun illumination. This value is increased to 2.6% when 1wt. % graphene is added to the electrolyte and processed properly. We have found that the presence of graphene in the IL can effectively reduced the oxidised form of the redox couple and hence reduces the diffusion length of the species in solution, resulting in an increase in solar cell efficiency. These results are a significant improvement from previous results reported by our group,[1] which showed that up to 30wt. % of graphene was required

to achieve such a noticeable increase in efficiency. We believe that this is due to the improvement in the way in which these electrolytes were processed. In this work we added liquid exfoliated graphene in $CHCl_3$ to the IL and evaporated the excess solvent to create the graphene IL composite. This method differed from our group's previous work where graphene was added in the solid state. Adding liquid exfoliated graphene to the IL allowed for an increased level of π -π interaction between the graphene sheets and the IL, allowing for the formation of a more stable composite to be formed with a more uniform dispersion of graphene. TGA studies using these electrolytes have also shown that they show thermal stabilities up to 300 °C, that is highly beneficial as DSSCs frequently operate at high temperature.

Additionally in this work we used an oxidised form of graphene, known as graphene oxide (GO) to act as a template for the deposition of metallic nanoparticles. This results in the formation of a 2D support material with plasmonic and catalytic properties. We found that both gold and platinum nanoparticles could be deposited onto GO using a reduction by borohydride. The nanoparticles formed without the need for a stabilising ligand and the reduction reaction also facilitated the partial reduction of GO to reduced graphene oxide (rGO). These materials were characterised with a range of techniques ranging from TEM, SEM, Raman and FT-IR spectroscopy, XRD and UV-Vis spectroscopy. The materials were deposited onto FTO glass substrates using an electrophoretic approach, whereby an electric field caused the material to deposit onto an electrode of opposite charge. The electrodes that were formed were examined as potential CEs for DSSCs. Electrochemical investigations revealed that PtrGO showed very prosing activity towards the reduction and oxidation of the iodide/tri-iodide redox couple. DSSCs that were fabricated using these electrodes performed extremely well. It was found that the PtrGO electrode could significantly outperform conventional thermally evaporated Pt. I-V results showed that PtrGO could reach efficiencies of 5.90% compared to 4% which was observed for Pt under 1 sun illumination. The AurGO composite also showed promising results, reaching an efficiency of 3.90 %. These results highlight the advantage of using a nano-structured composite electrode as the CE material in DSSCs.

In addition to this we have developed new routes to produce composites of GO and metal nanoparticles. Using a 2 step EPD approach it was found that Au NPs could be

successfully deposited into a porous GO electrode. These electrodes are currently under investigation as potential plasmonic photo sensing devices.

In this work we have also developed new photoactive electrodes for solar cells. These photoanodes were produced by infiltrating Au NPs into TiO_2 WEs. Using elemental line mapping it was found that the Au NPs could successfully infiltrate the electrode, given its porous nature. The infiltration of the Au NPs resulted in a significant increase in the optical absorption on the electrodes. We have also found that a heat treatment of the electrodes could be used to finely control the optical properties of the photoactive electrodes. We demonstrated that the sintering of the $AuTiO_2$ composite electrodes resulted in a significant increase in the plasmonic intensity associated with the optical resonance of the Au NPs. The position of the plasmon band was also observed to shift to the red region of the spectrum with increasing temperature. This indicated that the Au NPs were growing in size within the film and obtaining a narrower size distribution. We successfully demonstrated that the thermal treatment of the photoanodes could be used to increase the photocurrent generated from these devices as well as serving as a mechanism for tuning the electrodes optical properties. We have shown that the increase in the photocurrent response, post heat treatment, is a result of the insulating organic ligands being removed from the surface of the Au NPs and improving the sSchottky junction barrier between the Au and the TiO_2 particles. We have demonstrated that a purpose built IPCE experimental setup could be used to show that the Au NPs could inject plasmonic 'hot' electrons into TiO_2 with a quantum efficiency of 1.27% when compared to pure TiO_2. It was also observed that as well as generating plasmonic photocurrent the Au NPs also contributed to the photocurrent through interband contributions of Au NPs with a quantum efficiency of 0.6 %. In addition, looking at the UV region of IPCE spectra we observed Au NPs having a negative effect on the photocurrent values, decreasing photocurrent by 44 %. This decrease was attributed to the back transfer of UV excited TiO_2 electrons to trap states on the surface of the Au NPs. Crucially in this work we have provided theoretical modelling of this system and our theoretical calculations perfectly match our experimental observations.

Overall we believe that our work made several new contributions to the further development of solar energy harvesting devices with a particular emphasis on DSSCs. We Despite on the successful development of a range of new materials for solar cells, we acknowledge that some follow on research is necessary for further understanding and aid

the development of these materials further, towards potential commercialisation and the expansion of a greater range of applications for these new materials.

6.2 Future work

In order to further increase the photovoltaic performance of our new materials and to gain a greater understanding of the material properties it is important to consider some potential work which may be worth perusing in the future.

The research described in chapter 4 showed extremely promising results for composites if ILs and graphene. The IL used in this work, PMII, shows very poor efficiency as a standalone electrolyte. This is not the case for other types of ILs, in particular blended ILs. The group of Gratzel et al.[2,3] have shown that mixtures of ILs can be used to greatly increase the photovoltaic performance of IL electrolytes. They have produced a eutectic melt from 3 individual ILs to form a mixed electrolyte resulting in DSSCs with an efficiency of 6%. In addition they have blended various nanomaterials, such as SiO_2 NPs in IL electrolytes as a means of solidifying the IL electrolyte. Clearly there is more scope for producing a composite blended IL electrolyte with added graphene which may lead to an even greater enhancement in solar conversion efficiency. It is clear that the range of nanomaterials that can potentially be added to IL electrolytes may be largely expanded.and some further studies are necessary in this area.

The use of GO as a deposition substrate for metallic NPs could also be expanded considerably. Future work should focus on increasing the range of metal nanoparticles deposited onto GO and analysis of the resulting materials optical and catalytic properties. It may also be useful to see if GO can act as a support material for materials such as QDs, metal oxide nanoparticles and also for mixed deposition of metal nanoparticles. Such systems may greatly expand the potentials of such composite materials.

The work on GO included Raman mapping experiments, which were used to create detailed false colour images based upon the Raman spectra of GO. Similar Raman maps carried out on PtrGO and AurGO may show extremely interesting results and should be

explored in more detail in the future. These nanocomposites may act as promising materials for surface enhanced Raman scattering (SERS) and it may be possible to produce detailed images of the nanoparticles on the surface of GO using SERS. Raman mapping of these materials may also lead to a greater understanding of the structure of GO, which is still debated in the literature and may offer an insight into the nature in which particle adhere to the surface of GO, in particular the defect nature of GO at NP sites.

The catalytic properties of theses electrodes may be studied in the future, with particular attention paid to increasing the number of depositions through EPD. This may serve as a route to further increasing the photovoltaic performance of DSSCs fabricated using these CEs.

The work carried out in chapter 6 also opens up exciting routes for new research. The EPD approach and the development of the thermal treatment may offer opportunities to study mixed deposition of metal nanoparticles in TiO_2 layer. Initial results have shown that this is indeed possible with mixed solutions of Au and Pd NPs suspended in chloroform. This may allow us to extend the absorption range of these materials considerably and lead to an enhanced plasmonic photocurrent.

Future work is also necessary to examine altering the architecture of these plasmonic photocurrent devices. Using vertically aligned TiO_2 nanorods may allow for increased absorption of Au NPs into the photoactive electrode. Using nanorods may create porous channels which may be more suitable for sphericall NP infiltration when compared to the pores created by a TiO_2 nanoparticulate electrode. It is reasoned that the contact angle between a spherical Au NP and a vertically aligned TiO_2 rod may be favourable for contact between both nanostructures and hence charge separation and injection efficiency.

References

1) Ahmad, I.; Khan, U.; Gun'ko, Y. K. *Journal of Materials Chemistry* **2011**, *21*, 16990.

(2) Jhong, H.-R.; Wong, D. S.-H.; Wan, C.-C.; Wang, Y.-Y.; Wei, T.-C. *Electrochemistry Communications* **2009**, *11*, 209.

(3) Bai, Y.; Cao, Y. M.; Zhang, J.; Wang, M.; Li, R. Z.; Wang, P.; Zakeeruddin, S. M.; Gratzel, M. *Nature Materials* **2008**, *7*, 626.

Appendix

Optimisation of the fabrication procedure for TiO_2 working electrodes

A.1 Introduction

This appendix section on the development of a methodology for the fabrication of mesoporous TiO_2 photoanodes for DSSCs. The aim of the work was to develop a process for fabricating photoanodes with a reproducible thickness, topological profile, stability and with good adhesion to the FTO glass substrate, upon which the photoanodes are deposited. The development of this process would allow for DSSCs, or other solar cells to be fabricated with optimal efficiency and would also allow for comparisons to be made between devices when other parameters are changed.

The TiO_2 photoanode is the most important component of the DSSC. The TiO_2 photoanode serves multiple roles in the device and it is responsible for charge separation and the generation of high levels of photocurrent after sensitization has taken place. The TiO_2 photoanode is usually composed of a layer of 20 nm TiO_2 particles nanoparticles and a layer of TiO_2 particles with a size range between 150 – 200 nm. The layer of 20 nm particles is usually fabricated to be ~12 μm in thickness and it serves as a surface for molecular sensitisation, which expands the spectral absorption of the UV absorbing oxide into the visible region. This layer is commonly termed the light absorption layer, as it is the part of the cell which is primarily responsible for capturing and separating the electron – hole pair which is generated under illumination. The layer composed of the 150 – 200 nm particles is termed the scatter layer. This layer is not responsible for exciton separation (although electrodes fabricated solely from these particles do display moderate efficiency)[1] but acts to scatter the light which may have passed through the absorption layer, thus allowing for an increased chance of being absorbed by the sensitizer. Of all the phases of

TiO_2, anatase TiO_2 is generally chosen as the material of choice for working electrode fabrication, as it provides better device performance due to its broader bandgap (nanocrystalline titanium oxide electrodes for photovoltaic applications). Spherical or slightly truncated TiO_2 nanoparticles are usually used for the absorption of molecular sensitizers, as the large surface area afforded by these materials greatly enhances photocurrent. Other morphologies are also common. TiO_2 rods or wires have proven very effective as acting as a working electrode material, in particular for non-molecular sensitizers, such as semi-conducting quantum dots, or nanoparticles. The contact point between spherical nanoparticulate sensitizers, such as quantum dots or nanoparticles and TiO_2 rods or wires allows for increased loadings and has been shown to enhance photocurrent when compared to spherical TiO_2 nanoparticles. The wires also allow for enhanced electron transport to the conductive oxide when compared to spherical TiO_2 nanoparticles.

A.2 Fabrication of TiO_2 photoanodes

Initial attempts at fabricating TiO_2 photoanodes focused on using the doctor blade method for deposition of TiO_2 pastes onto conductive glass substrates. The doctor blade method uses a razor blade to deposit TiO_2 paste onto the FTO glass substrate. The deposition area is defined by a mask, which is fabricated from adhesive tape. The mask is placed onto the conductive glass substrate and a small portion of paste is placed in front of the mask opening. Using the razor blade, the paste is swiped over the mask opening, thus depositing a thin film of the paste onto the substrate. The resulting thickness of the deposited layer depends on the thickness of the tape employed, as well as the concentration of the TiO_2 and organic binders in the paste. Once the deposition had taken place the mask was then removed and the electrodes were sintered at 450 °C for 1 hour.

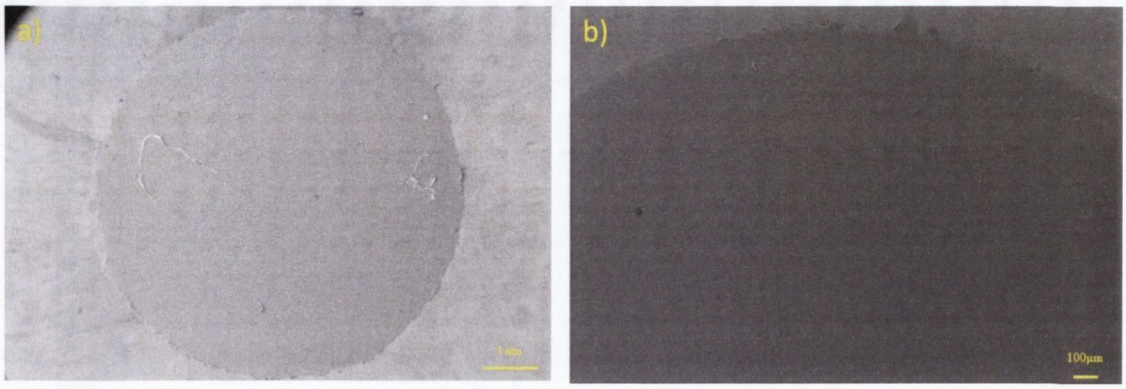

Figure A.1 Scanning electron microscopy images recorded for single layer deposition of TiO_2 onto FTO glass substrates using the doctor blade method.

Single layer deposition of the TiO_2 paste allowed for the formation of an even and crack free film of nanoparticulate TiO_2 to be deposited onto the substrate (Figure A.1). The thickness of the TiO_2 layer after a single deposition was measured to be ~ 3 µm in thickness, as measured through side profile imaging in SEM (Figure 3.2). In order for the DSSCs to operates with a reasonable efficiency it was deemed necessary to increase the thickness of the layer to ~15 µm in thickness, this would allow for much greater levels of dye adsorption for the WE and hence an increased photocurrent response.

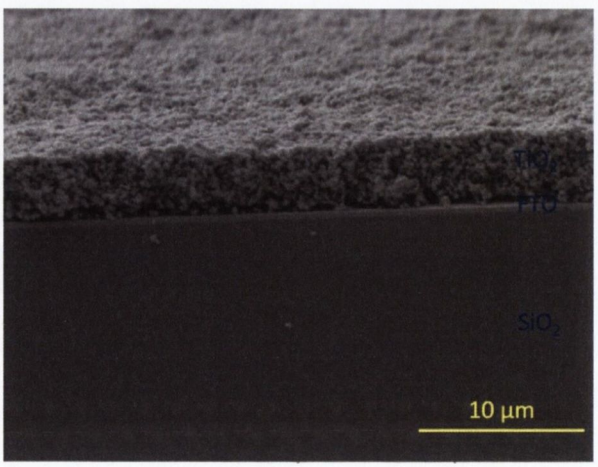

Figure A.2 SEM image of a single TiO_2 layer deposited onto FTO glass substrate through the doctor blade method.

In order to increase the thickness of the TiO_2 photoanodes, multiple depositions of TiO_2 were applied using the doctor blade approach. The deposition consisted of 4 layers of 20 nm TiO_2 and 1 layer of light scattering TiO_2 (150-200 nm particles). For the deposition of multiple layers of TiO_2, the tape template was reapplied to the slide, taking care to align the mask with the previous layer. After the addition of the final layer the tape mask was removed and the final TiO_2 coated FTO-glass slides were then sintered at 450 °C in an oven for one hour. The re-alignment of the mask after individual depositions proved to be a difficult step. Misalignment of the mask was frequently a problem and this would cause the electrodes to have multiple steps at the electrode edge thus leading to an uneven resulting electrode. The initial results from this approach were poor quality films showing severe cracking as well as poor adhesion of the TiO_2 layer to the FTO, as shown below in figure A.3. Cracks in the film measured by SEM were approximately 50 μm across and visible even to the naked eye. Multiple depositions of TiO_2 did allow for the fabrication of a much thicker TiO_2 electrode as can be seen from figure A.4 below. The side profile image of the electrodes show that the deposition of multiple layers led to a film thickness of ~20 μm. It was also observed that this method allowed for the formation of an electrode free from junctions between the individual printed layers which would increase electron transport through the depth of the film. From figure A.4 below the TiO_2 scatter layer (150 -200 nm particles) can clearly be observed on top of the TiO_2 absorption layer.

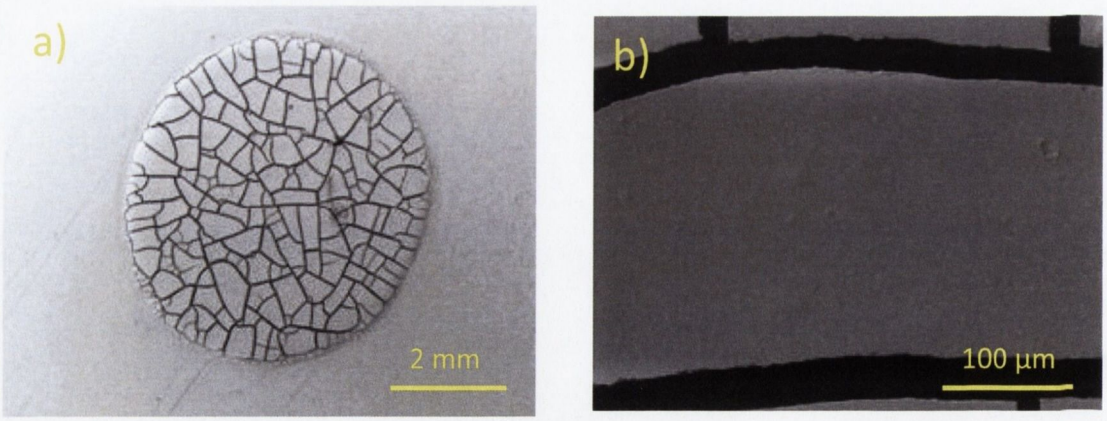

Figure A.3 SEM images of multiple layer TiO_2 electrodes fabricated using the doctor blade

method. Image a) shows a topographical image of the 2 cm^2 TiO_2 electrode with clear evidence of cracking. Image b) highlights the cracks in the film.

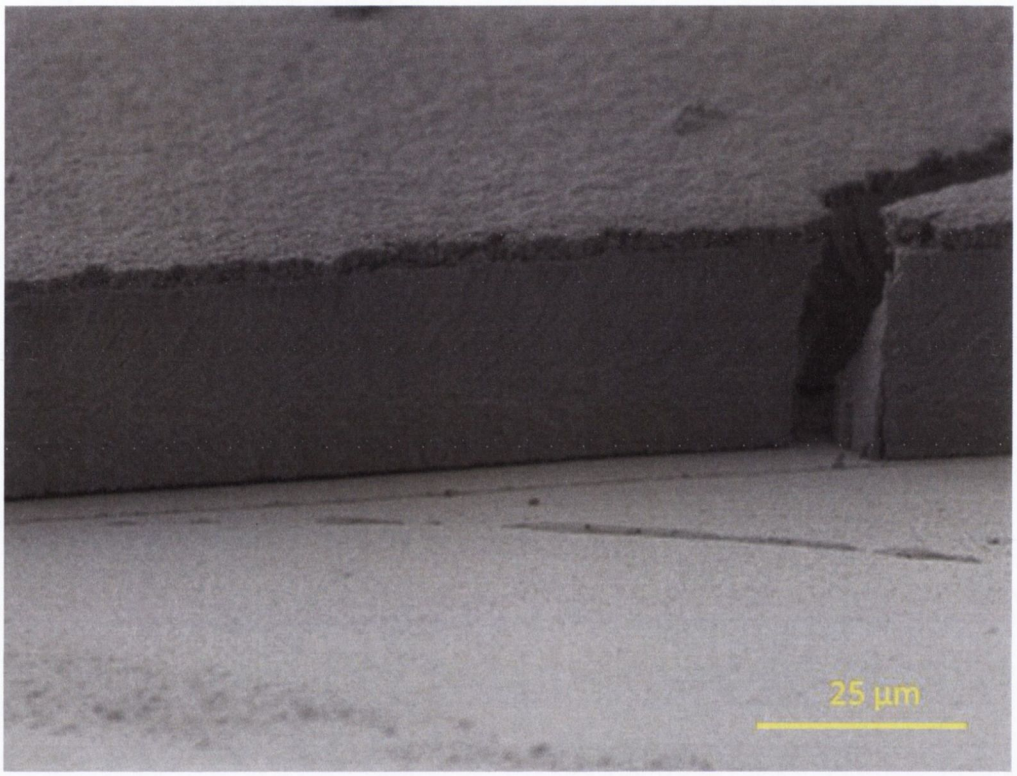

Figure A.4 Side profile SEM image of multiple layer TiO_2 deposition showing the light absorption layer and the scatter layer.

Cracking in the TiO_2 film is a result of outgassing from the TiO_2 paste during the sintering process. As the organic binders decompose at elevated temperatures, the gaseous products exit the film and cause the film to crack under the stress from the outgassing. Cracking was observed from almost all the electrodes and they were thus deemed unsuitable for further use. The profilometry image below (Figure A.5) was recorded for the sole un-cracked electrode that was produced using this method. The profile shows a very smooth film with a thickness profile matching that recorded through SEM imaging.

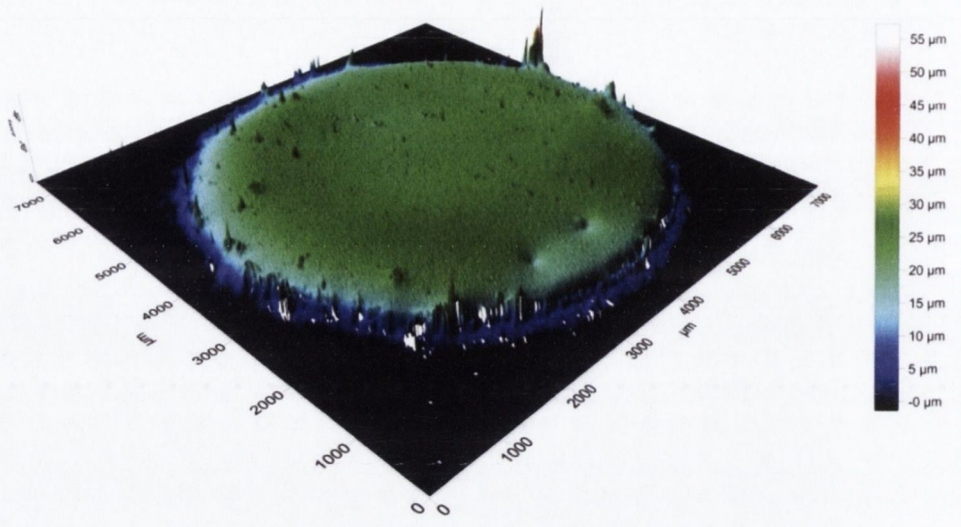

Figure A.5 Profilometry image recorded for a TiO_2 electrode fabricated using the doctor blade method.

As this was the only electrode fabricated using this approach, after approximately 60 attempts, this method of electrode fabrication was deemed unsuitable for further use and an alternative method was investigated.

The screen printing technique offered a more accurate and reproducible alternative to the doctor blade approach. This technique is a versatile method for the deposition of a whole host of materials, provided that the material can be homogenously dispersed in binding materials to form a paste. The binders can be removed with a thermal treatment, leaving only the material of interest behind. The manual screen printer which was designed consisted of a moveable screen holder; a pre designed polyester screen, a printing platform and a manual squeegee. The screen holder was adhered to a bench top and served as a stable, moveable support for the printing screen. The printing screens were designed using the *Inkscape* software package to create screen templates. The screens were fabricated with a 90T polyester mesh supplied by Serigraf Ltd.

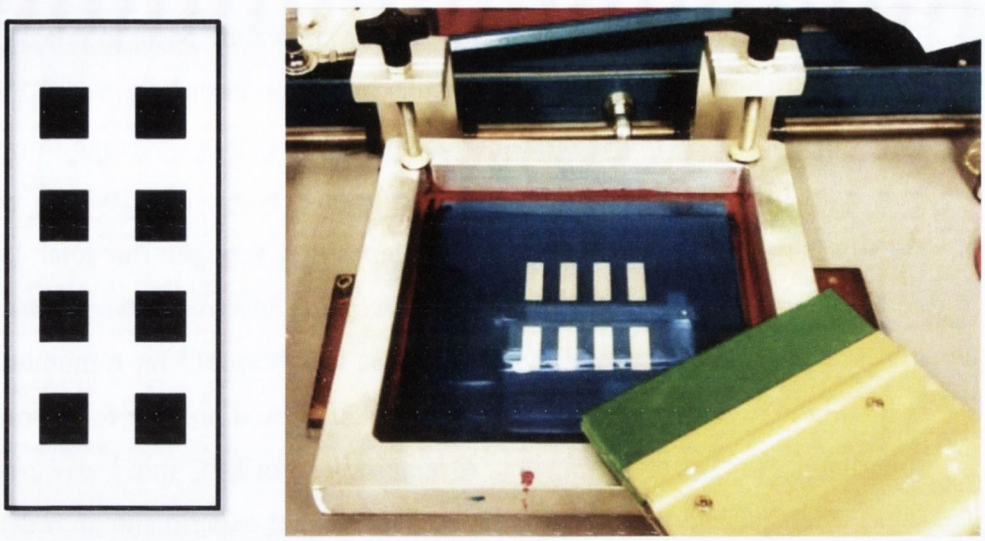

Figure A.6 Screen template design for 8 x 1cm^2 photoanodes and photographic image of the screen printing setup.

The TiO_2 electrodes were prepared on FTO (2.3 mm thick, 13 $\Omega\square^{-1}$) coated glass substrates. Before deposition the glass substrates were cleaned in a detergent solution with ultrasonication for 15 minutes followed by sonication in ethanol (10 min) and acetone (10 min). A bulk TiO_2 layer was applied to the FTO coated glass from a 40 mM aqueous $TiCl_4$ solution. FTO glass plates were submerged in the $TiCl_4$ solution at 70 °C for 30 minutes. Once removed, the glass was washed with water and alcohol. The function of the bulk TiO_2 layer is to increase the adhesion of the nanoparticulate layer to the glass substrate. It has also been suggested that this layer also functions as a blocking layer, in that it blocks back electron transfer from the conductive glass substrate to the electrolyte.[2] It has been shown that recombination occurs predominately in this region.[3] In order to form the mesoporous electrode, TiO_2 paste was applied to FTO coated substrates using the screen printing method. TiO_2 pastes were fabricated according to the procedure outlined by Ito et al.[2] The paste formulation procedure is described in the experimental section (chapter 2.2.16). Electrodes were produced by applying 7 individual coatings of the 20 nm TiO_2 paste onto FTO substrates. After application of each layer the electrodes were allowed to settle in an ethanol chamber for 6 minutes and were then dried for 3 minutes at 125 °C.

Placing the electrodes in the ethanol chamber allows the paste to relax in an environment with a constant vapour pressure and results in a smoother film to form. The deposition of 7 layers of 20 nm TiO_2 created a photoactive layer with an average thickness of ~11 μm. Following this, 2 layers of the light scattering TiO_2 (150–200 nm particles) (Dyesol WERO-2 paste) were deposited. This deposition brought the total layer thickness to between 14-17 μm after sintering. TiO_2 working electrodes were treated to a sintering profile which consisted of a drying period at 125 °C min^{-1} for 6 minutes, ramping to 350 °C and holding for 15 minutes, ramping to 450 °C and holding for 15 minutes and finally sintering at 500 °C for 15 minutes. A ramping rate of 8 °C min^{-1} was used for all ramping steps. The sintering protocol was tuned over several experiments in order to allow for the formation of stable, crack free films which were well adhered to the FTO. Once cooled the electrodes were immersed into a 40 mM aqueous $TiCl_4$ solution and heated to 70 °C for 30 minutes. This process allows for TiO_2 to enter the pores of the electrode and link adjacent particles of TiO_2 through the formation of TiO_2 bridges. This allows for more efficient electron transport through the film and is also thought to act as a recombination blocker. Upon removal from the $TiCl_4$ bath electrodes were cleaned with water and alcohol and treated to a second sintering step at 500 °C for 30 minutes. The electrodes were allowed to cool to 80 °C and were then immersed into a solution of cis-Bis(isothiocyanato)(2,2'-bipyridyl-4,4'-dicarboxylato)(4,4'-di-nonyl-2' bipyridyl)ruthenium(II) (Z907) (0.3 mM) in a mixture of acetonitrile and tert-butanol (vol ratio 1 : 1). TiO_2 electrodes were allowed to soak in the bath for periods of approximately 16 hours. The final TiO_2 thickness was measured to be between 14–17 μm as measured through SEM and profilometry.

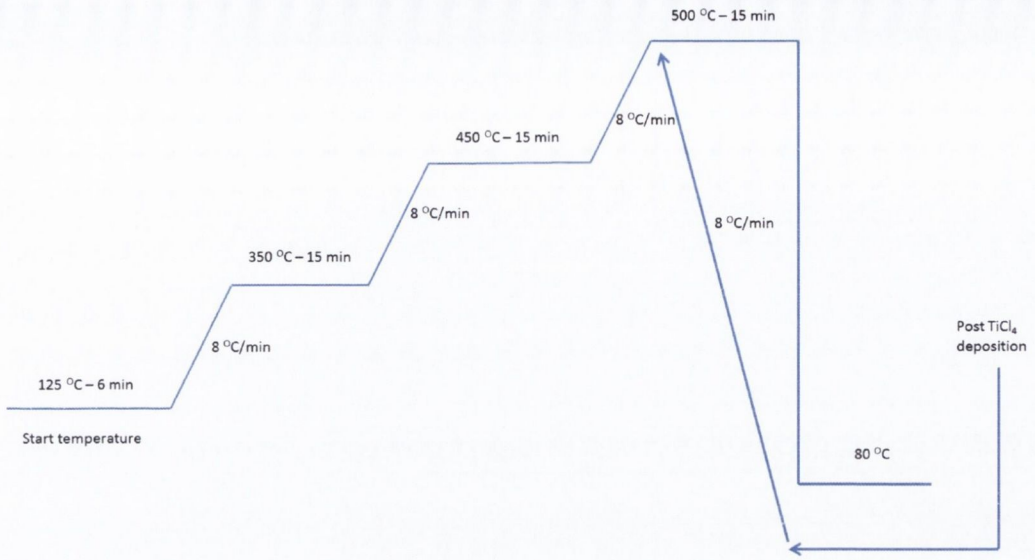

Figure A.7 Outline of sintering profile used for the heat treatment of TiO_2 photoanodes

The screen printing approach allowed for the controlled deposition of TiO_2 and electrodes could be fabricated uniformly and in large volumes as seen from the image below (Figure A.8)

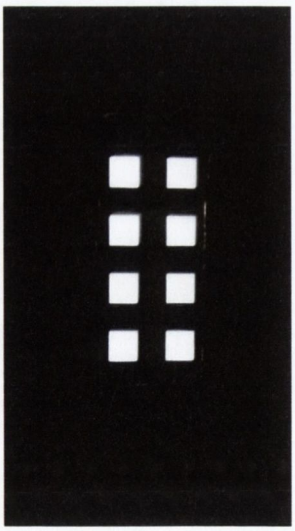

Figure A.8 Photographic image of 8, 1 cm x 1 cm TiO_2 photoanodes on an FTO glass substrate, post sintering.

A.3 Characterisation of TiO_2 photoanodes

Single layer deposition of TiO_2 onto glass substrates were transparent enough to allow for analysis with Uv-Vis spectroscopy. The optical absorption of the oxide reached a maximum at 372 nm. From this value an estimate of the band gap could be calculated using the following expression, whereby E(eV) is energy in electronvolts at wavelength λ, h is planks constant (eVs) and c is the speed of light (ms^{-1})

$$E(eV) = hv = \frac{hc}{\lambda} \quad (1)$$

Using this approach a band gap of 3.3 eV was calculated for the oxide. This value is exactly what would be expected for the bandgap of TiO_2 in the anatase phase.

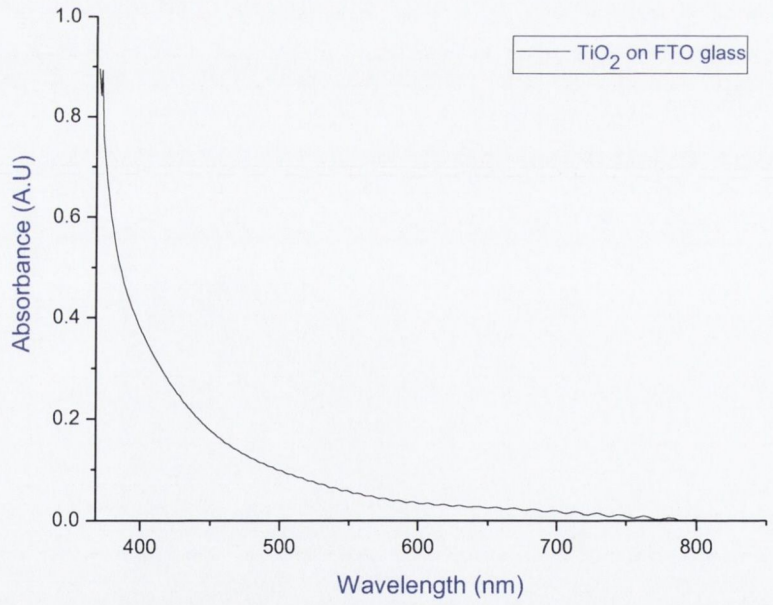

Figure A.9 Optical absorption of anatase TiO_2 film deposited onto FTO.

The phase of the material was also confirmed using Raman spectroscopy. The Raman scattering properties of TiO_2 can be used effectively to define the phase of TiO_2 present.[4] Figure A.10 below shows the Raman spectra recorded for a TiO_2 film deposited onto a glass substrate. The Raman scattering signal indicates the presence of anatase TiO_2[5,6] and

can be attributed to Raman-active fundamental modes of the anatase phase, which appear at 141.1 cm^{-1} (Eg) and 392.6 cm^{-1} (B1g), which correspond to O–Ti–O bending type vibrations, 513.2 cm^{-1} (doublet of A1g and B1g) and 633.8 cm^{-1} (Eg), that are related to Ti–O stretching type vibrations.

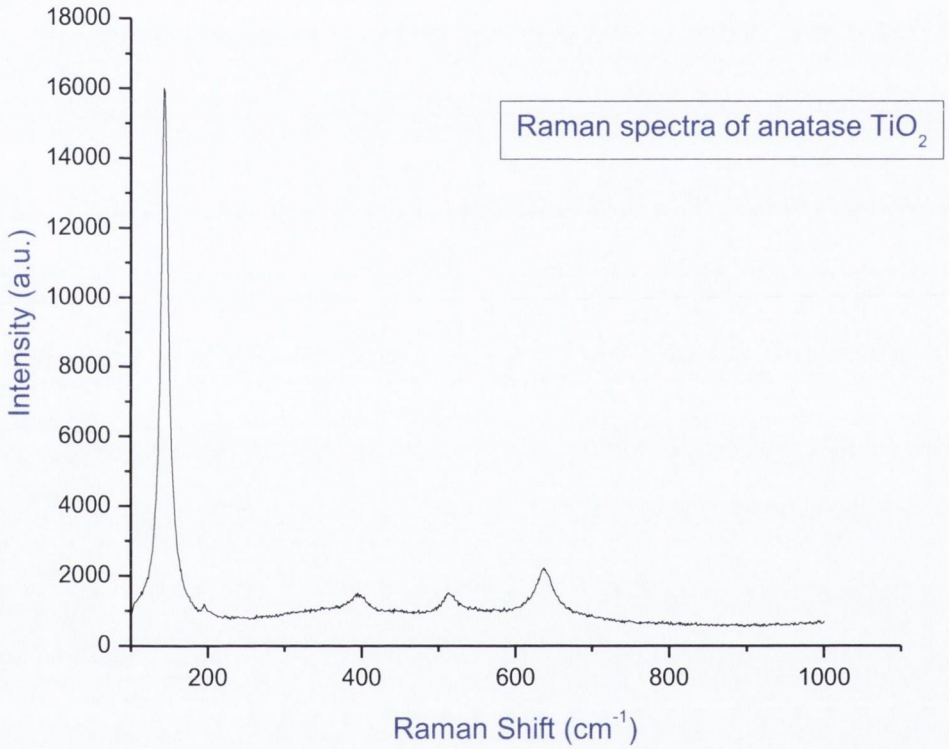

Figure A.10 Raman spectra recorded for anatase TiO_2 on a glass substrate.

X-Ray diffraction was also recorded for the Degussa P25 TiO_2 powder. The X-Ray diffraction pattern is presented in figure A.11 below. The diffraction pattern shows the associated diffraction peaks which are associated with the anatase (blue) and rutile (red) phase of TiO_2.

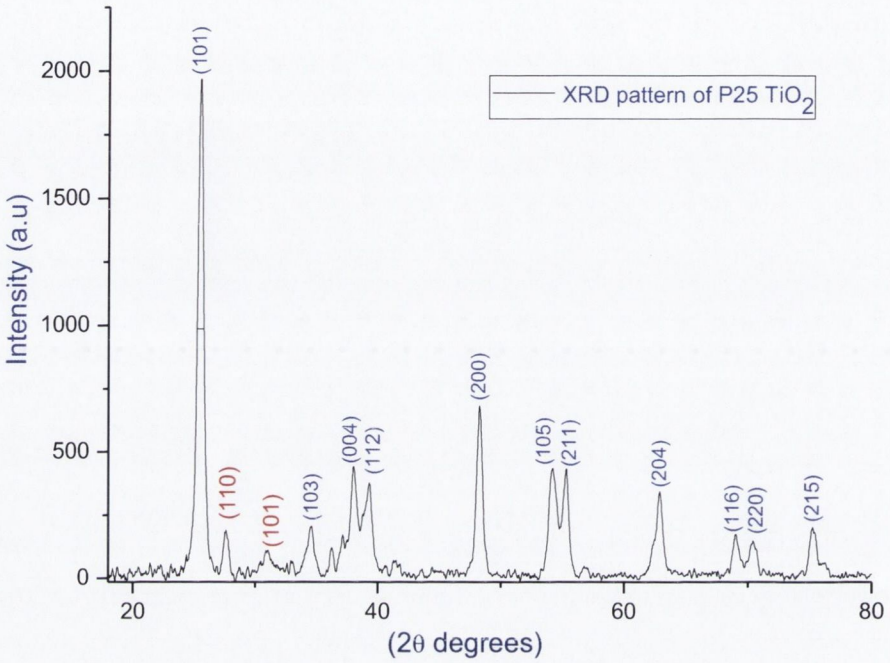

Figure A.11 X-ray diffraction pattern recorded for degussa P25 anatase TiO_2 powder.

Using the Scherrer equation it is possible to relate the size of the TiO_2 nanoparticles to the broadening of the peaks in the diffraction pattern. The Scherrer equation can be written as

$$S = \frac{k\lambda}{\beta cos\theta} \qquad (2)$$

Where S is particle size in nm, k is the Scheerer constant (generally close to unity and can vary depending on the shape of the crystal) β is the FWHM of the diffraction, measured in radians and corrected for equiptment line broadening while θ is the angle of Bragg diffraction.

Calculation of S for the (101) diffraction peak gave an S value of 20.3 nm and 27.4 nm for the (200) diffraction peak. These values are in the ideal range for fabricating photoanodes for DSSCs. This value is also in extremely close agreement with the values obtained for particle size in the TEM and SEM, as seen in figure A.12 and A.13.

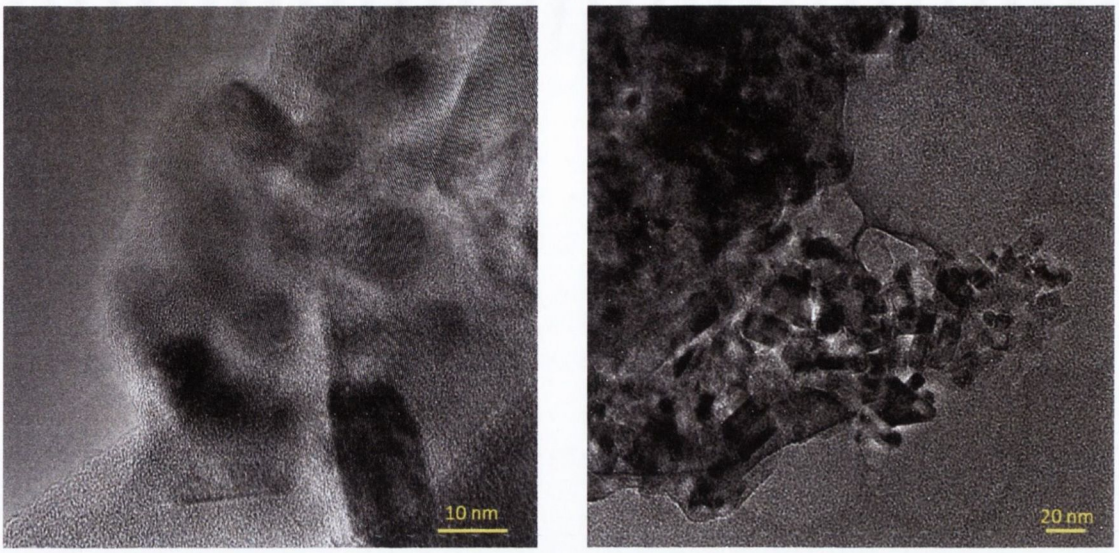

Figure A.12 HRTEM images of anatase TiO_2 nanoparticles

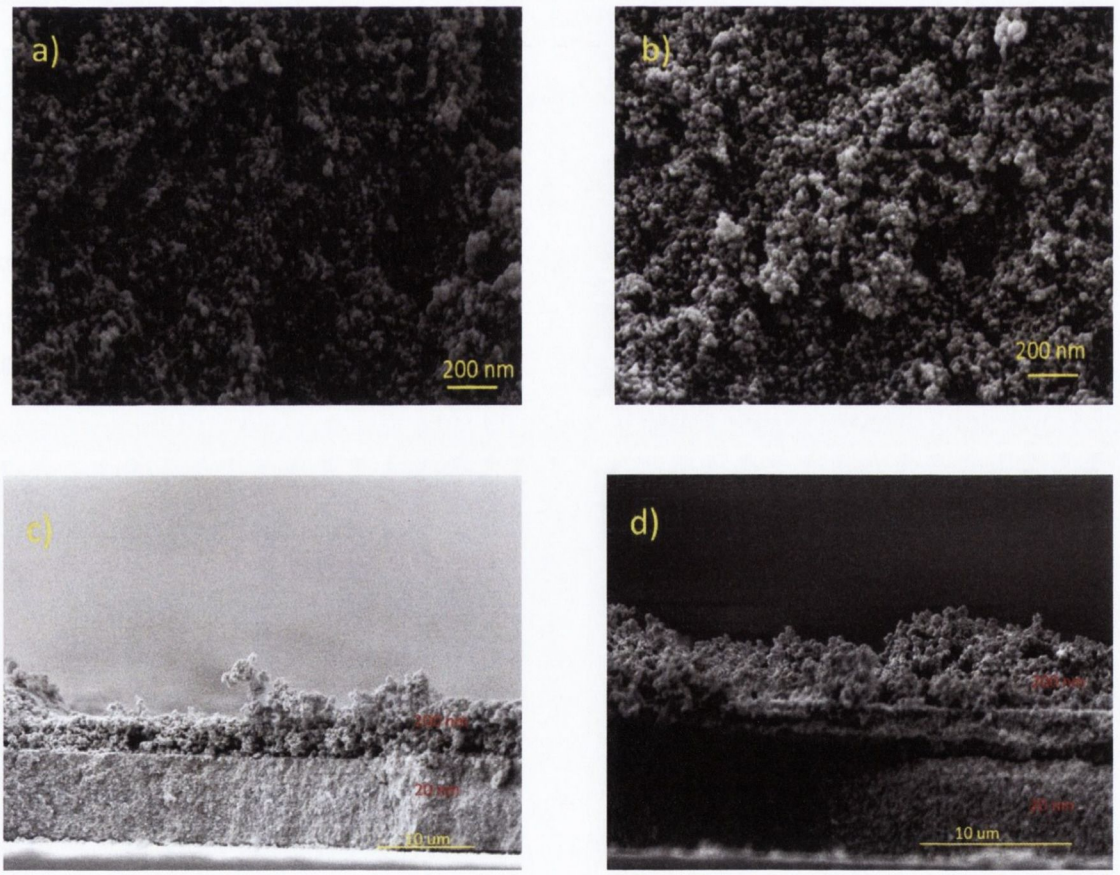

Figure A.13 SEM images recorded for TiO_2 photoanodes fabricated using the screen

printing method. Images a) and b) shows 20 nm TiO_2 nanoparticles, while images c) and d) show the side profile of the photoanodes, with both the light absorption and light scattering layers.

A.4 Profilometry

Side profile imaging of the electrodes in the SEM is a useful means of calculating the TiO_2 depth at that particular point, however side profile imaging does not give an insight into the film depth across the whole electrode. This can be facilitated through profilometry, which allows one to obtain useful information regarding film depth across the whole electrode. The data obtained through mapping the profile of the TiO_2 electrode in this manner gives a much more conclusive insight into the depth profile of the electrode. Figure A.14 below shows a characteristic profile map of a 1 cm x 1 cm TiO_2 electrode which was fabricated using the screen printing technique. As can be seen from the image the electrode is free from cracks and has a largely uniform profile across the surface of the film. The depth of the film is ~ 15 μm, which would agree well with the findings obtained through SEM. Figure A.15 below shows a highlighted region of the electrode, showing the stepped nature of the electrode and the clean boundary that can be obtained between the TiO_2 and the glass substrate after the deposition of 9 individual layers of TiO_2

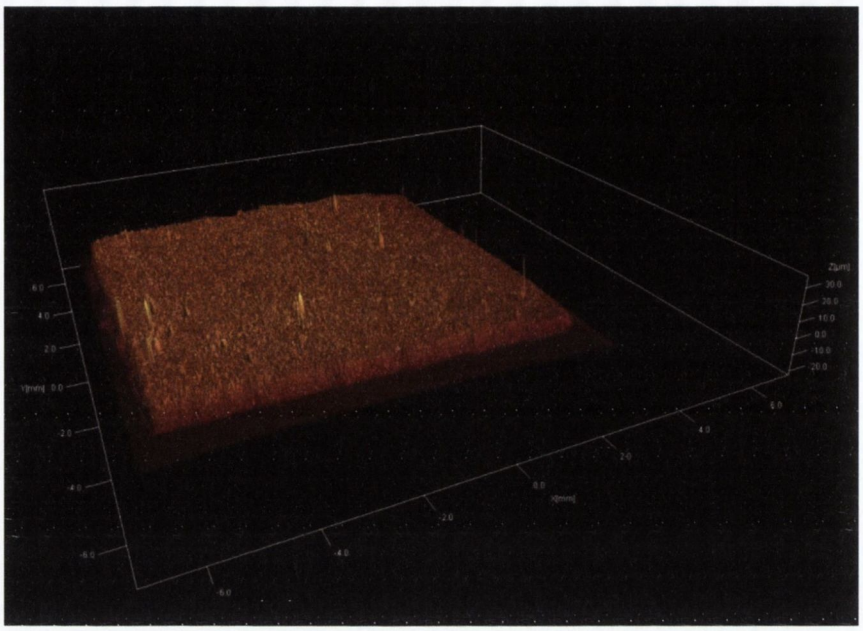

Figure A.14 Profilometry image recorded for a TiO_2 (1 cm^2) electrode fabricated using the screen printing method.

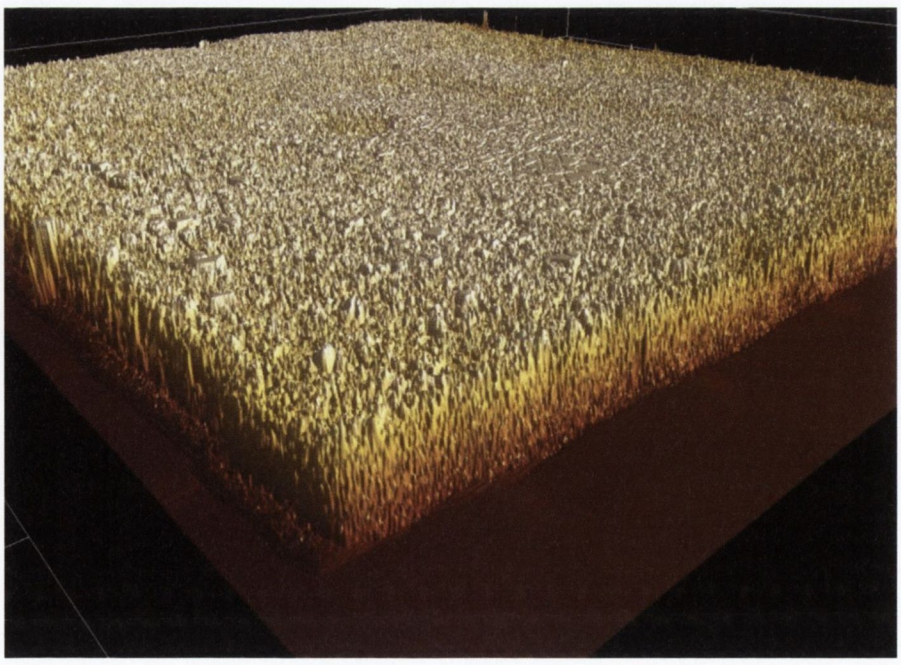

Figure A.15 Magnification of figure A.14 above highlighting the stepped nature of the TiO_2 working electrode

Analysis of the electrodes thickness profile could be carried out using the profilometry software package. The images below represent the average line spectra recorded across the electrodes with respect to X and Y. The averaged profiles shown represent 675 individual line profiles which were recorded for the electrode. As can be seen from the averaged profiles shown the film depth has a mean thickness of 13.6 μm ± 2.58 μm with respect to X (figure A.16) and a mean thickness of 16.91 μm ± 3.63 μm with respect to Y (figure A.17). Figure A.18 below shows the profile obtained for a single line scan which was taken across the film, highlighting some of the pitted features which can be observed in these electrodes.

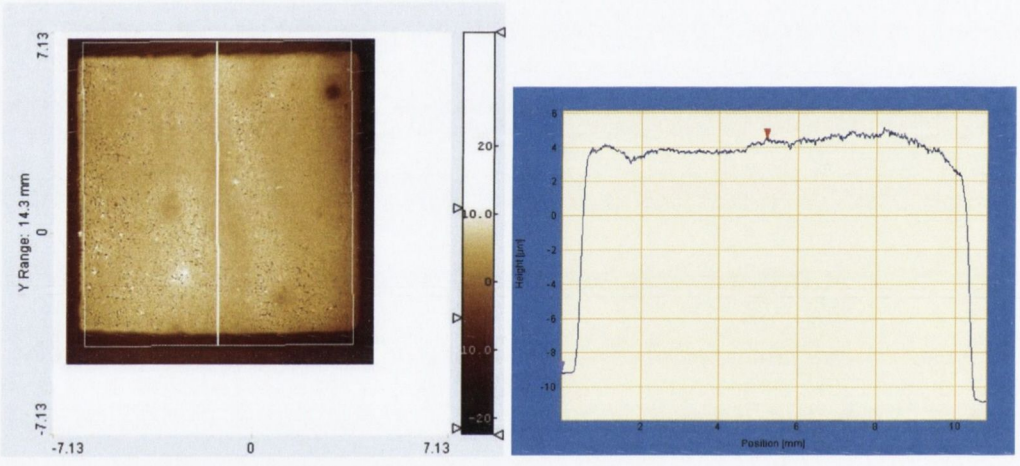

Figure A.16 Topographical image produced through profilometry and the average thickness profile recorded along X axis.

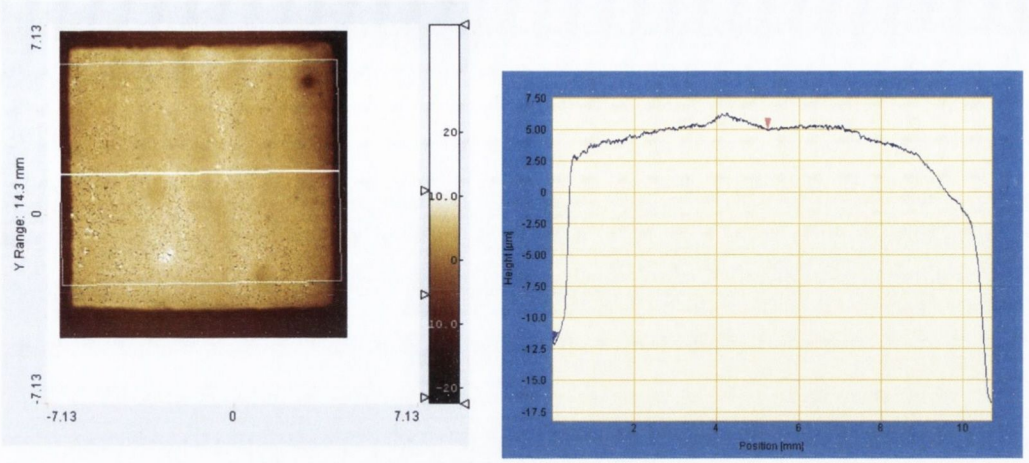

Figure A.17 Topographical image produced through profilometry and the average thickness profile recorded along Y axis

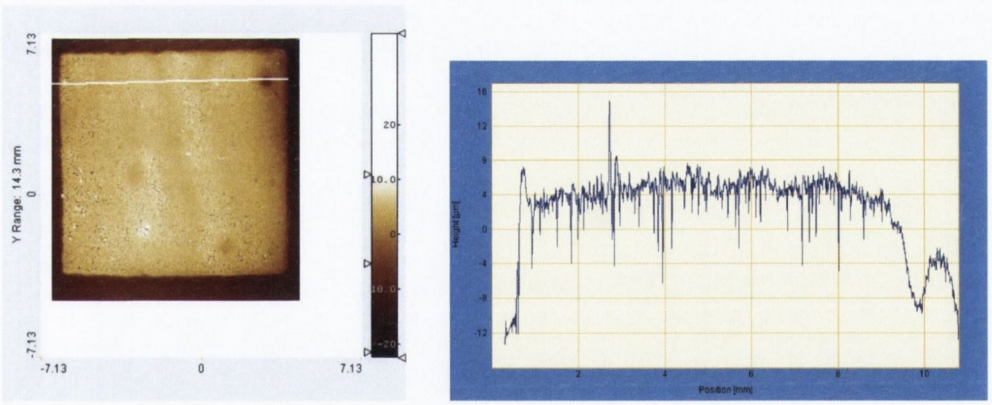

Figure A.18 Topographical image produced through profilometry and the line profile recorded along the trace above highlighting the pitted region.

In order to fully ensure that the screen printing technique was allowing the fabrication of electrodes of similar quality, chronoamperometric *I-t* analysis was frequently carried out on the electrodes after thermal treatment. This step was necessary, as any deviation obtained in the photocurrent values obtained at this stage would lead to misinterpretation of results of fully assembled cells. It would also cause significant errors in experiments

where very small photocurrents were being measured. Figure A.19 below shows the chronoamperometric *I-t* analysis that was obtained from 6 TiO_2 working electrodes that were fabricated using the screen printing technique. Chronoamperometric *I-t* data was obtained in a 3 electrode electrochemical cell using a TiO_2 working electrode obtained after thermal treatment, a FTO counter electrode and a saturated (KCl) calomel reference electrode. The results obtained show that the screen printing method allowed for electrodes to be fabricated which show a deviation of only 1 μA cm^{-2} when illuminated with UV radiation (365 nm)

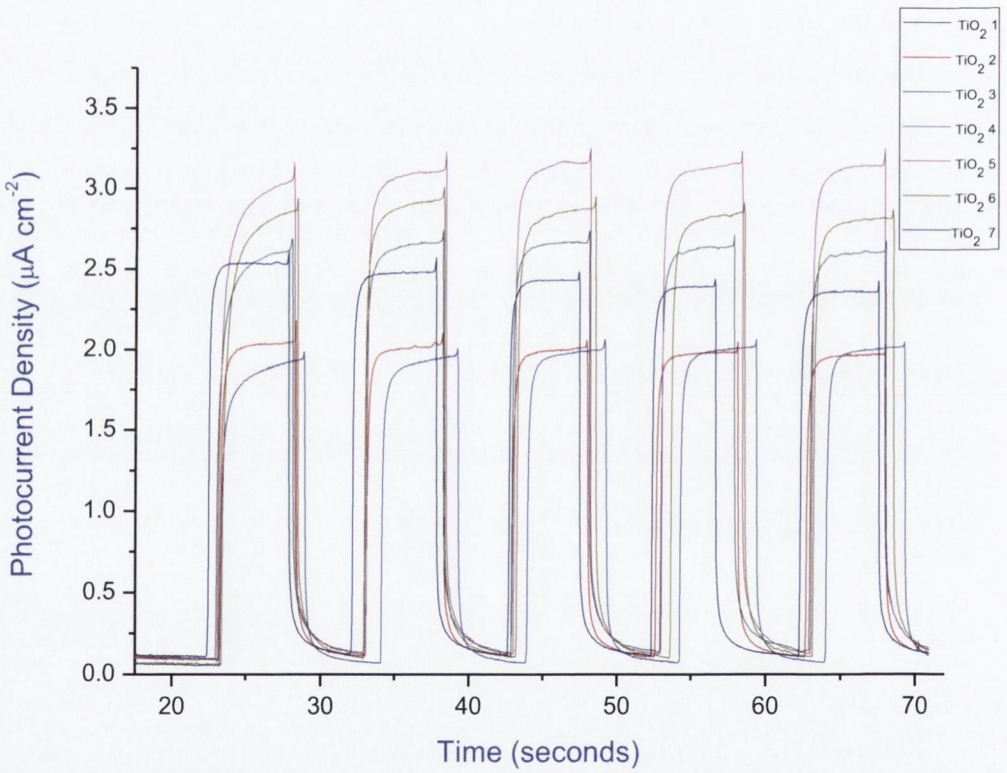

Figure A.19 Chronoamperometric *I-t* analysis obtained from 6 individual TiO_2 working electrodes fabricated using the screen printing technique

A.5 Conclusions

In conclusion, a reproducible method for the fabrication of TiO_2 photoanodes has been developed using a custom screen printing method. The screen printing method proved to be much more effective than the doctor blade method at producing stable and crack free photoanodes for solar cell electrodes. Using the screen printing method it was possible to fabricate TiO_2 electrodes with an average thickness of 13.6 μm ± 2.58 μm with respect to X and a mean thickness of 16.91 μm ± 3.63 μm with respect to Y. The TiO_2 photoelectrodes were fabricated from a commercial TiO_2 source (Degussa P25) which was used as the material for the deposition of the light absorption layer which the light scattering layer was deposited from a paste supplied from Dyesol Ltd.. The resulting photoanodes showed an extremely sharp switching response to on/off light cycles and the photocurrent produced from the electrodes varied as little as 1 μA cm^{-2} between individual electrodes when illuminated with UV radiation at 365 nm. The procedure outlined in this chapter has been used as the method for producing photoanodes for all subsequent chapters of this thesis and is thus deemed to be an important piece of work as it decreases the error in subsequent results.

References

(1) Z. Zhang, S. I., B. O'Regan, D. Kunag, S.M. Zakeeruddin, P. Liska, R.; Charvet, P. C., Md. K. Nazeeruddin, P. Péchy, R. Humphry-Baker, T.; Koyanagi, T. M., M. Grätzel *Z. Phys. Chem* **2007**, *221* 319.

(2) Ito, S.; Chen, P.; Comte, P.; Nazeeruddin, M. K.; Liska, P.; Péchy, P.; Grätzel, M. *Progress in Photovoltaics: Research and Applications* **2007**, *15*, 603.

(3) K. Zhu, E. A. S., N.-G. Park, J. Van de Lagemaat, A.J. Frank *Appl. Phys. Lett* **2002**, 685.

(4) Zhang, W. F.; He, Y. L.; Zhang, M. S.; Yin, Z.; Chen, Q. *J. Phys. D-Appl. Phys.* **2000**, *33*, 912.

(5) Cheng, H. M.; Ma, J. M.; Zhao, Z. G.; Qi, L. M. *Chemistry of Materials* **1995**, *7*, 663.

(6) Park, N. G.; Schlichthörl, G.; van de Lagemaat, J.; Cheong, H. M.; Mascarenhas, A.; Frank, A. J. *The Journal of Physical Chemistry B* **1999**, *103*, 3308.

Publications

Carbon Nanomaterials for Dye-Sensitized Solar Cell Applications: A Bright Future

Lorcan J. Brennan, Michele T. Byrne, Mazhar Bari and Yurii K. Gun'ko
Advanced Energy Materials, **2011**, 4, 472.

Graphene–ionic liquid electrolytes for dye sensitised solar cells

Lorcan J. Brennan, Sebastian T. Barwich, Amro Satti, Adeline Faure and Yurii K. Gun'ko
Journal of Materials Chemistry A **2013**, 1, 8379.

Fabrication of highly transparent and conducting PEDOT:PSS films using a formic acid treatment

Joseph E. McCarthy, Cormac A. Hanley, Lorcan J. Brennan, Vito G. Lambertini and Yurii K. Gun'ko
Journal of Materials Chemistry C, **2014**, 2,764.

Hot electrons for generation of enhanced photocurrent in gold - TiO_2 nanocomposites

Lorcan J. Brennan, Finn Purcell-Milton, Aurélien S. Salmeron, Hui Zhang, Alexander O. Govorov & Yurii K. Gun'ko

Nanoscale Research Letters 2015, **10**:38

Advances in the Organometallic Chemistry of Carbon Nanomaterials

Lorcan J. Brennan and Yurii K. Gun'ko

Organometallics DOI: 10.1021/om501258j